Seismic attenuation for Advanced Virgo
Vibration isolation for the external injection bench

Mathieu Blom

Cover: designed by Frans Mul, featuring a mixed media drawing of EIB-SAS.

Printed by: Proefschriftmaken.nl || Uitgeverij BOXPress.
Published by: Uitgeverij BOXPress, 's-Hertogenbosch.

This work is part of the research program of the Foundation for fundamental Research on Matter (FOM), which is part of The Netherlands Organization for Scientific Research (NWO).

VRIJE UNIVERSITEIT

Seismic attenuation for Advanced Virgo
Vibration isolation for the external injection bench

ACADEMISCH PROEFSCHRIFT

ter verkrijging van de graad Doctor aan
de Vrije Universiteit Amsterdam,
op gezag van de rector magnificus
prof.dr. V. Subramaniam,
in het openbaar te verdedigen
ten overstaan van de promotiecommissie
van de Faculteit der Exacte Wetenschappen
op woensdag 9 december 2015 om 9.45 uur
in de aula van de universiteit,
De Boelelaan 1105

door

Matheus Ronaldus Blom

geboren te Badhoevedorp

promotor: prof.dr. J.F.J. van den Brand
copromotor: dr. A. Bertolini

Panta Rhei,
Heraclitus (ca. 500 BC)

Contents

Introduction

"There is nothing more deceptive than an obvious fact."
– Sir Arthur Conan Doyle,
Sherlock Holmes: The Boscombe Valley Mystery (1891)

Gravitational waves *should* exist, but are hard to detect. According to Einstein's theory of general relativity, which he published in 1916 [1], space and time form one single entity: spacetime. What we observe as gravity is actually a curvature of spacetime and spacetime in turn is curved due to the presence of mass (Fig. 1).

Celestial objects that perform an oscillatory motion, say a binary neutron star system, periodically deform spacetime and hence generate gravitational waves* (Fig. 2). These deformations are modest, *i.e.* the amplitudes of the gravitational waves are small. The relative length change they induce is called *strain*. The strain that may be expected on Earth from a nearby (~100 Mpc), perfectly oriented source is only of the order of 10^{-23}, and thus gravitational waves are hard to observe.

There are convincing experimental indications that gravitational waves exist. The best known is the periastron (point of closest approach of a star that is not the Sun) shift of the Hulse-Taylor pulsar. In 1974, Russell Hulse and Joseph Taylor discovered a binary system of which one of the stars is a millisecond-pulsar [2]. After monitoring the orbit of the pulsar for a number of years they discovered that the changes in orbital parameters were consistent with the amount of energy the system should lose due to the emission of gravitational waves [4]. For this discovery they received the Nobel prize in Physics in 1993. Fig. 3 shows a 30-year measurement of the periastron shift of the pulsar together with the general relativity prediction. They agree remarkably well.

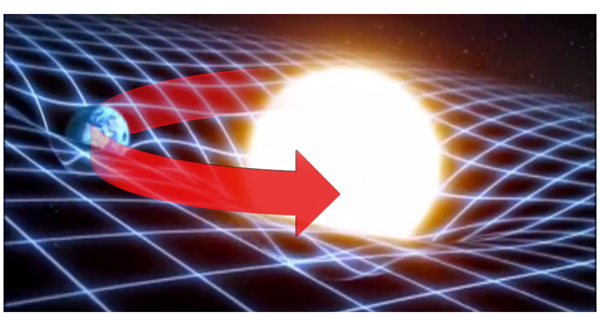

Figure 1: *Curvature of spacetime by the Sun causes the gravitational pull on the Earth. [Credit: WGBH Boston [3]]*

*To create a gravitational wave the body's mass distribution must give rise to a time-varying mass-quadrupole. Monopoles and dipoles are not possible because of conservation of energy and momentum.

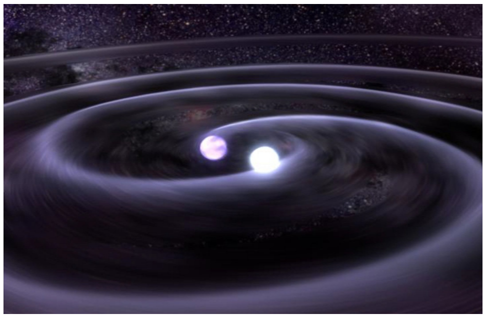

Figure 2: *Generation of gravitational waves by a binary system. [Credit: NASA [5]]*

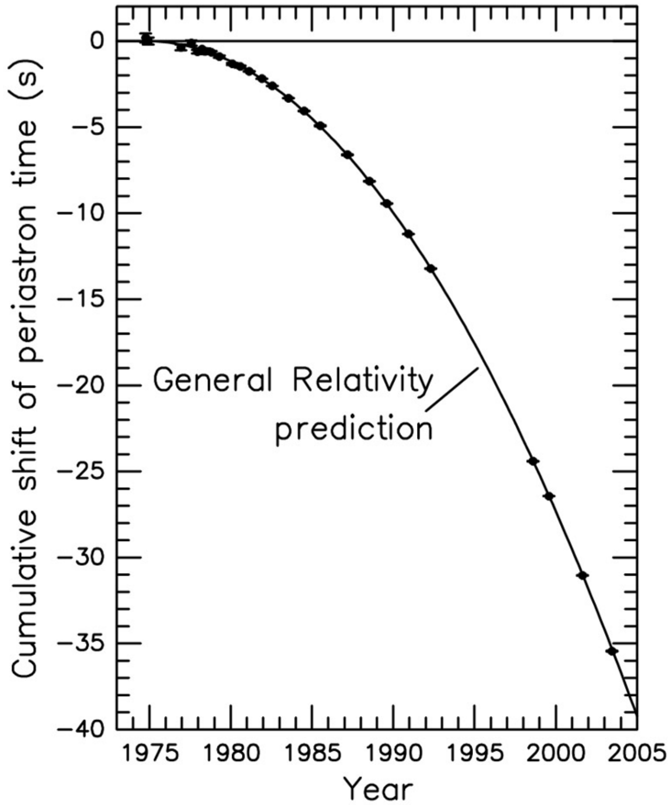

Figure 3: *Periastron shift of the Hulse-Taylor pulsar measured over a period of thirty years together with the prediction from general relativity where the system is losing energy due to the emission of gravitational waves. Figure taken from Ref. [6].*

How to observe a gravitational wave

The idea that gravitational waves may be measured with a Michelson interferometer was first put forward by M. Gertsenshtein and V. Pustovoit [7]. A gravitational wave that traverses the detector will effectively shrink one arm and elongate the other. The gravitational waves create length differences between the two interferometer arms which can be sampled with light. However, the challenge is formidable, since to detect a gravitational wave, we need to construct an interferometer capable of observing relative length changes of the order of the gravitational wave strain 10^{-23}.

The first large-scale interferometer was constructed by Forward *et al.* [8] at Hughes Research Laboratories (Malibu, California) in the 1970s. It had a an effective arm length of 8.5 m and a strain sensitivity of 3×10^{-16}. A full treatment of the possible sensitivity of such detectors was made by Rainer Weiss [9] who was the first to propose the construction of a km-scale interferometer that would have an adequate sensitivity to detect gravitational waves. Fig. 4 shows that several such interferometers exist around the world today: two LIGO [10] detectors in the USA and a third planned in India, GEO600 [11] in Germany, the cryogenic interferometer KAGRA [12] under construction in Japan, and Virgo [13] just outside Pisa, Italy.

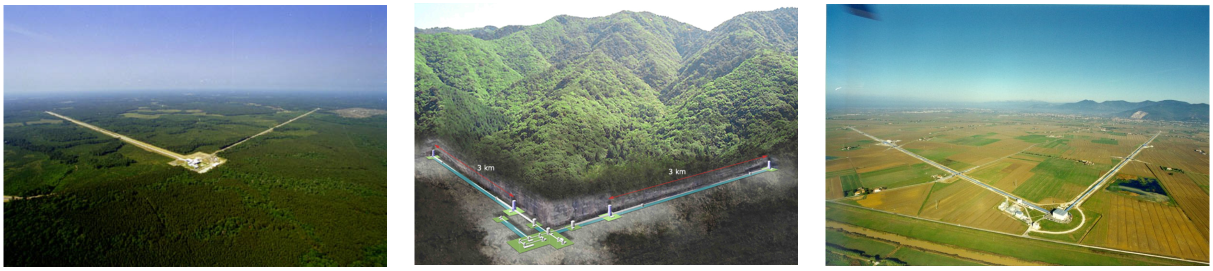

aLIGO. [Credit: LIGO [10]] *KAGRA. [Credit: KAGRA [12]]* *Advanced Virgo. [Credit: Virgo [13]]*

Figure 4: *Global network of interferometric gravitational wave detectors.*

Such interferometric gravitational wave detectors are limited by their ability to isolate their test masses (the main interferometer) from noise. The LIGO and Virgo detectors have reached sensitivities of $10^{-23}/\sqrt{\text{Hz}}$. Currently, they are undergoing a major upgrade which will enhance their sensitivities to the $10^{-24}/\sqrt{\text{Hz}}$ level [10, 14]. These 2$^{\text{nd}}$ generation detectors are called Advanced LIGO (aLIGO) and Advanced Virgo (AdV). With these improved detectors, the first direct observation of a gravitational wave is imminent.

New seismic isolation system for Advanced Virgo

A detailed study of Virgo's sensitivity revealed that seismically induced motion of the external injection bench (optical bench between the bench housing the laser and the Virgo vacuum system) caused a fluctuation in the laser beam's propagation direction, which caused so-called *beam jitter noise*. The unprecedented sensitivity of Advanced Virgo will only be reached if this noise source is eliminated.

To accomplish this, a new support structure for this optical bench was realized: the external injection bench seismic attenuation system, abbreviated to EIB-SAS (see Fig. 5). It is a single stage vibration isolation system that is operated in air. It uses passive mechanical resonators combined with anti-spring technology to provide isolation to seismic ground vibrations. The resonant motion of the system is actively damped with feedback. The design of EIB-SAS is derived from a prototype device that was constructed for Advanced LIGO at Caltech for R&D purposes [15] and which was improved upon at the Albert Einstein Institute in Hanover [16]. EIB-SAS has a neutral response at low frequencies and provides 40-60 dB of isolation above 10 Hz. The system was installed and commissioned in Virgo in early 2013 and was the first major upgrade for Advanced Virgo. This thesis contains a comprehensive description and characterization of the system and presents results of performance measurements.

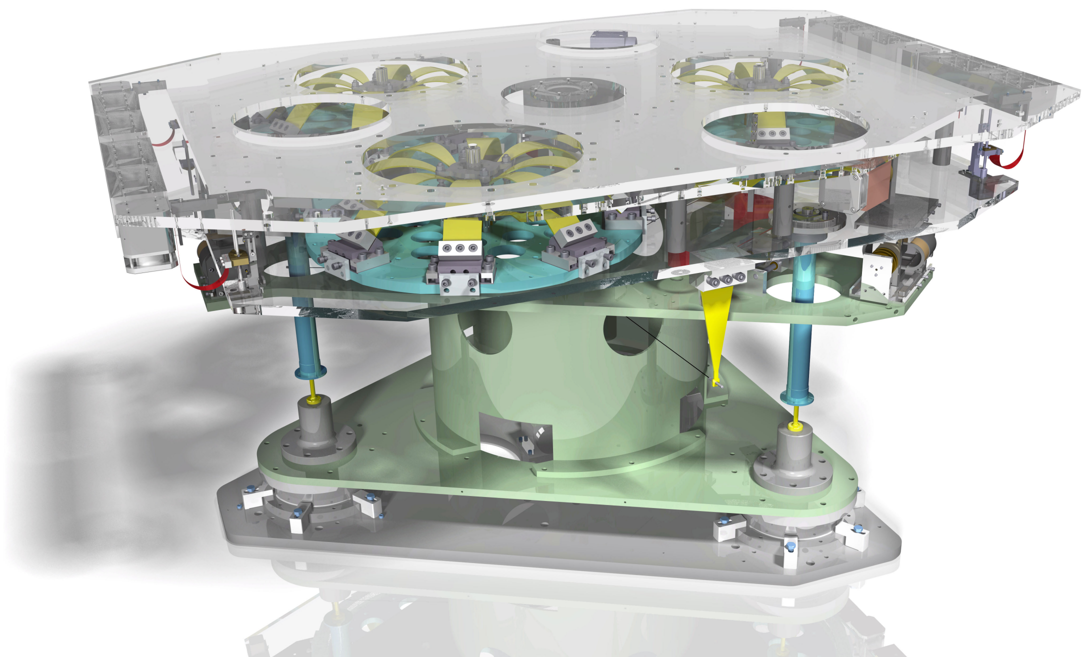

Figure 5: *The external injection bench seismic attenuation system: EIB-SAS.*

Thesis outline

Chapter 1 begins with a short introduction to general relativity and goes on to sketch how a time-varying mass distribution gives rise to gravitation waves and how one could go about to detect such a wave. The most relevant sources of gravitational waves are described and an estimate is made of the expected event rate for Advanced Virgo.

In chapter 2 we describe in detail the most important aspects of interferometric gravitational wave detectors and what steps have been made to maximize their sensitivity. Fundamental and practical limits of the detector are discussed, which leads to the introduction of a noise budget. We summarize the upgrade efforts of the Virgo detector to Advanced Virgo, motivate the necessity for EIB-SAS and list the requirements this system needs to meet.

A full description of EIB-SAS and the mechanical filters it contains is provided in chapter 3 along with a model of their isolation capabilities. In chapter 4 some finite element and Lagrangian models are given to demonstrate the internal modes of the system. Then, in chapter 5 we report on the characterization and validation measurements and compare EIB-SAS in situ to the old external injection bench support structure to show that the original problem of beam jitter noise has been solved and no new noise sources have been introduced. In chapter 6 we conclude with the characterization of two newly designed GAS filter blades whose shapes have been fashioned in such a way that the internal stress in the blades are minimized.

1 Theory

"There is more treasure in books than in all the pirate's loot on Treasure Island."
– Walt Disney.

1.1 Introduction

For over a century Einstein's theory of general relativity has been the reigning theory of gravity, replacing Newton's description of the gravitational force. In addition to being in better accordance with the observations of gravitational effects, general relativity predicts new phenomena, one of which is the existence of gravitational waves.

This chapter contains some theoretical background of gravitational waves: how they are generated, how they could be detected and what event rates may be expected in the initial and advanced detector networks. First, the basics of general relativity are summarized in sections 1.2 and 1.3. The prediction of the existence of gravitational waves is the subject of section 1.4. How these waves can be observed by monitoring the separation distance of a ring of freely falling test masses is described in section 1.5. The astronomical sources of gravitational waves that are expected to exist in the (early) Universe are treated in section 1.6. The most promising source for the first detection of a gravitational wave *i.e.* the one with the highest expected event rate is the coalescence of compact binaries. In section 1.7 we introduce a figure of merit for the detector's sensitivity: the horizon. The expected event rates in the initial and advanced detector networks for binary neutron stars, binary black holes and neutron star black hole binaries are discussed in section 1.8.

1.2 Descriptions of gravity

In the beginning of the 20^{th} century the leading theory of gravity was the one formulated by Isaac Newton. In his *Philosophiæ Naturalis Principia Mathematica*, published in 1687, he formulated his mathematical description of gravity and derived Kepler's laws of planetary motion. In Newtonian mechanics, the magnitude of the gravitational force between two objects of mass m_1 and m_2 separated by a distance r is

$$F_g = G\frac{m_1 m_2}{r^2}, \tag{1.1}$$

where G is the *Gravitational Constant*. In this description, gravity is an instantaneous force that can act without a medium. This aspect of the theory not even Newton himself liked, but it was an issue he was unable to resolve.

Newton's theory of gravity stood unchallenged for centuries, but by the beginning of the 19th century it was clear that it had its flaws. Although it described the motion of most celestial bodies quite accurately, Mercury did not seem to behave as it should. In 1859, Urbain Le Verrier had observed that the perihelion precession of Mercury deviated from the Newtonian prediction by 38" per century* [17].

In 1916, Albert Einstein's paper [1] was published in which he introduced his theory of general relativity and, amongst other things, showed that it correctly describes the anomalous perihelion precession of Mercury. In this description, gravity is not a force, but a feature of *spacetime*.

In general relativity the laws of physics are defined on spacetime similar to how they are defined on space *and* time in Newtonian mechanics. Spacetime is curved by matter and energy and what we perceive as a gravitational force is a manifestation of this curvature. Spacetime tells matter how to move, matter tells spacetime how to curve [18]. As far as the Earth is concerned, it's just freely falling along a straight trajectory in spacetime (*i.e.* traveling along a geodesic), which happens to be curved by the Sun. In turn, the curvature of spacetime created by the Earth dictates the motion of the Moon.

1.3 Basics of general relativity

One of the assumptions made in general relativity [19, 20] is that there exists a maximum speed at which information can travel. Therefore, in general relativity gravity is no longer an instantaneous force, but is communicated at this ultimate, but finite speed. This speed happens to be the speed of light c and it is constant in all inertial frames.

An inertial frame is a coordinate frame that is subject only to gravity. It is freely falling, but otherwise unaccelerated. The observers in the inertial frames agree on the speed of light, but the time and distance between events is no longer well-defined. Instead, there is the *interval*

$$ds^2 = -(cdt)^2 + dx^2 + dy^2 + dz^2, \tag{1.2}$$

which is *invariant under change of coordinates i.e.* it has the same value in all inertial frames.

*This was later adjusted to 43" per century.

The object that encodes the geometry of spacetime is the *metric tensor* $g_{\mu\nu}$. It describes how the basis vectors change expressed in local coordinates. A more general formulation of the interval is

$$ds^2 = g_{\mu\nu} dx^\mu dx^\nu. \tag{1.3}$$

Here, the Einstein summation convention is used, where repeated upper and lower indices are summed over all possible values (0 – 3).

The metric of uncurved spacetime is called *Minkowski space* and it has its own special notation

$$\eta_{\mu\nu} \equiv \begin{pmatrix} -1 & 0 & 0 & 0 \\ 0 & 1 & 0 & 0 \\ 0 & 0 & 1 & 0 \\ 0 & 0 & 0 & 1 \end{pmatrix}. \tag{1.4}$$

Note that inserting $\eta_{\mu\nu}$ for $g_{\mu\nu}$ in Eq. (1.3) reproduces the special interval in Eq. (1.2).

In curved spacetime we can no longer think of a vector as an object that stretches from one point to another, but rather an object that exists at a single point. At each point in spacetime we can define a tangent space as the space of directional derivative operators along curves through that point. The curvature of spacetime manifests itself when relating tangent vectors of nearby points. A unique connection can be constructed from the metric called the *Christoffel connection*

$$\Gamma^\lambda_{\mu\nu} = \frac{1}{2} g^{\lambda\sigma} \left(g_{\nu\sigma,\mu} + g_{\sigma\mu,\nu} + g_{\mu\nu,\sigma} \right), \tag{1.5}$$

where the , μ denotes the partial derivative $\partial/\partial x^\mu$.

The connection defines a way to keep a tensor constant along some path to a neighboring point. This is called *parallel transport* and quantifies the rate of change of a tensor field and makes it possible to compare nearby tensors.

The curvature of the metric is quantified by the Riemann tensor $R^\rho{}_{\sigma\mu\nu}$ which can be derived from the connections

$$R^\rho{}_{\sigma\mu\nu} = \Gamma^\rho_{\nu\sigma,\mu} - \Gamma^\rho_{\mu\sigma,\nu} + \Gamma^\rho_{\mu\lambda}\Gamma^\lambda_{\nu\sigma} - \Gamma^\rho_{\nu\lambda}\Gamma^\lambda_{\mu\sigma}. \tag{1.6}$$

A contraction of the Riemann tensor yields the Ricci tensor

$$R_{\mu\nu} = R^\lambda{}_{\mu\lambda\nu}, \tag{1.7}$$

and the trace of the Ricci tensor is known as the Ricci scalar

$$R = R^\mu{}_\mu = g^{\mu\nu} R_{\mu\nu}. \tag{1.8}$$

In general relativity the curvature of spacetime, *i.e.* of the metric tensor is related to the energy-momentum tensor $T_{\mu\nu}$ by a set of coupled non-linear differential equations known as the *Einstein field equations*

$$R_{\mu\nu} - \frac{1}{2} g_{\mu\nu} R = \frac{8\pi G}{c^4} T_{\mu\nu}. \tag{1.9}$$

1.4 Ripples in spacetime

When the gravitational field is weak, coordinates can be chosen such that the metric can be approximated by that of Minkowski space with small perturbations $h_{\mu\nu}$

$$g_{\mu\nu} = \eta_{\mu\nu} + h_{\mu\nu}, \qquad |h_{\mu\nu}| \ll 1. \tag{1.10}$$

In this approximation the Einstein equations can be linearized. From the metric the Christoffel symbols and hence the Riemann tensor can be calculated

$$R_{\mu\nu\alpha\beta} = \frac{1}{2}\left(h_{\mu\beta,\nu\alpha} + h_{\nu\alpha,\mu\beta} - h_{\mu\alpha,\nu\beta} - h_{\nu\beta,\mu\alpha}\right), \tag{1.11}$$

from which the Ricci tensor and scalar can be computed. If we then define the *trace reversed perturbation* as

$$\bar{h}_{\mu\nu} = h_{\mu\nu} - \frac{1}{2}h\eta_{\mu\nu}, \tag{1.12}$$

Eq. (1.9) becomes

$$-\frac{1}{2}\left(\bar{h}_{\mu\nu,\alpha}{}^{,\alpha} + \eta_{\mu\nu}\bar{h}_{\alpha\beta}{}^{,\alpha\beta} - \bar{h}_{\mu\alpha,\nu}{}^{,\alpha} - \bar{h}_{\nu\alpha,\mu}{}^{,\alpha}\right) = \frac{8\pi G}{c^4}T_{\mu\nu}. \tag{1.13}$$

Next, we choose to work in the Lorentz gauge* $\bar{h}^{\mu\nu}{}_{,\nu} = 0$, which simplifies Eq. (1.13) considerably to

$$-\frac{1}{2}\bar{h}_{\mu\nu,\alpha}{}^{,\alpha} = -\frac{1}{2}\Box\bar{h}_{\mu\nu} = \frac{8\pi G}{c^4}T_{\mu\nu}, \tag{1.14}$$

where $\Box = (-1/c \times 1/\partial t^2 + 1/\partial x^2 + 1/\partial y^2 + 1/\partial z^2)$ is the four-space d'Alembertian.

In vacuum, far away from any possible sources of gravitational waves, $T_{\mu\nu} = 0$ and Eq. (1.14) reduces to

$$\Box\bar{h}_{\mu\nu} = 0. \tag{1.15}$$

This can readily be recognized as a wave equation. Its solutions are

$$\bar{h}_{\mu\nu} = C_{\mu\nu}e^{ik_\sigma x^\sigma}; \tag{1.16}$$

plane waves traveling in the direction of the vector k_σ at the speed of light. From Eq. (1.15) follows that if we do not want the wave to vanish everywhere, the wave vector must meet the condition

$$k_\sigma k^\sigma = 0. \tag{1.17}$$

We are free to impose additional gauge conditions

$$A^{\mu\nu}k_\nu = 0, \quad A^\mu{}_\mu = 0, \quad A_{\mu\nu}U^\nu = 0, \tag{1.18}$$

*Also referred to as De Donder gauge or harmonic gauge.

where U^{ν} is any timelike unit vector. These are known as the *transverse traceless gauge*. Under these conditions $\bar{h}^{\mathsf{TT}}_{\mu\nu} = h^{\mathsf{TT}}_{\mu\nu}$.

We can choose our coordinates such that the wave is traveling in the x^3 direction and call k^0 the frequency of the wave ω. From Eq. (1.17) we know that $k^{\sigma} = (\omega, 0, 0, \omega)$. Then, the only non-zero components of $C_{\mu\nu}$ will be $C_{\mathsf{xx}}, C_{\mathsf{xy}}, C_{\mathsf{yx}}$ and C_{yy}. Because $C_{\mu\nu}$ is traceless and symmetric, we have

$$C_{\mu\nu} = \begin{pmatrix} 0 & 0 & 0 & 0 \\ 0 & C_{\mathsf{xx}} & C_{\mathsf{xy}} & 0 \\ 0 & C_{\mathsf{xy}} & -C_{\mathsf{xx}} & 0 \\ 0 & 0 & 0 & 0 \end{pmatrix} \quad \text{and} \quad h_{\mu\nu} = \begin{pmatrix} 0 & 0 & 0 & 0 \\ 0 & h_{+} & h_{\times} & 0 \\ 0 & h_{\times} & -h_{+} & 0 \\ 0 & 0 & 0 & 0 \end{pmatrix}. \tag{1.19}$$

This shows that our gravitational wave can have two polarizations. If $C_{\mathsf{xy}} = 0$, then it has the '$+$' polarization, while if $C_{\mathsf{xx}} = 0$ it has the '$\times$' polarization.

1.5 Observing gravitational waves

Imagine a ring of freely falling test particles that encounters a gravitational wave traveling in the *z*-direction. How are they affected? If we choose a coordinate frame with the Lorentz and transverse traceless gauge, the particles will remain at a constant coordinate position; they remain at rest forever. That is because in choosing the transverse traceless coordinates, we have attached our coordinate frame to the particles.

Now consider two nearby particles, of which one is at the origin and the other at $(d, 0, 0)$. The interval between the two particles can be obtained from Eqs. (1.3), (1.10) and (1.19)

$$ds^2 = -dt^2 + (1 + h_{+}(t - z))\, dx^2 + (1 - h_{+}(t - z))\, dy^2 + dz^2, \tag{1.20}$$

with h_{+} the amplitude of the gravitational wave. The interval is time dependent.

Now consider a photon that travels from one particle to the other, is reflected, and travels back. This photon travels along a lightlike path, so by definition $ds^2 = 0$. In addition, we were free to choose our coordinates such that $dy = dz = 0$. Assuming that the wavelength of the gravitational wave is much longer than d, and that h_{+} can be considered uniform over a distance d, the gravitational wave can be considered to have a constant amplitude during the traveling time of the photon. Its round trip time τ can be written as

$$\tau = 2\int_0^d dt = 2\int_0^d (1 + h_{+})^{\frac{1}{2}}\, dx \approx \int_0^d \left(1 + \frac{1}{2}h_{+}\right) dx = 2d\left(1 + \frac{1}{2}h_{+}\right). \tag{1.21}$$

In the absence of a gravitational wave the photon would travel a distance $\tau = 2d$, so it is clear that the distance between the two test particles probed by the photon changes by an amount $dh_+/2$. The relative change in distance between the test masses of the gravitational wave detector is called the *strain* h and is given by

$$h = \frac{\Delta d}{d} = \frac{1}{2}h_+. \tag{1.22}$$

Of course, for a gravitational wave with $\times$-polarization, we have $h = h_\times/2$. The effect of gravitational waves with these two polarizations on a ring of freely falling test masses is shown in Fig. 1.1.

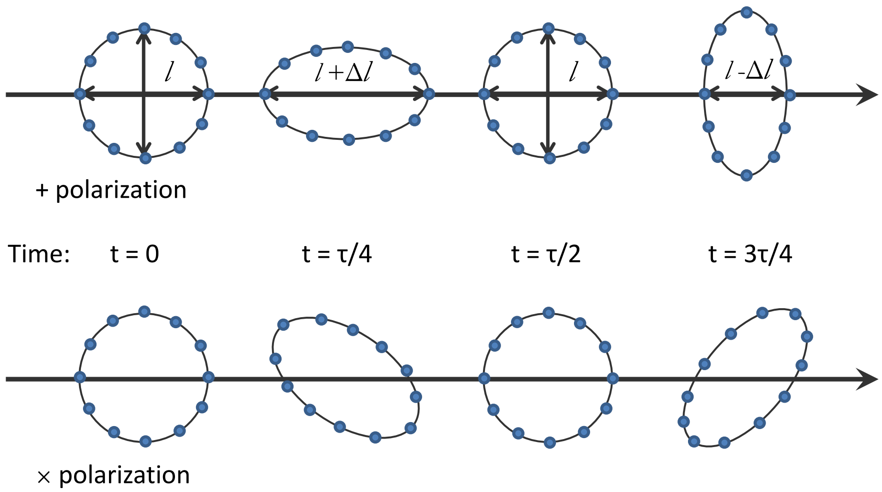

Figure 1.1: *Effect of a gravitational wave traveling in the z-direction (out of the page) on a ring of free falling test masses. Initially, the test masses lie on a ring of radius $l/2$. In the $+$ polarization, a time $\tau/4$ later the ring is stretched by an amount Δl in the x-direction and compressed by the same amount in the y-direction. A time $\tau/2$ after that, the ring is compressed in the x-direction and stretched in the y-direction. For the $\times$ polarization the stretching and compressing occurs in the xy-direction.*

Eq. (1.22) shows that the ability to measure an induced length change is proportional to the distance separating the test masses. This is the reason gravitational wave detectors are many kilometers long. The typical strain amplitudes of gravitational waves are of the order 10^{-25} – 10^{-23}. That means that such a wave would induce length changes of 3×10^{-20} m in the 3 km long arms of Virgo!

1.6 Sources of gravitational waves

Any accelerating, sufficiently asymmetric system will emit gravitational waves. But, only those produced by absolutely massive and compact objects or the most violent events will have sufficient amplitudes to be measured by ground-based detectors like Advanced Virgo. There are four categories of promising sources: compact binary coalescence, bursts, the stochastic background and sources of continuous waves.

1.6.1 Compact binary coalescence

Compact binaries are sources that consist of two compact objects, either neutron stars or black holes, that are trapped in each others gravitational field. As they orbit each other, general relativity predicts that they emit gravitational waves, which causes them to lose energy and angular momentum. As a result their separation distance shrinks until the two bodies collide and form one object. This process can be divided into three phases: *the inspiral, the merger and the ringdown*.

During the inspiral phase, the two bodies spiral towards each other and their orbital frequency increases. This phase can take millions of years. During most of this time, the frequency of the emitted wave is too low to be detected by ground-based interferometers, but in the period just before the merger, the frequency increases rapidly to approximately 2 kHz. This is the so-called *chirp*. It lasts from a few tenths of a second to several seconds and is well within the detection bandwidth of Advanced Virgo.

During the merger phase, the distance between the two objects becomes so small and the gravitational forces so strong that the two bodies no longer perform quasi-circular orbits around a common center of mass, but instead *plunge* towards each other. They collide and form a single object. The merger phase only takes milliseconds.

During the ringdown the two objects have merged into a single body. This newly formed object calms down to a stationary state by radiating away its deformations in the form of gravitational waves.

Modeling of the inspiral, merger and ringdown of compact binaries is an active field of research. The goal is to obtain waveforms of these events and to perform *matched filtering* [21]. In that procedure, analytical or numerical waveforms are compared to the output signals of the gravitational wave detectors, which allows to search deep into the noise [22].

Coalescence of compact binaries is seen as the most promising source candidate for a first detection of gravitational waves, because it has a relatively large strain amplitude. The theoretical strain amplitude [22] for a binary neutron star of masses m_1 and m_2 at a distance D from Earth is

$$h = 10^{-23}\left(\frac{100\ \text{Mpc}}{D}\right)\left(\frac{M_\text{c}}{1.2M_\odot}\right)^{\frac{5}{3}}\left(\frac{f}{200\ \text{Hz}}\right)^{\frac{2}{3}}, \tag{1.23}$$

where $M_\odot$ is the mass of the Sun and $M_\text{c} = (m_1 m_2)^{3/5}/(m_1+m_2)^{1/5}$ is the so-called *chirp mass*. According to Eq. (1.23) the strain amplitude of a binary neutron star at 100 Mpc, with a chirp mass of 1.2 $M_\odot$ and a inspiral frequency of 200 Hz is 10^{-23}.

1.6.2 Bursts

Bursts is a collective term to describe sudden, relatively short lived events. Two types of burst sources that are likely to produce gravitational waves are gamma ray bursts, commonly called GRBs, and (super)novae.

Gamma ray bursts are flashes of gamma rays whose origins are uncertain. Presumably, they are massive energy releases (jets) of stellar mass objects in events of catastrophic proportions [23]. Such a cataclysmic event would produce gravitational waves, although it is currently impossible to predict what the waveform would look like.

A supernova occurs only at the demise of the heaviest of stars. When a star of sufficient mass has depleted its supply of fuel for nuclear fusion, its gravitational potential is no longer balanced by pressure produced at its center and the star implodes. The remaining gas around the star's core is blasted away. This process is accompanied by a huge, temporary increase in the star's luminosity making it brighter than a galaxy. Depending on the star's initial mass, the remnant of the supernova will form a white dwarf, neutron star, or black hole.

It is difficult to model these sources and to predict the waveforms of their gravitational radiation. Confidence in the detection would increase if a signal was observed electromagnetically, by neutrino telescopes, by radio telescopes, *etc.* as well as by LIGO and Virgo. Therefore, a multi-messenger approach [24] for their detection is pursued.

1.6.3 Stochastic background

The stochastic background is a superposition of unresolved gravitational wave sources of astrophysical and cosmological nature. It is made up from dim gravitational wave sources, too weak to detect and too numerous to count as well as from signals produced in the early Universe such as during phase transitions or the Big Bang. The stochastic background level can be determined by looking at the correlation of the signals from the LIGO and Virgo detectors. So far, only an upper limit has been set [25].

1.6.4 Continuous waves

Spinning neutron stars will produce gravitational waves, when their mass distribution is non-axisymmetric, *i.e.* in a way that gives rise to a time-varying quadrupole moment. The rotational frequency of neutron stars is stable at observational time scales of the gravitational wave detectors, but does decrease slowly over time. Therefore, neutron stars emit quasi-monochromatic gravitational waves which allow for long observation times. Sudden increases in frequency can occur at random times. These are called glitches and are associated with a settling of the crust which lowers the star's moment of inertia; the rotation of the star speeds up due to conservation of angular momentum.

Many neutron stars spin rapidly. Many are also pulsars. The pulsars emit electromagnetic radiation along their magnetic field axis [26]. If the rotational and magnetic axis are not aligned, then the electromagnetic radiation can be directed at the Earth once every rotation. In that respect they are astronomical lighthouses; their flashes can be detected on Earth with radio telescopes. Alternatively, their flashes are never directed towards our planet and the pulsar remains undetected, until we measure its gravitational waves.

So far, several thousand pulsars have been detected. By extrapolation, a billion pulsars [27] are expected to exist in the Milky Way alone. A number of them have frequencies of several tens of Hz, well within the detection band-width of Advanced Virgo. The gravitational wave searches for these sources are divided in *targeted* and *broad-band* searches.

Targeted searches are for known pulsars [28]. Their position and phase parameters are known with high accuracy. For their measurement matched filtering techniques can be used and a smaller parameter space needs to be explored. The favorite pulsar of gravitational wave physicists are the Vela and the Crab pulsars [29]. Vela is a supernova remnant that has a frequency of $\sim$22 Hz, is relatively close by, loses a relatively large amount of energy and should be relatively easy to detect.

For all other neutron stars the parameter space is less restricted, so the number of templates is much larger. This makes matched filtering computationally challenging and their detection much harder. To address this issue a volunteer computing project has been introduced called Einstein@Home [30]*, in which private computers around to globe are linked to perform data-analysis. At present their combined computing power surpasses that of supercomputers.

1.7 Sight distances

To compare the sensitivity of gravitational wave detectors we can of course compare their sensitivity curves. However, at this point we would like to introduce an important figure of merit called *the horizon* or *sight distance* D. For a given detector, the horizon is defined as the distance at which an optimally oriented, overhead source can be detected with a signal-to-noise ratio SNR $= 8$. It can be computed for any source, but the most relevant sight distance is the one for binary black hole and binary neutron star coalescence as they are the most likely sources for first detection.

The SNR depends on the strain h of the source and the noise power spectral density $S_{\mathsf{n}}(f)$ of the detector [31]

$$\mathrm{SNR}^2 = 4\int_0^{\mathrm{f_{isco}}} \frac{|\bar{h}(f)|^2}{S_{\mathsf{n}}(f)} df, \tag{1.24}$$

*If the reader wants to participate, the software for running Einstein@Home can be downloaded at http://www.einstein-online.info/spotlights/EaH where f_{isco} is the frequency of the innermost stable orbit

$$f_{\mathsf{isco}} = \frac{c^3}{6.5^{\frac{3}{2}}\pi G M} \approx 4396 \frac{M_\odot}{M}\ \mathsf{Hz}, \tag{1.25}$$

and $|\tilde{h}(f)|$ is the frequency domain waveform amplitude

$$\tilde{h}(f) = \frac{2c}{D}\left(\frac{5G\mu}{96c^3}\right)^{\frac{1}{2}}\left(\frac{GM}{\pi^2 c^3}\right)^{\frac{1}{3}} f^{-\frac{7}{6}}, \tag{1.26}$$

where D is the luminosity distance of the source, M the total mass and μ the reduced mass.

The horizon is calculated for binary neutron stars $D_{\mathsf{NS-NS}}$, binary black holes $D_{\mathsf{BH-BH}}$ and neutron star black hole binaries $D_{\mathsf{NS-BH}}$, where the neutron stars have a mass of $1.4M_\odot$ and the black holes of $10M_\odot$. The greatest averaged horizons achieved by Virgo thus far are $D_{\mathsf{NS-NS}} = 13$ Mpc and $D_{\mathsf{BH-BH}} = 150$ Mpc [32].

1.8 Expected event rates

Predictions of the event rates for compact binary coalescence of binary black holes, binary neutron stars, and black hole neutron star binaries have been carried out for both the initial and advanced detector networks [31]. The expected event rate N for a given inspiral source is

$$N = R \times N_{\mathsf{G}}, \tag{1.27}$$

where R is the coalescence rate of that type of binary in the Milky Way and N_{G} the number of Milky Way equivalent galaxies that are within the detector's range. A good approximation of N_{G} visible by a gravitational wave detector is

$$N_{\mathsf{G}} = \frac{4\pi}{3}\left(\frac{D_{\mathsf{inspiral}}}{2.26\ \mathsf{Mpc}}\right)^3 N_*, \tag{1.28}$$

where the factor 2.26^{-3} is a correction factor to average over all sky locations and orientations of the inspiral sources and $N_* = 1.16\times10^{-2}\ \mathsf{Mpc}^{-3}$ is the density of Milky Way equivalent galaxies in space.

Equation (1.28) shows that the event rate of the detector scales with the third power of the horizon. Therefore, increasing the detector's sensitivity with one order of magnitude allows the detector to see further in all three directions and increases the number of sources within its detection range with three orders of magnitude. Equations (1.24) and (1.26) show that to accomplish this the detector's noise power spectral density needs to be reduced by one order of magnitude.

This is precisely what the Advanced Virgo project aims to do: increasing the sensitivity of the detector with one order of magnitude by reducing the detector's noise budget. The horizon distances for binary neutron stars and binary black holes will be 134 Mpc and 1 Gpc [14].

The main uncertainty in the expected event rate is due to the uncertainty in the number of compact binary coalescence rates. The most confident rate is the one for binary neutron stars which is extrapolated from the observed number of binary pulsars in the Milky Way. The most likely coalescence rate for this type of sources is 100 Myr^{-1} per Milky Way equivalent galaxy, but the certainty in coalescence rates is $1-2$ orders of magnitude in both directions. For this reason, it is common not to quote a single value for the expected event rate, but rather to provide one for a pessimistic, most likely, and optimistic scenario.

Besides depending on the coalescence rate, the actual event rates of the advanced detectors will rely on the speed at which they will be commissioned. A best estimate of the sensitivity evolution of Advanced LIGO and Advanced Virgo can be found in Ref. [33], hereafter just abstracted.

The roadmap of the advanced detectors is divided in three phases: construction, commissioning, and observation. The construction phase of the advanced detectors ends with their acceptance. At this stage the interferometers can maintain stable operation for several hours, regardless of the sensitivity that is achieved. In the commissioning phase the sensitivity of the detectors will be improved. Engineering and science runs will be undertaken to improve understanding of the detector and the analyses. These science runs could yield the first detection. Once a sensitivity is reached at which the detection of a gravitational wave becomes likely, the detectors enter the observation phase: a long-term campaign dedicated to observing gravitational waves.

The LIGO and Virgo collaborations strive to minimize the time to the first gravitational wave detection. Therefore, the duration of the engineering runs and science runs will depend on the detector's sensitivities. The anticipated evolution of the sensitivities of the advanced detectors and the associated binary neutron star ranges* are shown in Fig. 1.2.

The first science run of Advanced LIGO (aLIGO) is expected to take place in 2015 and will take about three months. Advanced LIGO is anticipated to have a BNS range between 40 and 80 Mpc. After that, all science runs will be joint science runs of Advanced LIGO and Advanced Virgo (AdV). A number of science runs, each lasting several months, are anticipated for the period 2016-2018. The detectors are expected to have BNS ranges between 80 and 170 Mpc (aLIGO), and between 20 and 115 Mpc (AdV). The design sensitivities, corresponding to BNS ranges of respectively 200 and 130 Mpc, are expected to be reached by aLIGO in 2019 and AdV in 2021. The first observing run may be undertaken ca. 2020.

The expected event rates for the initial LIGO-Virgo network and the *fully commissioned* advanced detector network are listed in Table 1.1. For the Advanced detector network the most likely binary black hole event rate is 20 per year, with a range between 0.4 and 1000 per

*The BNS range is the volume and orientation averaged distance at which the coalescence of two $1.4M_{\odot}$ neutron stars could be detected with a signal-to-noise ratio of 8. The BNS horizon is 2.26 times the BNS range.

year; the most likely binary neutron star event rate is 40 per year and ranges from 40 to 400 per year; and the most likely event rate for neutron star black hole binaries is 10 per year and ranges from 0.2 to 200 per year. This means that, while the maximum number of events we could expect to measure with the initial detectors was 0.8 per year, the number of events the advanced detector network at design sensitivity is expected to observe ranges from 1 to 1600 per year. The first direct observation of a gravitational wave is almost a certainty.

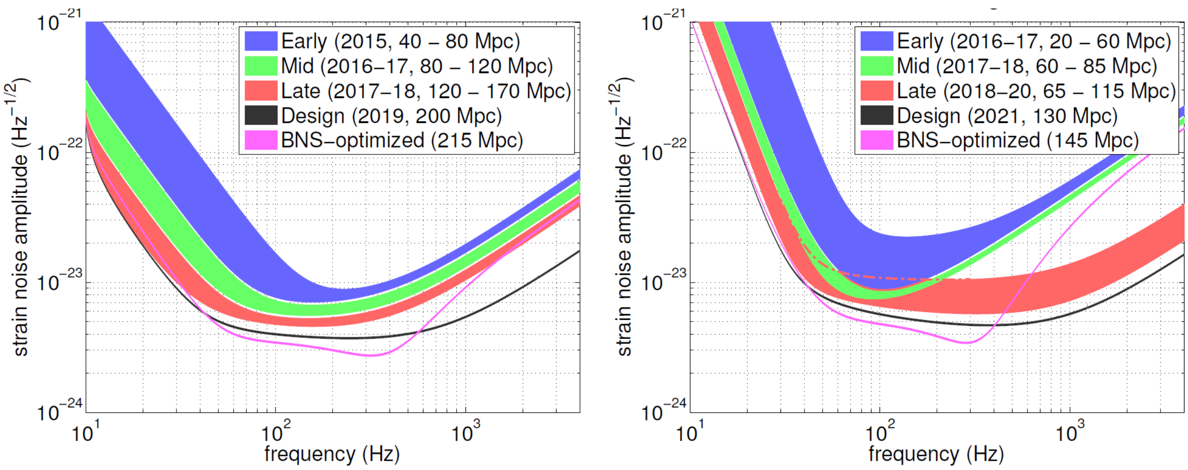

(a) *Advanced LIGO*

(b) *Advanced Virgo*

Figure 1.2: *Target strain sensitivity as a function of frequency for several commissioning phases of a) Advanced LIGO and b) Advanced Virgo. For each phase, the design sensitivty, and the BNS-optimized sensitivity (see section 2.11.2) the expected average distance at which the coalescence of binary neutron stars could be detected is indicated. The figure was obtained from Ref. [33].*

LIGO-Virgo network	Source	Pessimistic rate [yr^{-1}]	Realistic rate [yr^{-1}]	Optimistic rate [yr^{-1}]
Initial	NS-NS	2×10^{-4}	0.02	0.2
	BH-NS	7×10^{-5}	0.004	0.1
	BH-BH	2×10^{-4}	0.007	0.5
	Total	4.7×10^{-4}	0.031	0.8
Advanced	NS-NS	0.4	40	400
	BH-NS	0.2	10	200
	BH-BH	0.4	20	1000
	Total	1	70	1600

Table 1.1: *Expected number of compact binary coalescence events per year for the initial and advanced detector networks [34]. The three scenarios correspond to pessimistic, realistic and optimistic values for the number of compact binaries in a Milky Way equivalent galaxy.*

1.9 Summary

According to general relativity, gravity is not a force, but curvature of spacetime which is due to the presence of mass and energy. This curvature is encoded in the metric and is quantified by the Riemann tensor, which can be derived from the metric. Components of the Riemann tensor and energy-momentum tensor are related to each other by the Einstein field equations.

Any system that is accelerating and sufficiently asymmetric will create disturbances in spacetime called gravitational waves. These waves can be observed by looking at the separation distance of a ring of freely falling test masses. In practice, two test masses will suffice. A passing gravitational wave will effectively change their distance between them. The relative change in separation distance is called the strain and has typical values between 10^{-23} and 10^{-25}. Modern-day gravitational wave detectors are on the verge of reaching this level of sensitivity.

Sources of gravitational waves are divided in four categories: bursts, the stochastic background, sources of continuous waves *e.g.* spinning neutron stars, and the coalescence of compact binaries. The latter category is expected to have the largest event rate and is considered the best candidate for the first detection of a gravitational wave.

The main uncertainty in the compact binary coalescence event rate, which is approximately two orders of magnitude, is due to the uncertainty in the number of sources. These numbers hold for fully commissioned instruments that have achieved their design sensitivities. The advanced LIGO-Virgo network will measure between 1 and 1600 events per year, with a most likely value of 70 events per year. The first detection of a gravitational wave is imminent.

2 The Advanced Virgo gravitational wave detector

"But the truth of a theory can never be proven.
For one never knows if future experience will contradict its conclusion."
- Albert Einstein
Induction and Deduction in Physics,
Berliner Tageblatt, 25 December 1919.

2.1 Introduction

In the previous chapter we saw that disturbances of the metric, like gravitational waves, can be observed by sending two light beams in orthogonal directions towards two mirrors and measuring the difference in their round trip time. Gravitational wave detectors do just that. They are essentially Michelson interferometers: a laser beam is split in two identical beams, one for each arm, and the returning signals are recombined at the output of the interferometer in order to create an interference pattern. Passing gravitational waves effectively change the length difference between the two arms, which induces an intensity fluctuation of the interference pattern.

In this chapter the basic operation principles of interferometric gravitational wave detectors are introduced. In section 1.5 it was shown that the strain induced by gravitational waves are only of the order of 10^{-24}, which is tiny. So how do gravitational wave detectors reach this incredible sensitivity?

The sensitivity of interferometric gravitational wave detectors is determined by their signal-to-noise ratio: the power fluctuation due to the passage of a gravitational wave must exceed the noise at the output of the interferometer. The cumulative effect of the individual noise sources is referred to as the noise budget.

There is a fundamental limit to the detector's sensitivity due to the quantum nature of light. First, there is a fluctuation in the number of photons impinging on the photo-diode at the detector's output, which is called shot noise, and second there is a fluctuation in the force exerted by the photons on the mirrors, which is called radiation pressure noise. Increasing the number of photons lowers the amount of shot noise, but at the expense of enlarging the amount of radiation pressure noise.

Apart from these fundamental noise sources, the sensitivity of the first generation gravitational wave detectors, like Virgo, was limited by other noise sources. The contributions of relevant noise sources to the Virgo noise budget and the sensitivity achieved by the detector will be treated in sections 2.6 − 2.8.

In November 2011, a major upgrade of Virgo was started. The detector's sensitivity will be increased by an order of magnitude resulting in the second generation detector named *Advanced Virgo*. In section 2.11, the steps taken to transform Virgo into Advanced Virgo are summarized. The sensitivity of Advanced Virgo is expected to be limited by radiation pressure noise at low frequencies, by coating thermal noise at intermediate frequencies, and by shot noise at high frequencies [35].

During the second science run of Virgo an extensive noise investigation aimed at understanding the noise curve of the detector showed that the excitation of mechanical resonances of the external injection bench caused an amount of beam jitter noise that would limit Advanced Virgo. A seismic isolation system for this optical bench, EIB-SAS, was proposed to neutralize this noise source. The requirements that this system needs to meet are listed at the end of this chapter.

2.2 Interferometers as gravitational wave detectors

In chapter 1 it has been shown that a passing gravitational wave changes the proper distance between freely falling test masses, and that these variations in proper distance can be measured with photons traveling between two test masses. These two notions can be exploited to observe gravitational waves.

2.3 Basic principles

Looking at Fig. 1.1, we see that we don't need a ring of test masses; two would suffice. Sending two photons from the center of the circle in orthogonal directions, letting them reflect back from the test masses and measuring their travel time, the proper distance to each test mass is monitored. A passing gravitational wave with the $+$-polarization would shrink one distance and enlarge the other, causing a different arrival time for both reflected photons. The simplest interferometric gravitational wave detector is therefore a Michelson interferometer, where the test masses are mirrors.

2.3.1 Michelson interferometers

Fig. 2.1 shows the design of a basic Michelson interferometer. A highly stable laser beam is divided into two coherent beams with a 50/50 *beam splitter* positioned under an angle of 45°. After being reflected by the mirrors the two beams are recombined at the beam splitter, which projects their interference pattern on a photo-diode. A passing gravitational wave, optimally oriented and with the '+'-polarization, will change the proper distance to the mirrors by an amount $h_+/2$, which introduces a phase difference $\Delta\phi$ between the two laser beams equal to

$$\Delta\phi = \frac{4\pi}{\lambda} L h, \tag{2.1}$$

where h is the strain amplitude of the gravitational wave λ the wave length of the laser light and L the average length of the two arms. This phase difference on the beam splitter changes the interference pattern. In this way, an interferometer converts phase changes into a detectable light intensity signal.

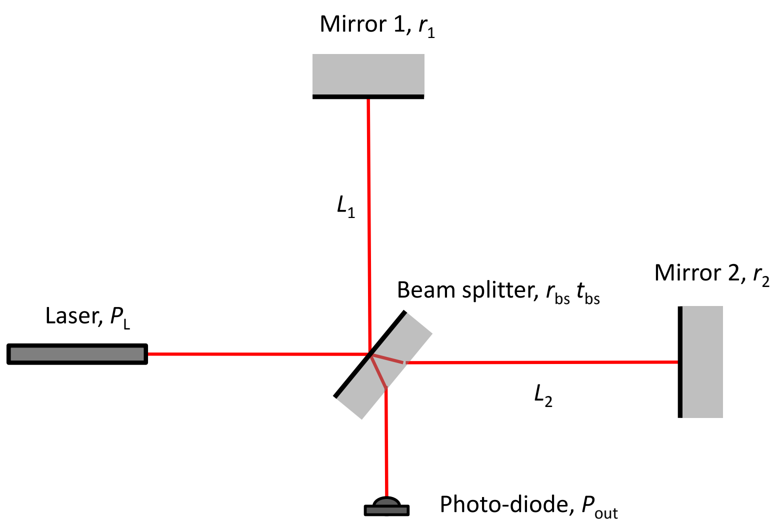

Figure 2.1: *Simple Michelson interferometer.*

Denoting the laser power P_{L}, the reflection coefficients of the two mirrors r_1 and r_2 and assuming the beam splitter being perfect, the power impinging on the photo-diode is [36]

$$P_{\mathsf{out}} = t_{\mathsf{bs}}^2 r_{\mathsf{bs}}^2 P_{\mathsf{L}} \left(r_1^2 + r_2^2 + 2 r_1 r_2 \cos\left[\phi_0 + \Delta\phi_{\mathsf{GW}}(t)\right] \right), \tag{2.2}$$

where $\phi_0 = 2\pi/\lambda \times (L_1 - L_2)$ is the default phase difference between the two returning beams at the beam splitter called the *static tuning* of the interferometer and $\Delta\phi_{\mathsf{GW}}$ the phase modulation induced by a gravitational wave traversing the detector given by Eq. (2.1). This shows that formally, the effect of the gravitational wave on the proper length of the arm is equivalent to a displacement of the end mirrors.

If the beam splitter is perfect and the mirrors totally reflecting, then $r_{\mathsf{bs}}^2 = t_{\mathsf{bs}}^2 = 1/2$ and Eq. (2.2) becomes

$$\begin{aligned} P_{\mathsf{out}} &= \frac{1}{4}P_{\mathsf{L}}\left(r_1^2 + r_2^2 + 2r_1r_2\cos\left[\phi_0 + \Delta\phi_{\mathsf{GW}}(t)\right]\right) \\ &= \frac{1}{4}P_{\mathsf{L}}\left(r_1^2 + r_2^2 + 2r_1r_2\cos\phi_0\cos\Delta\phi_{\mathsf{GW}}(t) - 2r_1r_2\sin\phi_0\sin\Delta\phi_{\mathsf{GW}}(t)\right) \\ &\approx \frac{1}{4}P_{\mathsf{L}}\left(r_1^2 + r_2^2 + 2r_1r_2\cos\phi_0 - 2r_1r_2\Delta\phi_{\mathsf{GW}}(t)\sin\phi_0\right), \end{aligned} \tag{2.3}$$

which can be separated into a DC part P_{DC} and a time varying part $\Delta P(t)$ as

$$P_{\mathsf{DC}} = \frac{1}{4}P_{\mathsf{L}}\left(r_1^2 + r_2^2 + 2r_1r_2\cos\phi_0\right) \quad \text{and} \tag{2.4}$$

$$\Delta P(t) = \frac{1}{2}P_{\mathsf{L}}r_1r_2\Delta\phi_{\mathsf{GW}}(t)\sin\phi_0. \tag{2.5}$$

The average power P_{DC} impinging on the photo-diode is maximized if $\phi_0 = 2n\pi$ and we say that the interferometer is tuned at the *bright fringe*. Alternatively, if $\phi_0 = (2n+1)\,\pi$ the power is minimized and the instrument is tuned to the *dark fringe*.

2.3.2 Working point of the interferometer

The signal $\Delta P(t)$ is maximized if $\phi_0 = (n + 1/2)\,\pi$. This condition is called *gray fringe*. In the absence of noise this would be the most sensitive condition of the interferometer. However, because of the quantum nature of light there is a statistical fluctuation in the number of photons collected on the photo-diode. This is called *shot noise*. To really maximize the sensitivity not the signal, but the *signal-to-noise ratio* needs to be maximized.

The counting statistics of photons is given by a Poisson distribution. The average number of photons detected per unit time is $N_\gamma = P_{\mathsf{DC}}/\hbar\omega$, with a standard deviation $\sqrt{N_\gamma}$, where $\hbar$ is the reduced Planck constant and ω the angular frequency of the laser light. The corresponding amplitude spectral density (ASD) of the shot noise is

$$S_{\mathsf{shot}}(f) = \sqrt{N_\gamma}\hbar\omega = \sqrt{P_{\mathsf{DC}}\hbar\omega} \quad [\mathsf{W}/\sqrt{\mathsf{Hz}}], \tag{2.6}$$

which is independent of frequency. The ASD of the signal is

$$S_{\mathsf{sig}}(f) = \frac{1}{2}P_{\mathsf{L}}r_1r_2\sin\phi_0 \times S_{\mathsf{x}}, \tag{2.7}$$

where S_{x} is the ASD of the phase induced by the gravitational wave. The signal to noise ratio SNR is then given by [36]

$$\mathsf{SNR} = \frac{S_{\mathsf{sig}}}{S_{\mathsf{shot}}} = \sqrt{\frac{2P_{\mathsf{L}}r_1^2r_2^2}{\hbar\omega}f(\phi_0)}S_{\mathsf{x}}, \tag{2.8}$$

where $\hbar$ is the reduced Planck constant and

$$f(\phi_0) = \frac{\sin^2 \phi_0}{r_1^2 + r_2^2 + 2r_1 r_2 \cos \phi_0}. \tag{2.9}$$

The SNR is optimized if $f(\phi_0)$ is maximal. This occurs when $\cos \phi_0 = -r_</r_>$, where $r_<$ is the smaller of r_1 and r_2 and $r_>$ the larger one. As $r_1 \approx r_2 \approx 1$, $\phi_0 \approx (2n+1)\,\pi$. That is, the SNR of the interferometer is optimal when it is operated close to the dark fringe. In that case $f(\phi_0) = 1/r_>^2 \approx 1$ and Eq. (2.8) gives [36].

$$\mathsf{SNR} = \sqrt{\frac{2P_\mathsf{L}}{\hbar\omega}} S_\mathsf{x}. \tag{2.10}$$

Equation (2.3) shows that at the dark fringe $P_\mathsf{out} = P_\mathsf{L}\left(r_1^2 + r_2^2 + 2r_1 r_2 \cos \Delta\phi_\mathsf{GW}\right)/4 \approx P_\mathsf{L} \Delta\phi_\mathsf{GW}^2/4$, which means that the signal induced by a gravitational wave with strain h is only at the second order: $P_\mathsf{out} \propto h^2$. A signal linear in h, with a high signal-to-noise ratio is obtained by operating the interferometer close, but not at the dark fringe.

2.3.3 Sensitivity of a shot noise limited interferometer

The sensitivity of the interferometer is defined as the signal for which SNR $= 1$. According to Eq. (2.10), the minimum signal that can be detected is

$$S_\mathsf{x} = \sqrt{\frac{\hbar\omega}{2P_\mathsf{L}}}. \tag{2.11}$$

Taking into account the photon counting efficiency of the photo-diodes η, which typically has values of $0.90 < \eta < 0.95$, Eq. (2.11) becomes

$$S_\mathsf{x} = \sqrt{\frac{\hbar\omega}{2\eta P_\mathsf{L}}}. \tag{2.12}$$

When the travel time of the photon T_γ is much smaller than the period of the gravitational wave T_GW: $T_\gamma = 2L/c \ll T_\mathsf{GW}$, we can consider the amplitude of the wave h_0 constant during the observation. In that case the phase difference induced on the beam splitter is $S_\mathsf{x} = 4\pi L/\lambda \times h_0$ and the minimum value of h_0 that can be detected represents the sensitivity of the detector

$$S_\mathsf{h} = \frac{\lambda}{4\pi L}\sqrt{\frac{2\hbar\omega}{\eta P_\mathsf{L}}}. \tag{2.13}$$

For a simple Michelson interferometer with arm lengths of 3 km and a laser providing 4 W (approximately the power of the laser used in Virgo) of 1064 nm light, the sensitivity would be

$$S_\mathsf{h} = 9 \times 10^{-21}\ /\sqrt{\mathsf{Hz}}. \tag{2.14}$$

2.4 Sensitivity enhancements

Equation (2.13) tells us that to improve the sensitivity of a simple shot noise limited Michelson interferometer we need to increase the length of its arms, increase the laser power of the laser and/or use light with a shorter wavelength.

2.4.1 Fabry-Perôt cavities

Let's say we are trying to measure gravitational waves with frequencies between 10 Hz and 10 kHz. As they travel at the speed of light these waves will have wavelengths of 30 to 30.000 km. To get the maximum amount of phase difference the arms of the interferometer would have to be a quarter of the wavelength of the gravitational wave, so 7.5 to 7.500 km. As there are several impracticalities to building Earth-based interferometers of this size, a trick is used to fold the arms: the arms of the interferometer are Fabry-Perôt cavities [37].

Figure 2.2 shows the layout of a power recycled Michelson interferometer where the two arms are Fabry-Perôt cavities of lengths L_1 and L_2. The laser enters the cavities through the so-called *input mirrors* and makes several round-trips before exiting again. If after one round-trip the light in the cavity is in-phase with the incoming light, then a high intensity laser beam will built up in the cavity.

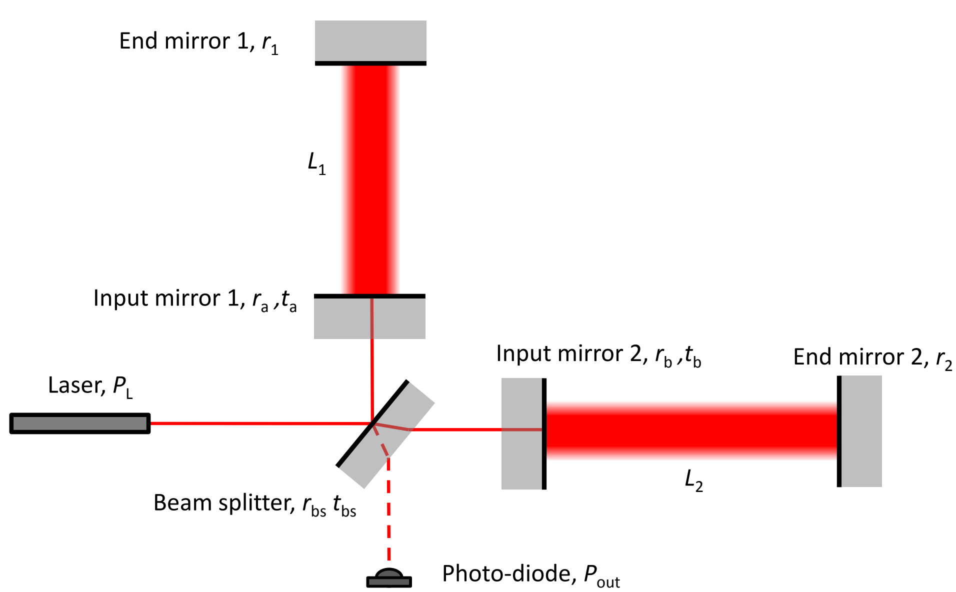

Figure 2.2: *Michelson interferometer with Fabry-Perôt cavities as arms.*

As the light receives a phase difference of 180° upon reflecting on the input mirror and end mirror, the resonance conditions for the light is $\lambda_\mathsf{n} = 2L/(n+1/2)$, where L is the length of the cavity and n an integer number [36]. Alternatively, keeping the length of the cavity constant the resonant frequencies of the cavity are given by $\nu_\mathsf{n} = c(n+1/2)/2L$. The difference between two adjacent resonant frequencies is called the *free spectral range* $\nu_\mathsf{FSR} = c/2L$.

The quality of the cavity is given by the relative sharpness of the resonant lines; the ratio of the free spectral range and the width (full width half maximum) of the resonant lines ν_FWHM $\mathscr{F} = \nu_\mathsf{FSR}/\nu_\mathsf{FWHM}$, which is called the *finesse* of the cavity. If r_1 and r_2 are the reflection coefficients of the cavity mirrors, the finesse is given by [37]

$$\mathscr{F} = \frac{\pi\sqrt{r_1 r_2}}{1 - r_1 r_2}. \tag{2.15}$$

The average number of round trips the light makes before being lost is the gain of the cavity [36]

$$\mathcal{N} = \frac{2\mathscr{F}}{\pi}. \tag{2.16}$$

By making the arms of the interferometer Fabry-Perôt cavities the effective length of the arms $L_\mathsf{eff} = \mathcal{N}L$. Furthermore, the power circulating in the cavities $P_\mathsf{circ} = \mathcal{N}P_\mathsf{L}$. The increase in arm length enhances the sensitivity of the detector. Substituting L_eff for L in Eq. (2.13) we obtain

$$S = \frac{\lambda}{8\mathscr{F}L}\sqrt{\frac{\hbar\omega}{2\eta P_\mathsf{circ}}}. \tag{2.17}$$

For Virgo, $L = 3$ km and $\mathscr{F} = 50$, so $\mathcal{N} \approx 30$ making $L_\mathsf{eff} \approx$ 100 km and $P_\mathsf{circ} \approx$ 120 W. Inserting these parameter values listed above we see that folding the arms in this way enhances the sensitivity to

$$S = 5 \times 10^{-23}\,\frac{1}{\sqrt{\mathsf{Hz}}} \tag{2.18}$$

2.4.2 Power recycling

As the interferometer is tuned to the dark fringe, all the power is reflected back towards the laser. Placing a *power recycling mirror* at the input of the interferometer, as shown in Fig. 2.3, would reflect this light back into the interferometer, effectively increasing the laser power.

The interferometer can be described as an effective mirror with a reflectivity close to 1 (when it is tuned to dark fringe) and the interferometer and the power recycling mirror form an additional Fabry-Perôt cavity. The optical gain of this cavity is 36, making the effective laser power $P_0 = 36 \times P_\mathsf{L} =$ 150 W and $P_\mathsf{circ} =$ 4.5 kW. Equation (2.13) tells us that the sensitivity of a power recycled Michelson interferometer is

$$S = 8 \times 10^{-24}\ /\sqrt{\mathsf{Hz}}. \tag{2.19}$$

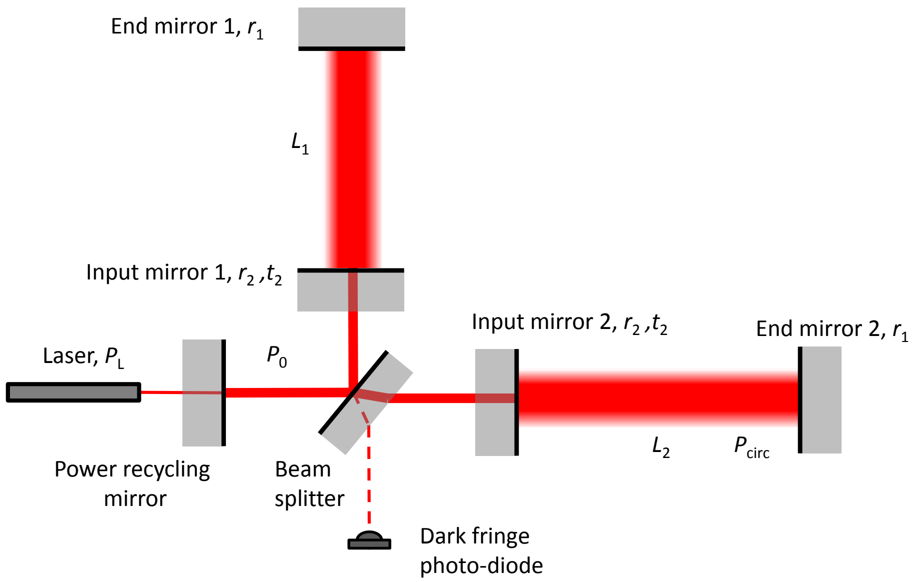

Figure 2.3: *Power recycles Michelson interferometer with Fabry-Perôt cavities as arms.*

2.4.3 Feedback control

The excursions of the Fabry-Perôt cavity mirrors, if left freely swinging, would be too great to keep the laser beam resonant in the cavity. Therefore, the longitudinal and angular degrees of freedom in the interferometer are actively controlled.

The blue dotted line in Fig. 2.4b shows the intensity of the light reflected back by one of the Fabry-Perôt cavities. When the cavity is on resonance this intensity is minimal. Slightly off resonance, which is called detuned, the intensity always increases. As the intensity of the reflected light does not contain any directional information of the detuning it cannot be used as an error signal for the longitudinal control loops.

An important control scheme that is widely used in gravitational wave detectors is Pound-Drever-Hall reflection locking [38], whose basic scheme is depicted in Fig. 2.4a. The laser light is phase-modulated on the laser bench. Phase modulation shifts some of the energy of the laser beam from its main frequency, *the carrier*, to the so-called *sidebands*. Writing the carrier as a plane wave electric field

$$E(t) = E_0 e^{i\omega_c t}, \tag{2.20}$$

the phase modulation with $\sin(\omega_m t)$ gives the modulated electric field

$$\begin{aligned} E_{pm}(t) &= E_0 e^{i\omega_c t + i\delta \sin \omega_m t}, \\ &\approx E_0 e^{i\omega_c t} \left(1 - \frac{\delta^2}{4} + i\delta \sin \omega_m t\right), \\ &= E_0 e^{i\omega_c t} \left(1 - \frac{\delta^2}{4} + \frac{\delta}{2} e^{i\omega_m t} - \frac{\delta}{2} e^{-i\omega_m t}\right). \end{aligned} \tag{2.21}$$

where δ is the modulation depth. Indeed, phase-modulation adds sidebands to the carrier that have frequencies of $\omega_c \pm \omega_m$. The modulation frequencies are chosen such that the sidebands are not resonant in the Fabry-Perôt cavities and hence, are reflected by them.

The demodulated signal, which is collected elsewhere in the interferometer, is shown in Fig. 2.4b (red curve). Clearly this demodulated signal is zero when the cavity is on resonance and is linearly proportional to the detuning of the cavity, providing a sensible error signal to keep the cavity on resonance. An appropriate correction signal is applied to the mirrors by exerting a small force on magnets glued to the mirrors with coil actuators.

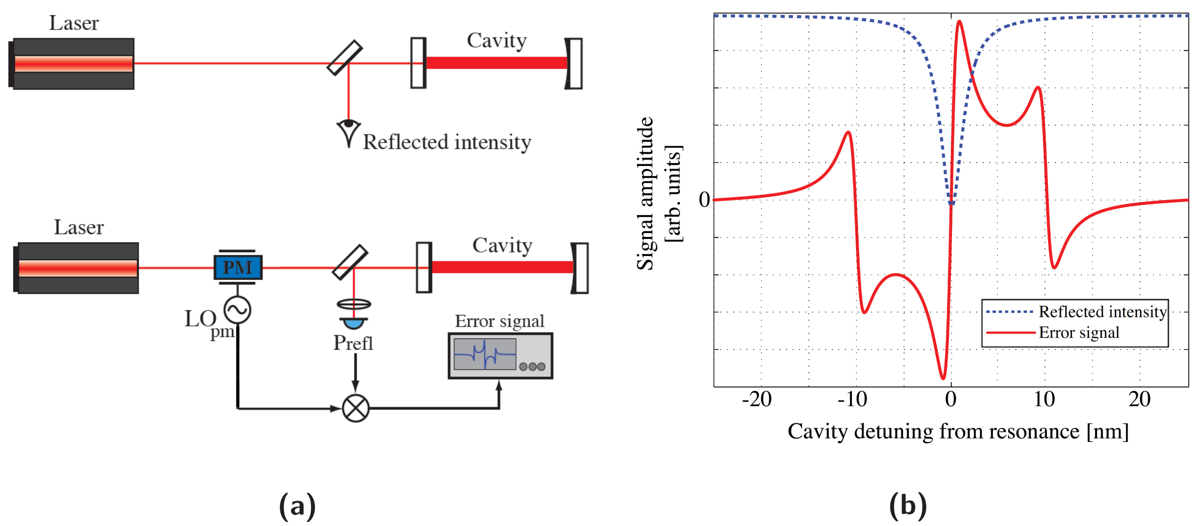

Figure 2.4: *Basic layout of the Pound-Drever-Hall error signal collection scheme [39]. The light coming from the laser, the carrier, is phase-modulated, which adds sidebands that are reflected by the cavity. This reflected light P_{refl} is measured with a photo-detector and demodulated to create the PDH error signal.*

2.5 Sensitivity of shot noise limited interferometer

By choosing a fixed value for $\mathscr{F}$ we have optimized the detector for gravitational waves of a particular frequency (the cavity pole)

$$f_p = \frac{1}{2\tau} = \frac{\pi c}{8\mathscr{F} L}, \tag{2.22}$$

causing the shot noise limited sensitivity to be frequency dependent.

Imagine that the light enters the cavity just as a gravitational waves with frequency f impinges on the detector in such a way that it starts elongating the arm. If $f > f_p$, more than half the wave will traverse the detector while the light is in the cavity and part of the phase built up by the elongation will be negated when the wave shortens the arm. On the other hand, if $f < f_\mathsf{p}$, less than half a wave will pass and the light is still picking up phase when it exits the cavity. Only when $f = f_\mathsf{p}$, exactly half the wave traverses the detector while the light was in the cavity, maximizing the phase change. Therefore f_p is known as the *frequency pole* of the cavity. For Virgo f_p was set at 785 Hz.

Up to now, to calculate the shot noise limited sensitivity we have assumed that the storage time of the cavity arms T_γ was much smaller than the gravitational wave period T_GW, *i.e.* $T_\gamma \ll T_\mathsf{GW}$. But, now that the arms are Fabry-Perôt cavities this time needs to be replaced by the *storage time* of the cavity $\tau = 2L_\mathsf{eff}/c$, which for Virgo is $\approx$ 0.3 ms, and which is of the same order of magnitude as T_GW. Therefore we can no longer consider the gravitational wave amplitude constant during the observation time, and the induced phase $\Delta\phi_\mathsf{GW} \neq h_0\tau$, and needs to be replaced by $\int \phi(t)dt$.

In the case where a gravitational wave in the $+$-polarization enters the detector at $t = 0$, the strain $h(t)$ is given by $h(t) = h_0 \sin\omega t$. During the storage time τ this wave induces a time delay

$$\Delta\phi_\mathsf{GW} = \int_0^\tau \frac{4\pi L}{\lambda} h(t)dt = \frac{4\pi L h_0}{\lambda}\int_0^\tau \sin\omega t \; dt = \frac{4\pi L h_0}{\lambda\omega}\left[1 - \cos\omega\tau\right]. \tag{2.23}$$

During the integration time the shot noise on the dark fringe will be $\tau\Delta P_\mathsf{shot}$. Calculating the sensitivity of the detector from the signal to noise ratio, as was done in section 2.3.3, Eq. (2.24) becomes

$$\frac{\Delta\phi_\mathsf{GW}}{\tau} = \frac{4Lh_0}{\lambda\tau}\frac{f_\mathsf{p}}{f}\left[1 - \cos\left(\frac{\pi f}{f_\mathsf{p}}\right)\right] = \sqrt{\frac{\hbar\omega}{2\eta P_0}}, \tag{2.24}$$

and the sensitivity of the detector

$$S = \frac{\pi}{8\mathscr{F}L}\sqrt{\frac{\hbar\omega}{2\eta P_0}}\frac{f}{f_\mathsf{p}\left[1 - \cos\left(\frac{\pi f}{f_\mathsf{p}}\right)\right]}. \tag{2.25}$$

The net gravitational wave signal is built up of contributions from light with storage times of all multiples of $2L/c$. The actual signal is then obtained from a phasor sum of all these contributions and is given by [40, 41]

$$S = \frac{\lambda}{8\mathscr{F}L}\sqrt{\frac{\hbar\omega}{2\eta P_0}}\sqrt{1 + \left(\frac{f}{f_\mathsf{p}}\right)^2}. \tag{2.26}$$

Fig. 2.5 shows the sensitivity curves of a power recycled simple Michelson (dashed curve), that of a Michelson with Fabry-Perôt cavity arms given by Eq. (2.25) (gray curve), and given by Eq. (2.26) (black curve). Replacing the arms with Fabry-Perôt cavities makes the sensitivity of the interferometer frequency dependent. The detector is optimized for frequencies corresponding to the cavity pole f_p, but at the cost of worsening it at frequencies $f = 2nf_\mathsf{p}$;

frequencies where the storage time of the cavity corresponds to multiple times the gravitational wave period. The phase acquired by the light due to one half of the wave is negated by the other half. The net sensitivity however comes from a combination of signals with a variety of storage times, which limits the effect. The sensitivity does decrease above the cavity pole, but gradually.

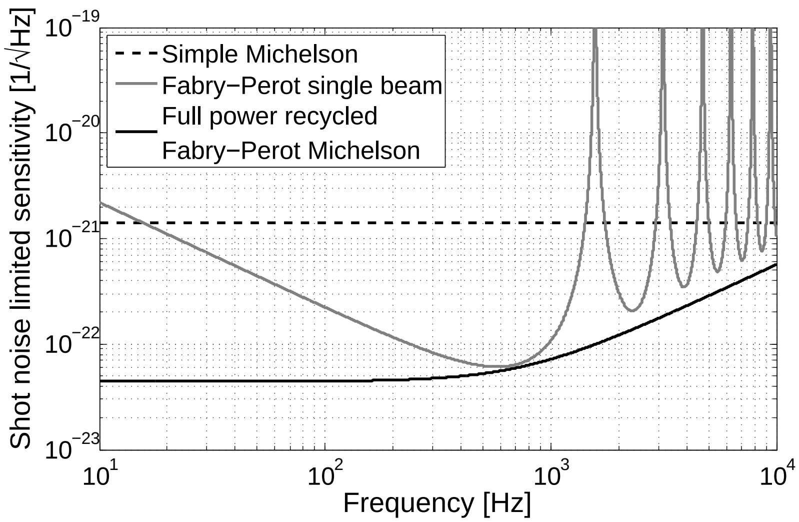

Figure 2.5: *Shot noise limited sensitivity of a simple Michelson interferometer, and a Fabry-Perôt Michelson, both with arm lengths $L = 3$ km and an effective laser power $P_0 = 150$ W.*

2.6 Noise sources

Equation (2.13) tells us what the smallest value of phase difference between the two laser beams is that still gives an optical signal observable by the dark fringe photo-diode. However, a change in proper length of the arms is equivalent to a displacement of the end mirror. Our Michelson interferometer converts all phase differences between the laser beams into an optical signal; regardless their origin. We are only interested in those induced by gravitational waves. The true sensitivity of the interferometer is then determined not only by the smallest power fluctuations that can be detected *but also by its ability to exclude phase noise from other sources*.

Any differential change in the interferometer arm lengths will produce an optical signal at the interferometer output. Usually, noise sources are classified in two categories:

1. Noise sources that change the position of the mirror surface, such as seismic noise, control noise, Newtonian noise, Brownian motion of the suspension, thermal noise in the mirror substrate and coating.

2. Noise sources that limit the measurement of the difference in arm cavity lengths, such as shot noise, radiation pressure noise, fluctuations in the laser's frequency and power, dispersion due to pressure fluctuations in the residual gas pressure in arm cavities.

These noise sources will be discussed in some more detail below.

2.6.1 Seismic noise

At low frequencies the Virgo sensitivity is limited by ground vibrations otherwise known as seismic noise. The ground at the Virgo site is vibrating continuously. At frequencies between 0.1 and 1 Hz, the ground is excited mainly by sea waves hitting the coast and pressing on the bottom of the sea causing the so-called micro-seismic peaks, which are present everywhere on Earth. The wind contributes as well. Apart from inciting the ocean's waves, it can excite the ground directly, or indirectly by blowing against trees and buildings [42].

At intermediate frequencies the ground is mainly excited by *cultural noise*. This is man-made noise such as due to traffic and industry and has clear daily and weekly variations: it is less severe during nighttime, on Sundays and even during lunch breaks.

A similar effect can be induced by machinery present at the Virgo site such as the air-conditioning systems or electronic equipment [14]. This kind of noise is referred to as technical noise, because it originates at the facility.

The seismic noise spectrum $S_{\text{seis}}(f)$ at Virgo is typically $S_{\text{seis}} = 10^{-7} \times f^{-2}$ m/$\sqrt{\text{Hz}}$ [43], making the ground vibrations of the order of 10^{-9} m/$\sqrt{\text{Hz}}$ at 10 Hz. This is orders of magnitude larger than the mirror motion induced by gravitational waves $hL/2$, which is of the order 10^{-19} m/$\sqrt{\text{Hz}}$.

The core optics of the interferometer such as the cavity mirrors, the beam splitter and the power-recycling mirror have stringent isolations requirements. The seismic isolation of these objects is provided by the *superattenuators* [44], which are further described in section 2.7.6. They provide isolation better than 10^{-14} at 10 Hz in both vertical as horizontal directions [43], reducing the motion of the mirrors and beam splitter to less than 10^{-25} m/$\sqrt{\text{Hz}}$ at 10 Hz.

With the main optics well isolated by the superattenuators, seismic noise may re-enter the interferometer mainly through scattered light [14]. Due to imperfections of the optics, light is scattered out of the main beam path and can, after reflecting on some surface of a bench or optical component, make its way back into the interferometer. If the reflective surface is seismically excited, then it will modulate the laser light and produce noise on the dark fringe. The search for such stray-light sources is never-ending.

2.6.2 Thermal noise

The mirrors and their suspensions are in thermal equilibrium with their surroundings. The thermal motion of the molecules excites the internal modes of the system. These modes cause vibrations of the mirror surface which introduce intensity fluctuations on the dark fringe. There are two important sources of thermal noise: internal modes of the coated mirror substrate and of its suspension.

The fluctuation spectra of the mirrors due to thermal noise can be obtained with the aid of the *fluctuation-dissipation theorem* [45]. It states that thermal noise amplitude spectrum $S_{\mathsf{x}}(\omega)$ is related to the real part of the mechanical admittance $Y(\omega)$ of the mirror [46]

$$S_{\mathsf{x}}(\omega) = \sqrt{\frac{4k_{\mathsf{B}}T}{\omega^2}\Re\left[Y\left(\omega\right)\right]}, \tag{2.27}$$

where k_{B} is Boltzmann's constant, T the absolute temperature of the mirror and ω the angular frequency of the fluctuation. The mechanical admittance $Y(\omega)$ of the system describes how much a structure yields when a harmonic force is applied and has units [(m/s)/N].

Suspension thermal noise

The suspensions of the mirrors are in vacuum. Therefore, viscous damping is negligible and structural damping dominates. In Ref. [47] the admittance of a structurally damped resonant mechanical system is calculated to be

$$Y\left(\omega\right) = \frac{\omega k\phi(\omega) + i\left(\omega k - m\omega^3\right)}{\left(k - m\omega^2\right)^2 + k^2\phi^2(\omega)}, \quad [(\mathsf{m/s})/\mathsf{N}], \tag{2.28}$$

where $\phi(\omega)$ is the loss angle: the phase lag of the response of the system to a sinusoidal force at a frequency $\omega \ll \omega_0$, k is the stiffness of the suspension, and m the mass of the suspended element. Substituting the real part in Eq. (2.27) and remembering that $k/m = \omega_0^2$, we obtain the amplitude spectral density of suspension thermal noise, which is

$$S_{\mathsf{x,sus}}(\omega) = \sqrt{\frac{4k_{\mathsf{B}}T\omega_0^2\phi(\omega)}{m\omega\left[\left(\omega_0^2 - \omega^2\right)^2 + \omega_0^2\phi^2(\omega)\right]}}, \quad \left[\mathsf{m}/\sqrt{\mathsf{Hz}}\right], \tag{2.29}$$

which falls of with $\omega^{-5/2}$, for frequencies $\omega \gg \omega_0$.

Substrate and coating thermal noise

Thermal excitations in the mirror substrate and coatings excite the internal modes of the mirror. In Ref. [46] the mechanical admittance of the mirror is derived for frequencies below the lowest internal mode frequency of the substrate, which usually has a frequency of several kHz. It is given by

$$Y(\omega) = \frac{\omega(1-\nu^2)}{2Er_0\sqrt{\pi}}\phi_{\mathsf{eff}}, \quad [\mathsf{m/s/N}], \tag{2.30}$$

where ν represents the Poisson ratio of the substrate material, E its Young's modulus, r_0 the radius of the Gaussian laser beam, and ϕ_{eff} the loss angle, which is equal to $1/Q$, where Q is the quality factor of the lowest frequency internal mode of the substrate. The amplitude spectral density of the thermal losses in the mirror substrate is then given by

$$S_{\mathsf{x,mirror}}(\omega) = \sqrt{\frac{4k_{\mathsf{B}}T(1-\nu^2)}{\omega\sqrt{\pi}r_0E}\phi_{\mathsf{eff}}}, \quad \left[\mathsf{m}/\sqrt{\mathsf{Hz}}\right], \tag{2.31}$$

which falls off with $\omega^{-1/2}$ for frequencies below the first internal mode of the substrate.

The Virgo mirrors are made of fused silica, their high-reflectivity coatings consist of layers of the dielectric materials Ta_2O_5 and SiO_2. Fused silica has low internal friction. Therefore its internal modes will have high quality factors, of the order of 10^7 [48], causing the material to exhibit little thermal noise below its lowest internal resonance frequency.

Mechanical friction in the coating will lower the quality factor of the mode and increase the amount of thermal noise. The coating mechanical loss is dominated by Ta_2O_5 rather than by SiO_2, whose loss angles were found to be 3.0×10^{-4} and 5×10^{-5} [49]. Their effect has been directly observed in small scale interferometers [50], where an effective loss angle $\phi_{\mathsf{eff}} = 6.5\times10^{-6}$ was observed. Thus, although the thickness of the coating is much smaller than that of the substrate, the thermal noise of the mirrors is dominated by mechanical losses in the Ta_2O_5 coating material. Therefore, significant effort is made to identify low-loss coating materials and further the understanding of mechanical loss mechanisms in existing coating materials [49, 51, 52].

2.6.3 Quantum noise

Quantum noise is noise that arises due to the quantum nature of light. In section 2.3.2 we have already seen an example of one such effect. Shot noise: the statistical fluctuations in the number of photons impinging on the dark fringe photo-diode causing a power fluctuation indistinguishable from a gravitational wave signal. The shot noise power spectral density is therefore given by Eq. (2.13), with the laser power P_{L} replaced by power at the beam splitter P_0

$$S_{\mathsf{shot}} = \frac{1}{4\pi L}\sqrt{\frac{2h_{\mathsf{p}}c\lambda}{P_0}}. \tag{2.32}$$

There is a second way in which the statistical fluctuation of the number of photons introduces noise in an interferometer. As each photon carries a momentum $p_\gamma = h_{\mathsf{p}}/\lambda$, where h_{p} is

Planck's constant, its reflection on the mirror surface exerts a force of twice that amount. The average force exerted by the photons does not introduce noise; it just gives a position offset of the mirrors, which will be compensated by the control system. However, the variation in the number of photons ΔN_γ produces fluctuations in the radiation pressure on the mirrors. The resulting mirror motion causes noise on the interferometer output. This is called *radiation pressure noise*.

The number of photons being reflected by the mirrors is also described by Poisson statistics and therefore varies with $\sqrt{N_\gamma}$. The ASD of the radiation pressure

$$S_{\mathsf{F}_{\mathsf{rpn}}} = 2p_\gamma\sqrt{N_\gamma} = 2\sqrt{\frac{h_\mathsf{p}P_\mathsf{circ}}{\lambda c}}. \tag{2.33}$$

The mirrors are suspended objects. Therefore, for frequencies well above the eigenfrequency ω_0 of the suspension, their displacement spectrum due to these force fluctuations is determined by the mechanical susceptibility of the suspension $X/F = \omega_0^2/\omega^2 = k_\mathsf{eff}/M\omega^2$, where X represents the Fourier transform of the motion of the mirror, M the mass of the mirror, and k_eff the effective spring constant of the mirror-suspension system*. The displacement spectrum of the mirror S_x is

$$S_\mathsf{x} = \frac{k_\mathsf{eff}}{M\omega^2}\Delta S_{\mathsf{F}_{\mathsf{rpn}}} = \frac{k_\mathsf{eff}}{2\pi^2 M f^2}\sqrt{\frac{h_\mathsf{p}P_\mathsf{circ}}{\lambda c}}. \tag{2.34}$$

The power in the two arm cavities are anti-correlated: every photon that enters one cavity does not enter the other. The total effect of the radiation pressure noise is therefore doubled. Furthermore, the phase shift is proportional to the arm length L, so the radiation pressure noise power spectral density S_rp is given by

$$S_\mathsf{rp} = \frac{2}{L}S_\mathsf{x} = \frac{k_\mathsf{eff}}{\pi^2 M L f^2}\sqrt{\frac{h_\mathsf{p}P_\mathsf{circ}}{\lambda c}}. \tag{2.35}$$

We have now found two noise sources that arise due to the statistical fluctuation in arriving photons: shot noise and radiation pressure noise. Because of their shared origin, shot noise and radiation pressure noise are usually combined into quantum noise S_q as

$$S_\mathsf{q} = \sqrt{S_\mathsf{rp}^2 + S_\mathsf{shot}^2} \tag{2.36}$$

where S_shot is given by Eq. (2.32) and S_rp by Eq. (2.35).

*This effective spring constant has two contributions. First, the mirror is suspended from the *marionette*; the last stage of the superattenuator (see section 2.7.6). The mirror is therefore a pendulum with a certain effective spring constant. Second, the radiation pressure pushes the cavity away from resonance. This reduces the power circulating in the cavity which in turn reduces the radiation pressure, moving the cavity closer to resonance. In this way, radiation pressure is an optical spring with its own effective spring constant. This optical spring will be dominant when the circulating power is large. A comprehensive treatment can be found in Ref. [53].

Fig. 2.6 shows the shot noise, radiation pressure noise and quantum noise of a power recycled Michelson interferometer with finesse $\mathscr{F} = 50$ and effective arm lengths $L = 3$ km and a power at the beam splitter $P_0 = 20$ kW. As the radiation pressure noise is proportional to f^{-2} it introduces noise at low frequencies, while at high frequencies the sensitivity is shot noise limited.

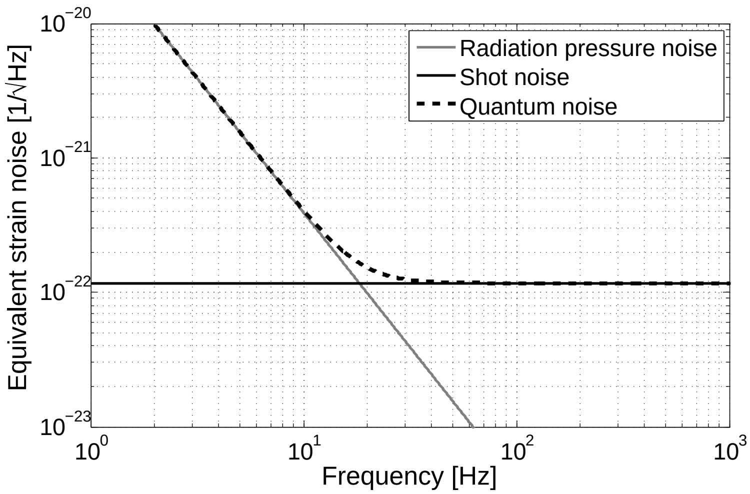

Figure 2.6: *Quantum noise of a power recycled Michelson interferometer with arms cavities of length $L = 3$ km, a finesse $\mathscr{F} = 50$, a power at the beam splitter of $P_0 = 20$ kW, and a circulating power $P_{\text{circ}} = 600$ kW.*

The standard quantum limit

Equation (2.35) shows that the amount of radiation pressure noise is proportional to $1/\sqrt{P}$, while Eq. (2.32) tells us that shot noise is proportional to $\sqrt{P}$. So, increasing the power will increase the amount of radiation pressure noise and reduce the amount of shot noise. This means that for every frequency there is an optimal power that minimizes the amount of quantum noise.

This optimal power P_{opt} is that value of P_0 at which the contributions of radiation pressure noise and shot noise are equal $S_{\text{rp}} = S_{\text{shot}}$. Equating Eqns (2.32) and (2.35) we find [40]

$$P_{\text{opt}} = \frac{c\lambda\pi M f^2}{k_{\text{eff}}\sqrt{8\mathscr{N}}}. \tag{2.37}$$

Substituting this expression in Eq. (2.36) we obtain an expression for the minimum amount of quantum noise at any frequency known as the *Standard Quantum Limit – SQL*

$$S_{\text{SQL}} = \frac{1}{\pi L f}\sqrt{\frac{\hbar k_{\text{eff}}\sqrt{2\mathscr{N}}}{M}} \tag{2.38}$$

Fig. 2.7 shows the quantum noise for P_0 = 20 W, 200 W, 2 kW and 20 kW together with the standard quantum limit. Increasing the power enhances the radiation pressure noise contribution and lowers that of shot noise, shifting the minimum amount of quantum noise to higher frequencies, but the total amount of quantum noise is never lower than the SQL.

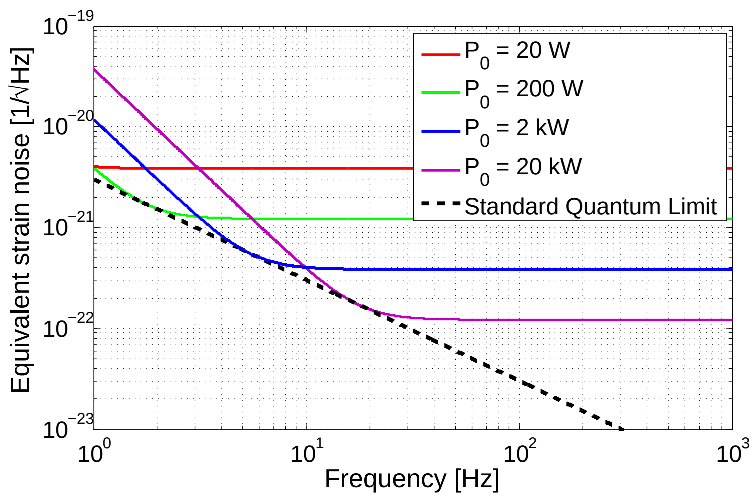

Figure 2.7: *Quantum noise curves for several values of P_0 and the Standard Quantum Limit – SQL.*

Squeezing

The existence of the SQL is a manifestation of the Heisenberg uncertainty principle [54]. To observe the effect that a gravitational wave has on the detector, we need to actually measure changes in the position of the Fabry-Perôt cavity mirrors. Increasing the power lowers the amount of shot noise, which results in a smaller error on the position measurement, but at the cost of increasing the uncertainty in the mirrors momentum *i.e.* increasing the amount of radiation pressure noise.

In 1980, a paper [55] was published by Caves in which he pointed out that an alternative but equivalent view of the source of radiation pressure noise exists: fluctuations of the electromagnetic field enter the interferometer at its output and produce the fluctuating force that disturb the mirrors. In a second paper [56] he introduced a way to decreasing one form of quantum noise at the cost of enhancing the other, not by changing the input power, but by injecting a *squeezed state* at the interferometer output.

The vacuum fluctuations are equal in both its quadratures. One quadrature phase can be seen as causing shot noise, while the other causes radiation pressure noise. By injecting a squeezed state, a state whose fluctuations in one quadrature are greater, and in the other quadrature lower than the vacuum fluctuations, we can exchange shot noise for radiation pressure noise and vice versa.

This is useful, because as can be seen in Fig. 2.7 for low enough input powers all quantum noise is shot noise. Moreover, the low-frequency sensitivity of gravitational wave detectors is not even limited by quantum noise, but by seismic and thermal noise. This means that reducing the amount of shot noise and raising the amount of radiation pressure noise by injecting squeezed states improves the high-frequency sensitivity without affecting the low-frequency sensitivity. Squeezing has already been successfully applied in large-scale gravitational wave detector [57].

Fig. 2.7 also shows that for a given input power the SQL is only reached for one particular frequency. Below this frequency there is an excess of radiation pressure noise; above it of shot noise. By injecting frequency dependent squeezing, the respective contributions of shot noise and radiation pressure noise can be altered is such a way that the total amount of quantum noise will closer resemble the SQL. Frequency-dependent squeezing has not yet been achieved in large-scale interferometers. Because gravitational wave detectors are close to being limited by quantum noise over their entire detection bandwidth, frequency-dependent squeezing is an active field of research [58, 59].

2.6.4 Fluctuations in optical path length

Density fluctuations in the gas between the Fabry-Perôt cavity mirrors causes changes in the optical path length of the circulating photons. This effectively changes the length of the arms, which produces intensity fluctuations on the dark fringe. In order for these path length changes to be negligible the pressure in the arm cavities needed to be of the order of 10^{-7} mbar for the initial detectors while for the advanced detectors the residual pressure needs to be below 10^{-9} mbar. [60]. To achieve this, Nikhef has developed cryolinks that have been placed between the arm vacuum chambers and those housing the Fabry-Perôt cavity mirrors [14].

2.6.5 Acoustic noise

The direct excitation of optical elements by pressure waves is called *acoustic noise*. It is mainly produced by electronic devices. Known sources of acoustic noise are the air-conditioning systems and cooling fans of the electronics racks. The former produce a broad spectrum of acoustic noise between a few Hz and about 200 Hz. The latter produce narrow lines at their rotation frequencies.

The way acoustic noise enters the interferometer is similar to that of seismic noise. Optics, or their mounts situated on benches in air can get excited by air currents, their motion imprinting itself onto the laser light. Alternatively, stray light reflecting on acoustically excited surfaces can make its way into the interferometer, introducing noise on the dark fringe.

2.7 The Virgo gravitational wave detector

Figure 2.8 shows a bird view of the Virgo detector [13]. It is located at the European Gravitational wave Observatory EGO, approximately 12 km South of Pisa, Italy. It is a power recycled Michelson interferometer where the arms are 3 km long Fabry-Perôt cavities.

Virgo was first proposed in 1989 and approved by the French and Italian funding agencies in 1994. Construction started in 1996 and ended in 2003. During years of commissioning the sensitivity of the detector increasingly improved [61] until the first science run VSR1 was undertaken in coincidence with LIGO between May and October 2007 [62]. A number of small upgrades, resulting in what is called *Virgo+* (see section 2.9), and three science runs later the NS-NS horizon of the detector had reached 13 Mpc [32].

In March 2012, Virgo shut down for a major upgrade. Its successor Advanced Virgo will be discussed in section 2.11.

Figure 2.8: *The Virgo gravitational wave observatory [13].*

2.7.1 Optical layout

Fig. 2.9 shows the optical layout of Virgo. It divides naturally into three parts: the injection system, the main interferometer and the detection system. The injection system consists of the laser, external injection bench and input mode cleaner (IMC); the main interferometer of the power recycling mirror, the beam splitter and the two 3 km long Fabry-Perôt cavities; the detection system of the output mode cleaner and the dark fringe photo-diodes. The parameters of all Virgo optical elements and cavities can be found in Ref. [63].

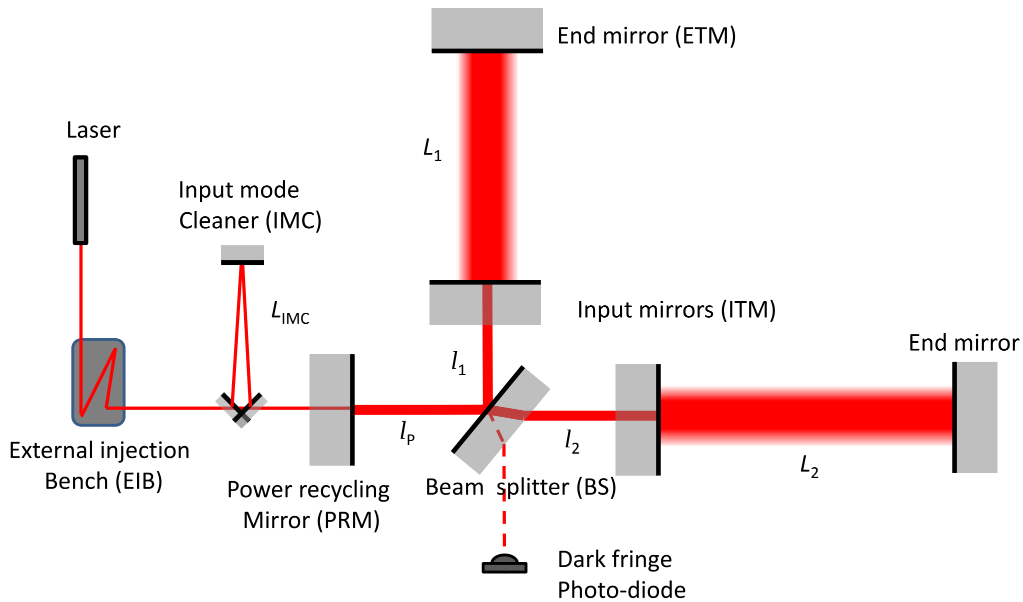

Figure 2.9: *Schematic representation of the optical layout of the Virgo detector.*

2.7.2 Injection system

The Virgo laser

Virgo utilized two lasers. A high-power Nd:YVO4 slave laser is locked to a low-intensity, highly stable solid state Nd:YAG master laser with a wavelength of 1064 nm. In this way the laser beam has the power of the slave laser and the stability of the master laser. Together they provide a laser beam of 20 W.

The intensity and frequency of the laser are stabilized with suitable servo loops. Nevertheless, the light will exhibit beam jitter: high frequency fluctuations in its pointing direction. Furthermore, the laser beam's transverse intensity profile will be a super position of spatial modes, the TEM modes. The Fabry-Perôt cavities are designed to keep the fundamental mode, the TEM_{00} mode, resonant; the radius of curvature of the end mirrors matches the spatial profile of the beams. The other spatial modes can cause unwanted intensity fluctuations at the interferometer's output and are therefore rejected as much as possible. A resonant cavity called the *pre-mode cleaner*, situated on the laser bench, acts as a first filter for these unwelcome fluctuations of the beam's geometry and pointing.

External injection bench

The external injection bench houses the *beam monitoring system* BMS. The pointing of the laser beam in the direction of the IMC is controlled with two piezoelectric actuated mirrors, using quadrant photo diodes (QPDs) as sensors.

The external injection bench also houses a number of quadrant photo-diodes that are used to stabilize the angular degrees of freedom of the input mode cleaner.

Input mode cleaner

The input mode cleaner is a 144 m long, suspended, triangular cavity (see Fig. 2.9) with a finesse of about 1000. It is made up by the *input mode cleaner end mirror* and two mirrors that together form the L-shaped *dihedron**. To make a stable cavity the mode cleaner end-mirror is concave and has a radius of curvature of 182 m. The dihedron is situated on the *suspended injection bench*.

The IMC filters the spatial modes of the laser beam, provides a reference to pre-stabilize the frequency of the laser and reduces the beam jitter. Every round trip in the triangular cavity each TEM mode acquires a longitudinal phase called the *Gouy phase* that has a different value for each TEM mode. The optical path length of the input mode cleaner is maintained at such a value that only the fundamental laser mode TEM00 resonates properly.

The suspended injection bench also hosts *the reference cavity*, a 30 cm long high finesse rigid Fabry-Perôt resonator, used in the laser frequency control chain below 100 Hz, and the photodetector used for the laser power stabilization.

2.7.3 Main interferometer

The laser beam coming from the input mode cleaner travels through the power recycling mirror and impinges on the beam splitter under an angle of 45°. The beam splitter reflects 50% of the light towards the West arm cavity and allows the other 50% to be transmitted towards the North arm cavity.

The light enters the cavities through the input mirrors (sometimes called input test masses ITM), which are flat. The waist of the beam is placed on the input mirror surface. The North and West end mirrors (end test masses ETM) are concave to match the Gaussian profile of the beam. Their radii of curvature are about 3600 m. The Fabry-Perôt cavities have a finesse of 50, which makes their effective length of 95 km.

The mirrors that make up the cavities are made of fused silica. They have a diameter of 0.70 m and weight 21 kg. In order for the losses in the cavities not to limit the sensitivity of the detector the mirror optical losses have to be smaller than 10^{-4}. To reduce the scattering losses, the mirrors have been polished to achieve a surface roughness of better than 0.05 nm RMS.

Absorption mainly takes place in the coating of the mirrors. It changes the index of refraction of the substrate and deforms the mirror surface. This distorts the large-scale flatness of the mirror and their radius of curvature, which in turn affects the spatial amplitude of the

*Developed at Nikhef.

light. As the power circulating in the arm cavities is large and the light has to travel through the input mirrors, this effect takes predominantly place in the input mirrors. To restore the flatness of these mirrors they have been fitted with ring heaters, that heat the area around the laser beam.

As the Virgo detector was operated on the dark fringe, the Fabry-Perôt cavities reflect all the light back towards the IMC, where it is in turn reflected back by the power recycling mirror (PRM). Together with the ITMs, the PRM forms the 12 m long power recycling cavity. The effect of the PRM can be better understood by representing the combination of the two arm cavities as a compound mirror whose reflectivity is basically 1 when the detector is operating at the dark fringe. The PRM and such an equivalent mirror form a Fabry-Perôt resonator which allows to boost the optical power impinging on the beam splitter by factor greater than 30 (300W compared to the 8W measured at the IMC output).

2.7.4 Detection system

The beams from the two arm cavities are recombined at the beam splitter and projected onto the dark fringe photo diode. To get to the photo-diode the light needs to pass through the *output mode cleaner* OMC: a 2.5 cm rigid triangular cavity made of fused silica. It filters out non-Gaussian spatial modes caused by misalignments and optical defects. The OMC length is controlled by changing the temperature of the cavity with a Peltier cell [60].

2.7.5 Control scheme

Longitudinal control

The laser light is modulated at 6.270777 and 8.361036 MHz. The modulation frequencies were chosen such that the sidebands are resonant in the input mode cleaner and central interferometer made up by the power recycling and input mirrors, and completely reflected by the Fabry-Perôt cavities. Referring to Fig. 2.9, the lengths thus controlled are [14]:

- CARM $= \frac{L_1+L_2}{2}$,
- DARM $= \frac{L_1-L_2}{2}$,
- MICH $= l_1 - l_2$,
- PRCL $= l_{\mathrm{P}} + \frac{l_1-l_2}{2}$.

A complete description of the control scheme employed by Virgo can be found in Ref. [64].

Angular alignment

When left untouched, the residual angular motion of the mirrors is of the order of a few micro-radians. This corresponds to beam misalignments of several millimeters per round trip in the arm cavities and does not make for a stable resonant cavity.

In stand-alone mode, the angular degrees of freedom of the suspended mirrors are controlled locally by means of optical levers and quadrant photo-diodes measuring their orientation with respect to the ground. Such a local control lowers the amplitude of the angular motion enough to acquire the lock of the interferometer but doesn't ensure a long-term stable global alignment. For this reason, after the lock is acquired, the relative orientation of the mirrors is controlled globally by reconstructing their alignment with respect to the nominal optical axis of the interferometer. The error signals for this so-called automatic alignment system are extracted by sampling the laser beam at different locations of the interferometer and imaging it with differential wavefront sensors. In this way a few nanoradians alignment accuracy is achieved for the most critical degrees of freedom. A complete description of the angular alignment scheme that was employed by Virgo can be found in Ref. [65].

Frequency stabilization

To stabilize the frequency of the laser, the length of the IMC is used as a reference. The laser beam is phase-modulated at 22 MHz. The side-bands thus added to the carrier are not resonant in the IMC, which allows the extraction of a Pound-Drever-Hall signal (see section 2.4.3). The bandwidth of the control loop is 300 kHz. Due to seismic noise, the length of the IMC is not a good reference at low frequency. A PDH signal in reflection of the rigid reference cavity (RFC) is used below 100 Hz. In this way a stability of a few Hz RMS is achieved; stable enough to lock the interferometer. After the Fabry-Perôt cavities have been put in a controlled state, the laser frequency is locked to the average length of the interferometer arms. The common mode of the arms, which is called the CARM degree of freedom, is free to vary with time; the laser frequency is adjusted to keep it resonant in the cavities. The RFC is used to prevent the laser frequency and CARM degree of freedom of wandering too far. With the full stabilization loop engaged, a residual frequency noise of $2 \times 10^{-7}/\sqrt{\text{Hz}}$ is achieved [64].

2.7.6 Virgo's seismic isolation

To cope with all the noise sources described in section 2.6, gravitational wave interferometers are outfitted with a number of isolation systems that either prevent the displacement noise from occurring, or remove it from the laser beam.

Superattenuator

The important optical elements of the interferometer: the power recycling mirror, the beam splitter and the four Fabry-Perôt mirrors, are seismically isolated by *superattenuators* [60, 66]. These are chains of mechanical filters from which the optical components are suspended. The mechanical filters are low-frequency resonators compliant in all 6 degrees of freedom. Above their resonance frequency the transmission of each filter is proportional to f^{-2}. Cascading n filters provides an isolation of the suspended mass of $A/f^{2\mathrm{n}}$, where $A = \prod_{\mathrm{i}=0}^{\mathrm{n}} f_{\mathrm{i}}$.

Fig. 2.10 shows a schematic representation of a Virgo superattenuator. The horizontal filters are simple pendulums with a length of 1.15 m. This makes their uncoupled resonance frequencies 0.5 Hz. The bob of each pendulum is a vertical mechanical filter [67]. A vertical filter consists of a set of pre-bent, triangular cantilever blades that are connected to a central keystone from which the wire (the next horizontal isolation stage) is hanging. This simple configuration provides each stage with an uncoupled resonance frequency of 1.5 Hz. To reduce this frequency to the level of the horizontal filters a magnetic anti-spring system is used. An array of permanent magnets are placed in the repulsive configuration. One array is placed on the keystone, the other on the filter body. The repulsive force lowers the vertical restoring force of the filter thus lowering its resonance frequency to 0.4 Hz.

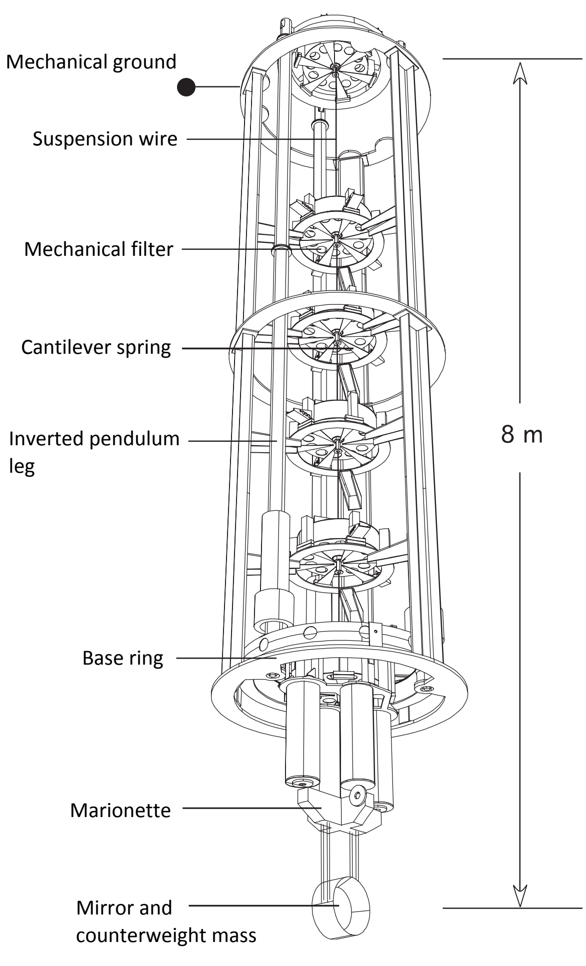

Figure 2.10: *Schematic representation of a Virgo superattenuator [44].*

A special device called the *marionette* [44] is suspended from the last vertical filter, the so-called filter-7 (F7). The mirror and its reaction mass are suspended from the marionette with four 1.9 m long wires; fused silica fibers for the mirror, steel ones for the reaction mass. The position and orientation of the mirror can be adjusted by moving the marionette, which is accomplished by applying forces from F7 with coil-magnet actuators. Above a few Hz, the control authority of the longitudinal degree of freedom is released to the coil-magnet set applying forces directly to the mirror from the reaction mass.

The filter chain is hanging from a rigid ring, the top stage, which is attached to ground by 6 m long *inverted pendulum legs* (see section 3.4), which have an resonance frequency of 30 mHz. These inverted pendulums provide the first stage of horizontal isolation. The top stage is equipped with position and inertial sensors as well as a number of coil-magnet actuators. These are used to damp the normal modes of the system (all below 2.5 Hz) and to suppress the very low frequency differential motion between different mirrors, the so-called tidal control. The superattenuator suppresses the transmission of seismic motion by more then 10 orders of magnitude [44].

2.8 Sensitivity of Virgo

Given Virgo's input power, its sensitivity is fundamentally limited by shot noise. However, other phenomena in the detector cause power fluctuations on the dark fringe that surpass the shot noise level and limit the sensitivity. Fig. 2.11 shows the design sensitivity together with the modeled amplitude spectral densities of relevant noise sources (the Virgo *noise budget*). Below 2 Hz the Virgo sensitivity is limited by seismic noise, between 2 and 200 Hz by thermal noise from the mirror and its suspension and above 200 Hz by shot noise. The narrow peaks belong to thermal excitations of the suspension (violin and vertical bouncing modes) and mirror normal modes.

Fig. 2.12 shows the Virgo design sensitivity together with the best sensitivity that was achieved during its last science run VSR4. It shows that Virgo had reached its design sensitivity at almost all frequencies. Only above 1 kHz Virgo experienced slightly more shot noise than originally foreseen. The NS-NS horizon (see section 1.7) that corresponds to this sensitivity curve is 11.8 Mpc.

2.9 Virgo+

After Virgo had been fully commissioned in 2007 and its first science run VSR1 had been completed, a number of upgrades were undertaken which would result in *Virgo+*. An extensive description of the upgrade activities may be found in Ref. [68]. The main upgrades were:

- the installation of a better and less noisy read-out and control electronics,
- the installation of a more powerful laser amplifier increasing the input power from 8 W to 17 W,
- the installation of a thermal compensation system (TCS) [69].

When these upgrades were finished and Virgo+ was fully commissioned, a second science run VSR2 was undertaken.

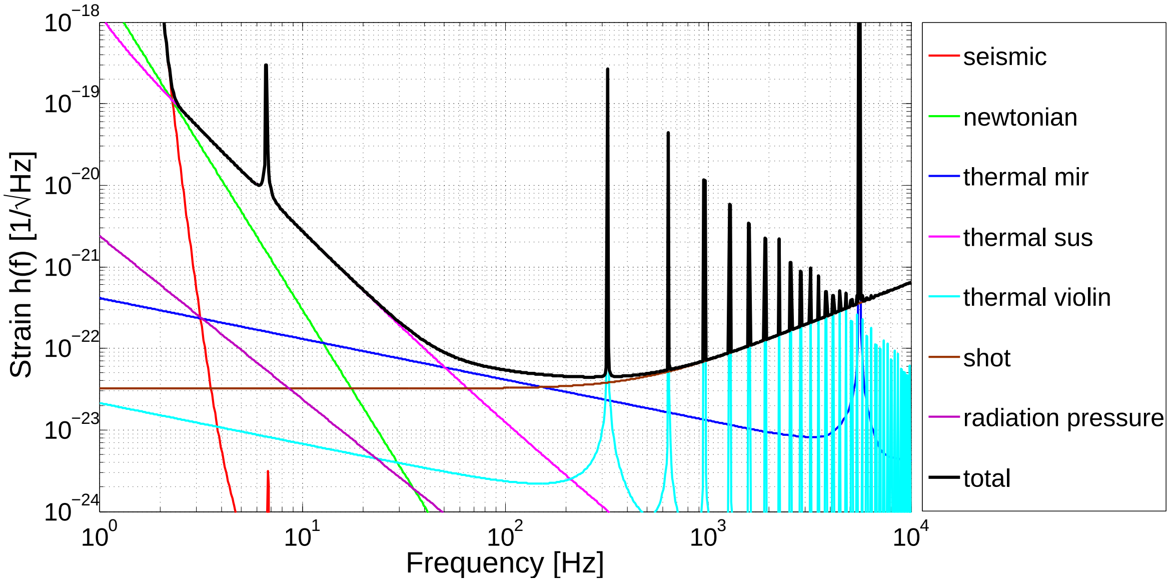

Figure 2.11: *Modeled Virgo noise budget. The colored curves are the amplitude spectral densities of the different noise sources. Their sum (black curve) is the design sensitivity of Virgo. The violin modes of the final suspension stage of the beam splitter and cavity mirrors cause a number of high-frequency lines.*

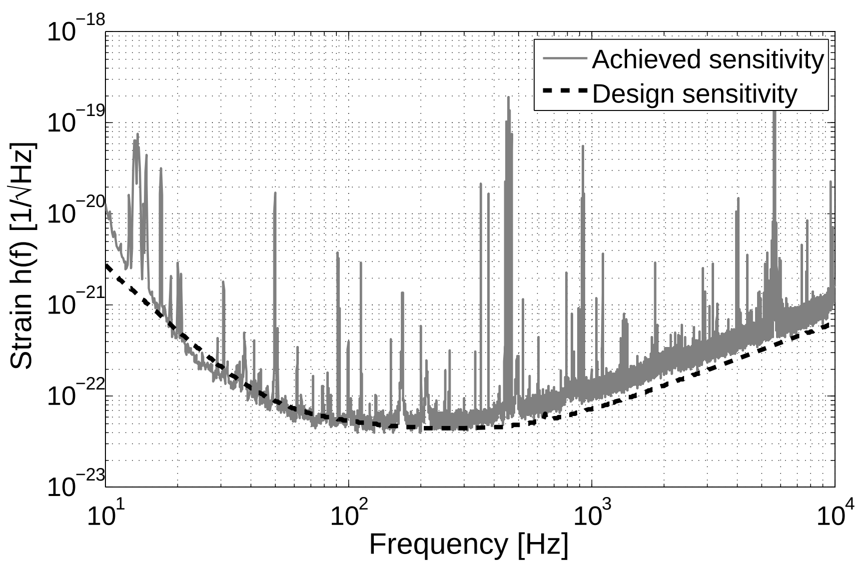

Figure 2.12: *The Virgo design sensitivity (black dotted curve) and the best achieved Virgo sensitivity (gray curve) measured on Friday, August 5$^{\text{th}}$ 2011, 7pm). Virgo had a NS-NS horizon of 11.8 Mpc.*

2.9.1 Thermal compensation

To enter the Fabry-Perôt cavities the laser light travels through the input mirrors. In this process a few ppm of the light is absorbed by the mirror substrate and coating. The resulting thermal expansion deforms the reflective surface and influences the resonant properties of the cavity. This leads to a worsening of the matching between the laser carrier and sidebands and prevents lock acquisition at high input powers.

To counter this effect, use is made of a *thermal compensation system* (TCS) [69]. It consists of a high power CO_2 laser whose Gaussian beam profile is converted into a ring profile with a special conical lens (axicon). Any remaining light in the center of the ring-shaped laser beam of the CO_2 laser is blocked by a mask to protect the center of the input mirror. In this way, the CO_2 laser heats up the peripheral region of the input mirrors and restores their flatness.

2.10 Virgo+MS

After VSR2, all four test masses were given monolithic suspensions. The steel suspension wires of the mirrors were replaced with fused silica ones in order to reduce the amount of suspension thermal noise. The fused silica wires are attached to custom silica supports called *ears*, which are in turn attached to the mirrors with a silica bonding technique, resulting in a full monolithic stage. This detector configuration in known as Virgo+MS [70].

2.11 Advanced Virgo

Between 2003 and 2013 Virgo has undergone a series of small upgrades, each of which enhanced its sensitivity, until during the 4^{th} science run, its design sensitivity was reached. However, after 1.2 years of running no detections were made. To significantly improve the detector's sensitivity still further a number of systems need to be radically changed. Therefore, Virgo is undergoing a major upgrade the result of which is called *Advanced Virgo*.

A full description of the upgrade activities can be found in Refs. [14, 35]. At the time of publication of this thesis the upgrade activities are ongoing and the injection system is being commissioned. Construction should be finished in January 2015, all installations should be concluded six months after that and the first 1 hour lock of the entire interferometer is foreseen for November 2015 [71].

2.11.1 Target sensitivity

The aim for Advanced Virgo is to improve its sensitivity by a factor 10 over the entire frequency range, which corresponds with an increase in detection rate of three orders of magnitude (the detection rate is proportional to the third power of the sight distance). Once Advanced Virgo is fully commissioned, the expected NS-NS and BH-BH horizons will be 134 and 1017 Mpc [14] and the expected rate 0.8 – 1400 events per year [34].

2.11.2 Advanced Virgo design

Fig. 2.13 shows the optical layout of Advanced Virgo. Although the basic detection strategy is identical to that of Virgo, there are some significant modifications and additional subsystems to improve the detector performance.

Laser power

To reduce the amount of shot noise and improve the high-frequency sensitivity the laser power needs to be increased. Once fully commissioned, Advanced Virgo will operate with an injection power (power coming from the input mode cleaner) of 125 W. Due to the losses in the input mode cleaner cavity the laser will need to deliver 200 W.

Initially, Advanced Virgo will be operated in low-power mode and the laser need only provide 60 W. During this phase the Virgo laser is used: a Nd:YVO4 (Neodymium doped Yttrium Orthovanadate) slave laser will be locked to a commercial 1 W master laser (Innolight NPRO) master laser. For the high-power laser, R&D work is done on fiber-lasers. The installation of the final laser is planned for 2018 [35].

Signal recycling

Advanced Virgo will be what is known as a *dual recycled* interferometer [41]. This means that, in addition to the power recycling, *signal recycling* will be employed.

A *signal recycling mirror* will be placed between the beam splitter and the dark fringe photo-diode. This mirror forms an additional cavity with the Fabry-Perôt cavities; the light containing the gravitational wave signal is returned to the interferometer arms to continue interacting with the gravitational wave. This is not equivalent to just increasing the storage time in the arm cavities. The position of the signal recycling mirror gives an additional degree of freedom which allows to re-inject the light into the arm cavities with exactly the correct phase to add coherently with the signal being produced by the gravitational wave. In this way the detector's sensitivity will be enhanced in a certain frequency range.

The frequency region at which the detector is most sensitive is called *the bucket*. The shape of the bucket can be altered by changing the position of the signal recycling mirror,

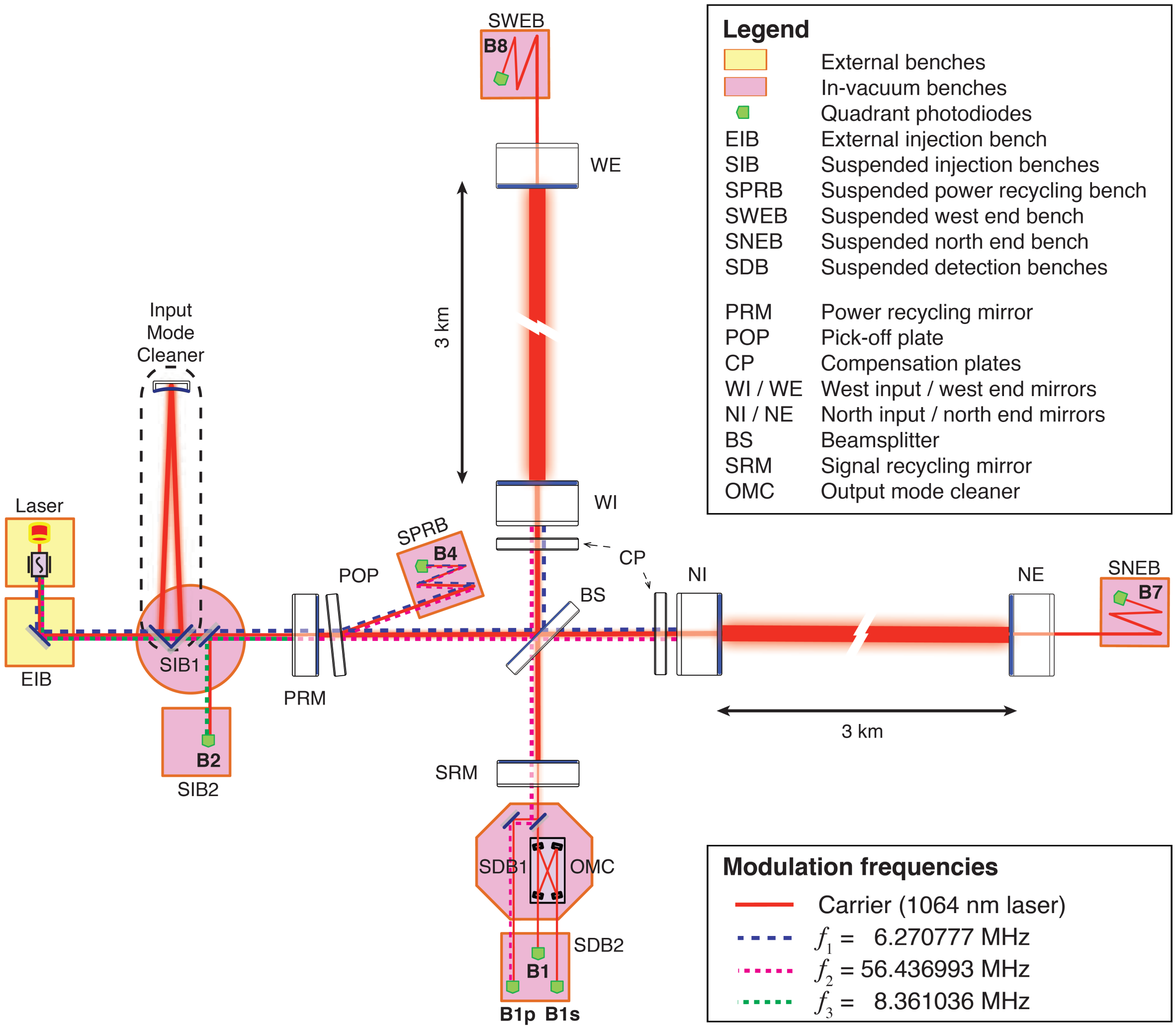

Figure 2.13: *Optical layout the Advanced Virgo gravitational wave detector [42].*

which changes the tuning of the signal recycling cavity. In this way the peak sensitivity or its bandwidth can be altered to optimize the detector for a certain source.

Fabry-Perôt cavity mirrors

The increased input power will increase the thermal noise from the mirror substrates and coatings. To lower the thermal noise from the mirror substrates, the input mirror substrates will be made of Suprasil 3002 fused silica, which has a bulk absorption three times lower than that of the Virgo mirrors (0.2 ppm cm^{-1}) [72]. The power absorbed in the coatings will be ten times more than that in the substrates. The coating material with the lowest mechanical losses is Ti doped Ta_2O_5 and will be used for the high-reflective coatings.

To further limit the amount of thermal noise, the spot size on the arm cavity mirrors is enlarged. Instead of putting the waist of the laser beam on the input mirror, it will be placed in the center of the arm cavities. The resulting spot sizes on the input and end mirrors will be 48.7 and 58 mm respectively. This means that both the input and end mirrors will be concave to match the spatial profile of the beam.

The finesse of the arm cavities will be increased to $\mathscr{F} = 443$. This makes the effective cavity length $L_{\text{eff}} = 2\mathscr{F}L/\pi = 850$ km, the storage time of the cavity $\tau = 2L_{\text{eff}}/c = 5.6$ ms and the cavity pole $f_{\text{p}} = 1/2\tau = 90$ Hz.

Due to the higher laser power and increased finesse of the cavities, the power circulating in the Advanced Virgo arm cavities will be 10 times higher than it was in Virgo. To reduce the amount of radiation pressure noise the mass of the mirrors will be 42 kg; twice as heavy as the Virgo mirrors.

Thermal compensation

Like Virgo, Advanced Virgo will employ a thermal compensation system to compensate for optical path length distortions due to *e.g.* thermal expansion of the reflective surfaces of the input mirrors. This system will also be used to correct for manufacturing errors in the power recycling, signal recycling and Fabry-Perôt cavity mirrors, such as errors in their radius of curvature, or inhomogeneities of their index of refraction.

Deviations in the wavefront at the different mirrors will be detected by dedicated wave front sensors called *phase cameras**. Ring heaters apply corrections to the radii of curvature in the Fabry-Perôt cavity mirrors as well as for the thermal expansion of the input mirrors due to absorption. Deviations in the optical aberrations of the recycling cavities are cured by applying a proper heating pattern with a CO_2 laser, but not directly onto the mirror as was done in Virgo, but on *compensation plates* which are suspended in front of the mirrors.

*These were designed and constructed at Nikhef.

Sensing and control

Because the sensitivity of Advanced Virgo will be an order of magnitude better than its predecessor, the requirements for its control system are more stringent. The longitudinal and angular degrees of freedom of the interferometer need to be controlled to better accuracy and with less noise. Initially, Advanced Virgo will not employ signal recycling and the longitudinal degrees of freedom that need to be controlled are the four listed in section 2.7.5. At a later stage, signal recycling will be added and also the length of the signal recycling cavity will need to be controlled.

A control strategy for the lock acquisition and science mode operation has been designed using frequency domain simulations in Finesse [73] and Optickle [74] and time domain simulation in e2e [75]. The interferometer needs to be brought into a controlled state in a reasonable amount of time (few tens of minutes), be stable and have a good duty cycle. In addition, the noise injected by the control loops should be a factor 10 below the detector's design sensitivity.

The longitudinal degrees of freedom need to be controlled down to the picometer level. Most of them will be controlled with PDH [38] error signals. Three modulation frequencies are foreseen. These need to meet five requirements:

- all sidebands must be transmitted by the Input Mode Cleaner (IMC),
- two of them must be resonant inside the PRC,
- one of these must also be resonant inside the Signal Recycling Cavity (SRC),
- the other's transmission to the dark port must be as small as possible,
- the third sideband must be anti-resonant inside the PRC.

The Advanced Virgo modulation frequencies will be: 6270777, 56436993 and 8361012 Hz. Only the DARM degree of freedom will be controlled with a DC signal. The studies of the control of the longitudinal degrees of freedom can be found in Ref. [76].

The angular degrees of freedom need to be controlled at the nanoradian level. Due to the higher injection power and the higher finesse of the Fabry-Perôt cavities, the power circulating in the arms will be 650 kW. The stronger radiation pressure effect changes the opto-mechanical transfer function of the detector and makes the control of the angular degrees of freedom of the mirrors more difficult. The studies of the control of the angular degrees of freedom can be found in Ref. [77].

Suspended benches

To reach the desired sensitivity of Advanced Virgo, a number of benches housing the ancillary optics used for the sensing and control of the main interferometer needs better seismic isolation. Without improved isolation these optical components would be a source of scattered light (see section 2.6.1). In addition, the (quadrant) photo-diodes on the end benches used for the angular alignment of Virgo were mostly situated on optical benches in air. The control system of Advanced Virgo requires these photo-diodes to be shot-noise-limited. This places stringent requirements on the residual motion of the benches housing these sensors. The motion in the horizontal and vertical degrees of freedom needs to be of the order of 2×10^{-12} m/$\sqrt{\text{Hz}}$ while that of the angular degrees of freedom needs to be about 3×10^{-15} rad/$\sqrt{\text{Hz}}$ above 10 Hz [42].

To this end, five optical benches, whose locations are depicted in Fig. 2.13, will be suspended, in vacuum, to isolate the optical systems from seismic and acoustic disturbances: one injection bench (SIB2), two benches in transmission of the end mirrors (the end benches: SWEB and SNEB), a bench in reflection of the power recycling mirror (SPRB), and the detection bench (SDB2). They will be suspended from a multi-stage seismic attenuation system called *multiSAS*, which will be housed in custom vacuum chambers called minitowers.

The multiSAS systems are made up from the same (or similar) components as EIB-SAS, but are essentially more like short superattuators. A chain of pendulums and geometric anti-springs (see section 3.5) is suspended from a platform that stands on short inverted pendulums (see section 3.4). Feedback is used to actively damp the system's rigid body modes and to maintain the long-term position and orientation. A full description of these systems can be found in Ref. [42].

2.11.3 Advanced Virgo noise budget

Fig. 2.14a shows the reference noise budgets of Advanced Virgo operated at 125 W of injection power and with signal recycling as reported in the Advanced Virgo Technical Design Report (TDR) [14]. Since the publication of the TDR, the detector design and noise estimations have progressed. Fig. 2.14b shows a more current and improved version of the Advanced Virgo noise budget, which was reported in Ref. [35].

Initially, it was estimated that the detector would be limited by thermal noise at low frequencies and by shot noise at high frequencies. Fig. 2.14a shows that with good performance of the thermal compensation system, the detector would be limited by quantum noise above 30 Hz.

The recoil mass of the payloads have been eliminated and experiments have shown that at the time of the TDR, the amount of suspension thermal noise was overestimated. Furthermore, improved modeling of the gravity gradient noise predicts that it will have a larger contribution to the noise budget. As a consequence, it is now estimated that Advanced Virgo will be quantum noise limited in the entire detection bandwidth, and that a contribution of gravity gradient noise may be observed at low frequencies.

The main improvements of Advanced Virgo over Initial Virgo are summarized in Table 2.1. Their combined effect increases the sight distances for neutron star and black hole binaries of this configuration from 13 and 150 Mpc to 134 and 1017 Mpc, respectively.

Parameter	Advanced Virgo	Initial Virgo
Arm length	3 km	3 km
Laser wavelength	1064 nm	1064 nm
Optical power at laser output (P_L)	$>$175 W	20 W
Optical power at interferometer input	125 W	8 W
Optical power on beam splitter (P_0)	4.9 kW	0.3 kW
Optical power at test masses (P_circ)	650 kW	6 kW
Mirror material	Fused silica	Fused silica
Diameter of the arm cavity mirrors	35 cm	35 cm
Weight of the arm cavity mirrors	42 kg	21 kg
Flatness of the arm cavity mirrors	0.5 nm RMS	$<$ 8 nm RMS
Finesse of the arm cavities	443	50
Beam radius at input/end mirror	48.7/58 mm	21/52.5 mm
Pressure of cavity vacuum	10^{-9} mbar	10^{-7} mbar
Test mass suspension	Fused silica wires	Steel wires
Number of in-vacuum suspended benches	7	2
Binary neutron star inspiral range	134 Mpc	12 Mpc
Minimum strain sensitivity	$3.5 \times 10^{-24}/\sqrt{\mathrm{Hz}}$	$4 \times 10^{-23}/\sqrt{\mathrm{Hz}}$

Table 2.1: *Main parameters of initial Virgo and the Advanced Virgo reference design taken from Ref. [14].*

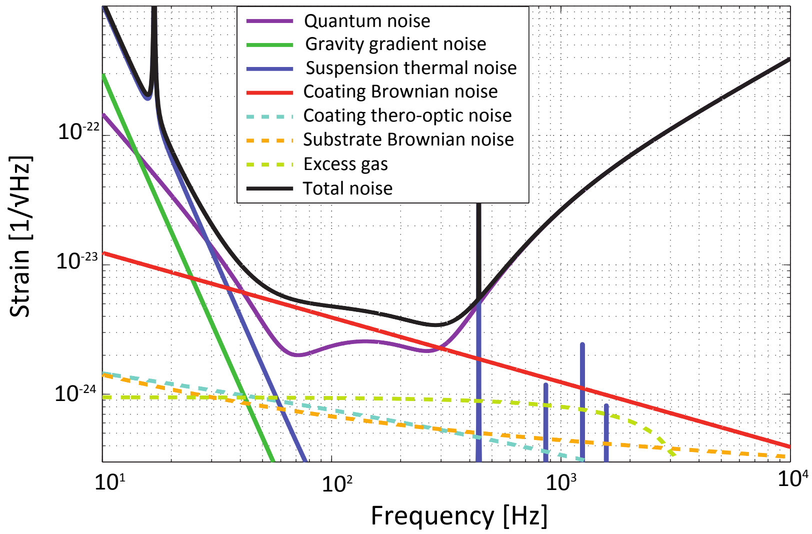

(a) *Reference sensitivity of TDR [14].*

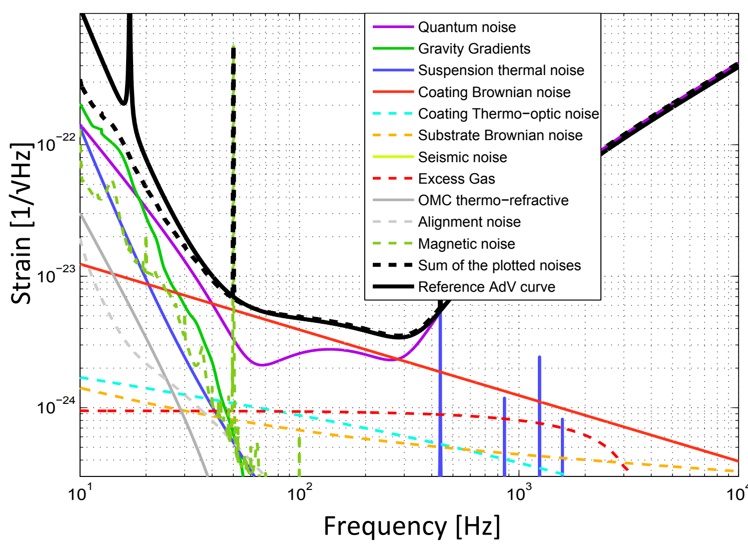

(b) *Updated Advanced Virgo noise budget [35].*

Figure 2.14: *(a) Reference sensitivity and expected noise contributions for Advanced Virgo (for the signal recycled configuration with an input power of 125 W) as described in the TDR [14]. Further details of the noise contributions can be found is Ref. [78]. (b) Advanced Virgo reference sensitivity (solid black curve) and noise budget (dashed black curve) as reported in Ref. [35], where improved models for the suspension thermal noise and gravity gradient noise have been used. According to the latest projections, Advanced Virgo will be limited by quantum noise, and the possibility exists that gravity gradient noise will be observed.*

2.12 Beam jitter noise from the external injection bench

By now you will hopefully be convinced that the sensitivity of Advanced Virgo will be sensational and the detection of the first gravitational wave in the history of mankind imminent. There is, however, one noise source that would limit the sensitivity of the detector and that we have yet to address.

During the combined commissioning and science run of the Virgo gravitational wave detector in 2010, an extensive noise study was conducted. It was aimed at understanding the detector sensitivity curve [79]. This revealed that the compliance of the bench support structure of the external injection bench resulted into several rigid body modes between 10 and 100 Hz, while the mounts of several optics situated on this bench had structural resonances between 200 and 300 Hz. The excitation of these mechanical resonances resulted in a significant amount of beam jitter at the corresponding frequencies, which is right in the middle of the frequency region in which Advanced Virgo aims to be most sensitive.

Fig. 2.15 shows the reconstructed sensitivity curve of Virgo during VSR2 (thin black curve), the design sensitivity of Advanced Virgo without signal recycling and the projected beam jitter noise from the external injection bench. Clearly, the beam jitter noise from these mechanical resonances would spoil the Advanced Virgo sensitivity.

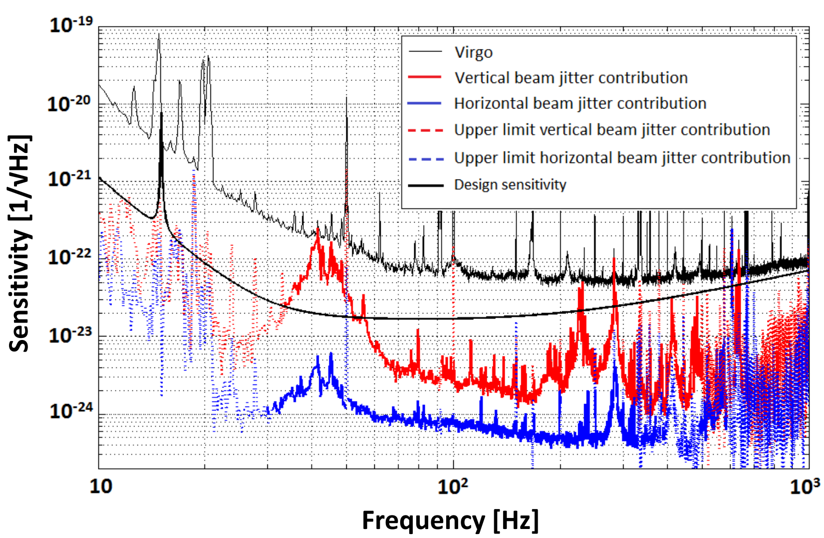

Figure 2.15: *Beam jitter noise due to mechanical modes of the external injection bench and its optics mounts [79]. The thin black curve is the reconstructed sensitivity of Virgo during its second science run VSR2, the blue and red curves are the projected contributions of beam jitter, originating from the external injection bench, to the Virgo noise budget and the thick black curve is the design sensitivity of Advanced Virgo, without signal recycling. Beam jitter from the external injection bench exceeds the design sensitivity of Advanced Virgo and would limit this detector's performance.*

2.13 The solution: EIB-SAS

To subdue the noise described in section 2.12, a new support structure for the EIB was designed and built at Nikhef: the so-called External Injection Bench Seismic Attenuation System, or EIB-SAS. It is a single stage vibration isolation system that employs both passive and active isolation schemes. Passive isolation is provided by mechanical resonators with a low eigenfrequencies (typically between 100 and 500 mHz): inverted pendulums for the horizontal degrees of freedom, geometric anti-spring filters for the vertical degrees of freedom. These resonators are second-order low pass filters; above their natural frequency f_0 they attenuate ground vibrations with f_0^2/f^2, where f is the Fourier frequency. Ground vibrations with a frequency f_0 are amplified by the inverted pendulums and geometric anti-spring filters. Feedback control is used to actively lower the quality factors of these modes. Chapter 3 contains an exhaustive description of EIB-SAS and its components.

2.14 Requirements for EIB-SAS

Several performance criteria for EIB-SAS were defined by the Virgo collaboration [80]. First and foremost, the motion of the EIB, induced by seismic motion of the ground, needs to be kept within limits such that beam jitter noise from the sensors mounted on the optical bench is negligible. Figure 2.16 shows the maximum allowed movement of the optical bench (dashed curve) and the motion of the bench with the old support structure (solid curve) that in several frequency regions exceeds the requirement by up to two orders of magnitude.

In addition, EIB-SAS needs to be stable over long periods of time: the RMS of its motion should stay within $\pm$ 20 μm for translational degrees of freedom and 10 μrad for rotational degrees of freedom on the time scale of 24 hours. The system has to be stable with respect to temperature variations of $\pm$1 °C. Finally, the effects of acoustic noise on the system have to be determined.

2.15 Summary

In this chapter the main operation principles of interferometric gravitational wave detectors have been introduced. These instruments are essentially Michelson interferometers whose sensitivity is determined by the signal to noise ratio at the interferometer output.

Two fundamental noise source arise from the quantum nature of light: shot noise, which is a fluctuation in the number of photons impinging on the photo-diode at the interferometer output, and radiation pressure noise, which is a fluctuation in the force exerted by the photons on the interferometer mirrors, which introduces fluctuations in the arm lengths of

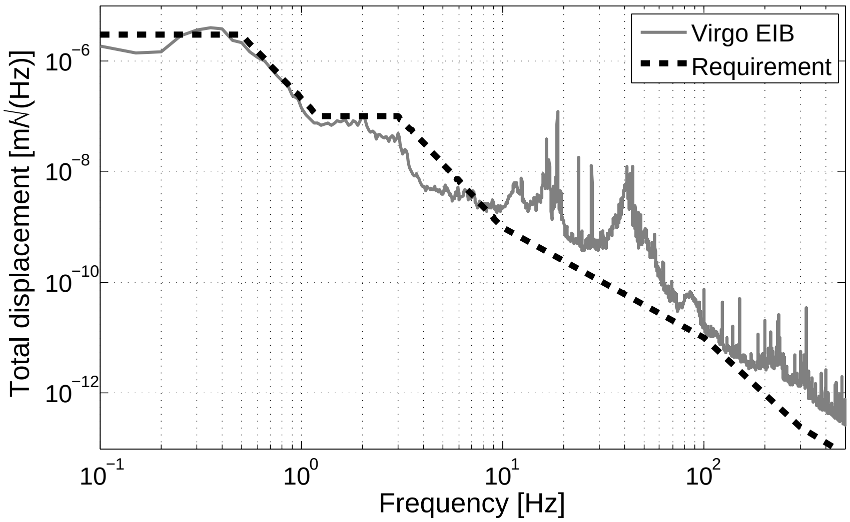

Figure 2.16: *External injection bench displacement requirements for Advanced Virgo: the dashed curve indicates the maximum allowed displacement for EIB-SAS, obtained by quadratically adding the displacements in* x, y *and* z *direction. The gray curve is the displacement spectrum measured at Virgo on top of the external injection bench.*

the interferometer. To minimize the amount of shot noise and make a first optimization of the signal-to-noise ratio, gravitational wave detectors are operated on the dark fringe: all light is reflected back in the direction of the laser, no light is transmitted to the output.

The sensitivity of the interferometer is enhanced when the laser power is increased. Therefore, gravitational wave detectors incorporate a power recycling mirror, positioned between the laser and the beam splitter, to coherently re-inject the light reflected by the interferometer. Furthermore, to optimize the interaction time of the photons with the gravitational wave, the interferometer arms are 3 km long Fabry-Perôt cavities. In addition, spatial mode purity and pointing of the laser beam are improved by keeping the laser carrier resonant in the input mode cleaner.

The sensitivity of the first generation detectors like Virgo, was limited by seismic noise at low frequencies, by thermal noise at intermediate frequencies, and by shot noise at high frequencies. At the end of 2011, a major upgrade, termed Advanced Virgo, was started to increase the sensitivity of the detector. For this upgrade: the power of the laser and the finesse of the arm cavities are increased, the quality of important optical components is improved and a number of benches that house important optical components are getting better seismic isolation. The sensitivity of Virgo's successor, Advanced Virgo, will be increased by a factor 10 and its expected event rate will be increased by a factor 1000. Advanced Virgo will only be limited by fundamental noise sources: shot noise at high frequencies and radiation pressure noise at low frequencies.

However, a detailed noise study undertaken while operating Virgo brought to light an additional noise source that would limit the sensitivity of Advanced Virgo: beam jitter due to seismically induced motion of the external injection bench. To eliminate this noise source, a new seismic isolation system for this optical bench was proposed: the external injection bench seismic attenuation system, or EIB-SAS. A number of requirements that EIB-SAS needs to meet were established by the Virgo collaboration:

1. The residual motion of the bench may not exceed the spectrum depicted in Fig. 2.16.
2. The system must be able to cope with temperature variations of ± 1 °C.
3. The system's static position must be maintained within $\pm$ 20 μm for translational degrees of freedom and 10 μrad for rotational degrees of freedom on the time scale of 24 hours (RMS values).
4. The mechanical modes of the system must be characterized.
5. As must be the acoustic noise coupling.

In the following chapters we discuss the design and performance of EIB-SAS.

3 The external injection bench seismic isolation system: EIB-SAS

"It's not just what it looks like and feels like. Design is how it works."
- Steve Jobs,
New York Times, 30 November 2003

3.1 Introduction

In section 2.12 we showed that the External Injection Bench (EIB) was a source of considerable noise for Virgo. Resonances of the EIB support structure between 30 and 60 Hz were excited by seismic ground motion, which caused a considerable amount of beam jitter noise. The optics mounts have resonances between 200 and 300 Hz that also caused beam jitter noise, but it was unclear whether these were excited by seismic ground motion or solely by the acoustic background. If no measures are taken, then the beam jitter noise would limit the sensitivity of Advanced Virgo.

In order to exploit the full potential of Advanced Virgo, the seismically induced motion of the EIB had to be reduced. The new EIB support structure should provide a neutral behavior with respect to the ground over the widest possible frequency range (it should not amplify the ground motion at any frequency). It was requested that it reduces the bench motion by at least two orders of magnitude between 30 and 60 Hz and between 200 and 300 Hz with respect to the original support [80]. For frequencies between 0.1 and 1 Hz the RMS of the ground motion should not be exceeded (see section 2.12) to limit re-introduction of noise in the form of diffused light.

To achieve the design goal, a new support structure for the external injection bench was designed and built at Nikhef: the External Injection Bench Seismic Attenuation System, EIB-SAS. It has been designed to reduce the motion of the EIB by more than 40 dB above 10 Hz in six degrees of freedom and it operates in air. In this chapter the system and is components are described in some detail.

This chapter focuses on the mechanical properties of EIB-SAS. The seismic isolation capabilities of EIB-SAS are provided by mechanical oscillators that can be tuned to low frequencies: inverted pendulums, and geometric anti-spring filters (GAS filters). After a historic introduction and an overview of the system, the mechanical properties of the inverted pendulums and GAS filters will be described respectively in sections 3.4 and 3.5.

Each section will start with a description of the mechanical filters, after which analytical models of the filters will be introduced. They will be concluded by an extensive report of the results of the characterization measurements that have been undertaken.

3.2 Short history of seismic attenuation systems

The first scientific device* in history that required soft springs was the torsion balance, independently invented by Charles-Augustin de Coulomb (1777) and John Michell (~1783). Coulomb used it to measure the electrostatic force, which let him to the formulation of Coulomb's law. In 1798, Henry Cavendish used a torsion balance in what is now known as the Cavendish experiment in which he measured the value of the gravitational constant.

3.2.1 Low-frequency resonators and anti-springs

In the 19th and 20th century, low-frequency resonators were mainly used in seismography. Early seismometers were not very sensitive, but were useful for the study of earthquakes. Only after the invention of the LaCoste suspension [81] in 1932 did high performance seismometers become available. LaCoste combined a suitable pre-stressed helical spring and a pendulum to make a very long-period (more than 30 seconds) compact vertical oscillator (the so-called *zero-length spring*). What started as a challenge posed by his professor, A. Romberg, ended up as the introduction of negative stiffness mechanisms in high-precision instruments. Together LaCoste and Romberg created a spin-off company (LaCoste and Romberg Company [82]) that made state-of-the-art gravimeters.

In the following decades the evolution of low-frequency resonators was driven by the desire to manufacture increasingly better seismometers. In the 1970s, E. Wielandt created the STS-1 seismometer, based on a single cantilever blade suspension, in which a geometric constraint created a negative stiffness effect sufficient to lower the natural frequency to 250 mHz [83]. Modern seismometers still work on the same mechanical principles as Wielandt's STS-1.

*Except maybe clocks. Spring-driven clocks appeared first in the 15$^{\text{th}}$ century.

3.2.2 Seismic attenuation systems for gravitational wave detectors

In search of good seismic isolation for the test masses of gravitational wave detectors, low-frequency resonators were an active field of study [84, 85] in the 1990s. Two main approaches to achieve seismic isolation were taken: the use of motion sensors with good low-frequency sensitivity and the application of feedback to actively reduce seismically induced motion, and passive isolation by mechanical filters. Both schemes employ low-frequency resonators. In the passive approach they are the filters, in the active one they are the sensors.

The Virgo collaboration selected the passive approach. The Pisa group designed the so-called superattenuator for the seismic isolation of Virgo [86]. They consisted of three newly developed inverted pendulums [87], which supported a platform from which a chain of vertical filters was suspended. These filters had to have low stiffness, while being able to carry loads of several hundred kilogram. They were compound vertical springs which consisted of $4-12$ pre-bent maraging steel blades. These springs could initially be tuned down to $\sim$1.4 Hz. By introducing a magnetic anti-spring [66], they brought the filter's resonance frequency down to $\sim$0.4 Hz.

By the end of the 1990s, the use of *anti-springs* (jargon for negative stiffness mechanisms) in seismic isolation systems had become common practice. But, although the magnetic anti-spring performed (and still performs) well, its mechanics were rather complex and alternatives were studied. One such alternative was the geometric anti-spring [88, 89]. Whereas the magnetic anti-spring filters of the Virgo superattenuator contained pre-bent cantilever blades that were straightened by their load, the blades of the *geometric* anti-spring filters (GAS filters) were flat when unloaded and bent by their load. For these filters, the anti-spring effect comes from geometrical constraints. This makes their mechanics less involved than that of the magnetic anti-spring filters. Furthermore, they contain fewer parts and are easier to assemble.

These geometric anti-spring filters were used in the seismic attenuation systems, conceptually similar to Virgo's superattenuator, of the Japanese gravitational wave detector TAMA [90]. Not much later, they were also employed in HAM-SAS [91, 15], a compact vibration isolation prototype device for the advanced LIGO output mode cleaner, which was built at Caltech.

HAM-SAS (Horizontal Access Module Seismic Attenuation System) comprises four short inverted pendulums for horizontal attenuation, four geometric anti-spring filters for the vertical attenuation, and a set of high-resolution position sensors and non contacting actuators for control of the position and pointing of the optical bench. This system is vacuum compatible and provides 40 dB of seismic attenuation in all degrees of freedom. It was improved upon at the Albert Einstein Institute in Hanover [16] to incorporate it in their 10 m prototype interferometer. EIB-SAS builds on these seismic attenuation systems.

3.3 EIB-SAS system overview

Fig. 3.1 shows a schematic representation of EIB-SAS. It is a single stage vibration isolation system that utilizes both passive and active attenuation mechanisms. The passive isolation is provided by mechanical oscillators that can be tuned to low frequencies: *geometric anti-spring filters* (GAS filters) [15] and *inverted pendulums* (IP) [92]. Above their resonance frequency these components act as second order low pass filters that attenuate ground motion by f_0^2/f^2, where f_0 represents the resonance frequency of the oscillator and f denotes the frequency. The resonance frequencies of the GAS filters and IPs are tuned below 400 mHz to meet the seismic attenuation and residual motion goals with a low unity-gain-frequency in the controls.

EIB-SAS has three GAS filters which support the optical bench and provide isolation for vertical (y-direction*), pitch (θ_x) and roll (θ_z) motion. These filters are housed in a so-called springbox which is supported by three IPs which provide isolation for the horizontal degrees of freedom (x and z direction and θ_y (yaw) motion).

At their resonance frequencies the mechanical oscillators amplify ground motion. To counter this effect, EIB-SAS is equipped with position sensors (LVDTs: Linear Variable Differential Transformers), inertial sensors (geophones) and voice-coil actuators. Feedback is used to actively lower the quality factor of these low frequency modes and to maintain the reference position of the bench. This feedback system is also used to damp the high frequency modes that originate from the horizontal compliance† of the GAS filters. High frequency modes due to vertical compliance of the IPs are damped with passive techniques.

Changes in the DC position on timescales of weeks or months due to *e.g.* movement of the building, can be compensated with stepper motors. EIB-SAS has four vertical stepper motors that act on the bench and three horizontal stepper motors that act on the springbox (see Fig. 3.1). These are also used to recover the working position of EIB-SAS after interventions on the bench, such as alignment of the optics.

Next, we discuss the two main passive isolation systems engaged in the design: inverted pendulums (IPs) and geometric anti-springs (GAS-filters).

3.4 Inverted pendulums

Fig. 3.2 shows the base of EIB-SAS. It contains three inverted pendulums (IPs) that are placed in an equilateral triangular configuration and support the springbox. The center of mass of the springbox is positioned approximately +5 cm in the x-direction above the center of the

*The Virgo coordinate system has been adopted for EIB-SAS. This is a right-handed coordinate system in which z is chosen to be in the direction of the laser beam and y points vertically upwards.

†Elastic deformation when subjected to a force. Compliance is the reciprocal of stiffness.

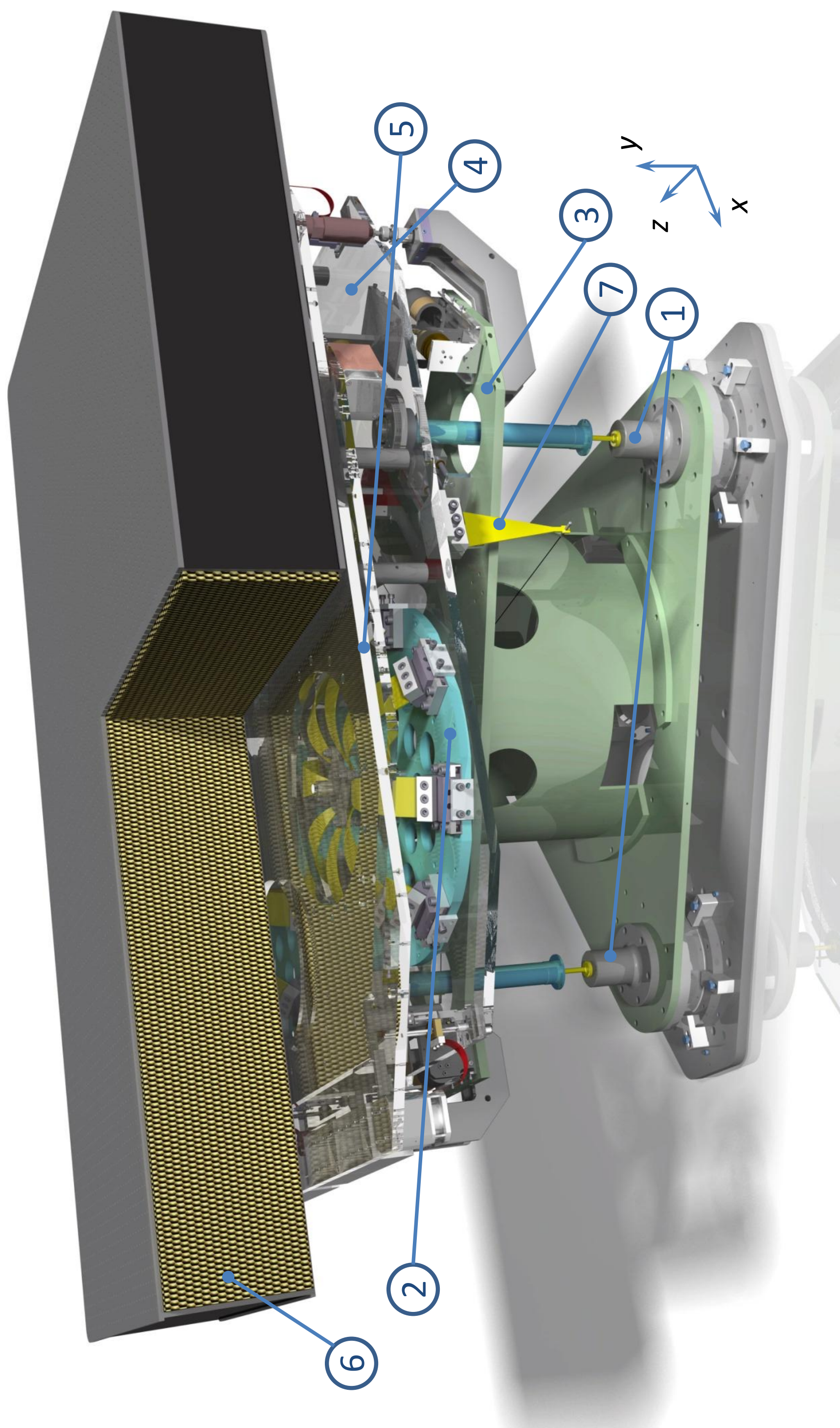

Figure 3.1: *Rendering of EIB-SAS indicating: the inverted pendulums (1), one of the geometric anti-spring filter (2), the LVDT platform (3), the springbox (4), top plate (5), the optical bench (6) and the tilt stabilizer (7).*

IPs; the IP that is located on the positive x side of the system carries a greater load than the other two. The position of the springbox is monitored with three LVDT position sensors (see section 5.4.2) that are located on a platform that is connected to ground by a stiff barrel-shaped support structure.

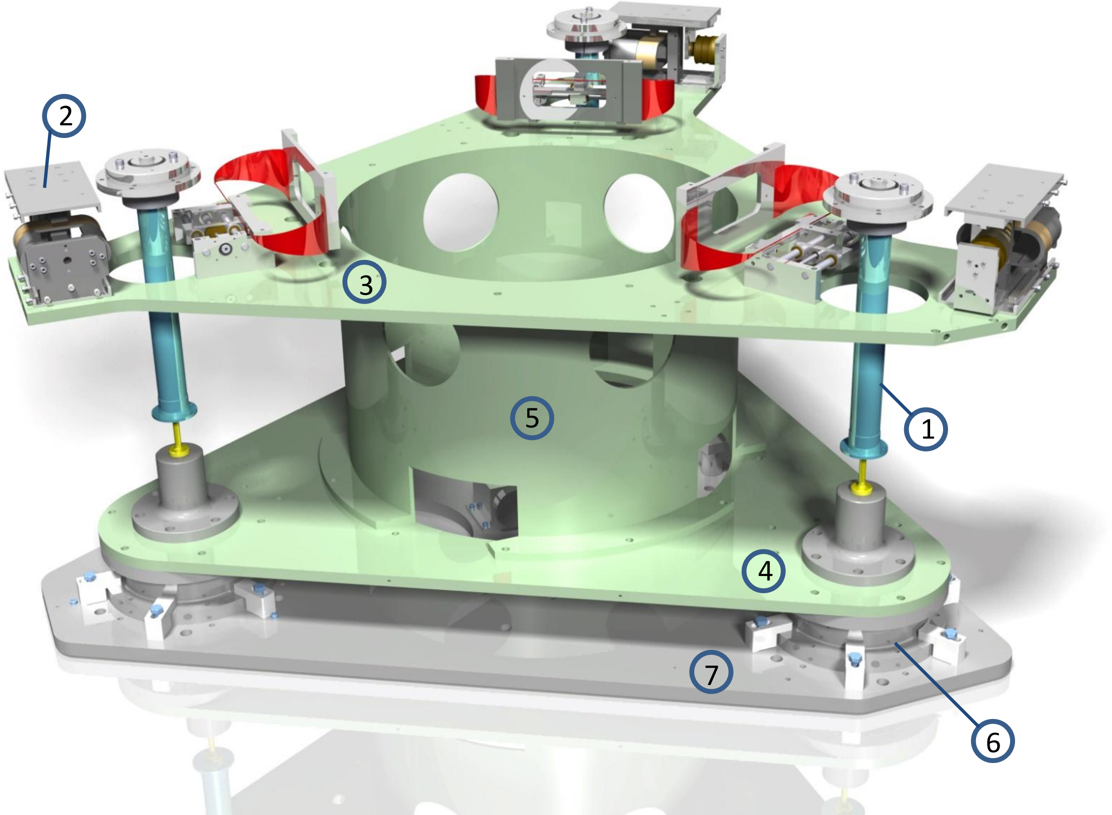

Figure 3.2: *Rendering of the base of EIB-SAS. EIB-SAS has three inverted pendulums (1) that support the springbox containing the vertical isolators. The horizontal LVDT position sensors (2) are housed on a sensor platform (3) that is connected to the base plate (4) with a stiff barrel shaped structure (5) and measure the position of the springbox with respect to the ground. The ground plate stands on three feet (6) that are positioned directly below the inverted pendulums. The feet in turn stand on the ground plate (7), which is glued to the floor.*

EIB-SAS was tested with two different sets of inverted pendulums. Fig. 3.3 shows a schematic representation of two versions of the IP leg.

Initially, EIB-SAS was equipped with Type-IP1 inverted pendulums. These consist of a 1 mm thick aluminum tube with a diameter of 50 mm which is connected to the ground via a flexible joint (Fig. 3.4a) with a diameter of 10.6 mm. The joint is attached to an aluminum foot. From the top of the tube a smaller flexible joint with a diameter of 3 mm is hanging (see Fig. 3.4c), which acts as universal joint and allows the springbox to move in the horizontal plane. The flexible joints are machined out of Marval 18 maraging steel [93] and have undergone a heat treatment (see section 3.5.6 and Ref. [94]) to increase their ultimate tensile strength. The top of the Type-IP1 inverted pendulum contains an eddy current damper that damps its internal modes (see section 3.4.6).

When the inverted pendulum is brought out of equilibrium, the flexible joint provides the restoring force, while the gravitational force on the load on top of the IP pulls it out of equilibrium. By balancing the positive spring constant of the flexible joint with the negative gravitational restoring force acting on the payload, the resonance frequency can (in principle) be tuned to arbitrarily low values.

The second version of the IP (called Type-IP2) has a 2.0 mm thick stainless steel tube and an 11.2 mm thick flexible joint (Fig. 3.4b). These modifications were made to make the IP stiffer and this approach will be motivated in section 3.4.5. Also, the Type-IP2 inverted pendulum does not comprise a counterweight holder. This was removed to reduce the weight of the IP. The motivation for removing it is discussed in section 3.4.6. The properties of Type-IP1 and Type-IP2 inverted pendulums are summarized in Table 3.1.

Property	Description	Type-IP1	Type-IP2
m	mass of tube	0.198 kg	1.14 kg
M	load of IP	429 kg	429 kg
L_{tube}	length of tube	0.472 m	0.472 m
d_{tube}	diameter of tube	50.0 mm	50.0 mm
κ	angular stiffness of joint	1960 Nm/rad	2425 Nm/rad
$d_{\text{lower flex}}$	diameter bottom flexible joint	10.6 mm	11.2 mm
$L_{\text{lower flex}}$	length bottom flexible joint‡	58.5 mm	58.5 mm
$d_{\text{upper flex}}$	diameter top flexible joint	3 mm	3 mm
$L_{\text{upper flex}}$	length top flexible joint	24.4 mm	24.4 mm

Table 3.1: *Properties of two versions of the IP legs that have been used. These are referred to as Type-IP1 (initial) and Type-IP2 (final design) inverted pendulums.*

3.4.1 One dimensional model of an inverted pendulum

An inverted pendulum can be described as a mass M supported by a rigid beam of length L, mass m and moment of inertia I, which is connected to the ground with a flexible joint of angular stiffness κ (see Fig. 3.5 and Ref. [95]). To allow tuning of its center of percussion (see page 67), the inverted pendulum comprises a counterweight of mass M_{cw} on a leg of mass m_2, length L_2 and moment of inertia I_2. The properties of the inverted pendulums used in EIB-SAS are listed in Table 3.1.

‡This is an effective length. See section 3.4.5.

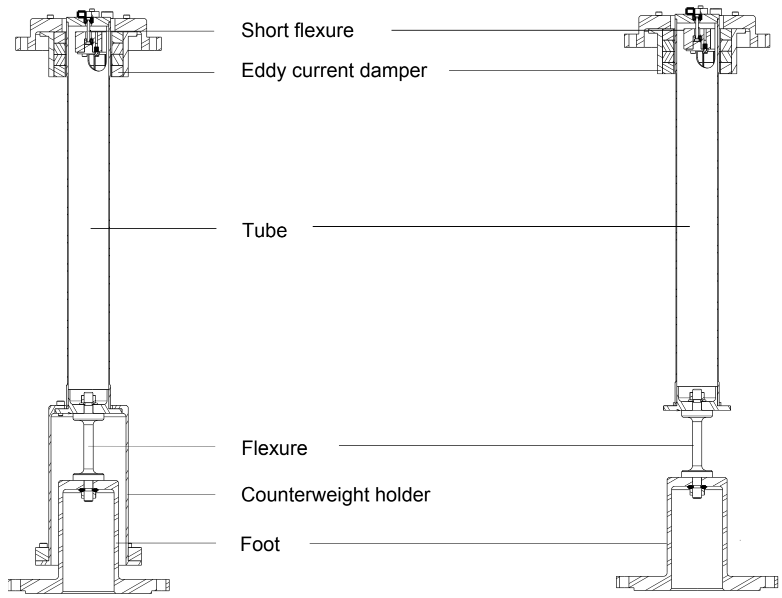

(a) *Type-IP1* **(b)** *Type-IP2*

Figure 3.3: *Two versions of the EIB-SAS inverted pendulums. (a) Type-IP1 was the first version of the inverted pendulum, which featured the Type-F1 bottom joint with a diameter of 10.6 mm and a tube of 1 mm thick aluminum. The second version of the inverted pendulum, Type-IP2, contained the Type-F2 bottom flexible joint, which has an increased diameter of 11.2 mm, and its tube is made of 2 mm thick stainless steel. Note also that the counterweightholder has been removed.*

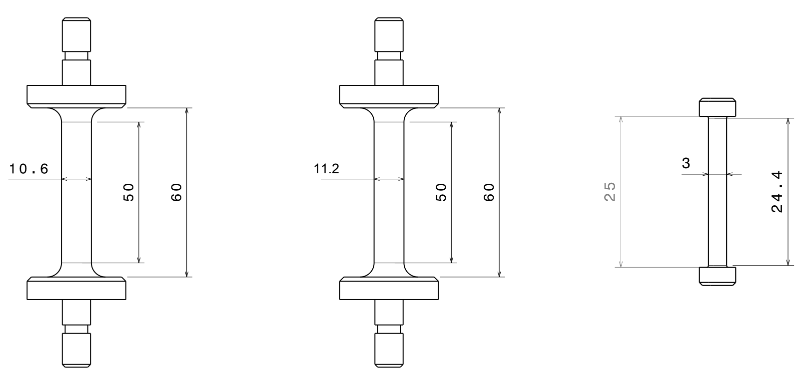

(a) *Type-F1* **(b)** *Type-F2* **(c)** *Type-F3*

Figure 3.4: *Different types of flexible joints of the inverted pendulums. The Type-F1 flexible joint (a) was used in the Type-IP1 inverted pendulum. In the final design, this inverted pendulum was replaced by the stiffer Type-IP2 inverted pendulum that incorporates the Type-F2 flexible joint (b). For both types of IP, the flexible joint of Type-F3 (c) connects the inverted pendulum and the springbox.*

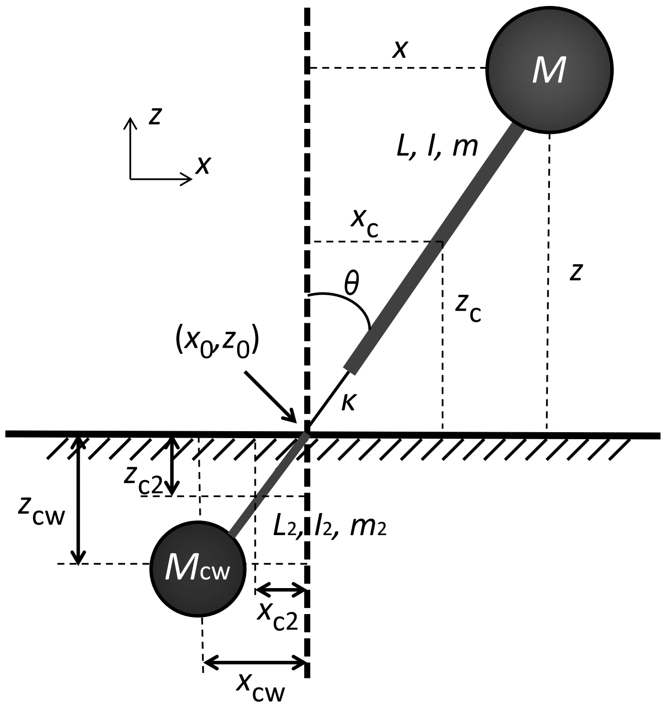

Figure 3.5:
One-dimensional model of an inverted pendulum [95].

For small angles θ, the Lagrangian of the system is given by the difference in kinetic energy T and the potential energy P and can be written as

$$\mathcal{L} = T_{\text{load}} + T_{\text{leg}} + T_{\text{cw}} + T_{\text{cw leg}} - U_{\text{load}} - U_{\text{leg}} - U_{\text{cw}} - U_{\text{cw leg}} - U_{\text{flexible joint}}, \tag{3.1}$$

with

$$\begin{aligned}
T_{\text{load}} &= \frac{1}{2}M\dot{x}^2, & U_{\text{load}} &= Mgz,\\
T_{\text{leg}} &= \frac{1}{2}m\dot{x}_{\text{c}}^2 + \frac{1}{2}I\dot{\theta}^2, & U_{\text{leg}} &= mgz_{\text{c}},\\
T_{\text{cw}} &= \frac{1}{2}M_{\text{cw}}\dot{x}_{\text{cw}}^2, & U_{\text{cw}} &= M_{\text{cw}}gz_{\text{cw}},\\
& & U_{\text{cw leg}} &= m_2gz_{\text{c2}},\\
T_{\text{cw leg}} &= \frac{1}{2}m_2\dot{x}_{\text{c2}}^2 + \frac{1}{2}I_{\text{cw}}\dot{\theta}^2, & U_{\text{flexible joint}} &= \frac{1}{2}\kappa\theta^2.
\end{aligned} \tag{3.2}$$

As can be seen in Fig. 3.5, $x_{\text{c}} = \frac{1}{2}x$, $z_{\text{c}} = \frac{1}{2}z$, $x_{\text{c2}} = \frac{1}{2}x_{\text{cw}}$, $z_{\text{c2}} = \frac{1}{2}z_{\text{cw}}$ and for small angles $x - x_0 = \theta L \rightarrow \theta = (x - x_0)/L$. Denoting the mass of the bell holding the counterweight with m_2, the Lagrangian is given by

$$\begin{aligned}\mathcal{L} = &\frac{1}{2}m_2\left(\dot{x}_0 - \frac{L_2\left(\dot{x}_0 - \dot{x}\right)}{2L}\right)^2 + \frac{1}{2}m\left(\frac{\dot{x}_0}{2} + \frac{\dot{x}}{2}\right)^2 + \frac{1}{2}M\dot{x}^2 + \frac{1}{2}M_2\left(\dot{x}_0 - \frac{L_2\left(\dot{x}_0 - \dot{x}\right)}{L}\right)^2 \\ &+ \frac{1}{2}\frac{I}{L^2}\left(\dot{x}_0 - \dot{x}\right)^2 + \frac{1}{2}\frac{I_2}{L^2}\left(\dot{x}_0 - \dot{x}\right)^2 - \frac{1}{2}\frac{\kappa}{L^2}\left(x - x_0\right)^2 + LMg\left(\frac{\left(x - x_0\right)^2}{2L^2} - 1\right) \\ &+ L_2M_2g\left(\frac{\left(x - x_0\right)^2}{2L^2} - 1\right) + \frac{1}{2}Lgm\left(\frac{\left(x - x_0\right)^2}{2L^2} - 1\right) + \frac{1}{2}L_2gm_2\left(\frac{\left(x - x_0\right)^2}{2L^2} - 1\right). \end{aligned} \tag{3.3}$$

Note that x_0 represents the ground motion which causes the displacement noise. The Euler-Lagrange equation $\partial L/\partial x = \partial/\partial t \times \partial L/\partial \dot{x}$ then gives

$$\begin{aligned}&\ddot{x}\left(M + \frac{m}{4} + \frac{I}{L^2} + \frac{I_2}{L^2} + \frac{{L_2}^2M_2}{L^2} + \frac{{L_2}^2m_2}{4L^2}\right) - \frac{L_2gm_2\left(x - x_0\right)}{2L^2} \\ &\quad - \ddot{x}_0\left(\frac{I}{L^2} - \frac{m}{4} + \frac{I_2}{L^2} + \frac{L_2M_{\text{cw}}\left(\frac{L_2}{L} - 1\right)}{L} + \frac{L_2m_2\left(\frac{L_2}{2L} - 1\right)}{2L}\right) \\ &\quad + \frac{\kappa\left(x - x_0\right)}{L^2} - \frac{Mg\left(x - x_0\right)}{L} - \frac{gm\left(x - x_0\right)}{2L} - \frac{L_2M_{\text{cw}}g\left(x - x_0\right)}{L^2} = 0. \end{aligned} \tag{3.4}$$

Solving it we obtain the equation of motion of the system,

$$\begin{aligned}\ddot{x} = &\left[\left(4\left(I + I_2\right) + L_2^2\left(4M_{\text{cw}} + m_2\right) - L^2m + 2LL_2\left(2M_{\text{cw}} - m_2\right)\right)\ddot{x}_0 - 4\kappa\left(x - x_0\right)\right. \\ &\left. + g\left(2L^2\left(2M + m\right) - 2LL_2\left(2M_{\text{cw}} + m_2\right)\right)\sin\left(\frac{x - x_0}{L}\right)\right] \Big/ \\ &\left[4\left(I + I_2\right) + L^2\left(4M + m\right) + L_2^2\left(4M_{\text{cw}} + m_2\right)\right]. \end{aligned} \tag{3.5}$$

Taking the Fourier transform of Eq. (3.5) and reordering terms we get the *transfer function* of an inverted pendulum,

$$\frac{X(\omega)}{X_0(\omega)} = \frac{\omega_0^2 + \beta\omega^2}{\omega_0^2 - \omega^2}, \tag{3.6}$$

where ω_0 is the resonance frequency of the inverted pendulum and is given by

$$\omega_0^2 = \frac{4\kappa - 2gL\left(2M + m\right) + 2gL_2\left(2M_{\text{cw}} + m_2\right)}{4\left(I + I_2\right) + L^2\left(4M + m\right) + L_2^2\left(4M_{\text{cw}} + m_2\right)}, \tag{3.7}$$

and β is the high-frequency asymptotic value of the transfer function, which is given by

$$\beta = \frac{mL^2 - 4\left(I + I_2\right) - L_2^2\left(4M_{\text{cw}} + m_2\right) + 2LL_2\left(2M_{\text{cw}} + m_2\right)}{4\left(I + I_2\right) + L^2\left(4M + m\right) + L_2^2\left(4M_{\text{cw}} + m_2\right)}. \tag{3.8}$$

In the case that $M \gg m$ and $M_{\text{cw}} = m_2 = 0$, as is the case for the final design of EIB-SAS, Eq. (3.7) becomes

$$\omega_0^2 = \frac{\kappa}{L^2M} - \frac{g}{L}. \tag{3.9}$$

The linear stiffness k, is given by $k = \kappa/L^2$. The resonance frequency of the system then becomes

$$\omega_0 = \sqrt{\frac{k}{M} - \frac{g}{L}}, \tag{3.10}$$

which shows how an inverted pendulum can remain compact, support a heavy load and be tuned to low frequencies all at once: gravity acts as an anti-spring. By carefully balancing the load of the IP and the stiffness of the flexible joint, the eigenfrequency of the IP can be tuned to frequencies as low as 100 mHz.

Center of percussion effect

The finite inertia of the leg limits the achievable vibration isolation at high frequencies. Taking the limit $\omega \to \infty$ in Eq. (3.6), we obtain $X(\infty)/X(0) = \beta$, with β the asymptotic transfer function value at high frequency given by Eq. (3.8). Fig. 3.6 shows the IP transfer function for several values of β, which depend on the weight distribution of the leg.

In the case of a simple beam without counterweight the moment of inertia $I = mL^2/12$ and β is simply $m/6M$. This leveling off of the transfer function at high frequencies is due to a residual momentum transfer from the leg to the load caused by the so-called *center of percussion effect*.

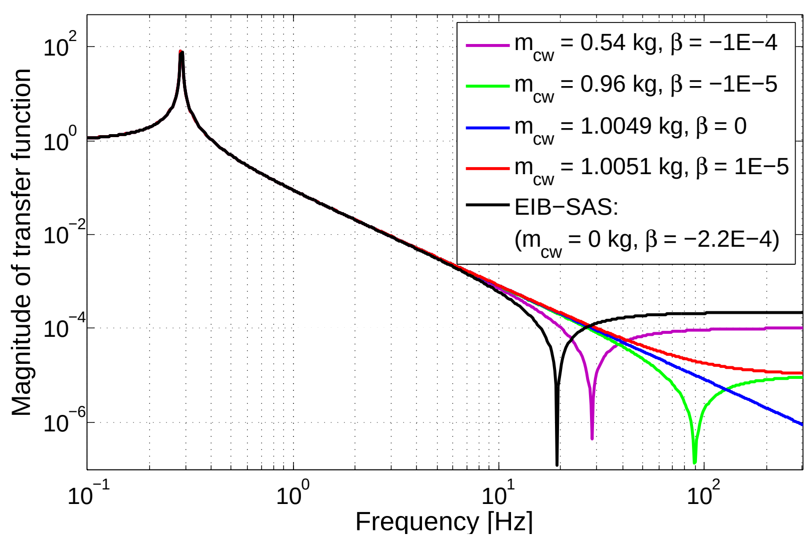

Figure 3.6: *Theoretical transfer function of EIB-SAS IP for several values of β. The limit of the transfer function at high frequency β, depends on the mass ratio of the leg and the payload. The parameters of the IP used in this plot are the same as those listed in Table 3.1. Additionally, the mass of the aluminum bell holding the counterweights is 0.15 kg, its length 133 mm and the mass of the counterweight has been varied between 0 and 1 kg. EIB-SAS is operated without counterweight (and counterweight holder). In this configuration the transfer function is given by the black solid curve and $\beta = -2.2{\times}10^{-4}$.*

When a perpendicular force $\vec{F}$ is applied to a free body* of mass m at its center of mass (COM), as in the left panel of Fig. 3.7, it will accelerate with a value $\vec{a}$ given by Newton's second law $\vec{a} = \vec{F}/m$. When $\vec{F}$ is not applied to the COM but some distance r_F above it, as shown in the right panel of Fig. 3.7, the body will not only accelerate, but also rotate around its COM with an angular acceleration $\vec{\alpha}$, given by Newton's second law for rotational motion $\vec{\alpha} = \vec{M}/I$, where $\vec{M}$ is the moment of $\vec{F}$ and I is the moment of inertia of the body.

At some distance d below the COM, there is a so-called pivot point PP whose translational motion is canceled by the rotational motion. One has

$$\vec{a} = \vec{\alpha} d \rightarrow \frac{\vec{F}}{m} = \frac{\vec{M} d}{I} \rightarrow \frac{\vec{F}}{m} = \frac{\vec{F} r_\mathsf{F} d}{I} \rightarrow \frac{I}{m} = r_\mathsf{F} d. \tag{3.11}$$

Substituting the moment of inertia of a point mass $I = mR_\mathrm{g}^2$ in Eq. (3.11) the expression reduces to

$$r_\mathsf{F} d = R_\mathrm{g}^2, \tag{3.12}$$

where R_g is the so-called radius of gyration of the body. The pivot point PP is the instantaneous center of rotation.

The motion of the body can be considered a pure rotation around the PP and R_g can be thought of as the radial distance from the PP at which the mass of a body could be concentrated without altering the rotational inertia of the body about that axis. The location of the PP depends of the mass distribution of the body and is not necessarily located within its boundaries. Should a hinge be attached to the PP, the body would rotate around the hinge without any reaction force from it. Fixing the hinge to a point other than the PP, the body would rotate around the hinge, but in this case a reaction force would be present.

The PP has a complementary point (see Fig. 3.7) on the other side of the center of mass: its *center of percussion* COP. Applying the force in the same direction to the PP†, the body would rotate around this COP.

The same holds for the inverted pendulum, where the hinge is the top flexure and the point where the external force (ground motion) acts, is the bottom flexure. In order to prevent any momentum transfer from the leg to the isolated mass above the natural frequency, the COP of the leg corresponding to the top flexure should coincide with the position of the bottom one. In general, this is not the case; which means that part of the force exerted by the ground is transmitted to the load of the IP, and in that case this load is not isolated completely.

The COP can be placed at the bottom flexure by adding a counterweight to the bottom of the leg (see Fig. 3.8). Alternatively, the counterweight could be added to the top of the IP, as the PP and COP are complementary.

*We consider the simple case of planar motion in which all parts of the body move along paths equidistant to a fixed plane.

†This is, of course, only possible if the PP lies inside the body.

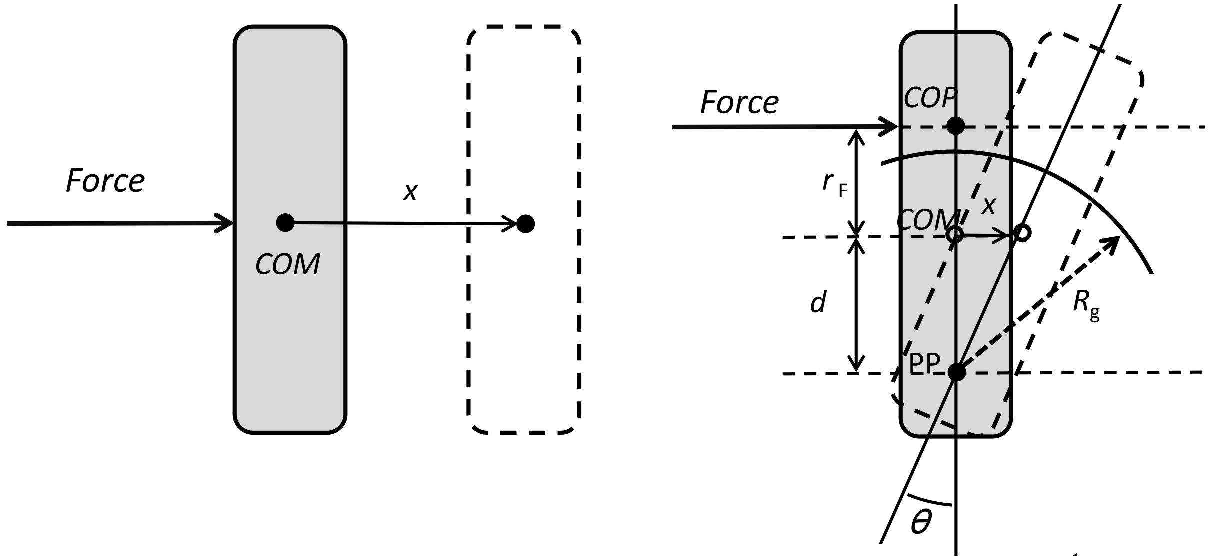

Figure 3.7: *Illustration of the center of percussion. When a solid body is subjected to a perpendicular force applied at a point that is not in line with the center of mass, the body will perform a translational motion of its center of mass and a rotation around its center of mass. At some point, which may lie outside the body, the translational and rotational motion will cancel and the motion of the body can be seen as a rotation around this point, which is called the pivot point. The pivot point has an associated center of percussion, which would be the center of rotation of the body, when the force would be applied in line with the pivot point.*

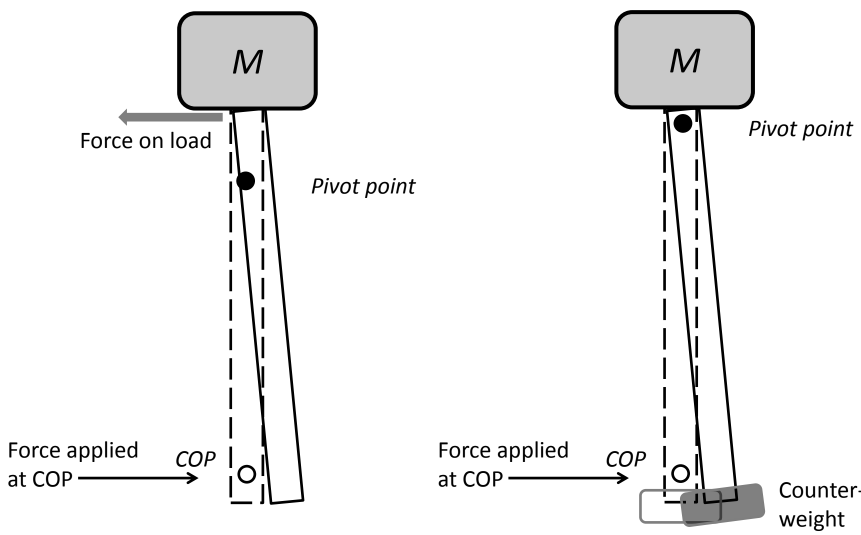

Figure 3.8: *Illustration of the effect of a counter mass on the pivot point. The location of the pivot point depends on the mass distribution of the leg. Adding the proper counterweight to the bottom of the leg, can place the pivot point at the top flexure, so that the leg can rotate around this point without exerting a force on the load, thereby isolating it perfectly from ground vibrations.*

This solution of adding a counterweight to tune the COP is common in the construction of swords. For centuries the weight of the pommel is chosen such that the COP of the sword coincides with the handle and PP with its striking zone. In this way, when dealing a blow, the sword does not rotate on impact, making the blow more efficient. This effect also applies to baseball bats, tennis rackets *etc.*, where the PP is known as *the sweet spot*.

We have designed and fabricated counterweights for EIB-SAS. However, the isolation performance of the IP was sufficient without counterweights (see Fig. 3.6). Therefore, the bells to hold the counterweights were removed to make the legs lighter and raise the frequency of their internal modes (see section 3.4.6).

3.4.2 Stiffness of the flexible joint

As described in section 3.4.1 the flexible joint is the part of the inverted pendulum that provides the restoring force for the load when it is taken out of equilibrium. This joint is operating in high-stress conditions which requires special materials and fabrication treatments (see section 3.5.6) to avoid creep and fractures. Here we describe the mechanics of the flexure.

Bending moment

To calculate the deformation of the flexible joint under the influence of bending moments, axial forces and shear forces we treat the joint as a rigid beam. Suppose it consists of fibers along its principle axis. Applying a bending moment to both ends of the beam, as shown in Fig. 3.9, will cause the beam to bend.

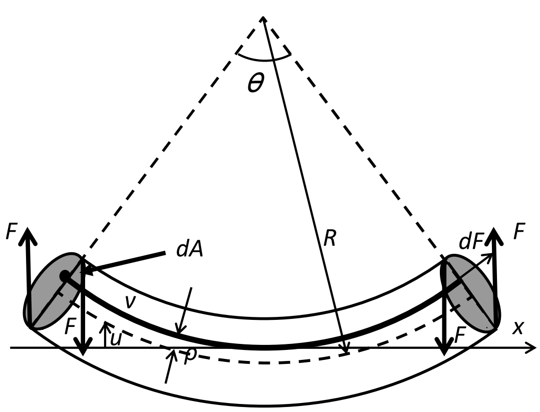

Figure 3.9: *Under the influence of pure bending moment S and for small deflection angles θ, the deflected flexure will have a uniform radius of curvature R.*

For small deflection angles θ, the beam will have a uniform radius of curvature R. The length of the fiber along the center of the beam will not change and is equal to $R\theta$. The bending profile of this neutral fiber is $u(x)$. The fibers at a distance ρ above the neutral fiber will be compressed by an amount $R\theta - (R + \rho)\theta = -\rho\theta$, and those below it will be stretched by the same amount. This causes a stress in the fibers of $E\rho/R$, where E is the Young's

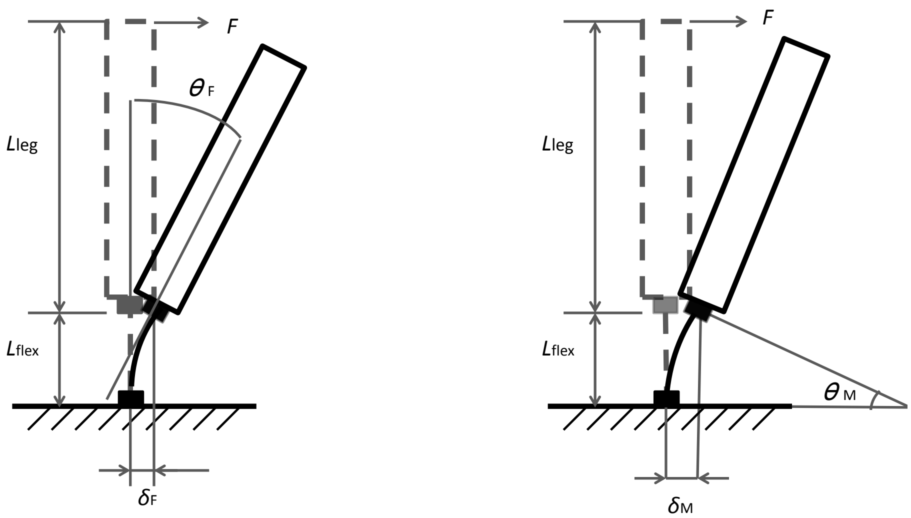

Figure 3.10: *Applying a force to the top of the IP will exert a force and a moment on the top of the flexible joint. The displacement of the top of the IP is the result of a displacement δ_F and deflection θ_F of the joint due to the force and a displacement δ_M and deflection θ_M due to the bending moment.*

modulus. The stress in the fiber results in a force $dF = (E\rho/R)\ dA$ at the end of this fiber, where dA is the cross sectional area of the fiber. The bending moment dM of this force is given by $dM = \rho dF = (E\rho^2/R)\ dA$. Integrating over the entire cross sectional area of the beam, we obtain the total bending moment

$$M = \frac{E}{R}\int \rho^2 dA = \frac{EJ}{R}, \tag{3.13}$$

where J is called the second moment of area, or the moment of inertia of the cross section.

The angular stiffness κ of a flexible joint is defined as the ratio between a pure bending moment applied to the top of the flexible joint and the bending angle θ_M (see right panel of Fig. 3.10) due to this bending moment and is given by

$$\kappa \equiv \frac{M}{\theta_\text{M}} = \frac{EJ}{L_\text{flex}} = \frac{\pi E r_\text{flex}^4}{4L_\text{flex}}. \tag{3.14}$$

Shear force

The stiffness k of a flexible joint is given by the ratio of the force F applied to the top of the flexible joint and the displacement δ_F (see Fig. 3.11) of the top due to this force.
Eq. (3.13) can be used to calculate the bending profile of the flexible joint when a force is applied to it and gives

$$k \equiv \frac{F}{\delta_\text{F}} = \frac{3EJ}{L_\text{flex}^3}, \tag{3.15}$$

where L_{flex} is the length of the flexible joint and $J = \pi r_{\text{flex}}^4/4$, where r_{flex} is the radius of the joint. The stiffness* of the joint can be written as

$$k = \frac{3\pi E r_{\text{flex}}^4}{4L_{\text{flex}}^3}. \tag{3.16}$$

3.4.3 Elastic stiffness of the inverted pendulum

The flexible joint provides the restoring force of the IP. The linear stiffness of the IP will be the reciprocal of its displacement due to a nominal force applied to the top of the leg (Eq. (3.15)). The displacement of the top of the IP δ_{IP} is due to a displacement of the top of the flexible joint δ_{flex} and the bending of the flexible joint θ_{flex} [96]

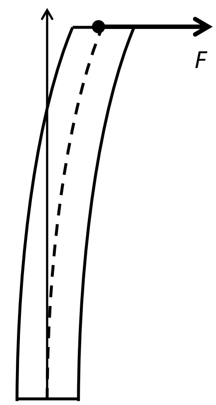

Figure 3.11: *Under the influence of a shear force the deflected beam will* not *have a uniform radius of curvature.*

$$\delta_{\text{IP}} = \delta_{\text{flex}} + \theta_{\text{flex}} L_{\text{leg}}, \tag{3.17}$$

where L_{leg} the length of the leg .

Assuming the leg is infinitely stiff, applying a force to the top of the IP applies a force and a moment to the top of the flexible joint. This force will induce a displacement δ_{F} and a deflection θ_{F}; the moment will induce a displacement δ_{M} and a deflection θ_{M} (see Fig. 3.10). So, δ_{flex} and θ_{flex} are given by

$$\delta_{\text{flex}} = \delta_{\text{F}} + \delta_{\text{M}} = \frac{L_{\text{flex}}^2 L_{\text{leg}}}{2EJ} + \frac{L_{\text{flex}}^3}{3EJ} \quad \text{and} \tag{3.18}$$

$$\theta_{\text{flex}} = \theta_{\text{F}} + \theta_{\text{M}} = \frac{L_{\text{flex}}^2}{2EJ} + \frac{L_{\text{flex}} L_{\text{leg}}}{EJ}, \tag{3.19}$$

and Eq. (3.17) becomes

$$\delta_{\text{tot}} = \frac{L_{\text{flex}} \left(L_{\text{flex}}^2 + 3L_{\text{flex}} L_{\text{leg}} + 3L_{\text{leg}}^2 \right)}{3EJ}, \tag{3.20}$$

and the stiffness of the IP becomes

$$k_{\text{IP}} = \frac{F}{\delta_{\text{tot}}} = \frac{\pi E r_{\text{flex}}^4}{4L_{\text{flex}}^3} \frac{1}{\left(L_{\text{leg}}/L_{\text{flex}}\right)^2 + L_{\text{leg}}/L_{\text{flex}} + 1/3} \quad [\text{N/m}]. \tag{3.21}$$

*The compliance C of a body is a measure of its deformation due to an applied force and hence, is the inverse of its stiffness $C = k^{-1}$

3.4.4 Stress in the flexible joint

We have calculated the stress in the flexible joint of the Type-IP2 inverted pendulum in order to check that it does not exceed the ultimate tensile stress of maraging steel. The flexible joint is under stress in three ways.

First, even when the IP is in its equilibrium position, the three flexible joints experience a compression stress S_c due to the weight of the springbox and bench. Second, applying a force F to the top of the IP, a force F and a moment M_M are applied to the flexible joint. Third, as the top of the IP is brought out of equilibrium the weight of the load of the IP induces a second moment M_L. Due to the compliance of the joint, it bends and is stressed.

The compression stress S_c due to the weight of the bench is given by $S_\mathsf{c} = F_\mathsf{g}/A_\mathsf{flex} = gM/\pi r_\mathsf{flex}^2$, where F_g is the gravitational force on the load of the IP, A_flex the cross sectional area of the flexible joint, g the gravitational constant, $M = 429$ kg is the load o the IP and r_flex the radius of the flexible joint. Inserting the values given in Table. 3.1 we find that $S_\mathsf{g} = 31$ MPa, which is two orders of magnitude below the ultimate tensile strength.

The bending moment M_F due to the force exerted on the flex is greatest at the top of the flex where is is equal to $M_\mathsf{F} = FL_\mathsf{flex}$. The bending moment due to the force exerted on top of the IP is equal to $M_\mathsf{M} = FL_\mathsf{IP}$. Clearly, $M_\mathsf{F} \ll M_\mathsf{M}$ and the bending induced by the force is negligible compared to that of the bending moment and can be ignored in the stress calculation.

The maximum bending moment due to the displacement of the load $M_\mathsf{L} = Mga_\mathsf{max}$, where M is the load of the IP and $a_\mathsf{max} = 10$ mm its maximum excursion out of equilibrium. The total bending moment M_b exerted on the flexible joint is then $M_\mathsf{b} = M_\mathsf{M} + M_\mathsf{L}$. Due to this bending moment a stress $S = Er_\mathsf{flex}/R = Er_\mathsf{flex}a_\mathsf{max}/L_\mathsf{flex}L_\mathsf{IP}$ will be induced in the flexible joint. Inserting the values given in Table. 3.1 we find that $S_\mathsf{g} = 3.6 \times 10^2$ MPa.

The total stress induced in the flexible joint is 31 MPa $+ 3.6 \times 10^2$ MPa $= 4.0 \times 10^2$ MPa. This is much smaller than 1.97 GPa, the ultimate tensile strength of maraging steel.

3.4.5 Modeling the stiffness of the IP

Finite element model of the flexible joint

Initially, the Type-IP1 inverted pendulum (see Fig. 3.3a) was used in EIB-SAS, which contained the Type-F1 flexible joint which has a diameter of 10.6 mm. To determine the stiffness of the joint a finite element model was created [97] in which the joint was modeled by 3D brick elements (see Fig. 3.12). According to this model the joint's stiffness κ is 1970 Nm/rad. The stiffness of the joint is given by Eq. (3.14). Combining this formula with the stiffness obtained from the FEM model gives an effective length of the flexible joint of 58.5 mm.

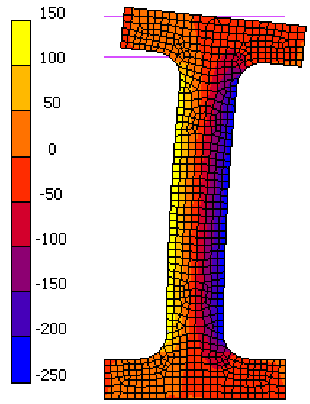

Figure 3.12: *Vertical component of the stress in the Type-F2 flexible joint predicted by the finite element model. The scale is in MPa. The displacement of the top of the IP is 6 mm. The resulting bending of the joint has been magnified by a factor 10 for this plot.*

In Fig. 3.13 the load curve of the IP as predicted by the model is compared to the results from a direct measurement. The model prediction is indicated by the dashed curve, the experimental values by the solid squares. A fit of the data with Eq. (3.10) is indicated by the solid curve. The fit gives a value for the joint's stiffness of 1870 Nm/rad, which is significantly lower than the value provided by our model *i.e.* 1970 Nm/rad. Clearly, the stiffness of the IP was overestimated. Furthermore, the data reveal a maximum load of 400 kg per leg, while 429 kg per leg is needed to support the optical bench and springbox. A detailed analysis showed that the stiffness of the IP is not solely caused by the stiffness of the joint; it is lowered due to compliance of other parts of the leg.

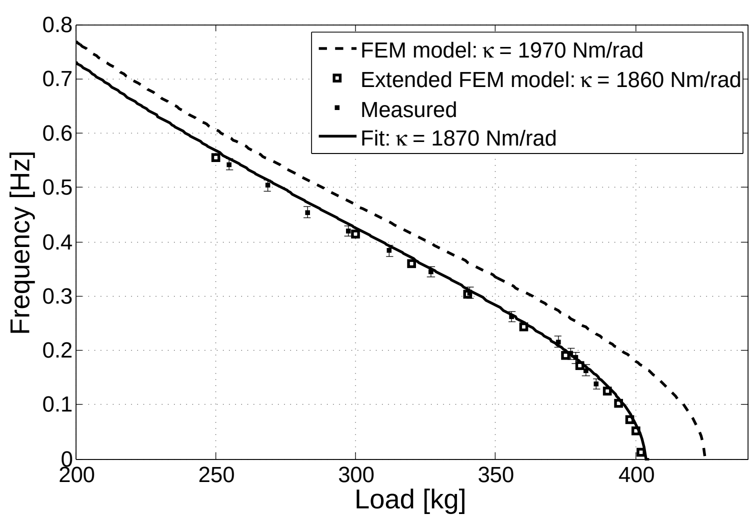

Figure 3.13: *Eigenfrequency of Type-IP1 inverted pendulum as a function of its load. The dashed curve represents the prediction of our initial FEM model, the open black squares that of our extended FEM model, the solid squares correspond to the measured values and the solid curve represents the fit with Eq. (3.10). The fit gives a value for the stiffness of the flexible joint of 1870 Nm/rad.*

Finite element model of the inverted pendulum

To further our understanding of the IP, we extended our FEM model. Apart from the flexible joint the following effects are taken into account:

- Compliance of the leg's tube, which lowers the stiffness of the IP by 2% (see Fig. 3.14a).
- Compliance of the foot on which the IP is mounted, which lowers the stiffness of the IP by 2% (see Fig. 3.14b).
- Compliance of the foot at the foot-flexible joint interface, which lowers the stiffness of the IP by 2%.
- Stiffness of the upper flexible joint, which does not affect the stiffness of the IP significantly (see Fig. 3.14c).

The prediction of our extended FEM model is indicated by the blue curve in Fig. 3.13. The model gives a good description of the EIB-SAS IP and we argue that the stiffness of the IP is well understood.

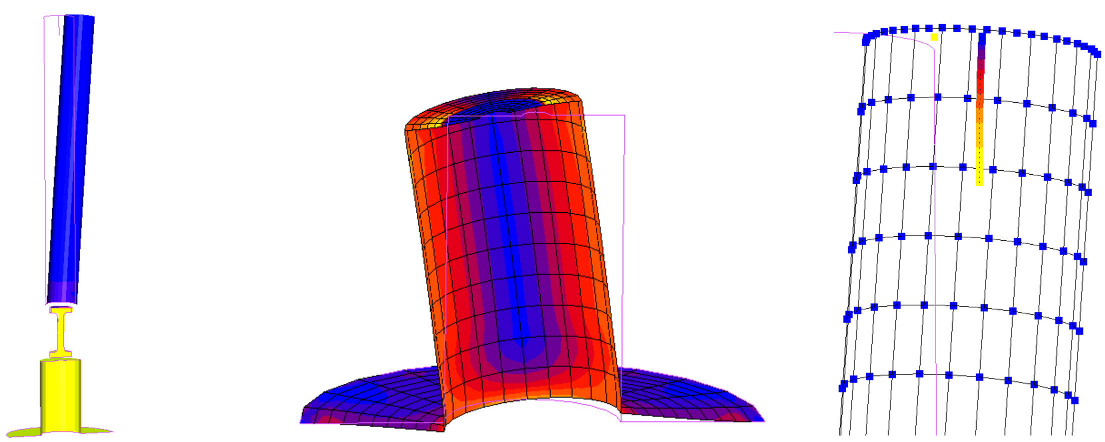

(a) **(b)** **(c)**

Figure 3.14: *(a) The FEM model includes the compliance of the tube of the IP, which is presented in blue. It is modeled by 3D shell elements. The limited stiffness of the tube lowers the total stiffness of the IP by 2%. (b) The bottom flexible joint of the IP is not attached to ground, but to an aluminum foot, which is bolted to a thick aluminum plate, which in turn is glued to the floor. The limited stiffness of the foot and the fact that it is bolted to the floor at a few discrete points is incorporated in the FEM model and lowers the total stiffness of the IP by 2%. The color indicates the stress level in the foot. (c) The springbox is not attached rigidly to the leg, but is hanging from small flexible joints, which act as a universal hinge. This is incorporated in the FEM model. The color indicates the tension in this joint when the IP is out of equilibrium.*

Based on the data for Type-IP1 inverted pendulum and the predictions of the model, the flexible joints were replaced by stiffer ones (diameter of 11.2 mm), which allowed the necessary load of 429 kg per IP. Additionally, the 1 mm thick aluminum tubes were replaced by 2 mm thick stainless steel ones to increase the lowest eigenfrequency of the system from 122 to 220 mHz. At this frequency the IP still provides the desired level of isolation above 10 Hz and the system is more robust *e.g.* it is easier to recover the working position after adjusting the optical layout on the bench. Fig. 3.15 shows the load curve of the final EIB-SAS IPs. A fit of the data points with Eq. (3.10) now gives a stiffness $\kappa = 2350$ Nm/rad, while the FEM model predicts 2370 Nm/rad.

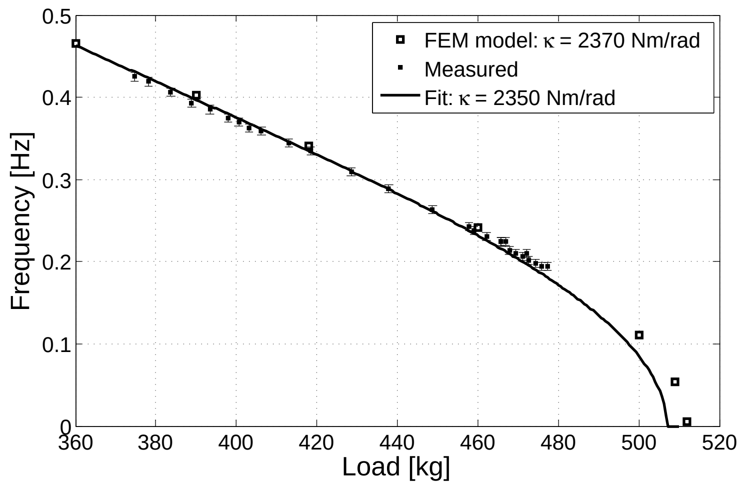

Figure 3.15: *Eigenfrequency of the Type-IP2 inverted pendulum as a function of its load. The black squares represent the measured values, the open black squares represent the prediction of our extended FEM model and the solid curve represents the fit result obtained with Eq. (3.10). The fit gives a value for the angular stiffness of the final IP (Type-IP2) of 2350 Nm/rad. The FEM model predicts 2370 Nm/rad.*

3.4.6 Modal analysis of the IP

As mentioned in section 2.14, a modal decomposition of EIB-SAS needs to be carried out. The frequencies of the IP modes have been measured with a tapping test: a small magnet is attached to the leg, the leg is excited by gently hitting it with a small hammer and its motion is measured with a pick-up coil. An example of a typical motion spectrum measured in the tapping test is shown in Fig. 3.16.

To help identify and understand the internal modes, a FEM model of the IP was constructed [97]. The flexible joint is modeled by 3D brick elements, the leg, the counterweight holder and the foot of the IP have been modeled by 3D shell elements. In this way the flexibility of the tube is taken into account. The parameters of the IP are those listed in Table 3.1.

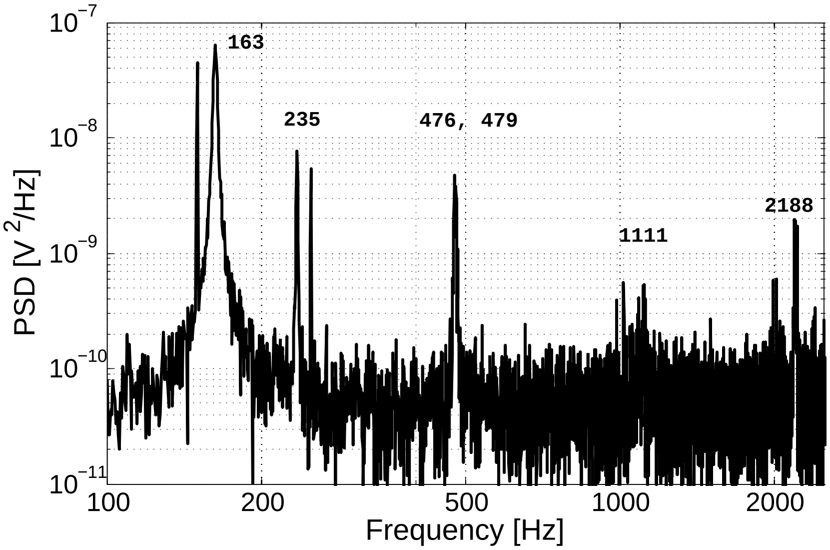

Figure 3.16: *Motion spectrum of an IP leg represented as power spectral density measured in a tapping test. A small magnet is attached to the IP leg, the leg is excited by gently hitting it with a small hammer and a current is induced in a small coil. Each of the peaks is due to a mode of the IP. The frequencies of the modes are denoted in the spectrum. The Q-factor of the mode follows from the frequency and width of the peak in this spectrum. The line at 150 Hz does not belong to modes of the IP, but is due to noise from the AC power supply.*

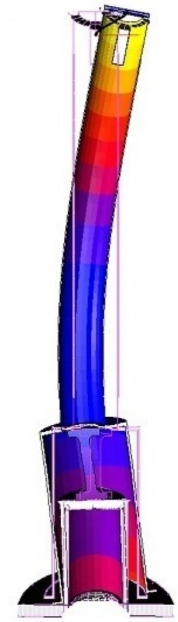

Figure 3.17: *FEM model of the Type-IP1 inverted pendulum contructed to determine the frequencies of its internal modes. A similar model has been created for the Type-IP2 inverted pendulum.*

The frequencies of the modes of Type-IP1 inverted pendulum predicted by the FEM model and the frequencies as measured in the tapping test are listed in Table 3.2. Fig. 3.17 shows the two leg modes and the so-called banana mode that the FEM model predicts.

The IPs have a number of internal modes, similar to the one depicted in Fig. 3.17, that involve a bending of the leg's tube and flexible joint, accompanied by an oscillation of the counterweight holder. In addition they have a torsion mode in this mode the IP rotates around its principle axis, winding up the flexible joint.

The lowest frequency mode of Type-IP1 inverted pendulum predicted by the FEM model is the torsion mode at 195 Hz. This mode was not measured in the tapping test. The first order leg modes (one for each horizontal direction) are predicted to have a frequency of 242 Hz and were measured at 235 Hz. In this mode the leg and counterweight holder are swinging while the flexible joint is rotating. The second order leg modes were predicted at 317 Hz and were measured at 335 Hz. In this mode the top and bottom of the leg oscillate in-phase. The third order leg modes were predicted at 423 Hz and were measured at 425 Hz.

Mode	Frequency predicted by the FEM model (Hz)	Frequency at which mode was measured (Hz)
Torsion	195	-
1^{st} leg mode	242	235
2^{nd} leg mode	317	335
3^{rd} leg mode	423	425

Table 3.2: *Frequencies of the modes of Type-IP1 inverted pendulum predicted by the FEM model and measured in the tapping test.*

3.4.7 Raising the frequency of the modes

It is preferable to have the modes of the IP at higher frequencies. At high frequencies the ground motion falls off with $1/f^2$ and the leg modes will be harder to excite, reducing the chance they will introduce noise when *e.g.* weather conditions are bad. This can be done by making the legs stiffer and/or lighter. This is the reason the Type-IP1 inverted pendulum was replaced for those of Type-IP2 (see section 3.4).

Table 3.3 shows the frequencies of the modes predicted by the FEM model of the Type-IP1 inverted pendulum and the Type-IP2 inverted pendulum with and without counterweight holder. The frequencies of the torsion and first order leg modes are lower for the Type-IP2 than for the Type-IP1. The second and third order leg modes have a higher frequency for Type-IP2 than for Type-IP1. The Type-IP2 inverted pendulum is thicker and made of stainless steel which has a higher Young's modulus. This makes it stiffer, but also heavier. For the two lowest frequency modes of the Type-IP2 inverted pendulum, the tube can be taken as rigid and the stiffness of the modes is provided by the flexible joints and the increase in inertia dominates the increase in stiffness of the leg. For example, for the third order leg mode the mass-stiffness ratio of the tube determines the frequency of the mode. Therefore the frequency of this mode is higher for Type-IP2 than for Type-IP1.

The frequencies of the modes predicted by the FEM model of the Type-IP2 inverted pendulum change when the bell to hold the counterweights is removed. The lowest order leg mode has a similar frequency in both cases, but removing the bell significantly increases the frequencies of the torsion mode, second and third order leg modes.

Removing the counterweight holder has only a small effect on the inertia of the first order leg mode mode, because the counterweight holder is situated around the bending point of the mode (the bottom flexible joint). For the second order leg mode, the mode fundamentally changes; when the bell is present it is mostly the bell that moves and not the leg. Removing the bell decreases the moment of inertia for the torsion and third order leg mode, thus increasing their frequency. To reduce the weight of the IPs and to increase the frequency of the modes, the counterweight holders were removed.

The frequencies of the modes predicted by the FEM model of the Type-IP2 inverted pendulum and those measured in the tapping tests are summarized in Table 3.4. In addition to these modes a high frequency mode was measured at 2188 Hz. The FEM model predicts several modes above 2 kHz. A second order banana mode in which the IP is shaped as the letter S and a mode in which the tube squeezes in one direction and expands in the orthogonal direction. It is uncertain which of these modes was measured at 2188 Hz.

Mode	Frequency predicted by FEM model		
	IP1 (Hz)	IP2 with counter-weight holder (Hz)	IP2 without counter-weight holder (Hz)
1st leg mode	242	180	182
Torsion	195	166	243
2nd leg mode	317	323	473
3rd leg mode	423	528	1080

Table 3.3: *Frequencies predicted by the FEM model of the modes of the Type-IP1 inverted pendulum, Type-IP2 inverted pendulum with and without counterweight holder. The Young's modulus of aluminum is 69 GPa, that of stainless steel 130 GPa and that of maraging steel 186 GPa.*

Mode	Frequency predicted by the FEM model (Hz)	Frequency at which mode was measured (Hz)	Measured Q-factor*
1st leg mode	182	159, 163	400
Torsion	243	235	470
2nd leg mode	473	476, 479	180
3rd leg mode	1080	1111	-
High-frequency mode	$>$ 2 kHz	2188	-

Table 3.4: *Frequencies of the modes of the stainless steel legs without bell to hold the counterweight, predicted by the FEM model and measured with a tapping test. The power spectral density result obtained in this test is shown in Fig. 3.16.*

*The Q-factors of the modes have been lowered by installing an eddy current damper in the top of the IPs. The Q-factors of the damped modes can be found in the next section.

3.4.8 Reducing the Q-factor of the in-band IP modes

The Q-factors of the modes have been determined in tapping tests. If ω_m is the frequency of the mode and $\Delta\omega_\mathrm{m}$ its half-power bandwidth, then the Q-factor of the mode is given by

$$Q = \frac{\omega_\mathrm{m}}{\Delta\omega_\mathrm{m}}. \tag{3.22}$$

To reduce the Q-factors of the internal modes of the legs and to eliminate any possible beam jitter noise in the Advanced Virgo detection band introduced by them, eddy current dampers were installed at the top of the legs as shown in Fig. 3.18.

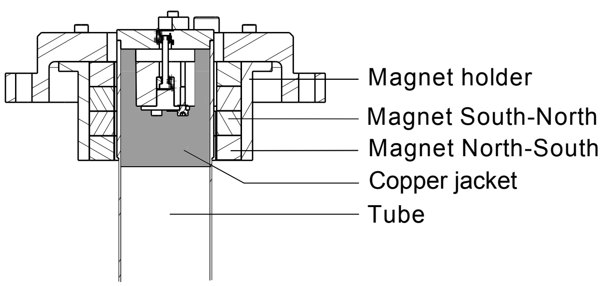

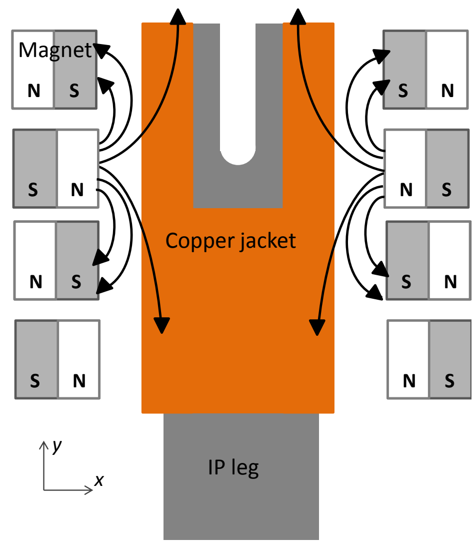

Figure 3.18: *Left panel: Schematic representation of the eddy current damper in the top of the IP. Two yokes are hanging from the springbox. They hold 38 magnets in a chessboard configuration. The magnets are pointing either towards or away from the IP to obtain a strong magnetic field gradient in the axial direction. Right panel: Schematic representation of the eddy current damper illustrating the magnet field configuration.*

Eddy current dampers

The top of the IP is surrounded by the two yokes shown in Fig. 3.19, which are fixed to the springbox. Together they hold 38 magnets (W-07-N magnets from Supermagnete of 7 mm cubed and magnetization of 860 - 955 kA/m). The magnets are ordered in a chessboard configuration and are either pointing at, or away from the leg's surface. This configuration provides a strong magnetic field along the surface of the IP in both vertical and axial direction, which will allow damping of translational movement in all three directions as well as rotational movement *and* ensures that there is no net dipole moment so that it will not interact with any stray magnetic fields.

Figure 3.19: *Photo of the eddy current dampers for the EIB-SAS IP legs. Two yokes hold 44 magnets of 7 mm cubed and ordered in a chessboard pattern. The top of the leg is surrounded by a 1.5 mm thick copper jacket.*

If the IP moves with a velocity $\vec{v}$, then the charge carriers in the top of the leg will feel a Lorentz force $\vec{F_\mathsf{L}} = q\left(\vec{v} \times \vec{B}\right)$, where q is their charge and $\vec{B}$ the magnetic field of the eddy current damper magnets. Due to this force the charge carriers will follow circular paths in the plane transverse to the magnetic field. These induced currents are known as eddy currents, because they flow in a circular fashion.

The current density $\vec{J}$ is proportional to the force per unit charge $\vec{J} = \sigma\vec{F_\mathsf{L}}$, where σ is the conductivity of the material. Therefore the current density induced by the movement of the IP is

$$\vec{J} = \sigma\left(\vec{v} \times \vec{B}\right). \tag{3.23}$$

If the IP moves in the positive *x*-direction (to the right in Fig. 3.18) and the magnetic field is directed along the surface, then according to Eq. (3.23), $\vec{J}$ is directed in the *z*-direction when the magnetic field is in the *y*-direction. The current $\vec{J}$ is directed in the *z*-direction when the magnetic field is directed in the *y*-direction. As the Lorentz force of the magnetic field on $\vec{J}$ is given by

$$\vec{F_\mathsf{M}} = \int_\mathsf{V}\left(\vec{J} \times \vec{B}\right) d\tau, \tag{3.24}$$

where we integrate over the volume of the conductor, $\vec{F_\mathsf{M}}$ always points in the negative *x*-direction, opposite to $\vec{v}$, damping the motion of the IP.

According to Eq. (3.23), the induced current density is linear with the conductivity of the medium. Because the steel of the leg is a poor conductor, 1.5 mm thick copper jackets have been glued to the top of the tube. The conductivity of copper is 5.96$\times 10^7$ S/m, which is a factor 42 larger than that of stainless steel (1.4 $\times$ 10^6 S/m), provides stronger damping.

Besides the damping force due to the magnetic field in the eddy current damper, the configuration of the magnets in the eddy current damper also provides a strong magnetic field gradient in the radial direction, which provides additional damping.

When the magnetic field is along the surface of the IP and the IP moves in the positive *x*-direction in Fig. 3.18, the change in flux due to the IP motion is equivalent to varying the *y* and *z* components of the magnetic field B_y and B_z. According to Faraday's law $\nabla \times \vec{E} = -\partial \vec{B}/\partial t$

$$\frac{\partial E_x}{\partial z} - \frac{\partial E_z}{\partial x} = \frac{\partial \vec{B}_y}{\partial t} = \frac{\partial \vec{B}_y}{\partial x}\frac{dx}{dt} = \frac{\partial \vec{B}_y}{\partial x} v_x \quad \text{and} \tag{3.25}$$

$$\frac{\partial E_y}{\partial x} - \frac{\partial E_x}{\partial y} = \frac{\partial \vec{B}_z}{\partial t} = \frac{\partial \vec{B}_z}{\partial x}\frac{dx}{dt} = \frac{\partial \vec{B}_z}{\partial x} v_x, \tag{3.26}$$

a changing magnetic field transverse to the IP's motion induces an electric field in these directions. This electric field exerts an electric force $\vec{F} = q\vec{E}$ on the charge carriers in the conductor and thus induces eddy currents in the plane transverse to the IPs motion, the *yz*-plane in this case. These eddy currents flow in the same direction as those induced by the magnetic field itself and therefore add to the damping force. They generate their own magnetic field which compensates the change in flux through the conductor.

Note that the eddy currents due the Lorentz force of the magnetic field are induced whether this field is uniform or not. The eddy currents due to the Lorentz force of the electric field is only present when there is a magnetic field gradient in the direction of the IP motion.

Due to the resistance of the copper, the energy associated with the eddy currents is dissipated into heat [98]. So, movement of the IP relative to the magnetic field induces eddy currents in the copper jackets, which remove energy from the system and lower the *Q*-factor of the modes.

The effects of the eddy current dampers on the *Q*-factors of the internal modes of the leg have been measured. The results are summarized in Table 3.5. The *Q*-factor of the first order leg mode is reduced from 400 to 25, that of the torsion mode from 470 to 40, and that of the second order leg mode from 180 to 95.

Mode	Frequency of mode (Hz)	*Q* of mode, damper disabled	*Q* of mode, damper enabled
1st leg mode	159, 162	400	25
Torsion mode	233	470	40
2nd leg mode	476, 479	180	95
1st high-frequency mode	1111	-	200
2nd high-frequency mode	2188	-	300

Table 3.5: *Frequencies and Q-factors of the internal modes of the IP with and without copper jackets for improved conductivity.*

3.5 Geometric anti-spring filters

EIB-SAS comprises three Geometric Anti-Spring (GAS) filters that provide seismic isolation for the vertical degrees of freedom: *y*, θ_x (pitch) and θ_z (roll). They are housed in the springbox (see Fig. 3.20), which is supported by the three inverted pendulums.

3.5.1 GAS filters: principle of operation

Fig 3.21 shows a schematic representation of the GAS filter. It consists of eight cantilever springs that are clamped to a base plate in a radial configuration. The blades are made of precipitation hardened maraging steel, which ensures an enormous tensile strength (up to 1.97 GPa) and high creep resistance. The tips of the blades point inwards and are clamped to a central keystone under a suitable angle. The blades are machined flat and bend when they are loaded. The position of the base plate clamps is adjusted to radially compress the blades. The radial forces of the blades cancel due to the symmetry of the filter. Their vertical force is counterbalanced by the weight of the optical bench resting on the keystone. When the keystone is displaced out of equilibrium, the radial force of the blades exerts a force away from equilibrium: the anti-spring effect. The stiffness of the system can be lowered by increasing the radial compression of the blades and thereby the anti-spring effect.

3.5.2 Isolation performance of a GAS filter

The equation of motion of a GAS filter is that of a harmonic oscillator

$$M\ddot{x} = -k(x - x_0). \tag{3.27}$$

Its transfer function is defined as the ratio of the Fourier transforms of the input and output; in this case the vertical motion of the base of the blades, *i.e.* the motion of the ground, and the motion of the keystone

$$H_Y = \frac{Y(\omega)}{Y_0(\omega)} = \frac{\omega_0^2}{\omega_0^2 - \omega^2}, \tag{3.28}$$

where $\omega_0 = \sqrt{k/M}$. For frequencies $\omega \gg \omega_0$, $H_Y \propto \omega_0^2/\omega^2$. Note that reducing the natural frequency ω_0 by a factor 2 increases its isolation capabilities by a factor 4.

If we now introduce damping and give the spring a finite mass [95], then the equation of motion becomes

$$M\ddot{x} = -k(1 + i\phi)(x - x_0) - m\ddot{x}_0 - \gamma\dot{x}, \tag{3.29}$$

where m represents the mass of the spring, γ the damping coefficient and ϕ denotes the so-called loss angle which takes into account the structural damping of the spring. In general the viscous damping is negligible compared to the structural damping in the filter blades, even in

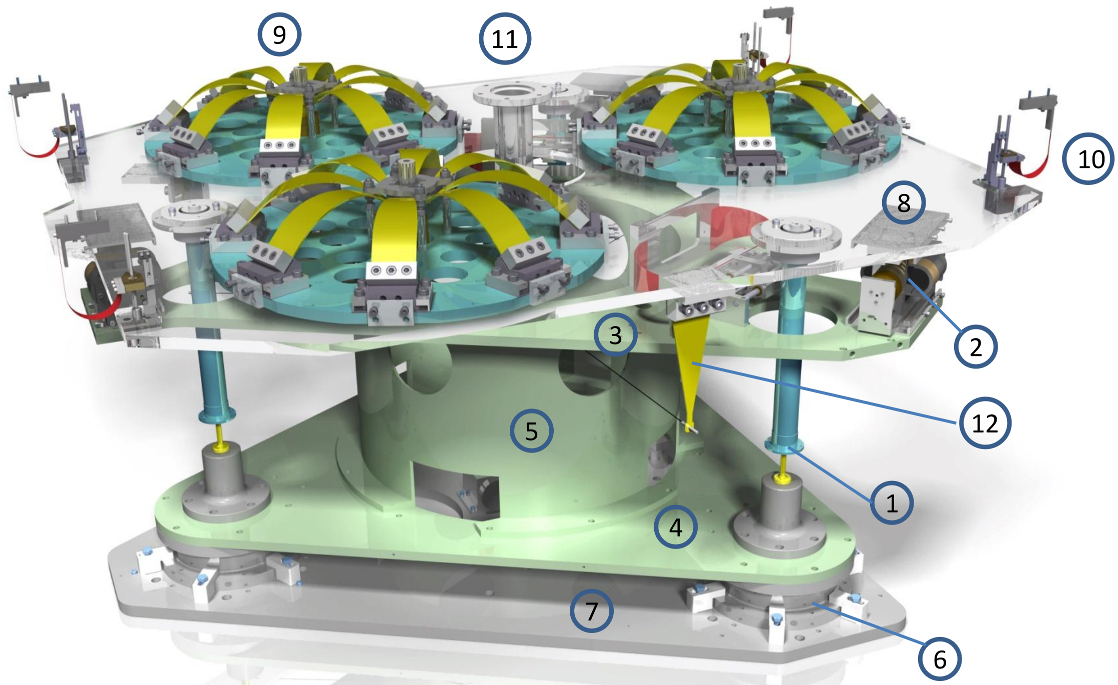

Figure 3.20: *Schematic rendering of the base and springbox of EIB-SAS. The base componenets are listed in Fig. 3.2. Three inverted pendulums (1) support a springbox (8) which houses three geometric anti-spring filters (9). The vertical position sensors and voice-coil actuators are positioned in the center of the GAS filters. Four stepper motor driven positioning springs (10) that can be used to adjust the DC position of the bench are positioned on the four corners of the springbox. EIB-SAS incorporates a tilt stabilizer, which increases the stiffness of the vertical tilt degrees of freedom Tx and Tz. It consists of a column hanging from the top plate (11), which is connected with steel wires to three cantilever blades (12).*

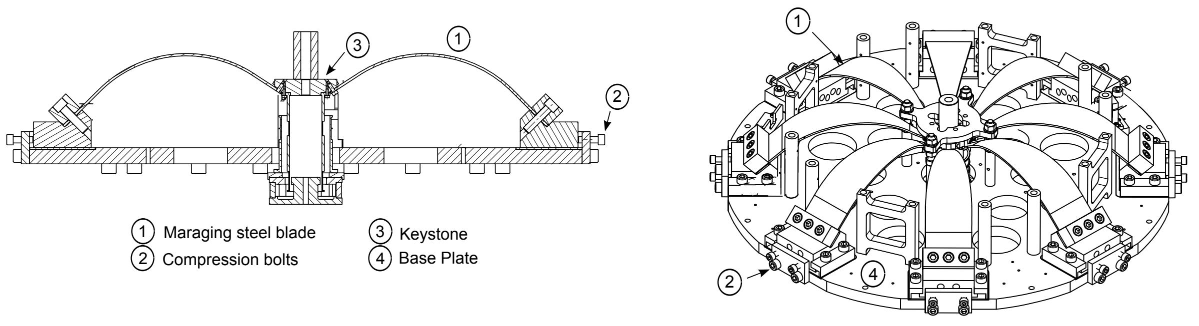

(a) **(b)**

Figure 3.21: *Schematic representation of a geometric anti-spring filter. a) Side-view, for clarity only two blades are shown. b) Entire filter with all 8 blades. The bases of the blades are clamped to the base plate at an angle of 45°. They meet in the center of the filter where they are clamped to a keystone at an angle of -33°. The tuning of the blades can be done by with the compression bolts.*

air, and the loss angle $\phi = 1/Q$, where Q is the quality factor of the oscillator. The transfer function of the system is then given by

$$H_{\mathsf{Y}} = \frac{\omega_0^2 (1 + i\phi) + \frac{m}{M}\omega^2}{\omega_0^2 (1 + i\phi) - \omega^2 + i\frac{\gamma}{M}\omega}. \tag{3.30}$$

Rather then decreasing $\propto 1/\omega^2$ for $\omega \to \infty$, the limit of $H_{\mathsf{Y}} = -m/M$. The mass distribution and inertia of the filter blades will limit the isolation performance at high frequency.

3.5.3 Linearized GAS filter model

The linearized model is not suitable for the design of a real GAS filter, but is useful to describe the qualitative behavior of such a mechanical system in an intuitive way. For the design of an actual GAS filter, use should be made of both the quantitative model abstracted in section 3.5.4, and the finite element modeling (see section 3.5.5).

A GAS filter can be described by a mass m suspended from one vertical spring with stiffness k_{y} and length $l_{0\mathsf{y}}$ and two compressed horizontal springs of combined stiffness k_{x} and length $l_{0\mathsf{x}}$ (see Fig. 3.22) [15].

In the situation depicted in Fig. 3.22a the forces of the horizontal springs cancel and the force of the vertical spring and the gravitational force on the suspended mass cancel. In this case the resonance frequency of the system will be minimal. We will call this special situation the *working point*. In the working point the equation of motion of the system is given by

$$m\ddot{y} = -k_{\mathsf{y}} (y_0 - l_{0\mathsf{y}}) - mg = 0, \tag{3.31}$$

where y_0 is the length of the vertical spring in the equilibrium position of the GAS filter.

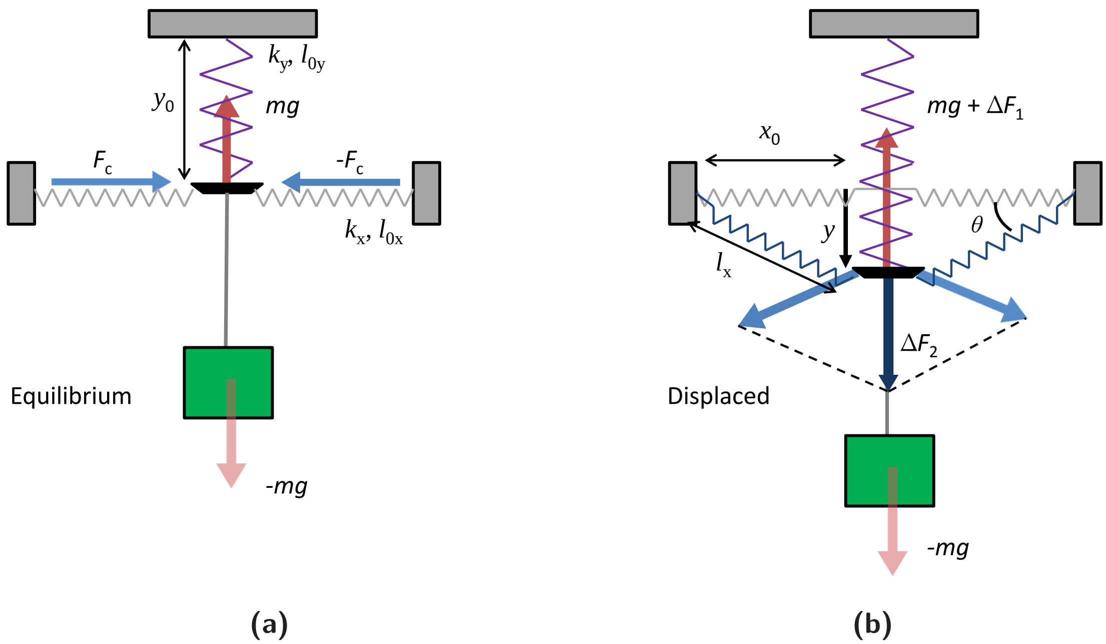

Figure 3.22: *Schematic representation of the working principle of a GAS filter. a) At the working point the radial forces of the blade springs cancel and their vertical components are canceled by the weight of the load. b) When the keystone is displaced the compression of the blade springs provides an anti-spring effect.*

For small excursions y from the working point the horizontal forces of the horizontal springs will still cancel. The force of the vertical spring will increase with $\Delta F_1 = -k_\mathrm{y} y$ and will be partially canceled by the vertical component of the forces of the compressed springs $\Delta F_2 \approx -k_\mathrm{x}(l_\mathrm{x} - l_\mathrm{0x}) \sin\theta = -k_\mathrm{x}\left(1 - l_\mathrm{0x}/l_\mathrm{x}\right) y$, where l_x is the length of the compressed horizontal springs.

For amplitudes y much smaller than the length of the compressed horizontal spring x_0 ($y^2 \ll x_0^2$), the equation of motion of the GAS filter can be written as

$$m\ddot{y} = \Delta F_1 + \Delta F_2 = -k_\mathrm{y} y - k_\mathrm{x}\left(1 - \frac{l_\mathrm{0x}}{l_\mathrm{x}}\right) y. \tag{3.32}$$

We see that for small amplitudes the system behaves as a harmonic oscillator with an effective stiffness

$$k_\mathrm{eff} = k_\mathrm{y} + k_\mathrm{x}\left(1 - \frac{l_\mathrm{0x}}{l_\mathrm{x}}\right). \tag{3.33}$$

Note that because $l_\mathrm{0x}/l_\mathrm{x} > 1$ the term in brackets in Eq. (3.33) is negative and the stiffness of the system is lowered. We can define the compression rate K as

$$K = \frac{l_\mathrm{0x} - l_\mathrm{x}}{l_\mathrm{0x}}. \tag{3.34}$$

Noting that $l_{\mathsf{x}} = \sqrt{y^2 + x_0^2}$, where x_0 is the horizontal distance between the two ends of the compressed horizontal spring, Eqs. (3.33) and (3.34) can be written as

$$k_{\mathsf{eff}} = k_{\mathsf{y}} + k_{\mathsf{x}} \left(1 - \frac{l_{0\mathsf{x}}}{\sqrt{y^2 + x_0^2}}\right), \quad \text{and} \tag{3.35}$$

$$K = 1 - \frac{\sqrt{y^2 + x_0^2}}{l_{0\mathsf{x}}}. \tag{3.36}$$

Equation (3.35) gives the effective stiffness of the filter as a function of displacement from the working point $k_{\mathsf{eff}}(y)$ at a compression $K(x_0)$.

Equilibrium position and resonance frequency

In the working point the vertical force of the blades is exactly balanced by the load of the filter m_0, and the filter will have a minimal frequency. When the load is changed by an amount Δm, the new equilibrium position will no longer coincide with the working point. It will change by an amount

$$\Delta y_{\mathsf{eq}} = \frac{\Delta F}{k_{\mathsf{eff}}} = \frac{g \Delta m}{k_{\mathsf{eff}}} = \frac{g}{k_{\mathsf{y}} + k_{\mathsf{x}} \left(1 - \frac{l_{0\mathsf{x}}}{\sqrt{y^2 + x_0^2}}\right)} \Delta m. \tag{3.37}$$

Fig. 3.23 shows the equilibrium position of the filter given by Eq. (3.37) for different compression rates. Table 6.2 gives the values of the parameters. The black curve corresponds to the nominal compression rate of the EIB-SAS GAS filters, $K = 0.0894$ (the measured compression rate of the EIB-SAS GAS filters is 0.0915). For $K = 0.0909$ (green curve) the slope of the curve approaches infinity, which means that the stiffness of the filter vanishes. Compressing the filter blades even more, the system becomes bistable (blue curve); increasing the load of the filter, the vertical position of the keystone would at some point jump to a low position and vice versa.

For loads corresponding to a value where the load curve has a negative slope the filter has two vertical positions where it is in equilibrium, depending on whether it is being loaded or unloaded. To go from the situation depicted by the black curve to that depicted by the blue curve, the blades need only be compressed by an additional 0.5 mm.

The resonance frequency of the filter at a particular vertical position is given by

$$\omega(y) = \sqrt{\frac{k_{\mathsf{eff}}(y)}{m(y)}}, \tag{3.38}$$

where $k_{\mathsf{eff}}(y)$ is given by Eq. (3.35). The load $m(y)$ of the filter at each position is $m_0 + \Delta m$. The change in load Δm to induce a change in equilibrium position Δy_{eq} is given by Eq. (3.37).

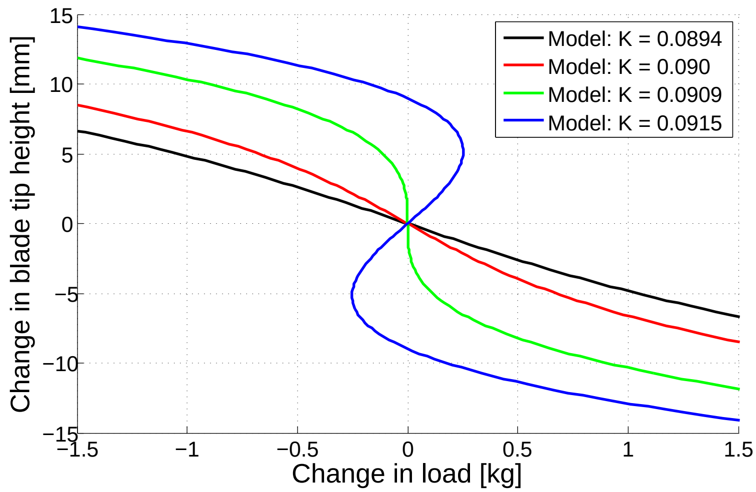

Figure 3.23: *Load-height curves from the linear GAS filter model. In the simulation the compression rate K is varied. $K = 0.0894$ corresponds to the nominal working point of the EIB-SAS GAS filters. At $K = 0.0909$ the filter is critically tuned* e.g. *about to become unstable. The curve for $K = 0.0915$ shows a bistable filter; the filter will never be in equilibrium between -5 and $+5$ mm. For data see Fig. 3.34.*

Property†	Value
$l_{0\mathsf{x}}$	273.75 mm
k_{x}	1.0×10^6 N/m
k_{y}	1.0×10^5 N/m

Table 3.6: *The parameters used in the GAS filter model.*

Remembering that Δy_{eq} is just the excursion from the working point *y* we obtain $m(y) = m_0 + \Delta m = m_0 + y k_{\text{eff}}(y)/g$ and Eq. (3.38) becomes

$$\omega(y) = \sqrt{\frac{k_{\text{eff}}(y)}{m_0 + \frac{y}{g} k_{\text{eff}}(y)}}, \tag{3.39}$$

where $k_{\text{eff}}(y)$ is given by Eq. (3.35).

Fig. 3.24 shows the square of the frequency given by Eq. (3.39) for several values of its compression rate (the same values as in Fig. 3.23). At $K = 0.0909$ (green curve), where the slope of the load-height curve approached infinity, the frequency of the filter indeed goes to 0. Compressing the filter even more (blue curve), the frequency becomes imaginary; the system is no longer able to perform stable oscillations. In such a state, the filter has two equilibrium positions. It is bistable. When disturbed it will jump from one equilibrium position to the other.

†A first estimate for these values was obtained by solving the numerical model for the blade's shape in section 3.5.4 for different compressions. They have been tuned by fitting the model parameters to data.

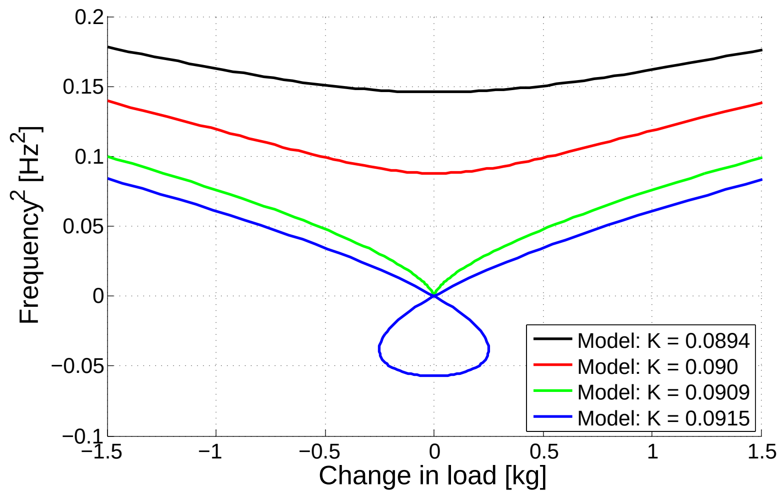

Figure 3.24: *Simulated load-frequency curves at different compression rates K. The setting K = 0.0894 corresponds to the nominal compression rate of the EIB-SAS filters. At K = 0.0909 the filter is tuned to 0 Hz and about to become bistable. At K = 0.0915 the filter is bistable and no longer performs stable oscillations. For data see Figs. 3.35 and 3.36.*

Thermal stability

For a given compression and load the GAS filter behaves as a soft vertical spring. Its frequency and equilibrium position depend on the temperature of the filter. Two effects influence the thermal stability of the filter: temperature changes alter the Young's modulus of the blades and a difference in thermal expansion coefficient of the maraging steel blades and the aluminum base plate alter the compression rate.

The load of the filter is carried by the vertical component of the force produced by the blades F_{y}. The force produced by the blades is linearly dependent on the Young's modulus. Therefore, a relative change in Young's modulus due to a temperature change is equivalent to relative change of its load at fixed temperature: $\Delta E/E = \Delta m/m$ [99].

The rate of change in equilibrium position due to mass change $\partial y/\partial m = k_{\mathrm{eff}}$. The change in equilibrium position Δy due to a change in temperature is $\Delta y = \Delta F/k_{\mathrm{eff}} = g\Delta m/k_{\mathrm{eff}}$. As $k_{\mathrm{eff}} = m\omega_0^2$, $\Delta y = g\Delta m/\omega_0^2 m = g\Delta E/\omega_0^2 E$. The relative change of Young's modulus $\Delta E/E$ of maraging steel with respect to temperature can be found in Ref. [100] and is 2.54×10^{-4} °C^{-1}. So, $\Delta y = -2.54\times10^{-4} g/\omega_0^2$ [m/K]. The EIB-SAS GAS filters have been tuned to 390 mHz, so their equilibrium position changes -415 µm°C^{-1}.

The thermal expansion coefficients of maraging steel and aluminum are 10.3×10^{-6} °C^{-1} and 23.1×10^{-6} °C^{-1} respectively. We will denote their difference: -12.8×10^{-6} °C^{-1} by η. Due to this difference in thermal expansion rates of the blade and the base plate, a change in temperature will alter the compressed length of the blades l_{x}. This changes the compression rate of the springs and therefore the stiffness of the filter. Note that the direction of the change in working point due to the thermal expansion depends on the tuning of the filter. If the equilibrium position of the filter is slightly above the working point, the equilibrium position will go up, when it is tuned below it, it will go down.

The rate of change of the compression rate (Eq. (3.34)) due to temperature changes is $\partial K/\partial T = \partial K/\partial l_{\mathsf{x}} \times \partial l_{\mathsf{x}}/\partial T = -\eta/l_{0\mathsf{x}} = -4.7 \times 10^{-5}$ °C^{-1}. This change in compression rate is so small that its effect on the equilibrium position of the filter is negligible compared to the thermal effect of the Young's modulus. Fig. 3.23 shows that vertical position of the keystone only changes significantly when the compression changes in the order of $10^{-2} - 10^{-3}$. However, changing the compression rate does alter the frequency of the filter.

The filter's frequency will increase with temperature. The angular frequency of the filter $\omega_0 = \sqrt{k_{\mathsf{eff}}/m}$, where m is the mass per blade and k_{eff} is given by Eq. (3.33). The change in frequency $\Delta\omega$ due to a change in temperature is then given by $\Delta\omega = \partial\omega/\partial k_{\mathsf{eff}} \times \partial k_{\mathsf{eff}}/\partial l_{\mathsf{x}} \times \partial l_{\mathsf{x}}/\partial T \times \Delta T = k_{\mathsf{x}}\eta l_{0\mathsf{x}}/2\omega_0 m l_{\mathsf{x}} \times \Delta T$. Since $l_{\mathsf{x}} \approx l_{0\mathsf{x}}$, $\Delta\omega = 1.90\times10^{-2} \times \Delta T/\omega_0$ [Hz/K].

3.5.4 Blade design

Special care was taken when designing the GAS filter blades, such that the maximum stress in the blades would not exceed the ultimate tensile stress of maraging steel, which is 1.97 GPa. Both analytical and finite element models have been used for this purpose.

Single blade analytical model

An analytical model has been developed by Cella *et al* [101], hereafter just abstracted. In the model the blade is represented by a one-dimensional elastic line (see Fig. 3.25), whose ends are held at fixed angles θ_0 and θ_{L}.

Due to the load and the geometric constraints a moment M_{L} and a force F with horizontal and vertical components F_{x} and F_{y} are applied to the blade tip. The position of the blade tip at the equilibrium is $(x_{\mathsf{L}}, y_{\mathsf{L}})$ (see Fig. 3.25). Because of the radial symmetry of the GAS filter the blade tips can only move in the vertical (*y*) direction and because the blade is thin and mirror symmetric it can be approximated with a line shaped blade with curvilinear coordinate $\lambda \in [0, L]$ that has a bending profile $\theta(\lambda)$ depending on the bending moment $M(\lambda)$

$$M(\lambda) = \frac{EI(\lambda)}{R(\lambda)} = EI(\lambda)\frac{\partial\theta}{\partial\lambda} = M_{\mathsf{L}} + F_{\mathsf{y}}(x_{\mathsf{L}} - x(\lambda)) - F_{\mathsf{x}}(y_{\mathsf{L}} - y(\lambda)), \tag{3.40}$$

where $R(\lambda)$ is the radius of curvature of the blade. The moment of inertia of the cross section is $I(\lambda) = w(\lambda)d^3/12$, where $w(\lambda)$ is the width profile of the blade and d is the thickness of the blade. Fig. 3.26 shows the width profile of the EIB-SAS GAS filter blades. Taking the derivative with respect to λ and noting that $\partial x/\partial\lambda = \cos\theta$ and $\partial y/\partial\lambda = \sin\theta$ we get

$$E\left(\frac{\partial I}{\partial\lambda}\frac{\partial\theta}{\partial\lambda} + I(\lambda)\frac{\partial^2\theta}{\partial\lambda^2}\right) = -F_{\mathsf{y}}\cos(\theta(\lambda)) + F_{\mathsf{x}}\sin(\theta(\lambda)). \tag{3.41}$$

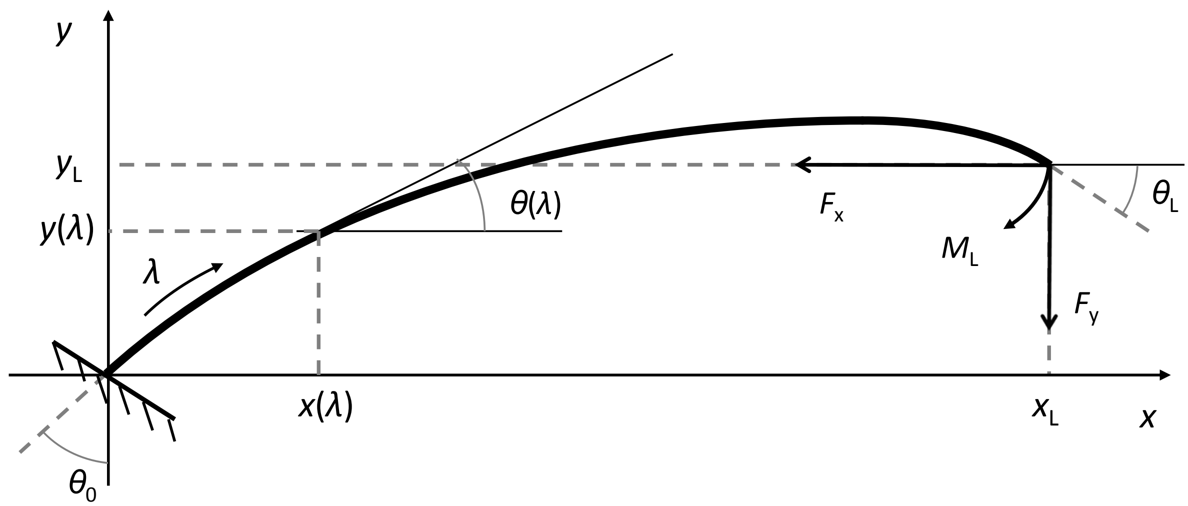

Figure 3.25: *Model of a single GAS filter blade from Ref. [101]. The keystone exerts a vertical force F_y, a horizontal force F_x, and a moment M_L on the blade which will cause the blade to bend. The blade has length L. Denoting the distance along the blade with λ, the blade shape $\theta(\lambda)$ is determined by M_L and the bending moments of F_x and F_y.*

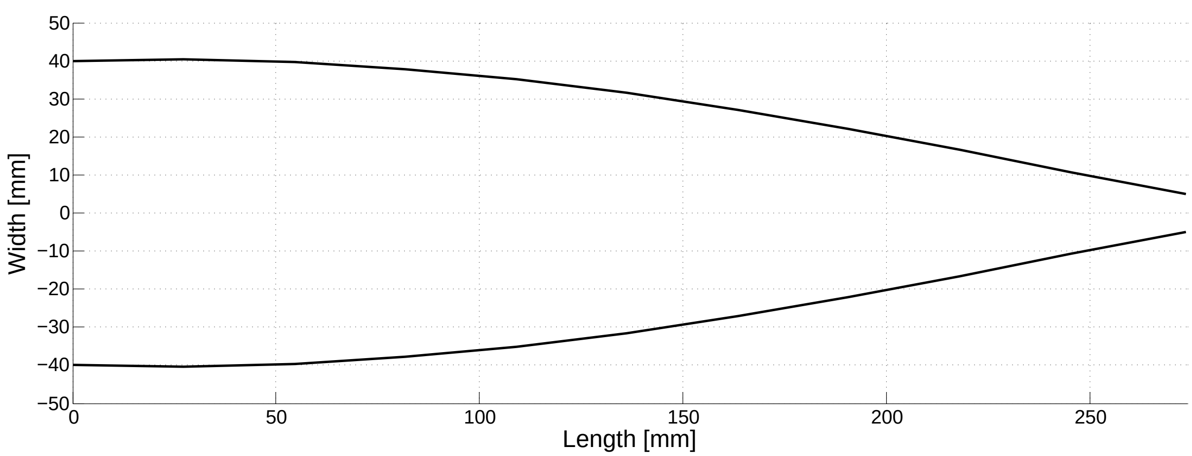

Figure 3.26: *Width profile of the EIB-SAS GAS filter blades.*

Solving for $\partial^2\theta/\partial\lambda^2$ we obtain

$$\frac{\partial^2\theta}{\partial\lambda^2} = \frac{1}{I(\lambda)}\left(\frac{1}{E}\left[F_{\mathsf{x}}\sin(\theta(\lambda)) - F_{\mathsf{y}}\cos(\theta(\lambda))\right] - \frac{\partial\theta}{\partial\lambda}\frac{\partial I}{\partial\lambda}\right). \tag{3.42}$$

Following the approach of [101] we change to the normalized parameters $\xi = \lambda/L$, $X = x/L$ and $Y = y/L \in [0,1]^*$. This yields

$$\frac{\partial^2\theta}{\partial\xi^2} = \frac{1}{I(\xi)}\left(\frac{L^2}{E}\left[F_{\mathsf{x}}\sin(\theta(\xi)) - F_{\mathsf{y}}\cos(\theta(\xi))\right] - \frac{\partial\theta}{\partial\xi}\frac{\partial I}{\partial\xi}\right), \tag{3.43}$$

and introducing the normalized blade shape function $\gamma(\xi) = w(0)/w(\xi)$ gives

$$\frac{\partial^2\theta}{\partial\xi^2} = \frac{12L^2}{Ew(0)d^3}\gamma(\xi)\left[F_{\mathsf{x}}\sin(\theta(\xi)) - F_{\mathsf{y}}\cos(\theta(\xi))\right] - \frac{\partial(\gamma^{-1})}{\partial\xi}\frac{\partial\theta}{\partial\xi}. \tag{3.44}$$

We define the dimensionless force parameters $G_{\mathsf{i}} = 12L^2/Ew(0)d^3 \times F_{\mathsf{i}}$, where $i = x, y$, that correspond to the vertical and horizontal forces, E is the Young's modulus of maraging steel and d the thickness of the blade. We obtain

$$\frac{\partial^2\theta}{\partial\xi^2} = \gamma\left(\xi\right)\left[G_{\mathsf{x}}\sin\left(\theta\left(\xi\right)\right) - G_{\mathsf{y}}\cos\left(\theta\left(\xi\right)\right)\right] - \frac{\partial\left(\gamma^{-1}\right)}{\partial\xi}\frac{\partial\theta}{\partial\xi}. \tag{3.45}$$

Written in this form, it is clear that for a given blade shape $\gamma(\xi)$, G_{x} and G_{y} completely characterize the system.

Choosing a compression and load, x_{L} and y_{L} are defined and Eq. (3.45) can be solved numerically with boundary conditions $\theta(0) = \theta_0$ and $\theta(1) = \theta_1$ to obtain the bending profile of the blade $\theta(\xi)$. The working dimensionless point $(X_{\mathsf{L}}, Y_{\mathsf{L}})$ is then given by

$$\begin{aligned} X_{\mathsf{L}} &= \frac{x_{\mathsf{L}}}{L} = \int\cos\theta\left(\xi\right)d\xi, \\ Y_{\mathsf{L}} &= \frac{y_{\mathsf{L}}}{L} = \int\sin\theta\left(\xi\right)d\xi, \end{aligned} \tag{3.46}$$

and the radius of curvature along the blade by $R(\xi) = L\left(\partial\theta/\partial\xi\right)^{-1}$. The stress S in the blade is then given by

$$S(\xi) = \frac{Ed}{2R(\xi)} = \frac{Ed}{2L}\frac{\partial\theta}{\partial\xi}. \tag{3.47}$$

Solving Eq. (3.45) multiple times, keeping X_{L} constant and varying Y_{L} the vertical force delivered by the blades $G_y(Y)$ is obtained.

The full weight of the load is compensated by the vertical force $F_{\mathsf{y}} = mg$. Therefore we can write $G_{\mathsf{y}} = 12L^2mg/Ew(0)d^3$ and $m(Y) = Ew(0)d^3/12gL^2 \times G_{\mathsf{y}}(Y)$, which is the load necessary to arrive at an equilibrium position Y.

*Note that the boundary condition $\theta(\mathsf{L}) = \theta_{\mathsf{L}}$, becomes $\theta(\xi = 1) \equiv \theta_1$. Similarly, $x_{\mathsf{L}} \to x_1$ and $y_{\mathsf{L}} \to y_1$.

The rate of change of the vertical force gives the effective spring constant of the filter $k_{\text{eff}}(Y) = Ew(0)d^3/12L^2 \times \partial G_{\text{y}}/\partial Y$. So, the resonance frequency $f_0(Y) = \sqrt{k_{\text{eff}}(Y)/m(Y)}/2\pi = \sqrt{g\left(\partial G_{\text{y}}(Y)/\partial Y\right)/G_{\text{y}}(Y)}/2\pi$. Noting that $G_{\text{y}}(y) = G_{\text{y}}(LY)$ and $\partial G_{\text{y}}/\partial y = 1/L \times \partial G_{\text{y}}/\partial Y$, $f_0(y)$ is given by

$$f_0(y) = \frac{1}{2\pi}\sqrt{\frac{g}{L}\frac{\frac{\partial G_{\text{y}}}{\partial Y}}{G_{\text{y}}}}, \tag{3.48}$$

and $m(y) = Ew(0)d^3/12gL^2 \times G_{\text{y}}(y)$. The nominal load of the filter is that load for which f_0 is minimal and $y = y_1$ and is given by

$$m_0 = \frac{gEw(0)d^3}{12L^2}G_{\text{y}}(y_1). \tag{3.49}$$

The first solution investigated by Cella *et al*, was the *constant curvature solution*. This solution would minimize the stress in the blade because it would be equally distributed over the entire blade. In this case $\theta(\xi) = \theta_0 + \xi(\theta_1 - \theta_0)$ and

$$\gamma_{\text{const.cur.}}(\xi) = \frac{(\theta_1 - \theta_0)^2}{(\theta_1 - \theta_0)^2 - G_{\text{y}}\left[\sin\theta(\xi) - \sin\theta_0\right] - G_{\text{x}}\left[\cos\theta(\xi) - \cos\theta_0\right]}. \tag{3.50}$$

They studied the uniform curvature solution space extensively and found that none of the solutions have a critical point; none of the solutions provides a blade with vanishing vertical stiffness. They did find a solution that looked similar to the constant curvature solution *and* had a critical point. The blade shape function of this solution is

$$\gamma_C(\xi)^{-1} = c_1 + c_2\cos\beta\xi + c_3\sin\beta\xi, \quad \text{with} \tag{3.51}$$
$$\theta_0 = \frac{\pi}{4}, \quad \text{and} \quad \theta_1 = \frac{-\pi}{6},$$

with $c_1 = -0.377$, $c_2 = 1.377$, $c_3 = 0.195$ and $\beta = 1.361$.

The blades of the EIB-SAS GAS filters are similar in shape to the blades designed by Cella *et al*. The main difference is that $\theta_1 = 33°$ instead of 30° for the Cella-type blades.

EIB-SAS blade shape function

The EIB-SAS blade shape function can be parametrized as

$$\gamma_{EIB-SAS}(\xi)^{-1} = p_0 + p_1\xi + p_2\xi^2 + p_3\xi^3 + p_4\xi^4, \quad \text{with} \tag{3.52}$$
$$\theta_0 = \frac{\pi}{4}, \quad \text{and} \quad \theta_1 = 33°,$$

with $p_0 = 1$, $p_1 = 0.177$, $p_2 = -1.109$, $p_3 = -0.455$ and $p_4 = 0.51$. The remaining properties of the EIB-SAS GAS filter blades are listed in Table 3.7.

Property	Value
E	186 GPa
L	273.75 mm
$w(0)$	80 mm
d	2.4 mm
θ_0	45°
θ_L	-33°

Table 3.7: *Properties of the EIB-SAS GAS filter blades.*

With the aid of Eq. (3.48) and by using the parameter values listed in Table 3.7 the simulation can be tuned such that in the working point f_0 has the desired value of 390 mHz. This is the case when the compression rate of the filter $K = 0.1024$. The normalized blade tip height is then $y_L/L = 0.091$ and the normalized vertical force $G_y = -1.571$. According to Eq. (3.49) this corresponds to a nominal load of the filter $m_0 = 293$ kg.

Blade design procedure

When designing a new GAS filter blade, the goal is to find a blade shape function $\gamma(\xi)$ such that:

- The frequency of the filter can be tuned to arbitrarily low frequency; it has to have a critical point.
- The filter can support the desired load.
- The stress in the blades never exceeds the ultimate tensile stress (UTS) of the material they are made of. The EIB-SAS blades are made of maraging steel, which has a UTS of 1.97 GPa.

When you have designed new blades for a GAS filter: built a prototype! Do not rely blindly on the theoretical values for G_y and hence f_0 and m_0. The strength and stiffness of your blade could be different then predicted by the model, due to phenomena that are not taken into account by the model.

The first step towards a blade design to determine appropriate clamping angles θ_0 and θ_L for the blade. In Ref. [101] by Cella *et al* the parameter space has been explored and they give a range of clamping angles (boundary conditions) that provide interesting solutions *i.e.* solutions with practical values for x_0 and G_y.

To design a blade it is easiest to start from an existing blade and scale it to fit your needs. This guarantees that the blade will have a critical point.

For a given blade shape function the dimensionless force parameters G_x and G_y completely define the dimensionless properties of the blade. The physical properties of the blade are a function of dimensionless blade parameters with an appropriate scale factor. If the angles under which the blade is clamped to the baseplate and keystone remain unchanged, then we may scale the length, width and thickness of the blade in such a way that the dimensionless working point remains unchanged while the physical properties of the blade are altered.

Looking at the definition of G_{i} we see that 3 parameters can be altered: the length of the blade L, its thickness d and its overall width $w(0)$. As long as the quantity $L^2/d^3w(0)$ remains unchanged, so do G_{i}, X_{L} and Y_{L}. According to Eq. (3.46), (3.47), (3.48) and (3.49), the working point (x_{L}, y_{L}) scales with L, the load m of the filter scales with $w(0)d^3/L^2$ and its resonance frequency scales with $1/\sqrt{L}$. The stress S in the blade scales with d. With these scalings in mind we can set out to alter the blade's properties while conserving its ability to have vanishing vertical stiffness.

As an example we treat the case where we want to reduce the stress in the blade by 10%. This means reducing the thickness d of the blade by 10%. The dimensionless blade parameters will not change if we at the same time increase the overall width $w(0)$ of the blade by 37%. That is, from 80 mm to 109.7 mm. Alternatively, the length L of the blade can be reduced by 15%, making it 233.75 mm instead of 273.75 mm. The latter solution would also change the working point and natural frequency of the blade. The fact that the frequency changes when the length of the blade changes can always be remedied by adjusting the blade's compression rate. In turn, this will change the stress in the blade. In short, the recipe to design a blade is:

1. Find a blade shape function that satisfies Eq. (3.45) with some set of boundary conditions that give adequate values for x_0 and G_{y}.

2. Solve Eq. (3.45) for a number of equilibrium positions and compression rates $(X_{\mathrm{L}}, Y_{\mathrm{L}})$. For each solution, calculate the dimensionless vertical force G_{y}.

3. The blade needs to have a critical point. Use Eq. (3.48) to calculate the frequency of the filter as a function of blade tip height. Check that the frequency vanishes for some value set of x_0, y_{L}. This will be the working point of the blade.

4. Make sure that the stress in the blade does not exceed the ultimate tensile stress of the material with Eq. (3.47).

5. Check that the filter can support the necessary load with Eq. (3.49).

6. If the stress in the blade is too high, then adjust the blade geometry. Note that the dimensionless properties remain unchanged as long as $L^2/d^3w(0)$ remains unchanged. Hence, reducing the thickness of the blade while at the same time adjusting L and $w(0)$, will lower the stress at the cost of changing f_0, m_0, x_{L} and y_{L}.

7. Alternatively, the properties of the blade may be altered at the cost of changing the stress in the blade.

3.5.5 Blade model incorporating the Poisson effect

The stress in the blades as calculated in the numerical model will underestimate the real maximum stress in the blades. In the numerical model the stress is divided equally over the full width of the blade, and only the curvilinear coordinate matters. In practice, the maximum stress will be higher due to the Poisson effect.

The Poisson effect

The Young's modulus of a material E is defined as the slope of the stress-strain curve in the region where Hooke's law applies. Ignoring the Poisson effect and denoting the stress and strain in the Euler directions σ_i and ϵ_i $(i = x, y, z)$, we can write

$$\begin{pmatrix}\epsilon_\mathrm{x}\\ \epsilon_\mathrm{y}\\ \epsilon_\mathrm{z}\end{pmatrix} = \frac{1}{E}\begin{pmatrix}1 & 0 & 0\\ 0 & 1 & 0\\ 0 & 0 & 1\end{pmatrix}\begin{pmatrix}\sigma_\mathrm{x}\\ \sigma_\mathrm{y}\\ \sigma_\mathrm{z}\end{pmatrix}. \tag{3.53}$$

However, straining the material in one direction will induce a stress in the orthogonal directions and compressing the material in one direction will cause it to expand in the orthogonal directions. This effect is called the *Poisson effect*. The ratio of the expansion in one direction due to the compression in the other direction is called the *Poisson ratio* ν $(|\nu| < 1)$ and is a measure for the strength of the Poisson effect. Therefore Eq. (3.53) becomes

$$\begin{pmatrix}\epsilon_\mathrm{x}\\ \epsilon_\mathrm{y}\\ \epsilon_\mathrm{z}\end{pmatrix} = \frac{1}{E}\begin{pmatrix}1 & -\nu & -\nu\\ -\nu & 1 & -\nu\\ -\nu & -\nu & 1\end{pmatrix}\begin{pmatrix}\sigma_\mathrm{x}\\ \sigma_\mathrm{y}\\ \sigma_\mathrm{z}\end{pmatrix}. \tag{3.54}$$

When the GAS filter blades are bend in the symmetry plane (*xy*-plane in Fig. 3.25), the upper half of the blade will be stretched which will cause a contraction of the blade in the direction perpendicular to the applied force *i.e.* across the width of the blade. Likewise, the bottom half of the blade will be compressed, which causes an expansion across the width of the blade. The curved blade will have the shape of a saddle instead of an arc. This is called corrugation*. Its effect will increase the maximum stress level in the blade.

Bending the blade in this way, it is both compressed and stretched in the direction orthogonal to the bending plane (the *z*-direction). Therefore, the strain in this direction

*If you have an eraser you can do this yourself. Bend it and you will see the rims curve upward. This is corrugation of the eraser.

$\epsilon_z = 0$, $\sigma_z = \nu(\sigma_x + \sigma_y)$ and instead of Eq. (3.54) we can write

$$\begin{pmatrix} \epsilon_x \\ \epsilon_y \end{pmatrix} = \frac{1}{E} \begin{pmatrix} 1-\nu^2 & -\nu-\nu^2 \\ -\nu-\nu^2 & 1-\nu^2 \end{pmatrix} \begin{pmatrix} \sigma_x \\ \sigma_y \end{pmatrix} \approx \frac{1}{E} \begin{pmatrix} 1 & -\nu \\ -\nu & 1 \end{pmatrix} \begin{pmatrix} \sigma_x \\ \sigma_y \end{pmatrix}. \tag{3.55}$$

Inverting the above equation we obtain

$$\begin{pmatrix} \sigma_x \\ \sigma_y \end{pmatrix} = \frac{E}{(1-\nu^2)} \begin{pmatrix} 1 & \nu \\ \nu & 1 \end{pmatrix} \begin{pmatrix} \epsilon_x \\ \epsilon_y \end{pmatrix} = E^* \begin{pmatrix} 1 & \nu \\ \nu & 1 \end{pmatrix} \begin{pmatrix} \epsilon_x \\ \epsilon_y \end{pmatrix}, \tag{3.56}$$

with $E^* = E/1-\nu^2$.

Due to the Poisson effect the Young's modulus, and hence the strength of the blade, increases with a factor $(1-\nu^2)^{-1}$. The Poisson ratio of maraging steel is 0.32, so the strength of the blades increases with 11%. Therefore, the nominal load predicted by the model in section 3.5.4 increases by the same amount from 293 kg to 326 kg, which lies close to the experimental values of: 314, 317 and 323 kg.

In the analytical model, the stress in the blade has only a single component. Now, due to corrugation also the stress across the blade needs to be taken in to account. In this case, under which stress conditions the material will yield is well described by an experimental law known as the *Von Mises yield criterion*, rather than a single stress component exceeding some critical value.

Von Mises stress criterion

The stress in the blades is more accurately described by the Cauchy stress tensor, which is a 3×3 tensor containing the stresses in the 3 Euler directions σ_{xx}, σ_{yy} and σ_{zz} and 3 shear stress components σ_{xy}, σ_{yz} and σ_{zx}. The Cauchy stress tensor has a hydrostatic component s_{ij} which can be thought of as the pressure in the system and a deviatoric stress component $\delta_{ij} = \sigma_{ij} - s_{ij}$. According to the Von Mises yield criterion, the *second deviatoric stress invariant* J_2 of the deviatoric stress tensor δ_{ij} is a measure for how close the material is to yielding. In general $J_2 = \sqrt{(\sigma_{xx}-\sigma_{yy})^2 + (\sigma_{yy}-\sigma_{zz})^2 + (\sigma_{zz}-\sigma_{xx})^2 + \left(\sigma_{xy}^2 + \sigma_{yz}^2 + \sigma_{zx}^2\right)}/\sqrt{2}$. The value of J_2 at which the material yields is known as the *equivalent tensile stress* or *Von Mises stress* σ_v. The Von Mises yield criterion states that the Von Mises stress in the blades should not exceed the ultimate tensile strength of maraging steel, or the blades will plastically deform.

Finite element model of the blade

To take into account the Poisson effect a FEM model was constructed. Due to symmetry of the blade it suffices to model half a blade. The properties of the blade are those listed in Table 3.7, the *x*-direction is taken to be along the symmetry line of the blade and *y* along the width of the blade. The blade is elastically deformed from straight to curved (loaded) in 100 steps. In the loaded configuration it obeys the boundary conditions listed in Eq. (3.52). Our FEM model takes the Poisson effect into account by calculating the Von Mises stress in the blade.

FEM model results

Fig. 3.27 shows the equivalent tensile stress in a blade of an EIB-SAS GAS filter tuned to 250 mHz as predicted by the FEM model when the Poisson ratio $\nu = 0$ and Fig. 3.28 for $\nu = 0.32$. In both figures the top curve shows the stress in the upper part of the blade, the bottom curve in the lower part of the blade.

For $\nu = 0$ the stress in the top and bottom surface of the blade are similar and is equally distributed along the width of the blade. For $\nu = 0.32$ the stress in the blade is not distributed uniformly. Neither along x nor y. A blade that is loaded does not just bend along its longitudinal axis, its rims curve upward. In the top part of the blade the stress is highest at the rim, in the bottom part the stress is highest in the central region.

Fig. 3.29 shows the stress on a line along the width of the blade passing through the maximum stress region of the top surface (squares) and bottom surface (dots). According to the FEM model, the maximum stress is 1.62 GPa in the bottom surface of the blade and 1.80 GPa in the top surface of the blade. The maximum stress in the top surface is 90% of the ultimate tensile strength of maraging steel.

3.5.6 Other design considerations

Maraging steel

The GAS filter blades will operate at constant stress levels close to the ultimate tensile strength of the material. In these conditions the blade may undergo a continuous plastic flow at the level of the microscopic structure of the material known as *creep*. The creep rate is large at high temperature, but might be considerable even at room temperature.

Creep is undesirable in a seismic isolator because over time it leads to macroscopic non-reversible deformation of the blades. It is also associated with a high rate of acoustic emission events known as mechanical shot-noise ("glitches"). That latter effect is not an issue for EIB-SAS, but it is severe for the mechanics employed for the core optics of the interferometer like the super attenuator. Dedicated R&D studies on materials were carried out by the Virgo collaboration [102]. Maraging (acronym from martensitic aging) steel resulted as the best available metal in terms of both tensile strength and creep rate.

Strength and creep behavior are governed by the dynamics of imperfections of the crystal lattice. These imperfections are called *dislocations*. High strength metal alloys are poly-

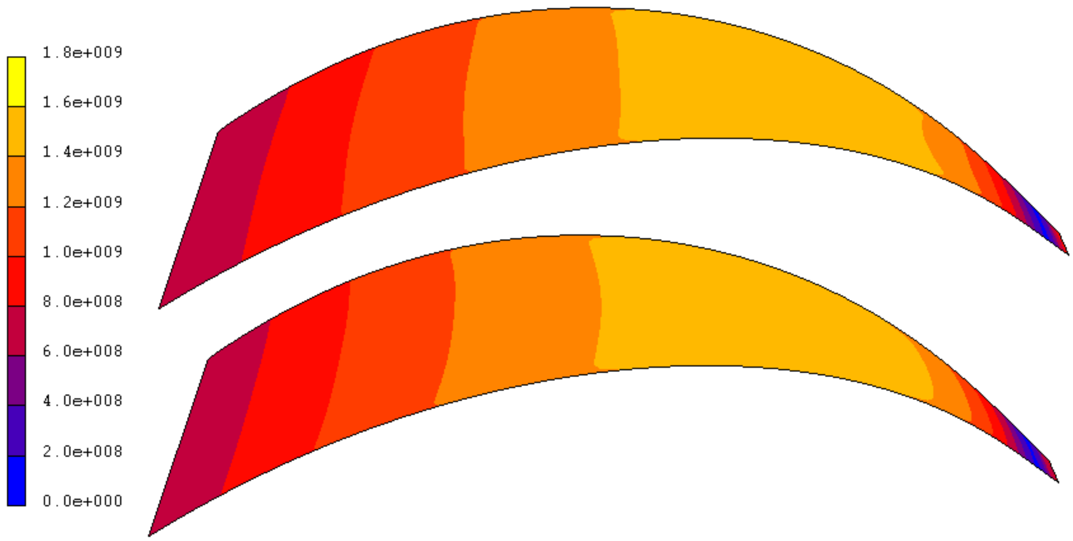

Figure 3.27: *Stress in the top (upper) and bottom (lower) surface of the GAS filter blades according to the finite element model for a Poisson ratio ν = 0. Without corrugation of the blade the stress is evenly distributed over the width of the blade. The maximum stress is 1.53 GPa.*

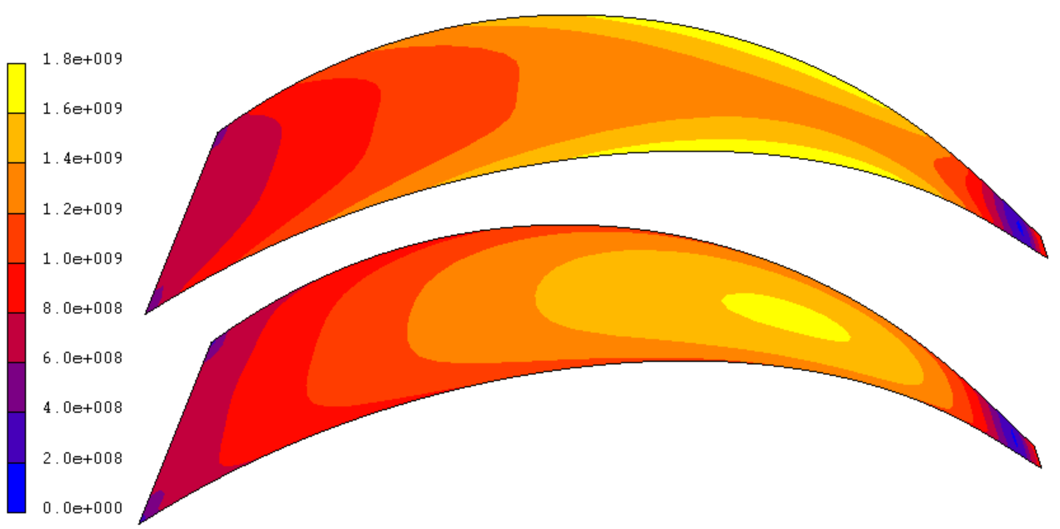

Figure 3.28: *Stress in the top (upper) and bottom (lower) surface of the GAS filter blades according to the finite element model for a Poisson ratio ν = 0.32. Due to corrugation of the blade the stress is reduced in the middle of the top surface and along the rim of the bottom surface. The stress is enhanced along the rim of the top surface and in the middle of the bottom surface. The maximum stress is 1.80 GPa in the top surface and 1.62 GPa in the bottom surface.*

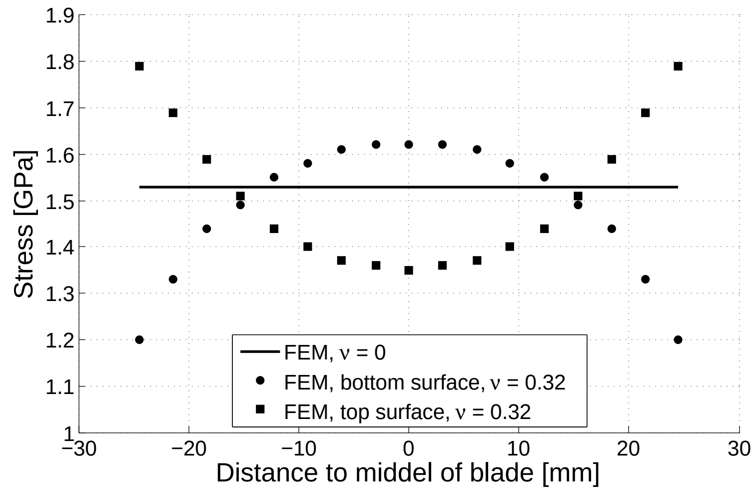

Figure 3.29: *Corrugation stress obtained with the FEM model. The FEM model with $\nu = 0$ gives 1.53 GPa. The blade shape measurements give a radius of curvature of 0.54 m, which gives a Von Mises stress of 1.29 GPa in the center of the top surface.This is in good agreement with 1.35 GPa predicted by FEM. The highest stress predicted by the FEM model is on the rim of the top surface and is 90% of the ultimate tensile strength of maraging steel.*

crystalline solids. When stress is applied to them, each grain elongates or gets compressed according to the local strain field. The dislocations inside the grain can be freed due to energy exchange with the thermal bath. They then travel through the crystal until they reach either the edge, or a *pinning point*.

Pinning points are nanometer-size structures that strongly bind the dislocations so that they need a relatively large energy to start moving again. Free dislocations that do not encounter a pinning point will accumulate at the interface of two crystals. In this way stress builds up between the crystals, weakening the bonds between them. Eventually, the body may deform [102].

Processing maraging steel

The GAS filter blades are made of Marval 18 maraging steel from Aubert & Duval. This steel contains 0.03% carbon, 18% nickel, 8% cobalt, 5% molybdenum and 0.5% titanium [93]. It is supplied in solubilized state; a solid solution of all the elements in iron. Crystals are in form of martensite. The material is ductile and can be machined easily.

The solid solution is stable at room temperature, but unstable above a few hundred degrees centigrade. After machining, the parts undergo a heat treatment to increase their ultimate tensile strength and lower their creep rate.

During the thermal treatment the metal ions can precipitate into the martensitic crystals forming a matrix of nanometer size precipitates (small crystals inter-metallic Ni-Ti and Ni-Co compounds) embedded into the iron grains. Typical distance between precipitates is 20-30 nm. The results of the heat treatment is that millions of nano-crystals are formed inside each 5-10 μm size iron grain. These precipitated nano-crystals provide pinning points for the dislocations. This is why the thermal treatment increases the ultimate tensile strength of the material.

The effectiveness of the heat treatment depends on the size and density of these nano-structures. Dedicated studies of the properties of maraging steel [94] resulted in the discovery of an effective heat treatment of the material.

The greatest increase in ultimate tensile strength of the material was obtained when the steel was heated to 435°C for 100 hours. Prolonging the heat treatment the size of the nano-structures would become too large and their density too low to effectively trap the dislocations.

Untreated, the ultimate tensile strength of Marval 18 maraging steel is 1.07 GPa. After administering the proper heat treatment it has an ultimate tensile strength of 1.97 GPa.

It was discovered that not only the ultimate tensile strength, but also the hardness of the material increased due to the thermal treatment. When the ultimate tensile strength was maximal, so was the hardness. The hardness could be used as a good indicator of the ultimate tensile strength. The hardness of the material on the Rockwell scale was 53 when the ultimate tensile strength was greatest.

Fig. 3.30 shows two photo's of the thermal treatment of the GAS filter blades and inverted pendulum flexible joints carried out at Nikhef. To prevent oxidation of the maraging steel parts, they were placed in a steel box through which argon was flowing during the thermal treatment. The temperature in the box was monitored with three thermal sensors (type K thermal couples chromel - alumel). Sensor 1 was placed in the back of the furnace, sensor 2 in its front and sensor 3 between the maraging steel parts.

Hardness of the blades

The hardness of the blades was measured before and after the thermal treatment with an Otto Wolpert-Werke Dia testor 2n. Fig. 3.32 shows the results of these measurements.

Before the thermal treatment the average Rockwell hardness of the blades was 32.5. After the thermal treatment the average Rockwell hardness was 54.7, the lowest was 52.8 ± 0.8 and the highest was 56.4 ± 0.8. As a Rockwell hardness of 53 should correspond to an ultimate tensile strength of 1.97 GPa we are confident that the thermal treatment was successful and the ultimate tensile strength of the blades is high enough to withstand the stresses they will have to endure in EIB-SAS. (In section 3.5.5 we will see that according to our FEM model the stress can be as high as 1.8 GPa.)

After their heat treatment all maraging steel parts undergo nickel flash plating to protected them from corrosion.

(a) **(b)**

Figure 3.30: *Photo's of the heating treatment equipment. a) The maraging steel GAS filter blades and IP flexible joints are put in an air-tight box, which is welded shut. b) The box is placed in an oven (right) and argon is flushed through the box to prevent oxidation of the maraging steel parts.*

Minimizing the creep rate

The creep rate $\dot{\epsilon}$ is defined as the fractional elongation per unit time. It can be expressed in the form of an Arrhenius law: $\dot{\epsilon} = A\sigma^{\mathsf{m}} \exp(-E_{\mathsf{a}}/k_{\mathrm{B}}T)$, where σ represents the constant applied stress, T the absolute temperature, k_{B} the Boltzmann constant, while A and m are constants that depend on the material and on its microscopic structure, and E_{a} the activation energy (threshold) [103]. The activation energy for a dislocation is the energy threshold necessary to pass over an obstacle, *e.g.* another dislocation or a pinning point.

According to the Arrhenius formula, the change in reaction rate due to a 1 K temperature increase is given by $\partial\dot{\epsilon}/\partial T = \dot{\epsilon}\,(1 + E_{\mathsf{a}}/k_{\mathrm{B}}T^2) = \dot{\epsilon}\; C_{\mathsf{arr}}$, where C_{arr} is known as the *Arrhenius acceleration factor* or *time acceleration factor*. Increasing the temperature with ΔT increases the creep rate with a factor $C_{\mathsf{arr}}^{\Delta T}$.

For maraging steel at room temperature, $E_{\mathsf{a}} = 2 \pm 1$ eV and $C_{\mathsf{arr}} = 1.28 \pm 0.13$ [103]. Increasing the temperature from 20 to 65°C increases the creep rate by over four orders of magnitude.

In heat treated maraging steel, the precipitates that prevent dislocations to travel all across a grain will pile-up at its boundary and cause grain slippage. When stress is applied a few grain slippages may occur at an early stage until all the dislocations are trapped by the precipitates. Then, unless the stress level is increased or the temperature is raised, the creep rate decreases to a negligible level.

Dedicated studies by the Virgo collaboration [102] showed that accelerated aging of the maraging steel filters eliminates (nearly) all dislocations and lowers the creep rate to

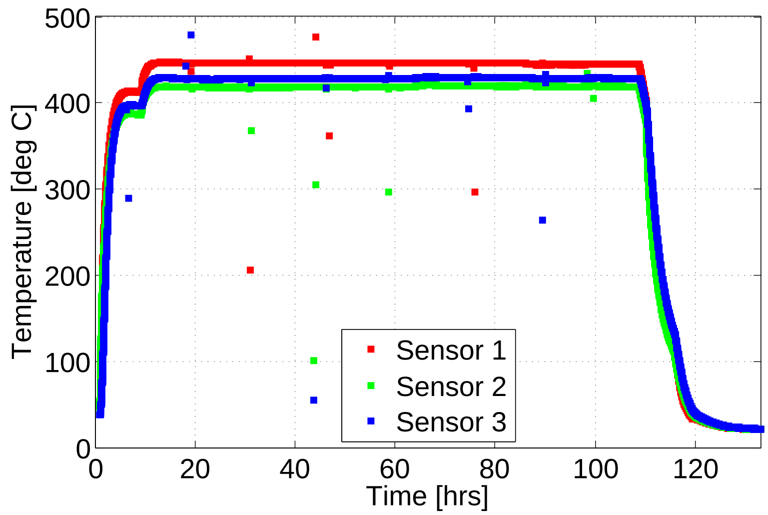

Figure 3.31: *The temperature of the GAS filter blades and IP flexes during the heat treatment. They were heated to 435°C for 100 hours to harden the maraging steel and to reduce its creep. The temperature was monitored with three chromel-alumel thermocouples. Sensor 1 was positioned in the back of the furnace, sensor 2 in its front and sensor 3 close to the maraging steel parts.*

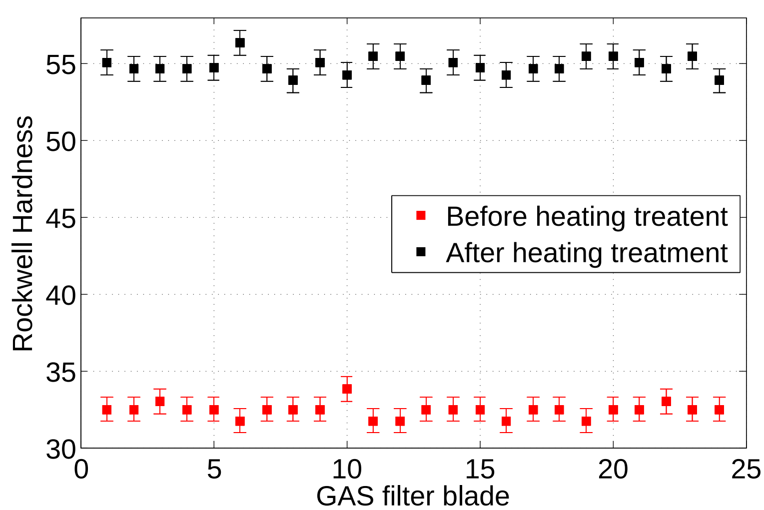

Figure 3.32: *Rockwell hardness of the blades before (red markers) and after (black markers) the heating treatment. Their hardness was measured with an Otto Wolpert-Werke Dia testor 2n. The size of the error bars is ± 0.8.*

negligible levels in a matter of days in what would otherwise take decades or even centuries at room temperature. Therefore the assembled filters have undergone such a heating treatment. Fig. 3.33 shows the filter temperature during the heating process. The filters were aged in an oven at Nikhef at 65°C for nearly 40 hours, which is equivalent to aging for over 128 years at room temperature.

(a)

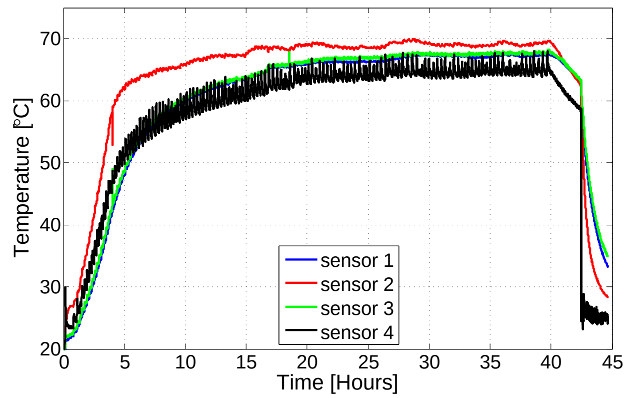

(b)

Figure 3.33: *Heat treatment of the assembles GAS filters to eliminate their creep. a) The assembled filters are placed in an oven and heated to 65 °C for 40 hours. This process increases the creep rate by several orders of magnitude and eliminates all dislocations and therefore all creep. b) The temperature of the filters was monitored with four chromel-alumel thermo-couples.*

3.5.7 GAS filter experimental characterization

Tuning the EIB-SAS GAS filters

Fig. 3.34 shows two load-height curves of one of the GAS filters. The first was measured loading the filter (dots), the second unloading it (squares). Apparently, the height of the keystone does not only depend on the instantaneous load, but also on the load history. Dependence of a system's behavior on its history is known as hysteresis.

The slope of the load-height curve is a measure for the stiffness of the filter. The filter's frequency is given by $f = 1/2\pi \times \sqrt{k/m}$. The two load curves would give different values for this stiffness and resonance frequency. In section 6.6 it will be shown that the correct stiffness and resonance frequency can be obtained while taking hysteresis into account.

Comparison between experimental results and model predictions

Fig. 3.35 shows the frequency of the three EIB-SAS GAS filters as a function of difference between their working point and their equilibrium position together with the model of

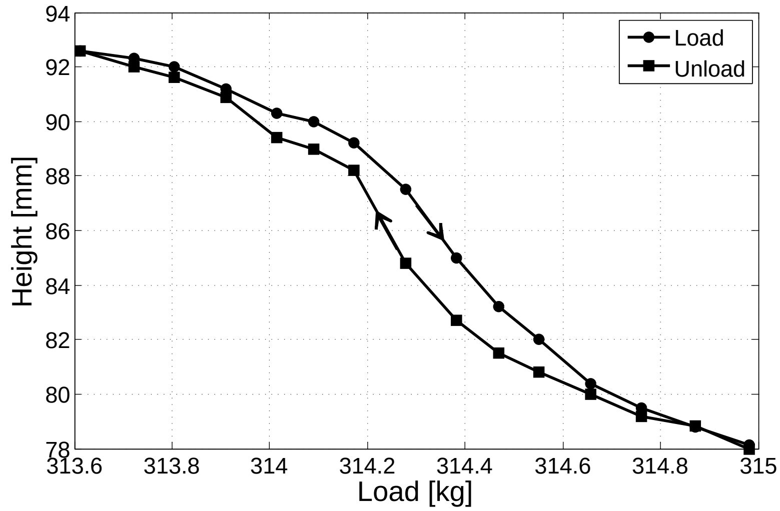

Figure 3.34: *Hysteresis in maraging steel GAS filter blades. The height of the keystone of the filter with Type-A blades (EIB-SAS) as a function of its load for increasing weight (dots) and decreasing weight (squares). There is a clear difference between loading and unloading the filter, which implies that the filter exhibits hysteresis.*

section 3.5.4 with the parameter values of Table 6.2. At their working point, all three filters have a resonance frequency of 387 mHz.

Fig. 3.36 shows measured height frequency curves of a single GAS filter for two values of its compression, together with the model predictions. The measured compression rate of the filters is 0.0915 and 0.0926. The model describes the data well if the compression rate is set to 0.1024 and 0.1033, which is about 10% higher than the experimental value. Also, the model predicts a normalized blade tip height $y_{\mathsf{L}}/l_{0\mathsf{x}} = 0.091$, while in reality it is 0.109. For this parameter the simulated value is 20% too low. The values of the measured and modeled parameters are listed in Table 3.8.

Property	Experimental value	Simulation value
Resonance frequency f_0	387 mHz	387 mHz
Load m_0	314, 317 and 323 kg	326 kg
Compression rate K	0.0915	0.1024
Normalized blade tip height $y_{\mathsf{L}}/l_{0\mathsf{x}}$	0.109	0.091
Blade−base plate clamp angle θ_0	45°	45°
Blade−keystone clamping angle θ_1	-33°	-33°

Table 3.8: *GAS filter and blade parameter values from experiment and model.*

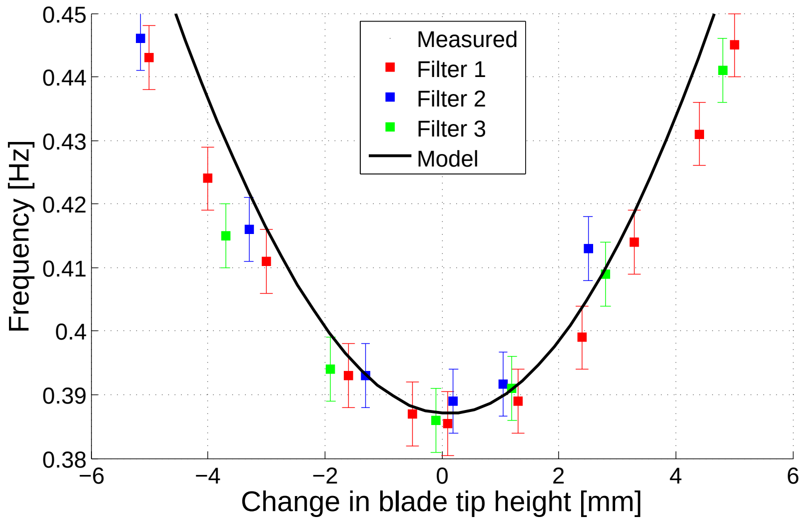

Figure 3.35: *Measured and modeled height-frequency curve of the three GAS filters. Varying the load of the GAS filters changes the equilibrium position and thus the stiffness of the filter. In the working point the frequency has a minimum of 387 mHz. The data agrees well with the model of section 3.5.4.*

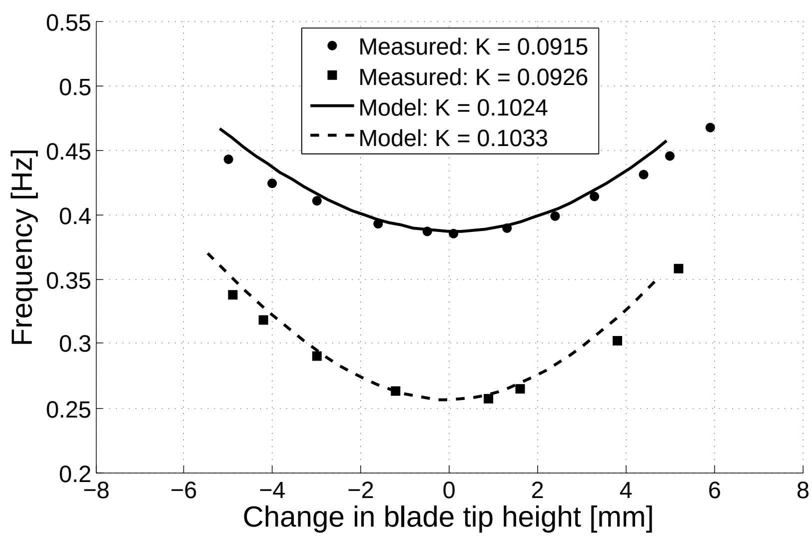

Figure 3.36: *Load-frequency curves of one of the GAS filters at different compression rates K. The markers correspond to the results of the measurements, the curves represents the model of section 3.5.4.*

There are a number of known effects that could cause the observed difference between the experimental and simulated values listed in Table 3.8.

In section 3.5.5 we saw that due to the Poisson effect the Young's modulus of the maraging steel blades increases. In the plane-strain condition (the strain across the blade = 0) the predicted load of 326 kg is higher than the actual load of the filter ∼315 kg. Without the Poisson effect the predicted load was 293 kg. In reality the plane strain condition will not be fully fulfilled and the predicted loads should be taken as upper and lower bounds. As far as the load is concerned, the model agrees well with our measurement.

The manufacturer delivers maraging steel sheets that have been rolled to 3 ± 0.2 mm The maraging steel blades are cut from these sheets and ground down to a thickness of 2.4 mm ± 10 μm. As the stiffness of the blades is proportional to d^3, the 0.5% error in the thickness of the blades causes a 1.5% error in the stiffness of the blade. The load of a filter is approximately 320 kg, so a difference in required load of the filters up to 5 kg should be expected. In section 3.5.7 we will see that indeed the load needed to tune the GAS filters to the same frequency differs from filter to filter by as much as 8 kg. However, for this to be caused by an increased thickness, each of the 8 blades of the filter would have to be relatively thick.

The second effect is an effect of different amounts of pre-stress in the blades. The sheets from which the blades are made, are flat. They remain flat due to a non-uniform internal stress field. If the thickness of the steel would be decreased enough, the blades would warp due to this internal stress. Because of the different amounts of pre-stress in the blades, their stiffnesses differ.

Finally, there is a deviation in Young's modulus of our maraging steel. According to the manufacturer the Young's modulus of the blades' steel is 1.86 GPa. An error of 1% in this value would change the stiffness of the GAS filters by 1%.

Transfer function measurement of a single GAS filter

To measure the transfer function of the GAS filter we suspended it from a stiff frame with four helical springs. A speaker was used to drive the base plate of the filter in the vertical direction at the desired frequency. A dummy load of 316.6 kg was suspended from the filter which was tuned to 290 mHz. The movement of the base plate of the filter and of the dummy load were measured with Wilcoxon accelerometers type 731-207. Fig. 3.37 shows a photo of the setup.

Making a swept sine excitation of the filter we measured the transfer function shown in Fig. 3.38. The measurement clearly shows the resonant peak of the GAS filter at 290 mHz, with a Q-factor of 10. Above this frequency it falls of with f^{-2} up to 10 Hz. The transfer function reaches a plateau of 4.0×10^{-4} at 40 Hz. Above 55 Hz a number of resonances are visible. These do not belong to the GAS filter, but to the frame from which the filter is suspended.

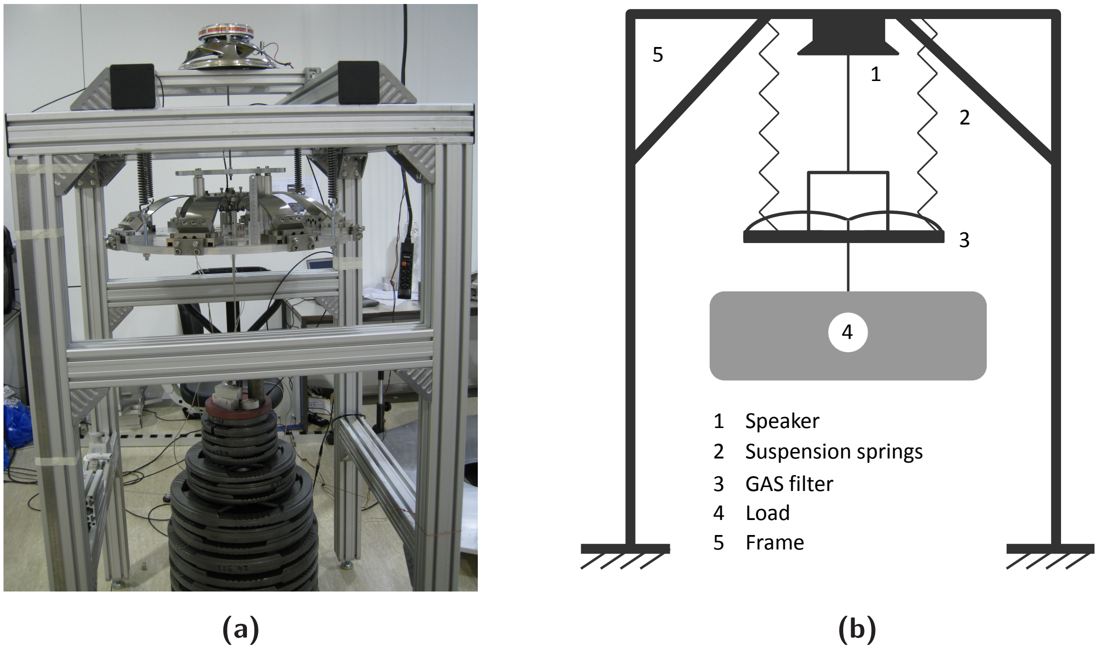

Figure 3.37: *Setup to measure the transfer function of a GAS filter. a) Photo. b) Schematic representation. The filter is suspended from a stiff frame with four springs. The base plate of the GAS filter is driven by means of a loudspeaker. The relative motion of the base plate and the load gives the transfer function.*

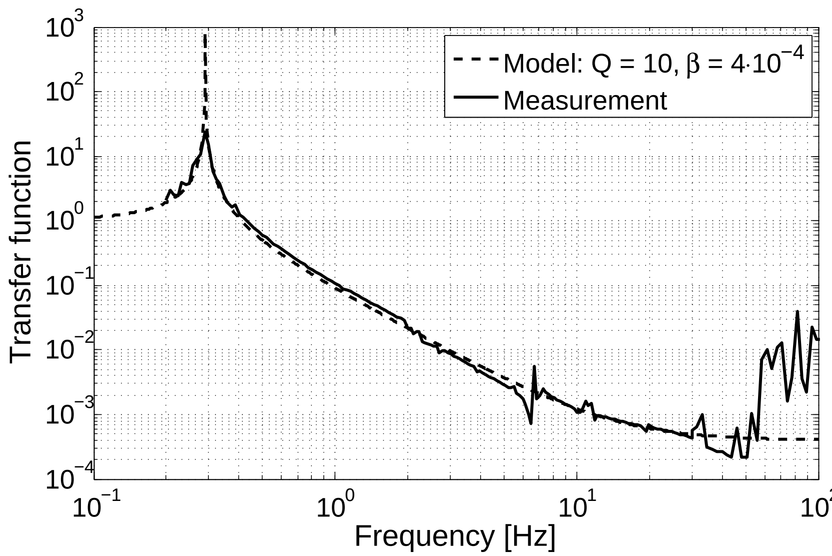

Figure 3.38: *Modeled and measured transfer function of a GAS filter. The filter is tuned to 290 mHz. The Q-factor of the resonance is 10. The transfer function decreases with f^{-2} as expected and levels off at 4×10^{-4}. The structure above 50 Hz do* not *belong to the GAS filter, but to the transfer function measurement setup.*

Stress level measurement

The shape of all 8 blades of two GAS filters have been measured with a precision better than 10 μm with a Wenzell CMM 3D-measuring machine. The local radius of curvature of the blades at $(x(\lambda), y(\lambda))$ can be obtained from these measured coordinates. Referring to Fig. 3.39, θ_1 and θ_2 are the slopes of the tangent lines of the neighboring points of $(x(\lambda), y(\lambda))$, α is their difference and U is the absolute distance between the points. The local radius of curvature is then given by $R = 1/\alpha U$ and the local stress $S = Ed/2R$.

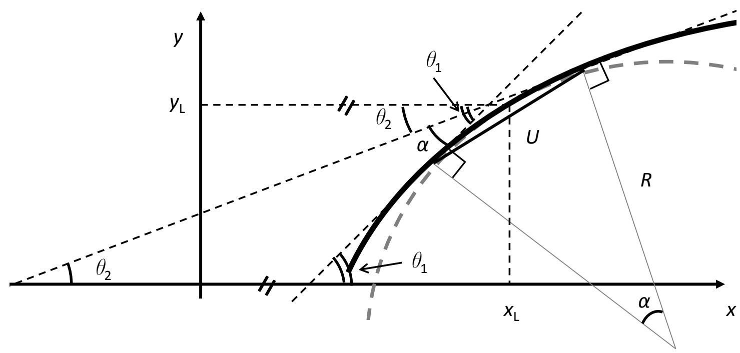

Figure 3.39: *Calculating the local radius of curvature from the measured blade shape. The radius of curvature in $(x(\lambda), y(\lambda))$ can be calculated by looking at the difference between its neighboring points. The absolute distance between the points is U, the change in slope is $\alpha = \theta_1$ - θ_2. The local radius of curvature R is given by $R = 1/\alpha U$.*

Fig. 3.40 shows the results of these measurements together with the numerical solution of Eq. (3.45) and a shape predicted by our FEM model (see section 3.5.5). There is good agreement between the measured shape of the GAS filter blades and those obtained from the numerical and FEM model.

Fig. 3.41 shows the radius of curvature along the blade obtained from the measured blade shape, and given by the numerical and FEM model. The minimal radius of curvature occurs at $x/L =$ 0.7. This is where the stress in the blade will be highest. At $x/L =$ 0.96 the radius of curvature is infinite. At this point the blade shape changes from concave to convex and the stress in the blade will be 0.

The stresses calculated from the measurements and those predicted by the numerical and FEM model are given in Fig. 3.42. The maximum stress in the GAS filter blades is 1.45 GPa according to the measured blade shapes, 1.48 GPa according to the numerical blade shape model, and 1.53 GPa according to the FEM model. This is approximately 75% of the ultimate tensile strength of maraging steel.

The maximum stress predicted by the FEM model is higher than that based on the measurement of the blade's bending profile. At the ends of the blades it predicts a lower stress. This is probably due to the compliance of the base plate. During the blade shape

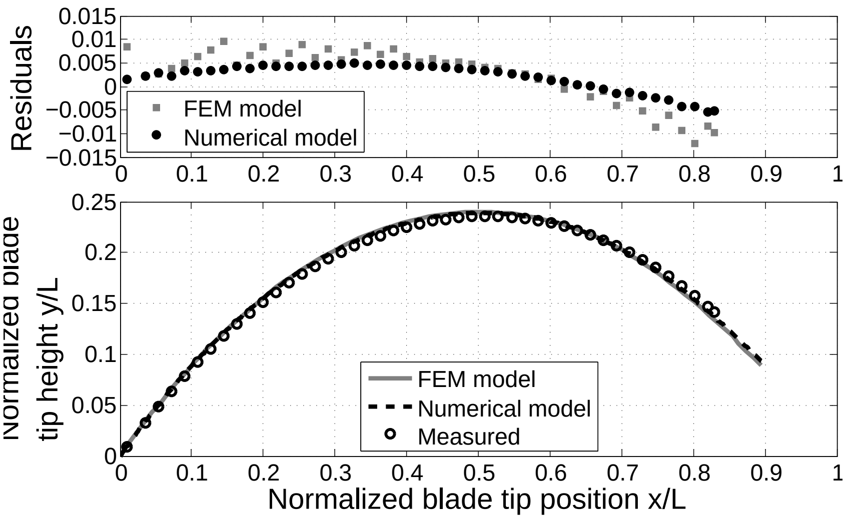

Figure 3.40: *Measured, modeled and calculated blade shape of the GAS filter blades. The shapes of the blades of two GAS filters have been measured with a Wenzell CMM 3D-measuring machine. The black dots represent the average shape of the 16 blades. The black dotted curve represents the numerical solution of Eq. (3.45) with the boundary conditions of Table 3.8. The gray curve represents the shape obtained from our finite element model. The residuals between the data and the FEM model (gray dots) and the numerical model (black squares) are also shown.*

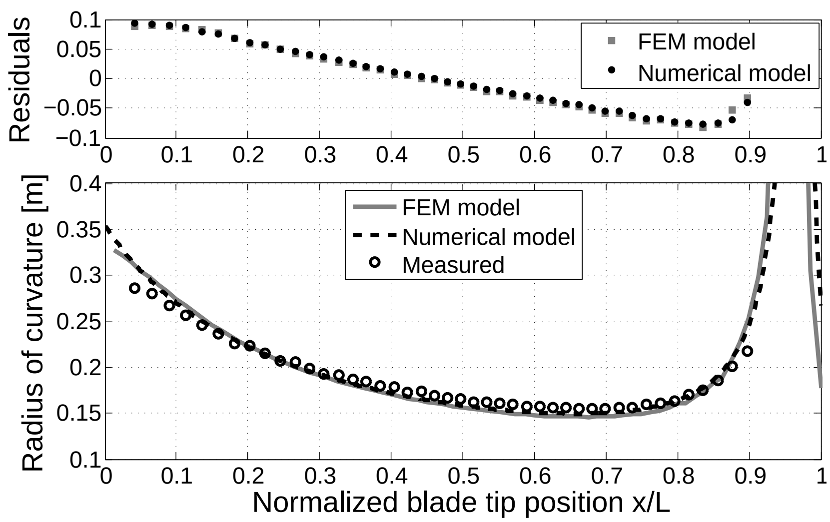

Figure 3.41: *Radius of curvature of the GAS filter blades. The radius of curvature is given by the second derivative of the blade shape, which was given in Fig. 3.40. The gray curve represents the radius of curvature according to the numerical model, the black dotted curve those according to the finite element model and the black dots those calculated from the blade shape measurement. At $x/L = 0.96$ the radius of curvature goes to infinity. This is where the blade goes from concave curvature to convex curvature. The residuals between the data and the FEM model (gray dots) and the numerical model (black squares) are also shown.*

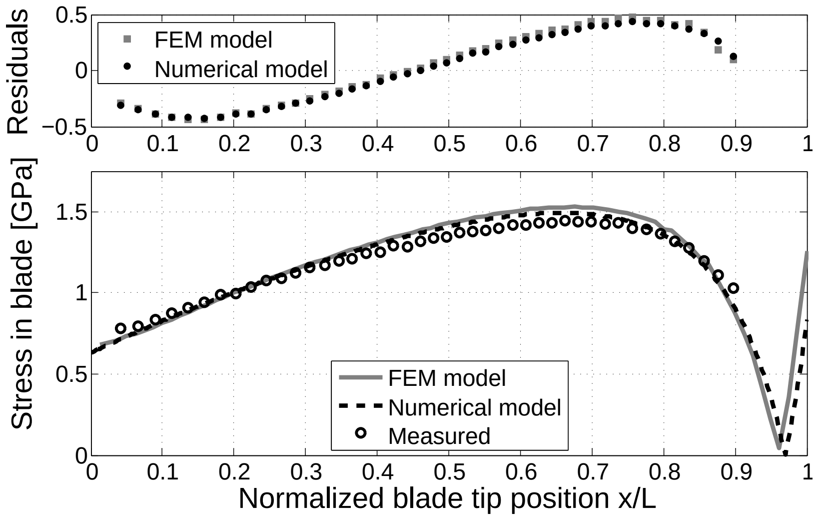

Figure 3.42: *Stress in the GAS filter blades. The stress S in the blades is given by $S = Ed/2R$, where E is the Young's modulus, d the thickness and R the radius of curvature of the blade. The dashed curve represents the stress predicted by the numerical model, the gray curve the one predicted by the finite element model and the open dots the stress calculated from the blade shape measurement. The maximum stress occurs at x/L = 0.7 and is 1.45 GPa, which is approximately 75% of the ultimate tensile strength of maraging steel. The residuals between the data and the FEM model (gray dots) and the numerical model (black squares) are also shown.*

measurement, the filter is laying freely on the 3D measuring machine and the blades bent the base plate. In EIB-SAS the filter is bolted to the structure, which stiffens the base plate.

Stress level measurement including Poisson effect

The shape along the width of the GAS filter blades under stress have been measured. These measurements, which are shown in Fig. 3.43, are used to calculate the radius of curvature due to corrugation of the blade R_{corr}. As shown in Fig. 3.44, denoting the horizontal distance between the two sides of the blade with Z and the vertical distance between the blade's center and its edge as δ is, $R_{\text{corr}} = Z^2/8\delta$.

For the EIB-SAS GAS filter blades Z = 0.300 m and δ = 200 µm. The radius of curvature due to corrugation is 0.54 m. From this radius of curvature we can calculate the stress due to corrugation which is given by $S = Ed/2R_{\text{corr}}$. The stress in the center of the top surface of the blade due to corrugation is -0.41 GPa.

The blade shape measurements without corrugation indicated a maximum stress of 1.45 GPa. The two stresses calculated from the blade shape measurement and corrugation measurement can be combined into a single value of the Von Mises stress σ_{v} (see section 3.5.5). The stress σ_{v} in the top surface of the EIB-SAS blades is 1.29 GPa. This

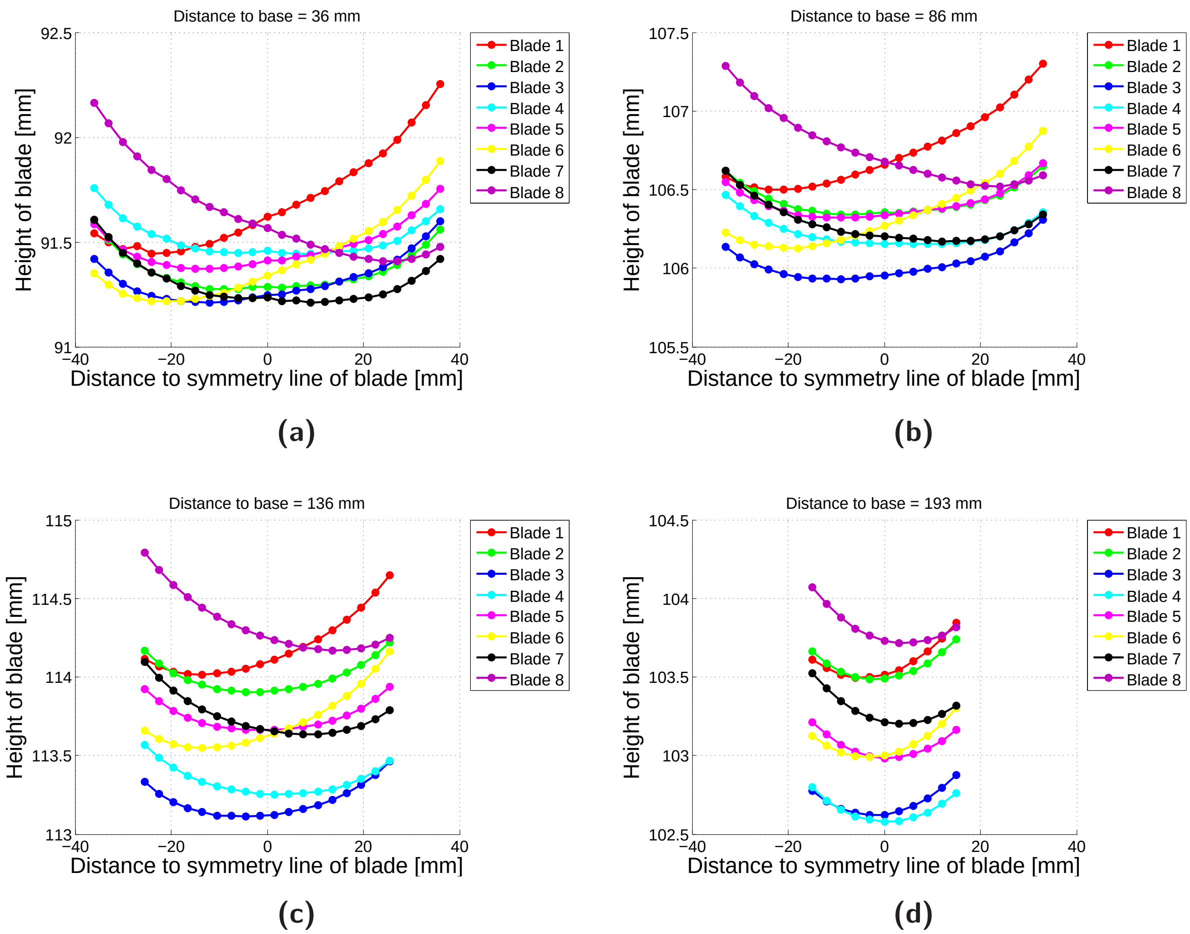

Figure 3.43: *Corrugation measurement. The blade shape along the width of the blade has been measured at several places along the blade. The plot in (d) contains the measurement along the line of minimum stress in the blade top surface. From these measurements the local radius of curvature due to corrugation can be calculated. At the minimal stress point on the upper surface of the blade this radius of curvature is 0.54 m.*

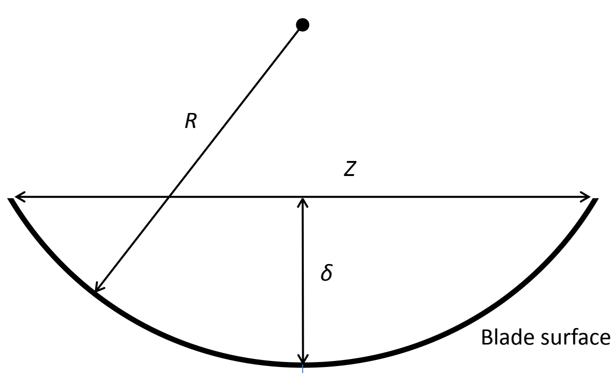

Figure 3.44: *Calculation of the radius of curvature due to corrugation of the blade. Given the horizontal distance between the edges of the blades Z and the height of the edges compared to the middle of the blade δ, the radius of curvature R due to corrugation of the blade is given by $R = Z^2/8\delta$.*

agrees well with the 1.35 GPa predicted by the FEM model (see section 3.5.5). The stresses predicted by the numerical and FEM model as well as those calculated from the radius of curvature measurements are summarized in Table 3.9.

Source	Maximum stress (GPa)	
No Poisson effect	Entire blade	
Numerical model	1.48	
FEM model	1.53	
Measurement	1.45	
Including Poisson effect ($\nu = 0.32$)	Bottom surface	Top surface
FEM model	1.80	1.62
Measurement*	n.a.	1.29

Table 3.9: *Summary of the stresses in the blades according to the models and measurements.*

Thermal stability measurements

Fig. 3.45 shows three load curves of an EIB-SAS GAS filter measured at 16.0, 20.1 and 24.2 °C. Increasing the temperature by 8.2 °C lowers the load needed to get the filter in its working point by 0.9 kg. Also, the minimal frequency of the filter increases by 15 mHz.

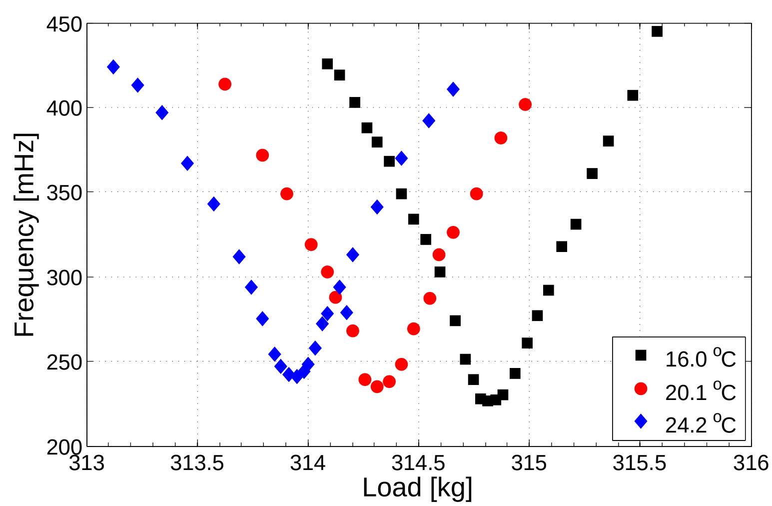

Figure 3.45: *Load frequency curve of an EIB-SAS GAS filter at different temperatures. Increasing the temperature increases the minimal frequency of the filter and reduces the load it can support.*

*This measurement gives the stress in the central region of the top surface of the blade. The maximum stress will occur at the rim. The FEM model predicts a stress of 1.35 GPa at this location.

In section 3.5.3 we reasoned that a relative change in Young's modulus due to a temperature change is equivalent to a load change at fixed temperature. Therefore, the temperature change of 8.2 °C in the measurement should lower the needed load by $M\Delta E/E = -2.54\times10^{-4}\times 320 = 0.67$ kg. This agrees well with the 0.9 kg from the measurement.

Furthermore, $\Delta\omega = 1.95 \times 10^{-2} \times \Delta T/\omega_0$. During this measurement the GAS filter was tuned to a frequency of 235 mHz. So we find that $\Delta\omega = 17.3$ mHz, which agrees well with the 15 mHz from the measurement.

3.5.8 Modal analysis of the GAS filter

As for the inverted pendulums (see section 3.4.6), tests to determine the modal composition of the GAS filters were carried out. The frequencies of the modes were measured with tapping tests and a FEM model of the filter was created for a better understanding of their origin.

Fig. 3.46 shows three amplitude spectral density plots obtained from tapping tests performed on three different blades of one filter. The spikes at 150, 250, 350 Hz have all been measured in blade 3 and are picked up from the power grid. All three spectra show a large peak between 344 and 350 Hz. They have a second resonance peak at 588 Hz measured in all three blades. Finally, all three blades have resonances at 692, 711 and 725 Hz.

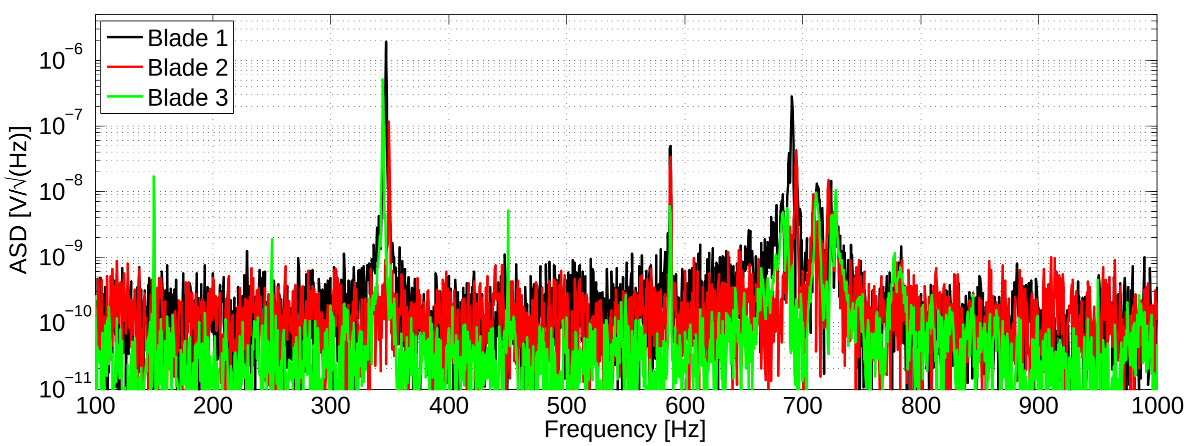

Figure 3.46: *GAS filter amplitude spectral densities obtained from tapping tests performed on three different blades of the same filter. The blades were excited with a small hammer. The motion of a small magnet attached to the filter blades is sensed with a coil. Modes were measured at 344 – 351 Hz, at 588 Hz and between 692 and 725 Hz.*

Finite element model of the GAS filter

In our FEM model [97] of the EIB-SAS GAS filters, the blades of the filters have been modeled by 160 quadratic shell elements. The tips are rigidly connected to the keystone, which has a mass of 0.5 kg and a diameter of 73.6 mm. The most important difference between the FEM model and the real system, is that only a single "free" filter has been modeled, while in EIB-SAS the keystones of the three GAS filters are connected by the top plate and optical bench. Some of the modes of the modeled GAS filter should be suppressed by this connection between the filters. Indeed the first three modes (those with lowest frequency) predicted by the FEM model have not been observed in the tapping test.

The lowest mode predicted by the FEM model is at 78 Hz where the blades move together which results in a swinging of the keystone. Second, at 313 Hz a mode is predicted where the keystone rotates in the horizontal plane, but does not perform any translational motion. Third, at 445 Hz a mode is predicted where the blades not only bend, but also twist, which results in rotations of the keystone around multiple axes.

These modes have not been observed in the tapping test. We believe that they are suppressed due to the rigid connection between the keystones when the tapping tests were performed on the filters *in* EIB-SAS. They should then only be observed in a tapping test performed on a single suspended filter. The rest of the modes predicted by the FEM model can be linked to the modes measured in the tapping tests.

At 349 Hz the filter has a mode where the keystone does not perform any rotation, nor translation (Fig. 3.47). This frequency corresponds to the internal modes of the blades. This mode has been observed in the tapping test at 344.0, 346.5 and 349.5 Hz.

At 500 Hz the filter has modes where the blades rotate in the same direction and the keystone in the opposite direction. We believe this mode is the 588 Hz mode measured in the tapping test. Because this mode is more a coordinated movement of the entire filter and not an internal blade mode, we would expect to measure it at the same frequency when tapping different blades. All three blades that were involved in the tapping test showed a mode at precisely 588 Hz. The frequency of this mode is underestimated by the FEM model, which means that it underestimates the stiffness of the keystone. As mentioned before, the keystone of the modeled filter is not attached to anything. In reality, it attached to the bench which increases its rotational stiffness and hence the frequency of the mode.

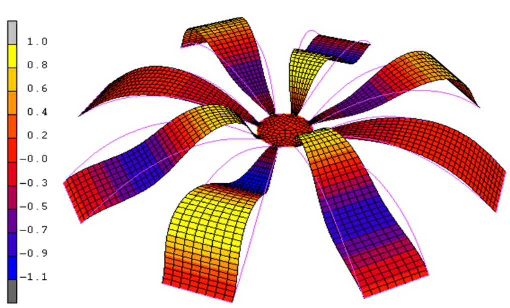

Figure 3.47: *High frequency GAS filter modes are predicted by our FEM model. Depicted is the 348 Hz mode.*

At 722 Hz the filter has modes where some of the blades again bend and twist and some remain stationary, without translating or rotating the keystone. In the tapping test we measured several modes between 690 and 728 Hz. Seven discrete frequencies in total. These could correspond to this 722 Hz FEM mode. The mode would be degenerate due to differences between the blades. Not all seven frequencies have been measured in all three blades, because not all blades participate in all degenerate modes. A summary of the modes and their frequencies is given in Table 3.10.

Mode	Frequency (Hz)			
	FEM	Tapping test		
		Blade 1	Blade 2	Blade 3
Internal blade modes, keystone stationary	348	346.5	349.5	344
Coherent torsion of all blades and keystone	500	588	588	588
Modes including blade twist	722	691, 694 712 724 728	694 709, 712 722, 728	- 712 728

Table 3.10: *Summary of frequency of GAS filter modes. The FEM model predicts modes for a single filter. In EIB-SAS the keystones of the filters are connected by the top plate, which increases the stiffness of the rotational degrees of freedom. Therefore, the modes in which the keystone performs a rotation are suppressed.*

3.6 Summary

EIB-SAS has been designed to provide seismic isolation for the Advanced Virgo external injection bench. The system is based on the AEI-SAS system of the Albert Einstein institute in Hanover, which was, in turn, derived from a prototype device (HAM-SAS) constructed for R&D purposes at Caltech.

EIB-SAS comprises three inverted pendulums and three geometric anti-spring filters that provide seismic isolation for the horizontal respectively vertical degrees of freedom. These filters are mechanical resonators whose transfer functions roll of with f_0^2/f^2, where f_0 represents the resonance frequency of the filter and f the frequency.

The stiffness of the filters comes from elastic, maraging steel elements: blade springs for the GAS filters and flexible joints for the inverted pendulums. An anti-spring effect is employed to tune their resonance frequencies to values between 0.2 and 0.5 Hz. For the GAS filters, this anti-spring effect is provided by the tension in the blades, and for the inverted pendulums by the gravitational pull on their load. The resonance frequency of the inverted pendulums have been tuned to 220 mHz and those of the GAS filters to 390 mHz. In this configuration the seismic isolation goals are met, while the robustness of the system is maximal.

Analytical models of the filters have been introduced, which allow us to calculate their resonance frequencies as a function of their load, and in case of the GAS filters, as a function of their compression. These frequencies have been measured and agree well with the model predictions. The vertical transfer function of a single GAS filter has also been measured and is well described by the model.

Finite element models of the GAS filter blades and the inverted pendulum's flexible joints have been created to determine their stiffnesses and the internal stresses they have to endure. Due to an unforeseen compliance of the inverted pendulum leg the stiffness of the IP was lower than initially predicted. Therefore, the inverted pendulums have been fitted with thicker, stiffer flexible joints and their aluminum tubes have been replaced by thicker stainless steel ones.

For the GAS filter blades, the stress predicted by the FEM model can be compared to a numerical model as well as to measurement results. They show that the maximum stress in the blades can reach values that are about 75% of the ultimate tensile strength of maraging steel.

However, up to now the influence of the Poisson ratio on the operations of GAS filters have not been considered. Consequently, the stresses in the maraging steel blades has been underestimated significantly. We have carried out FEA calculations that for the first time included such effects. If the Poisson effect is included, then the FEM model predicts a maximum stress in the blades of 1.80 GPa, which is 90% of the ultimate tensile stress.

For a given thickness, the stress distribution in the blades depends on the width profile of the cantilever blades. New blade shapes have been designed in which the stress distribution has been optimized and hence, the maximum stress that occurs has been minimized. These new GAS filter blades are further described and characterized in chapter 6.

Temperature changes induce a differential thermal expansion of the maraging steel blades and aluminum base of the GAS filters. This alters the compression of the blades and therefore the resonance frequency and equilibrium point of the filters. The vertical degree of freedom will be affected strongest by temperature changes. In uncontrolled state, the vertical position of the bench would change by $-415\ \mu\text{m}/^{\circ}\text{C}$, with the controls engaged these excursions will be reduced.

Finally, modal analyses of the inverted pendulums and GAS filters have been performed and compared to the FEM model predictions. The observed frequencies of the internal modes are close to the predicted values. The internal modes of the inverted pendulum legs have frequencies between 160 and 500 Hz. Eddy current dampers have been fitted in the top of the inverted pendulums to lower the quality factors of these modes. The GAS filters are rigidly connected to the bench which suppress modes that involve rotations of the keystones.

Therefore, the lowest frequency modes predicted by the FEM model have not been observed in the measurements. The first internal modes observed in the GAS filter spectra are internal modes of the cantilever blades and have frequencies between 340 and 350 Hz. These modes do not need to be damped.

4 | Full system model

"That faith makes blessed under certain circumstances, that blessedness does not make of a fixed idea a true idea, that faith moves no mountains but puts mountains where there are none – a quick walk through a madhouse enlightens one sufficiently about this."
– Friedrich Nietzsche,
The Antichrist, section 51 (1895)

4.1 Introduction

In chapter 3, the internal modes of the GAS filters and inverted pendulums have been modeled and results of measurements were presented. The observed values of the modes are in good agreement with the values predicted by the FEM models. In addition to these internal modes, the compliance of the mechanical filters allows for a number of high-frequency rigid body modes that will be addressed in this chapter.

EIB-SAS can be modeled as a system composed of two rigid bodies: the springbox and the bench, each with six degrees of freedom. Therefore, twelve rigid body modes are expected: six low-frequency modes (< 1 Hz, due to the tuning of the IPs and GAS filters) where the two bodies move in-phase and six higher-frequency modes, where they move out-of-phase.

The modes will be coupled. For instance, due to the compliance of the GAS filters and the inertia of the optical bench, horizontal translation of the springbox will not only induce a translation of the bench in that direction, but also a rotation around the orthogonal horizontal axis.

In this chapter, we will first set out to predict the frequencies of the high-frequency rigid body modes with the aid of a FEM model. Then, to further our understanding of these modes and their couplings and aid us in our measurements, a number of Lagrangian models are introduced. In this chapter we will report the results of our models and compare them to the measurements results.

4.2 FEM model

To facilitate making a modal analysis of EIB-SAS, a finite element model was created [97]. The system was modeled as two rigid masses connected to each other and to the ground by a number of light flexible elements: the IP legs, the IP flexures and the GAS filter blades. Fig. 4.1 shows a rendering of the EIB-SAS model.

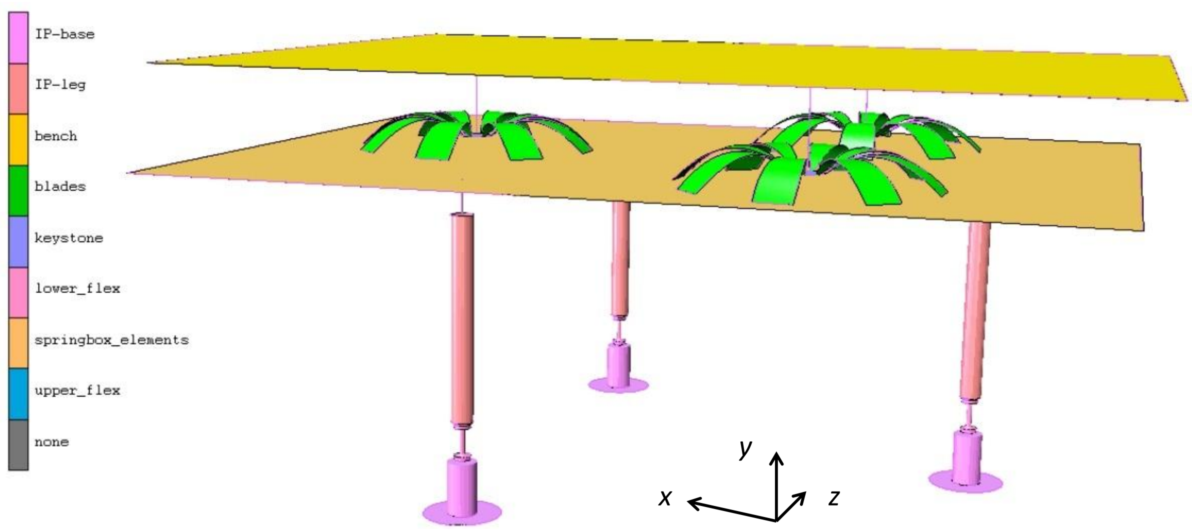

Figure 4.1: *Schematic representation of the finite element model used for the modal analysis. The load of the IP leg on the right is about 90 kg heavier than the other two.*

The IP legs and flexible joints are represented by appropriate flexible beam elements. The bench, springbox, GAS filter blades and keystones are represented by shell elements of appropriate thickness and density. The GAS elements are the only flexible ones.

In this model, the GAS blades are not pre-stressed. The 6 $\times$ 6 stiffness matrix of a real, pre-stressed GAS filter turns out to be practically the same as in the non-pre-stressed case, except for the vertical element (k_{yy}). The vertical stiffness of the filter is lowered significantly by the stress in the blades, as it should. To account for this effect, a vertical spring with the appropriate negative stiffness has been added between keystones and springbox. As a consequence, the gravitational load of the bench is not acting on the keystones, but on the springbox.

The mass distribution of the bench reflects the experimental prototype setup. Point masses have been added to account for mass concentrations. Due to the asymmetry in the horizontal position of the GAS filters, the IP legs are not loaded equally: the single front leg carries about 90 kg more than the other two legs.

4.2.1 Modal analysis

Low-frequency modes

The FEM model predicts six low-frequency modes with natural frequencies between 0.1 and 0.5 Hz listed in Table 4.1. Their values are determined by the stiffness of the IPs and GAS filters as well as the mass and inertia of the bench and springbox. In the FEM model the stiffness of the flexible joint and GAS filter are tuned to match the measured mode frequencies. As expected, the *Tx* mode has the higher frequency, because the moment of inertia of the bench is smaller around the *x*-axis.

Fig. 4.2 shows the six low frequency modes. According the FEM model, the vertical (*y*) motion does not couple strongly to the other degrees of freedom; only the green curve has a peak at 460 mHz. The coupling between *z* and *Ty* is always large due to the asymmetrical load of the IPs. As expected, the coupling between *x* and *Tz* and between *z* and *Tx* are also sizable.

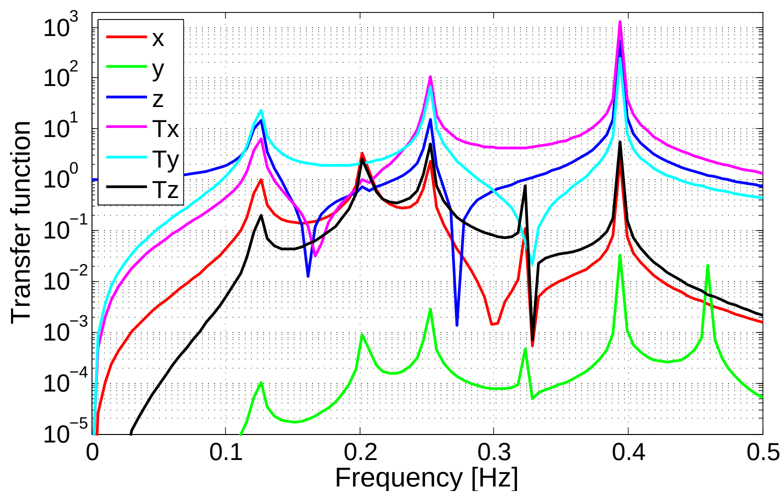

Figure 4.2: *FEM model predictions of the EIB-SAS low-frequency transfer functions of ground motion in the z-direction to the different degrees of freedom. There is a clear coupling between the various degrees of freedom.*

High-frequency modes

The frequencies of the high-frequency modes, in which the springbox and bench will move out-of-phase, are listed in Table 4.2. The first mode is the *Ty* mode at 13 Hz, where the springbox and bench rotate in the horizontal plane. At 18 Hz the springbox and bench oscillate in the *x* (Fig. 4.3a) and *z* directions. The *Tz* (Fig. 4.3b) and *Tx* modes have frequencies of 45 and 57 Hz respectively. Again, the frequency of the *Tx* mode is higher than that of the *Tz* mode, due to the difference in moment of inertia. Finally, the highest frequency rigid body mode is the one in which the springbox bounces on the IPs due to the vertical compliance of the top flexible joints and the tube of the IP at 60 Hz.

Frequency (mHz)	Degree of freedom
126	z, Ty
202	x, Tz
253	Ty, Tx
323	Tz, x
394	Tx, z, Ty
460	y

Table 4.1: *Frequencies of the low-frequency rigid body modes predicted by the FEM model.*

Frequency (Hz)	Main degree of freedom
13	Ty
18	x
18	z
45	Tz
57	Tx
60	y

Table 4.2: *Frequencies of the high-frequency rigid body modes predicted by the FEM model.*

4.3 Lagrangian models

To get a better understanding of the origin of the couplings, we constructed a Lagrangian model of the system. The transfer functions thus obtained are compared to our measurement results in chapter 5.

EIB-SAS will be modeled as a system of rigid bodies connected with angular and linear springs. We will ignore the internal modes of the individual components and only focus on the coupled vibrations of the rigid elements.

Writing down the kinetic and potential energies T and U of the system, the Lagrangian L is given by $L = T - U$. The equations of motion of the system can then be determined with the aid of the Euler-Lagrange formalism

$$\frac{d}{dt}\frac{\partial L}{\partial \dot{x}_{\mathrm{i}}} - \frac{\partial L}{\partial x_{\mathrm{i}}} = 0, \tag{4.1}$$

where x_{i} are the generalized coordinates of the system. The solutions to the Euler-Lagrange equations are the equations of motion of the system.

4.3.1 State space description

These differential equations can be rewritten as a *state space* representation, in which the dynamics of a linear system with n degrees of freedom is described by the four state space matrices $\{A, B, C, D\}$

$$\dot{\mathbf{x}} = A\mathbf{x} + B\mathbf{u} + C\mathbf{x} + D\mathbf{u}. \tag{4.2}$$

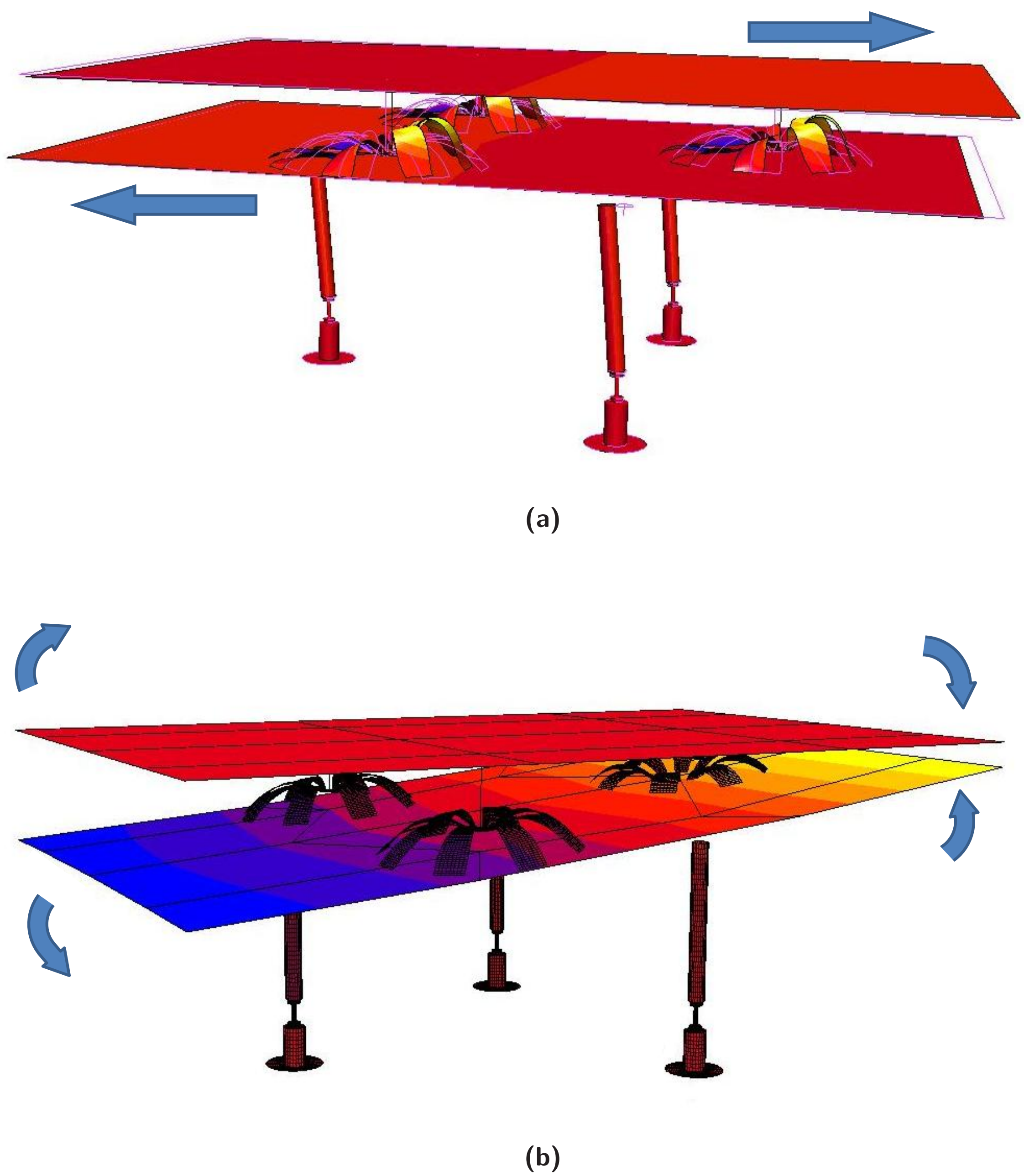

(a)

(b)

Figure 4.3: *Modes predicted by FEM model: (a) high-frequency horizontal (x) mode at 18 Hz, (b) high frequency Tz tilt mode at 45 Hz. Similar modes in the orthogonal directions z and Tx are predicted at 18 Hz and 57 Hz, respectively.*

Here, $\mathbf{x} = (x_0,\, x_1,\, \partial x_0/\partial t,\, \partial x_1/\partial t)$ is the *state vector* describing the state of the system; in this case its positions x_i and velocities v_i. The matrix denoted A is called the *state matrix*. It is an $n \times n$ matrix that contains the information about the stiffness of the mechanical system along each degree of freedom and the couplings between them. The matrix denoted B is called the *input matrix*. It contains the coupling of the states to outside disturbances **u**, which in our case will be ground vibrations. The matrix denoted C is called the *sensing matrix* and determines which degrees of freedom are the observables. Finally, all direct couplings to the input signals (noise) are contained by the *feedthrough matrix* D.

4.3.2 Vertical model

Fig. 4.4 shows a the rigid body description of the system for the vertical (y) degree of freedom. The springbox of mass m_0 stands on the IP legs. The vertical stiffness of the IPs is denoted $k_{\text{top\_flex}}$ and is dominated by the stiffness of the upper flexible joint and the vertical compliance of the legs' tubes. The bench has mass m_1 and is connected to the springbox with a vertical spring of stiffness k_{GAS}, which is the combined vertical stiffness of the three GAS filters. As they are tuned to $f_0 = 460$ mHz (see section 3.5), $k_{\text{GAS}} = 4\pi^2 f_0^2 m_1$.

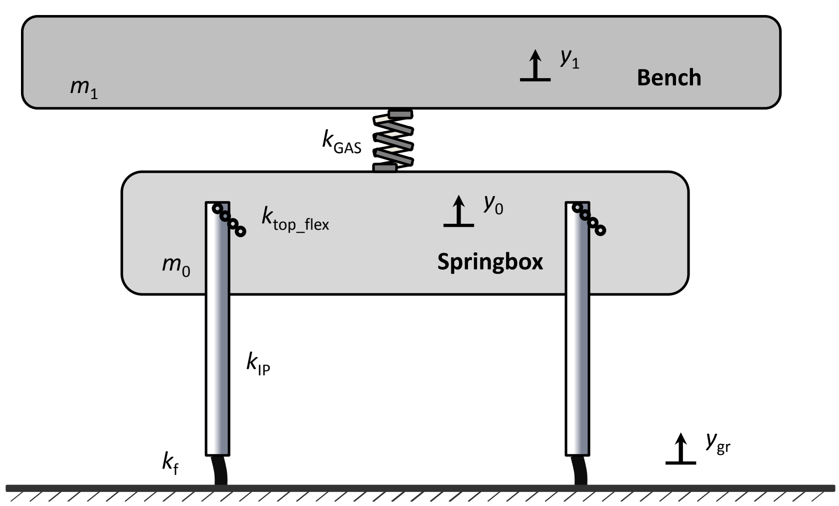

Figure 4.4: *Rigid body model of EIB-SAS for the vertical degree of freedom. The vertical compliance of the IP legs and upper flexible joint are incorporated in the vertical springs with stiffness* $k_{\text{top\_flex}}$. *The three GAS filters have been replaced by a single vertical spring of stiffness* k_{GAS}.

Denoting the vertical ground motion by y_{gr}, that of the springbox by y_0 and that of the bench by y_1, the kinetic energy T_{v} and the potential energy U_{v} of the system are given by

$$\begin{aligned} T_{\mathsf{v}} &= \frac{1}{2}m_0\dot{y}_0^2 + \frac{1}{2}m_1\dot{y}_1^2, \quad \text{and} \\ U_{\mathsf{v}} &= \frac{1}{2}k_{\mathsf{top}}y_0^2 + \frac{1}{2}k_{\mathsf{GAS}}\left(y_1 - y_0\right)^2. \end{aligned} \tag{4.3}$$

With the aid of the Euler-Lagrange formalism we can calculate the equations of motion of the system which are given by

$$\begin{aligned} m_0\ddot{y}_0 &= k_{\mathsf{GAS}}(y_0 - y_1) + k_{\mathsf{top}}y_0, \quad \text{and} \\ m_1\ddot{y}_1 &= k_{\mathsf{GAS}}(y_0 - y_1). \end{aligned} \tag{4.4}$$

In addition, we have the trivial differential equations $v_0 = \dot{y}_0$ and $v_1 = \dot{y}_1$. These four equations can be rewritten as a *state space* representation

$$\underbrace{\begin{bmatrix} \dot{y}_0 \\ \dot{y}_1 \\ \ddot{y}_0 \\ \ddot{y}_1 \end{bmatrix}}_{\dot{\mathbf{y}}} = \underbrace{\begin{bmatrix} 0 & 0 & 1 & 0 \\ 0 & 0 & 0 & 1 \\ -\frac{(k_{\mathsf{top}}+k_{\mathsf{GAS}})}{m_0} & \frac{k_{\mathsf{GAS}}}{m_0} & 0 & 0 \\ \frac{k_{\mathsf{GAS}}}{m_1} & -\frac{k_{\mathsf{GAS}}}{m_1} & 0 & 0 \end{bmatrix}}_{A} \underbrace{\begin{bmatrix} y_0 \\ y_1 \\ \dot{y}_0 \\ \dot{y}_1 \end{bmatrix}}_{\mathbf{y}} + \underbrace{\begin{bmatrix} 0 & 0 \\ 0 & 0 \\ \frac{k_{\mathsf{top}}}{m_0} & 0 \\ 0 & 0 \end{bmatrix}}_{B} u_{\mathsf{y}} + C \begin{bmatrix} y_0 \\ y_1 \\ \dot{y}_0 \\ \dot{y}_1 \end{bmatrix} + D u_{\mathsf{y}}, \tag{4.5}$$

where C=I_4 and D=*0*.

The *Q*-factors of the system's resonances will be dominated by the structural damping of the elastic elements. This can be incorporated by introducing a complex stiffness $k' = k\left(1 + i\phi\right)$, where $\phi = 1/Q$ is called the loss-angle. This adds a suitable damping term proportional to the displacement and in-phase with the velocity. For the elastic elements of EIB-SAS ϕ is of the order 0.1.

Fig. 4.5 shows the vertical transfer function of the system predicted by our Lagrangian model (dashed curve) together with the measurement result (solid curve) which is reported in section 5.3.2. The frequency and *Q*-factor of the mode are tuned such that they correspond to their experimental values: *Q* = 20 for the low-frequency vertical mode and *Q* = 125 for the high frequency mode at 49 Hz. These measurements are reported in section 5.3. The model parameter values are listed in Table 4.3.

Between 2 and 10 Hz the model agrees well with the measurement. But, above 10 Hz, the measurement is dominated by structural modes of the springbox (see section 5.3.2).

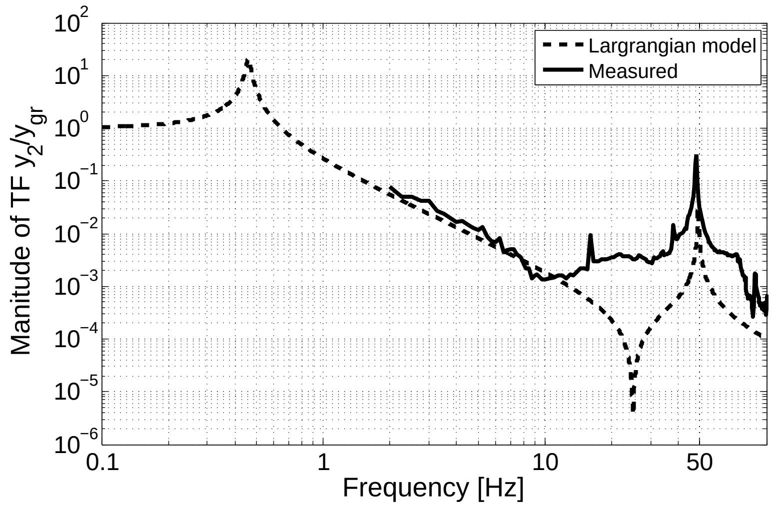

Figure 4.5: *Modeled and measured transfer functions of vertical ground vibrations to vertical bench motion. The solid curve represents the measured transfer function, which is reported in section 5.3.2. The dashed curve represents the vertical transfer function predicted by the Lagrangian model. The damping parameters ϕ_{top} and ϕ_{GAS} are tuned so that frequencies and Q-factors of the modes agree with our measured values (see section 5.2.1).*

Parameter	Value	Parameter	Value
m_0	329 kg	k_{GAS}	2.3×10^7 N/m
m_1	942 kg	ϕ_{GAS}	0.048
k_{top}	1.1×10^4 N/m	ϕ_{top}	0.008

Table 4.3: *Model parameters of the vertical Lagrangian model.*

4.3.3 Horizontal model

Fig. 4.6 shows the rigid body description of the system for the *x*-degree of freedom. The IPs have stiffness k_{IP}. They are connected to the ground with their bottom flexible joints of stiffness k_{f}. The springbox is suspended from the top flexible joints, which allow it to move in the horizontal directions. The horizontal stiffness of the three GAS filters is modeled by a linear spring of stiffness k_{x}. The vertical compliance of the GAS filters together with their position in the springbox allows tilt motion of the bench. The stiffness of this tilt mode is modeled with an angular spring of stiffness κ_{θ}. Its rotation angle is denoted θ. Due to the inertia of the optical bench and its elevation of its center of mass H above the GAS filters, we expect that horizontal ground vibrations not only excite the system in the horizontal direction, but also in the tilt direction.

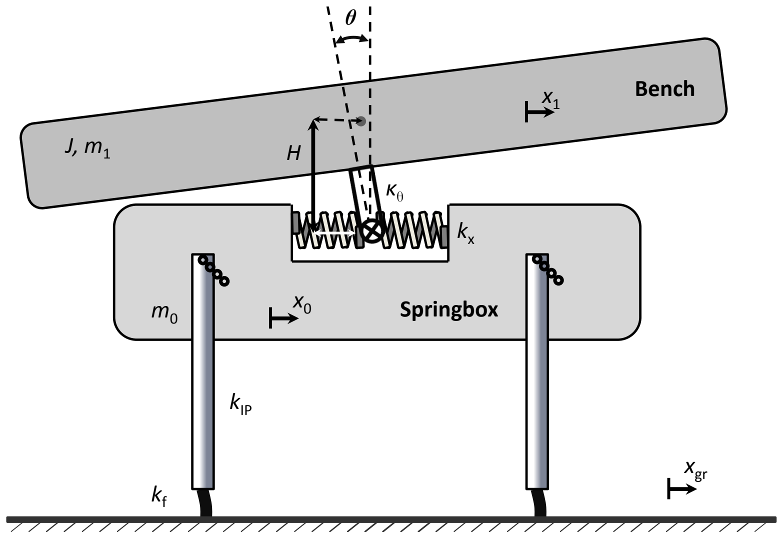

Figure 4.6: *Rigid body model of EIB-SAS for the horizontal degree of freedom. Due to the distribution of the GAS filters and the inertia of the optical bench, horizontal ground motion induces a tilt motion of the bench.*

Denoting the horizontal ground motion x_{gr}, that of the springbox x_0 and that of the bench x_1, the kinetic energy T_{h} and the potential energy U_{h} of the system are given by

$$\begin{aligned} T_{\mathsf{h}} &= \frac{1}{2}J\dot{\theta}^2 + \frac{1}{2}m_0\dot{x}_0^2 + \frac{1}{2}m_1\dot{x}_1^2, \\ U_{\mathsf{h}} &= \frac{1}{2}\left(\kappa_\theta - m_1 g H\right)\theta^2 + \frac{1}{2}k_{\mathsf{IP}}x_0^2 + \frac{1}{2}k_{\mathsf{x}}\left(x_1 - x_0 + H\theta\right)^2. \end{aligned} \tag{4.6}$$

Solving the Euler-Lagrange equations (Eq. (4.1)) we obtain the equations of motion which are given by

$$m_0\ddot{x}_0 = k_{\mathsf{x}}(x_1 - x_0 + H\theta) - k_{\mathsf{IP}}x_0, \tag{4.7}$$

$$m_1\ddot{x}_1 = k_{\mathsf{x}}\left(x_0 - x_1 - H\theta\right), \quad \text{and} \tag{4.8}$$

$$J\ddot{\theta} = -\left(\kappa_{\mathsf{GAS}} - Hgm_1\right)\theta + Hk_{\mathsf{x}}\left(x_1 - x_0 + H\theta\right), \tag{4.9}$$

where $J = m_1/12 \times (h^2 + d^2) + m_1 H^2$ is the moment of inertia of the optical bench of width d and height h around the axis through the center of the angular spring. Additional to the equations of motion, we have the differential equations $v_0 = \dot{x_0}$, $v_1 = \dot{x_1}$ and $\alpha = \dot{\theta}$.

Together, these six differential equations can be rewritten into a state space representation

$$\begin{bmatrix}\dot{x}_0\\ \dot{x}_1\\ \dot{\theta}\\ \ddot{x}_0\\ \ddot{x}_1\\ \ddot{\theta}\end{bmatrix} = \underbrace{\begin{bmatrix} 0 & 0 & 0 & 1 & 0 & 0\\ 0 & 0 & 0 & 0 & 1 & 0\\ 0 & 0 & 0 & 0 & 0 & 1\\ -\frac{(k_{\mathsf{IP}}+k_{\mathsf{x}})}{m_0} & \frac{k_{\mathsf{x}}}{m_0} & \frac{Hk_{\mathsf{x}}}{m_0} & 0 & 0 & 0\\ \frac{k_{\mathsf{x}}}{m_1} & -\frac{k_{\mathsf{x}}}{m_1} & -\frac{Hk_{\mathsf{x}}}{m_1} & 0 & 0 & 0\\ \frac{Hk_{\mathsf{x}}}{J} & -\frac{Hk_{\mathsf{x}}}{J} & \frac{m_1 gH-\kappa_{\theta}-H^2k_{\mathsf{x}}}{J} & 0 & 0 & 0\end{bmatrix}}_{A}\begin{bmatrix}x_0\\ x_1\\ \theta\\ \dot{x}_0\\ \dot{x}_1\\ \dot{\theta}\end{bmatrix} + \underbrace{\begin{bmatrix}0 & 0 & 0\\ 0 & 0 & 0\\ 0 & 0 & 0\\ \frac{k_{\mathsf{IP}}}{m_0} & 0 & 0\\ 0 & 0 & 0\\ 0 & 0 & 0\end{bmatrix}}_{B} u_{\mathsf{x}} + C\begin{bmatrix}x_0\\ x_1\\ \theta\\ \dot{x}_0\\ \dot{x}_1\\ \dot{\theta}\end{bmatrix} + D, \tag{4.10}$$

where $C = I_6$ and $D = 0$.

Fig. 4.7 shows the transfer function of horizontal ground motion to horizontal bench motion (dotted curve), and to tilt motion in the *Tz* direction (dashed curve). The parameter values are given in Table 4.4. The stiffnesses κ_{θ}, k_{IP} and k_{x} are chosen such that the model reproduces the measured frequencies of the low-frequency rigid body modes: 172 mHz for the *Tz* mode, 317 mHz for the low-frequency *x*-mode and 16 Hz its the high-frequency mode. As for the vertical transfer functions, the damping parameters ϕ_{i} have been tuned so that the *Q*-factors of the modes have the measured values: $Q = 110$ for the low frequency tilt mode, $Q = 20$ for the low-frequency horizontal mode and $Q = 40$ for the high frequency tilt mode at 16 Hz.

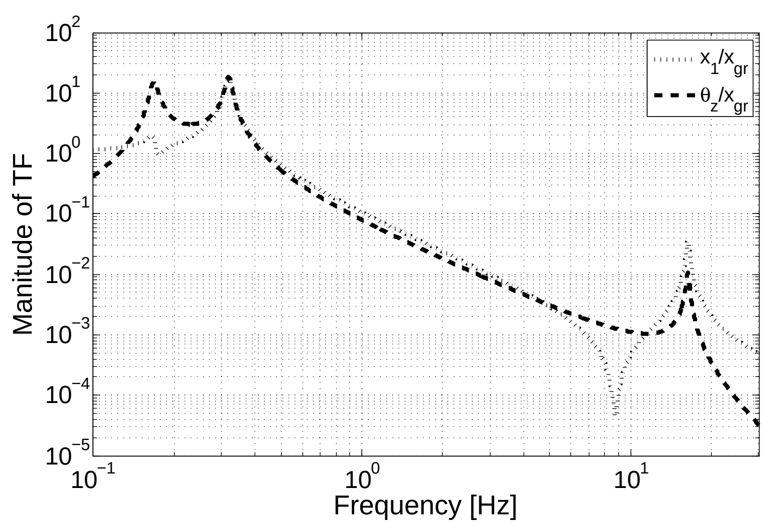

Figure 4.7: *Transfer functions from horizontal ground displacement to displacement in the x-direction (dotted curve) and rotation in the Tz-direction (dashed curve) of the bench. The damping parameters ϕ_{IP}, ϕ_{Tz} and ϕ_{x} are tuned so that the Q-factors of the modes agree with our measured values.*

Parameter	Value	Parameter	Value
m_0	329 kg	m_1	942 kg
k_{IP}	4.4×10^3 N/m	κ_θ	2.1×10^3 Nm/rad
k_{x}	2.5×10^6 N/m	ϕ_{IP}	0.048
ϕ_{Tz}	0.009	ϕ_{x}	0.025
H	0.2 m		

Table 4.4: *Model parameters of the horizontal Lagrangian model.*

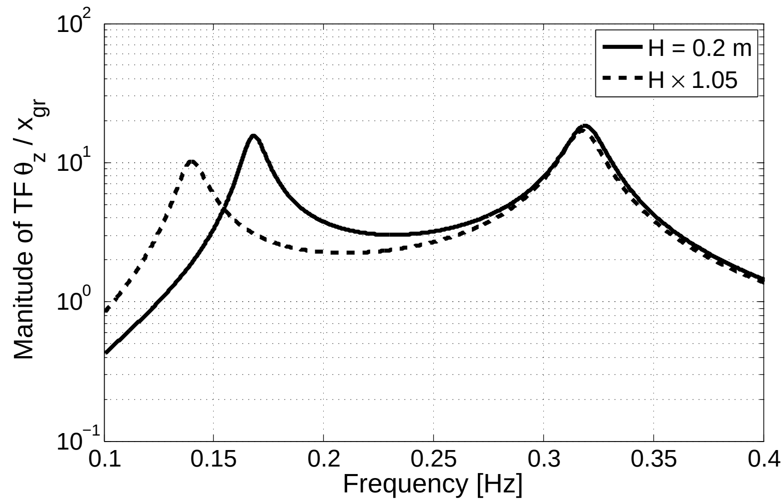

Figure 4.8: *The gravitational pull on the bench lowers the effective stiffness of the angular spring. The height of the center of mass of the bench is 20 cm. Increasing it by 5% lowers the frequency of the tilt mode from 172 mHz (solid curve), to 140 mHz (dashed curve).*

The two transfer functions are of the same order of magnitude. As expected, horizontal ground motion induces a significant amount of tilt motion around the orthogonal horizontal axis.

Increasing the height of the center of mass of the bench H lowers the effective stiffness of the angular spring. Fig. 4.8 shows the transfer function where H has been increased by 5%. This enhancement of the anti-spring effect of the bench lowers the frequency of the tilt mode from 172 to 140 mHz. To allow an independent tuning of the tilt mode frequencies, EIB-SAS incorporates a tilt stabilizer.

4.3.4 Horizontal model including tilt stabilizer

Fig. 4.9 shows the rigid body model for the horizontal degrees of freedom with tilt stabilizer. A column of length $L_{\mathsf{ts}} = 73$ cm hangs from the top plate. The bottom of the column is connected to triangular cantilever springs with steel wires. The springs have a stiffness of $k_{\mathsf{ts}} = 4.3\times10^3$ N/m and are in turn connected to the springbox.

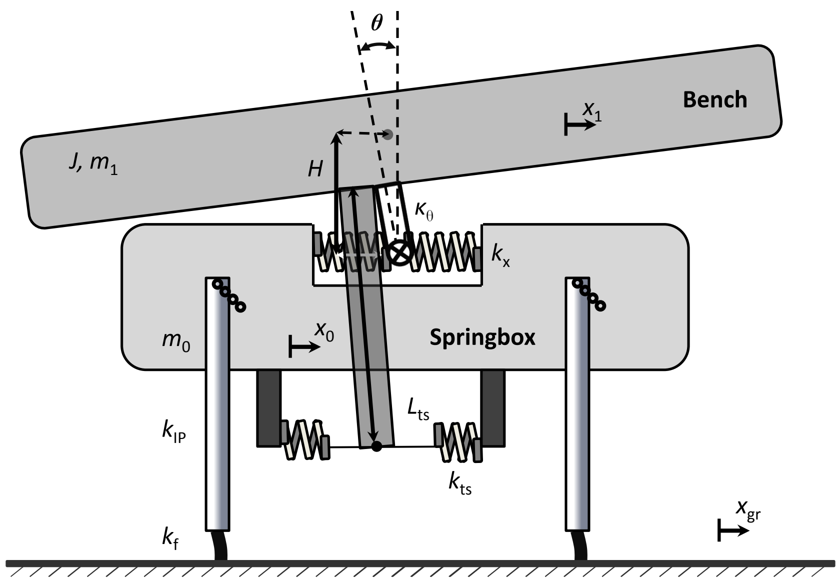

Figure 4.9: *Rigid body model of EIB-SAS for the horizontal degrees of freedom with tilt stabilizer. To stiffen EIB-SAS in the tilt degrees of freedom a column of length U is attached to the bottom of the bench. The lower end of the column is connected to ground via wires attached to cantilever springs of stiffness k_{ts}.*

The tilt stabilizer adds a term $-k_{\mathsf{ts}}\left(\theta L_{\mathsf{ts}}\right)^2/2$ to the Lagrangian which then becomes

$$\frac{1}{2}\left(J\dot{\theta}^2 + m_0\dot{x}_0^2 + m_1\dot{x}_1^2 - \left(\kappa_\theta - m_1 g H\right)\theta^2 - k_{\mathsf{IP}}x_0^2 - k_{\mathsf{x}}\left(x_1 - x_0 + H\theta\right)^2 - k_{\mathsf{ts}}\left(\theta L_{\mathsf{ts}}\right)^2\right). \tag{4.11}$$

The equations of motion for horizontal displacement of the springbox and bench remain unchanged, but that of rotation of the bench becomes

$$J\ddot{\theta} = -\left(\kappa_{\mathsf{GAS}} - Hgm_1 + k_{\mathsf{ts}}L_{\mathsf{ts}}^2\right)\theta + Hk_{\mathsf{x}}\left(x_1 - x_0 + H\theta\right). \tag{4.12}$$

In the state-space representation, only the input matrix A changes to

$$\begin{bmatrix} 0 & 0 & 0 & 1 & 0 & 0 \\ 0 & 0 & 0 & 0 & 1 & 0 \\ 0 & 0 & 0 & 0 & 0 & 1 \\ -\frac{(k_{\mathsf{IP}}+k_{\mathsf{x}})}{m_0} & \frac{k_{\mathsf{x}}}{m_0} & \frac{Hk_{\mathsf{x}}}{m_0} & 0 & 0 & 0 \\ \frac{k_{\mathsf{x}}}{m_1} & -\frac{k_{\mathsf{x}}}{m_1} & -\frac{Hk_{\mathsf{x}}}{m_1} & 0 & 0 & 0 \\ \frac{Hk_{\mathsf{x}}}{J} & -\frac{Hk_{\mathsf{x}}}{J} & \frac{m_1 gH - \kappa_\theta - H^2 k_{\mathsf{x}} - k_{\mathsf{ts}}L_{\mathsf{ts}}^2}{J} & 0 & 0 & 0 \end{bmatrix}. \tag{4.13}$$

Fig. 4.10 shows the transfer functions of ground motion to motion in the *x* (dotted curve) and *Tz* (dashed curve) degrees of freedom with the tilt stabilizer stiffening the tilt modes. The solid curve represents the transfer function, whose measurement is described in section 5.3.2. The tilt resonance has shifted up from 172 to 548 mHz, while the horizontal resonance frequency has shifted down from 317 to 282 mHz. The measured effect of the tilt stabilizer (see section 5.2.1) was a shift of the *Tz* rigid body mode from 172 to 479 mHz and that of the horizontal *x* mode decreased from 317 to 294 mHz. The tilt stabilizer does not increase the stiffness of tilt mode as much as the model predicts.

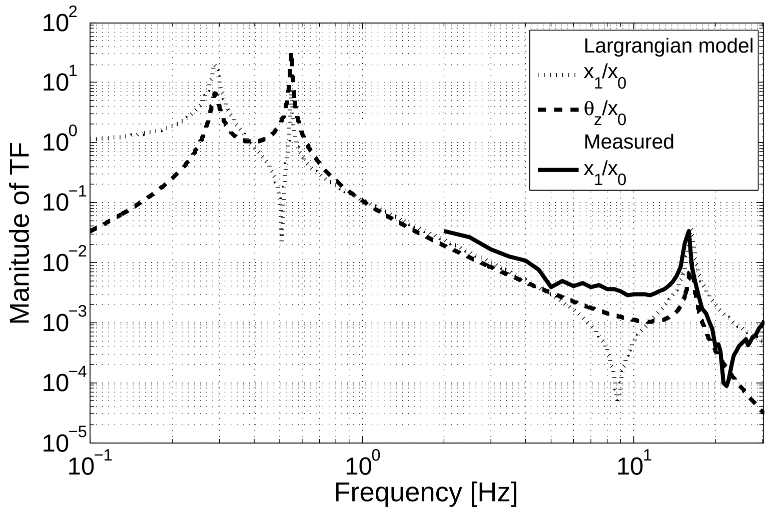

Figure 4.10: *The tilt stabilizer increases the frequency of the low frequency tilt modes while leaving all other modes unchanged. The dotted and dashed curves represent the transfer function of horizontal ground motion to respectively horizontal and rotational tilt motion of the bench. The black solid curve represents the result of the horizontal transfer function measurement described in section 5.3.2. According to the model, the tilt stabilizer increases the frequency of the Tz mode from 172 to 479 mHz. The frequency of the high-frequency rigid body mode remains 16 Hz.*

4.4 Summary

The compliance of the inverted pendulums and GAS filters allows for six low-frequency and six high-frequency rigid body modes. The low-frequency ones are responsible for the seismic attenuation characteristics at high-frequency, while the high-frequency modes are unwanted.

To predict the frequencies of the modes, FEM models of EIB-SAS have been created. In these models, the system is described as two rigid objects: the springbox and the bench, that are connected to each other and the ground with appropriate flexible elements. The stiffness of these elements are chosen such that the frequencies of the low-frequency rigid body modes match the measurements results described in section 5.2.1. The FEM model predicts that the horizontal high-frequency rigid body modes occur at 13 Hz (*Ty*) and 18 Hz (*x* and *z*), and the vertical modes at 45 Hz (*Tz*), 57 Hz (*Tx*) and 60 Hz (*y*).

To help understand their nature, Lagrangian models for the vertical and horizontal (x) degrees of freedom have also been developed. Assigning the appropriate stiffness to the GAS filters and IPs reproduces the frequencies of the observed high-frequency rigid body modes.

For the *Tx* and *Tz* degrees of freedom the angular stiffness of the three GAS filters can be described by an angular spring. Similar to the anti-spring effect that is exhibited by the inverted pendulums, an increase in the height of the center of mass of the bench with respect to the spingbox lowers the stiffness of this effective angular spring. This effect, has been taken into account in the Lagrangian model. To counter this effect and raise the frequencies of the vertical tilt modes, a tilt stabilizer has been incorporated in EIB-SAS. The tilt stabilizer has also been added to the model. According to the model, the frequencies of the *Tx* and *Tz* low-frequency rigid body modes is raised by the tilt stabilizer, while the other degrees of freedom remain unaffected. The nature of the high-frequency rigid body modes and their couplings are well understood.

5 | Performance and characterization measurements

"According as circumstances are favorable, one should modify one's plans"
– Sun Tzu, The art of war (~512 BC)

5.1 Introduction

In section 2.14 we listed the requirements for EIB-SAS that were set by the Virgo collaboration. Here, we will present the measurements we performed to show EIB-SAS meets them.

First, the low-frequency rigid body modes of the system are identified. Second, we will report the direct transfer function measurements from vertical and horizontal ground motion to bench motion in the relevant degrees of freedom. These demonstrate the isolation performance of the system and at the same time provide us with its high-frequency rigid body modes and structural modes. We will continue with a description of the control system and show that it successfully damps all rigid body modes below 20 Hz. Rigid body modes and structural modes with higher frequencies are damped with custom tuned dampers if necessary. After that, we will report the long-term, and thermal stability measurements to show that the residual motion of the system stays below the required values. Then, we will present performance tests done with the Virgo+ (see Section 2.9) injection system to show that the beam jitter noise that was present in Virgo has been reduced to negligible levels. We will conclude with acoustic noise measurements done in the Advanced Virgo laser laboratory and show the effects of acoustic noise under realistic science mode conditions.

5.2 Characterization of low frequency behavior

The seismic isolation capabilities of EIB-SAS are provided by the geometric anti-spring filters and inverted pendulums described in chapter 3. These passive filters give rise to six low-frequency (< 0.1 Hz) rigid body modes.

5.2.1 Measurement of the low-frequency rigid body modes

EIB-SAS is equipped with a number of inertial sensors (geophones) and displacement sensors (LVDTs) to monitor its residual motion. These sensors are described in section 5.4. Fig. 5.1a shows the motion spectra measured by the LVDTs. As expected, there are 6 rigid body modes with frequencies well below 1 Hz. Their frequencies are listed in Table 5.1.

The resonance frequency in the vertical y direction is 460 mHz, while in section 3.5.7 we showed that the GAS filters have been tuned to 387 mHz. This deviation is due to the compliance of the baseplates of the GAS filters. When the filters are tuned they are not bolted to any other structure and the blades can bend the baseplate a little. When installed in EIB-SAS, the baseplates of the filters are bolted to the springbox which increases their stiffness resulting in a slight change in the blade clamping angle θ_0. According to the numerical model described in section 3.5.4 the frequency of the filters can be raised from 387 mHz to 460 mHz by increasing θ_0 by just 2.6 mrad.

The spectra in Fig. 5.1a show that there is a strong coupling between the x and Tz degrees of freedom and between the z and Tx degrees of freedom. As described in chapter 4, these couplings are due to the compliance of the GAS filters and the inertia of the optical bench they support. Because of that, shaking the springbox in one of the horizontal directions induces tilt motion of the bench around the orthogonal horizontal axis.

Yaw motion (Ty) is also coupled to motion in the z-direction. This is due to a difference in load and hence, difference in stiffnesses of the three IPs. Due to the position of the GAS filters the IP at the positive x side of the system carries a heavier load than the other two IPs. Due to the asymmetrical horizontal compliance of the system horizontal motion in the z-direction induces motion in the Ty-direction.

The frequency of the Tx and Tz modes does not only depend on the value of the load of the GAS filters but also on its distribution *i.e.* its moment of inertia and the location of the center of mass. The load of the GAS filters is of course fixed as is the vertical resonance frequency. The part of the load that can be moved around is light compared to the weight of the optical bench itself. Therefore, the inertia of the load does not change significantly and the dominant effect on the tilt resonance frequencies is the height of the center of mass. Raising the center of mass would increase the Tx and Tz resonance frequencies.

The lowest resonance frequency is that of the Tx degree of freedom, which was rather low at 172 mHz and caused strong hysteresis in this mode. Consequently, the Tx position of the system was not sufficiently reproducible. To cure this, we installed a tilt stabilizer that increases the resonance frequency of the tilt modes without altering the vertical stiffness.

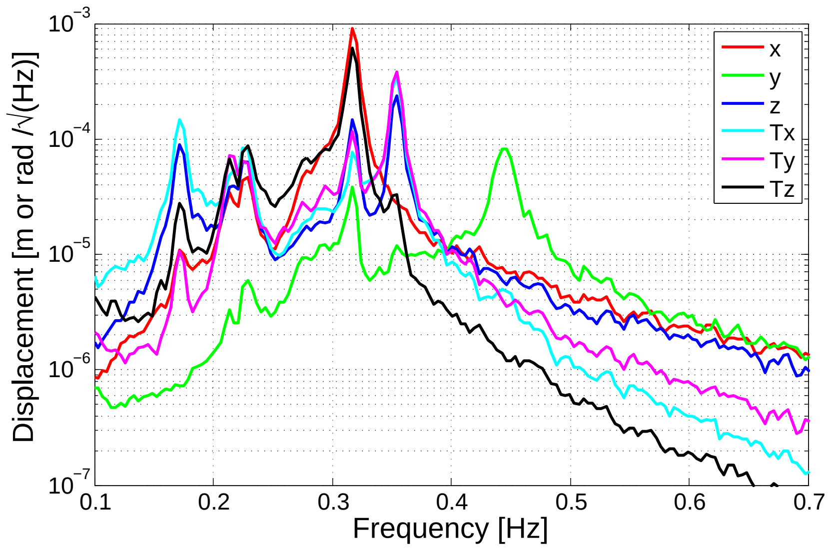

(a)

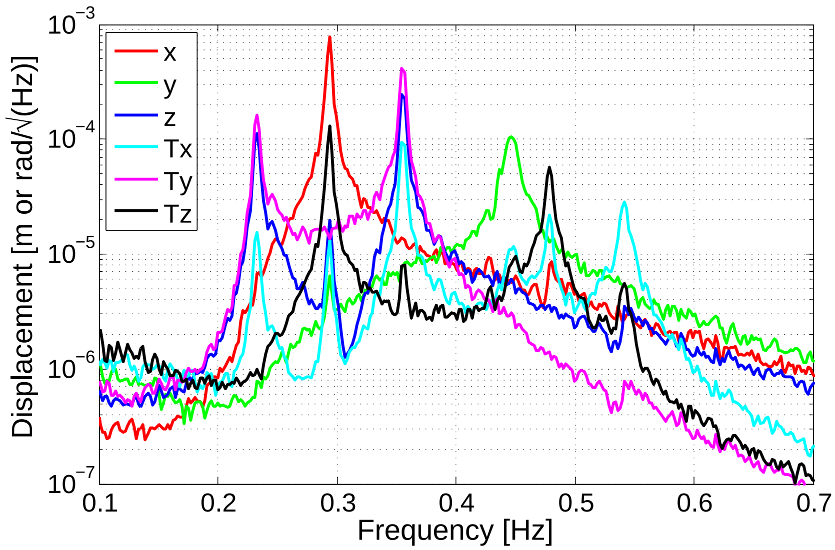

(b)

Figure 5.1: *Displacement spectra of the virtual sensors without (a) and with (b) tilt stabilizer. There are 6 low-frequency (< 1 Hz) rigid body modes. Their frequencies are: 203 mHz, 282 mHz, 315 mHz, 420 mHz, 460 mHz and 549 mHz. The 460 mHz mode belongs to the vertical degree of freedom and does not couple to any other degree of freedom. At the other frequencies there is significant coupling between the horizontal and vertical degrees of freedom e.g. motion in the x-direction induces motion in the Tz direction and vice versa. Without tilt stabilizer, the coupling between the different degrees of freedom is smaller and the resonance frequencies of the Tx and Tz modes are significantly lower.*

Stiffening the tilt modes

Fig. 5.2 shows a rendering of the tilt stabilizer. It consists of an aluminum column that is hanging from the top plate and whose bottom is connected with stainless steel wires to three maraging steel triangular cantilever blades that are attached to the springbox. The wires are under tension to place their lowest internal mode (the violin mode) well above 50 Hz as not to affect the system. In this way, when the bench tilts the wires pull on the blade springs. This stiffens the tilt mode and increases their natural frequency.

Fig. 5.1b shows the displacement spectra with tilt stabilizer. The tilt stabilizer raises the resonance frequency of the *Tx* mode from 172 mHz to 549 mHz, that of the *Tz* mode from 214 mHz to 420 mHz, while that of the vertical rigid body modes remains at 460 mHz. The mode frequencies with and without tilt stabilizer are summarized in Table 5.1.

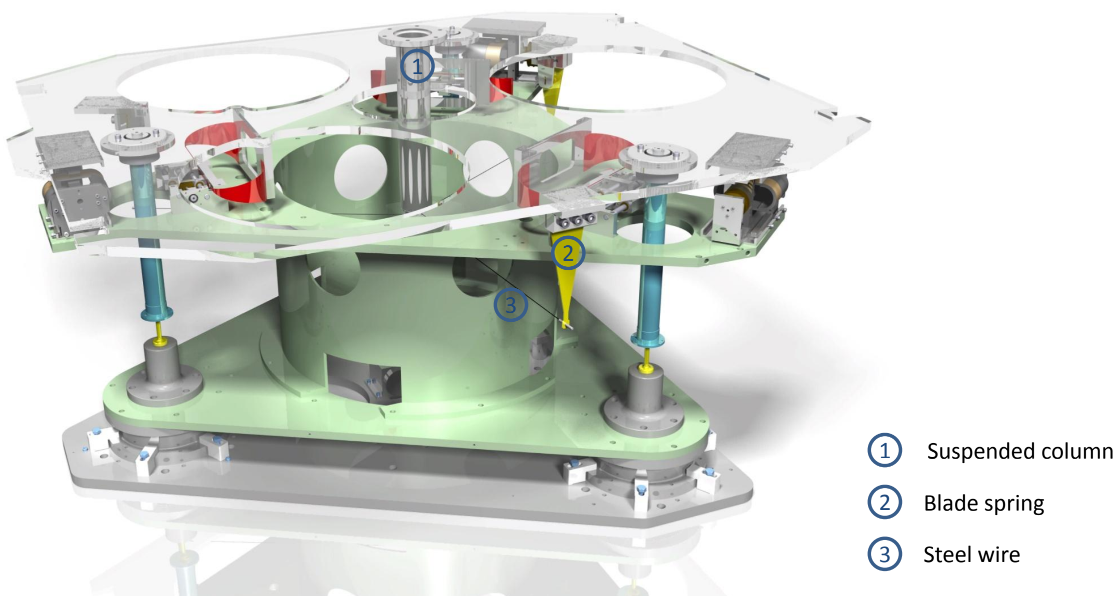

Figure 5.2: *Rendering of the tilt stabilizer. A column (1) hangs from the top plate of EIB-SAS. The bottom of the column is connected to 3 blade springs (2) with 3 steel wires (3) under tension. When the bench tilts a force is exerted on the bench by the blade springs, thus stiffening the vertical tilt modes.*

Mode	Without tilt stabilizer		With tilt stabilizer	
	Frequency (mHz)	Component	Frequency (mHz)	Component
1	172	z, Tx	233	z, Ty
2	214	x, z, Tx, Ty, Tz	294	x, Tz
3	229	x, z, Tx, Ty, Tz	355	z, Tx, Ty
4	317	x, Tz	446	y
5	355	z, Tx, Ty	479	Tx, Tz
6	446	y	542	Tx, Tz

Table 5.1: *Frequencies of the rigid body modes with and without tilt stabilizer. The modes are coupled. The resonance peak of each mode therefore shows up in multiple virtual sensors.*

5.3 Characterization of passive seismic isolation behavior

The ground motion spectrum at Virgo differs from that in Amsterdam. Therefore, the motion spectrum of EIB-SAS as measured at Nikhef cannot be compared directly to the requirement. Excitation by natural seismic activity is not sufficient to raise the motion of the bench above the noise level of the available inertial sensors. In order to determine the structural resonances of EIB-SAS and quantify its seismic isolation performance the motion of the ground needs to be enhanced such that the motion of the bench top is measurable. This is achieved by mounting EIB-SAS on a piezoelectric shaker system that can move the base of the system in the horizontal, vertical and pitch (Tz) direction.

By multiplying the measured transfer function with a ground motion spectrum of the Virgo site [104], realistic estimates of the EIB-SAS performance at the Virgo site are obtained. Furthermore, comparing the different transfer functions to the predictions from the FEM model the structural modes of the system can be identified.

Fig. 5.3a shows EIB-SAS on the piezoelectric shaker system. EIB-SAS was mounted on a stiff triangular frame (the yellow frame in the photo). Each corner of the frame was supported by a piezoelectric shaker as shown in Fig. 5.3b.

Fig. 5.4 shows a schematic cross section of a shaker. Each of these shakers contains two piezoelectric actuators; one vertical and one horizontal. The frame supporting EIB-SAS stands on the vertical piezoelectric actuator. It is situated in a platform that is connected to the ground via two hinges that allow it to move in the horizontal direction. Applying an in-phase signal to the piezoelectric actuators EIB-SAS can be excited in the vertical or horizontal direction.

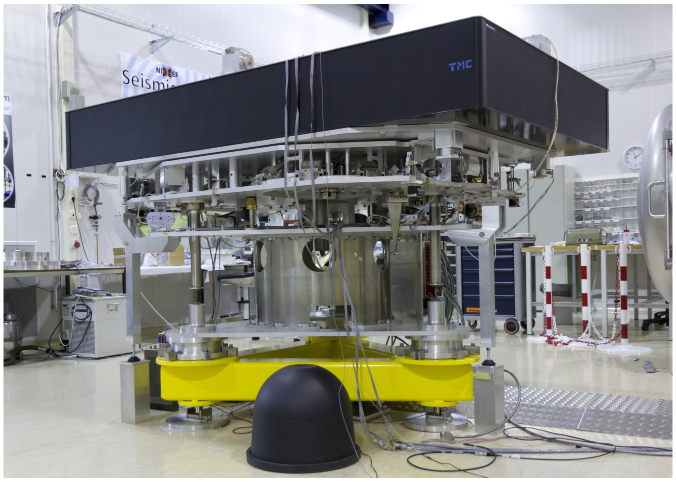

(a)

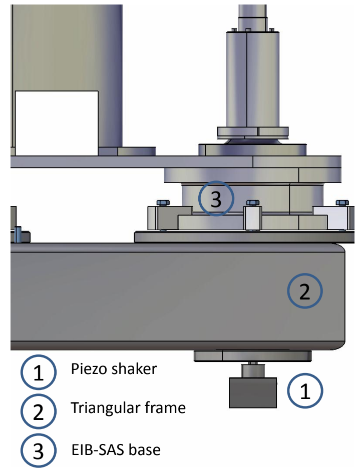

(b)

Figure 5.3: *a) Photo of EIB-SAS mounted on the piezoelectric shaker setup. EIB-SAS is mounted on a stiff, triangular metal frame (yellow structure in the photo). b) Each corner of the frame stands on a hinge with two piezoelectric ceramics; one to shake in the vertical direction, one to shake in the horizontal direction. Fig. 5.4 shows a cross section of an individual shaker.*

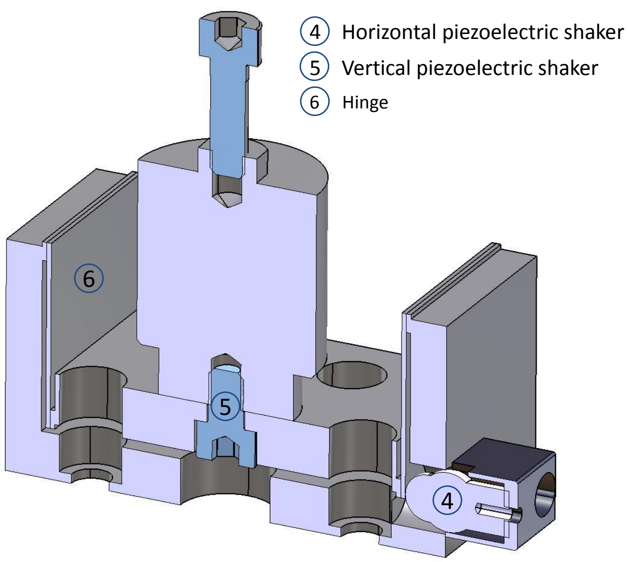

Figure 5.4: *Three piezoelectric shakers are used to shake the base of EIB-SAS. EIB-SAS rests on three piezoelectric actuators that can vibrate in the vertical direction. These three pieces of ceramic carry the full weight of EIB-SAS. They are placed on a platform that is free to move in the horizontal direction with the aid of two hinges. The piezoelectric actuators that vibrate in the horizontal direction are pressing against these hinges.*

The motion of the base and top of the system is measured with two accelerometers*. The accelerometers monitoring the shaker frame are placed on the far right and far left of the frame (sensors 1 and 2 in Fig. 5.5), below the middle of the short sides of the optical bench. The motion of the frame is given by their average signal. On the bench, one accelerometer is placed at the center of the optical bench to measures its vertical (sensor 4), or horizontal motion (depending on its orientation). A second accelerometer is placed in the middle of the short end of the optical bench to measure its tilt (sensor 3).

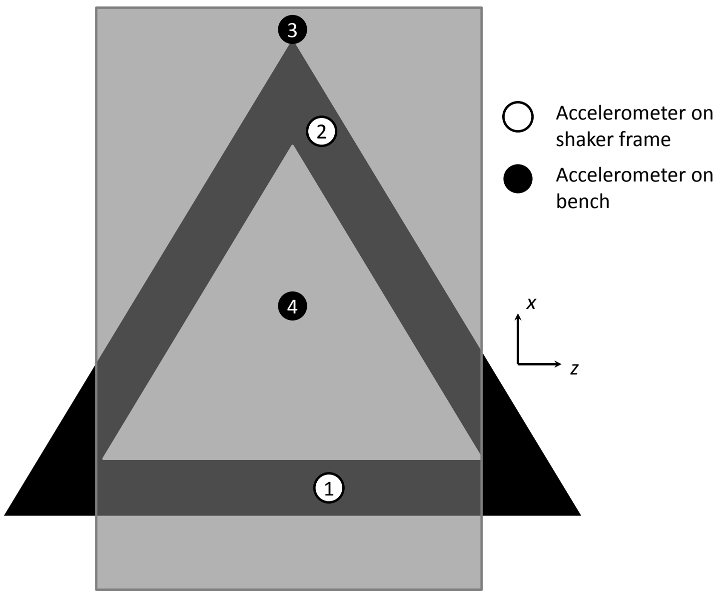

Figure 5.5: *To measure the ground to bench transfer function two accelerometers are used to sense the motion of the frame: sensors 1 and 2, and two to sense the motion of the bench: sensors 3 and 4. The orientation of the accelerometers can be changed to measure vertically or horizontally. Combinations of their signals are made the measure translation and tilt.*

5.3.1 High frequency modes

In chapter 4 we showed that next to the 6 low frequency rigid body modes there will be 6 rigid body modes with frequencies above 10 Hz. They have been identified by comparing the results of the transfer function measurements to predictions of our Lagrangian and FEM models. Modes within the bandwidth of the control loop are damped with the actuators, while those outside the control loop tuned dampers were used when necessary.

Mode measurement

Fig. 5.6a shows the measured vertical and horizontal transfer functions of the system between 10 and 60 Hz. The measurements show the six peaks that belong to the high frequency rigid body modes. The first peak in the horizontal (excitation in *z* direction) transfer function (black curve) corresponds to the *Ty* resonance and has a frequency of 12 Hz. The second

*Wilcoxon 731-207 accelerometers.

peak corresponds to the z structural resonance which has a frequency of 16.0 Hz. The third peak is the Tx resonance and has a frequency of 41 Hz.

The first peak in the horizontal (excitation in x direction) transfer function (red curve) corresponds to the x resonance and has a frequency of 15.75 Hz. The second peak corresponds to the Tz resonance which has a frequency of 36.5 Hz. The vertical to vertical transfer function shows that the y resonance has a frequency of 48 Hz.

Fig. 5.6b shows the amplitude spectral densities of the sensors between 10 and 20 Hz without any enhancement of the ground motion. The Ty mode is measured at 11.90 Hz, the x mode 15.80 Hz and the z-mode 16.05 Hz. This latter mode couples to the Ty degree of freedom for the reason explained in section 5.2. The measured frequencies of the structural modes together with the values predicted by the FEM model of chapter 4 are summarized in Table 5.2.

Mode	FEM model prediction of frequency (Hz)	Measured frequency (Hz)
x	18	15.8
y	60	48.0
z	18	16.0
Tx	57	41.0
Ty	13	11.9
Tz	45	36.5

Table 5.2: *Frequencies of the structural modes as predicted by the FEM model and from the transfer function measurements.*

Damping the modes

Under normal seismic conditions the signals induced by the horizontal modes are above the noise floor of the geophones. The typical accelerations of the springbox, which has a mass of 300 kg, are of the order of 10^{-6} m/s$^{-2}/\sqrt{\text{Hz}}$. So, the force needed to control it are 0.3 mN/$\sqrt{\text{Hz}}$. Each horizontal actuator can deliver a force of 0.9 N, which means that they are easily capable of damping the high-frequency rigid body modes. This will be shown section 5.4.

The vertical modes have a higher frequency. The energy in these modes is too high and they cannot be damped by the controls. Instead, the 48 Hz y and 36.5 Hz Tz modes are damped with custom built tuned dampers as the one shown in Fig. 5.7a.

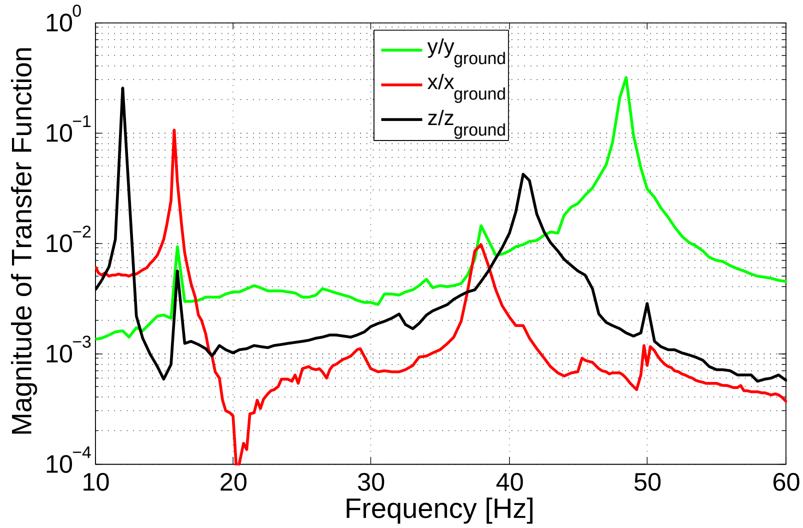

(a)

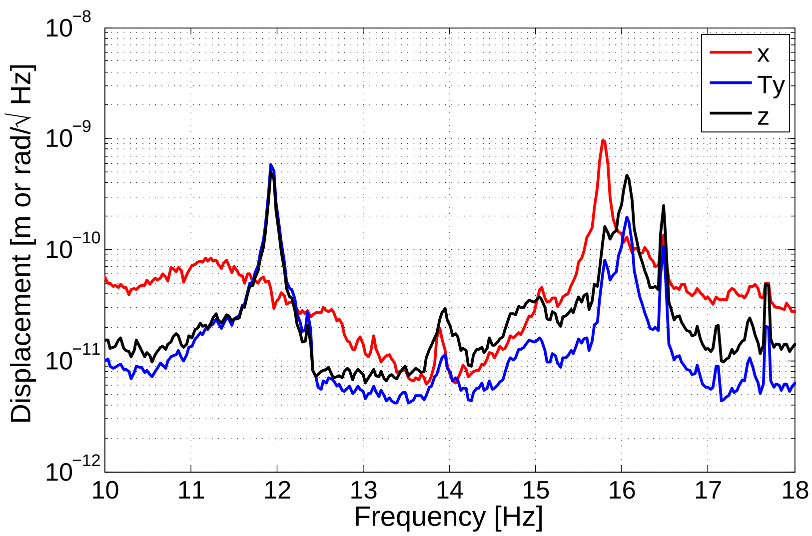

(b)

Figure 5.6: *The structural modes of EIB-SAS. a) EIB-SAS transfer functions measured by exciting its base in the vertical and horizontal degrees of freedom and measuring the motion of its top. b) Spectra of the horizontal virtual geophones under normal seismic conditions. The Ty mode has a frequency of 12 Hz, the x mode of 15.80 Hz, the z mode of 16.05 Hz, the Tz mode of 37 Hz, the Tx mode of 41 Hz and the y mode of 48 Hz.*

Tuned dampers

Fig. 5.7a shows a photo of the tuned damper and a schematic representation of one of its damping units. The damper consists of a tunable mechanical oscillator with adjustable quality factor. It consists of eight copper bars positioned between two rows of magnets. The magnets face each other north-north or south-south to produce a strong magnetic field perpendicular to the copper bars. The magnets are attached to the central body with eight blade springs, and are free to move along the damper's symmetry axis. Eddy currents are induced by the moving magnetic field providing a viscous damping force. By adjusting the moving mass and the stiffness of the blade springs the resonance frequency of the damper is matched to that of the springbox mode that is to be damped. The damper is placed in a position of the bench were the mode has an anti-node for maximum effect.

For optimal damping the Q-factor of the damper must be optimized with respect to the Q-factor of the mode. If the Q-factor of the damper is too high, then the damper oscillates strongly, but is hardly damped and does not remove energy from the system. If, on the other hand, the Q-factor of the damper is too low, then the damper starts losing its resonant properties and hence, its damping capabilities, and we have effectively just added an extra load to the system.

The amount of damping for several values of the Q-factor was analytically calculated. Fig. 5.8 shows the results of these calculations. The optimal Q-factor of the damper for this mode is 8.

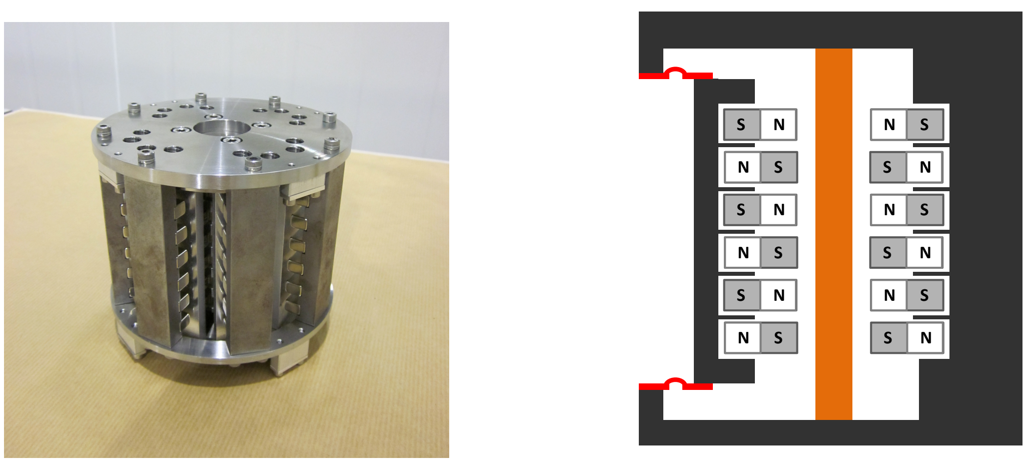

(a) **(b)**

Figure 5.7: *a) Photo of the custom built eddy current damper that is used to damp the structural modes at 37 and 48 Hz. b) Schematic representation of a damping unit of the eddy current damper: 12 magnets face a copper bar. One set of magnets is connected to the main structure with small blade springs so that it can oscillate. The stiffness of the springs determines the frequency of the damper; the number magnets its Q-factor.*

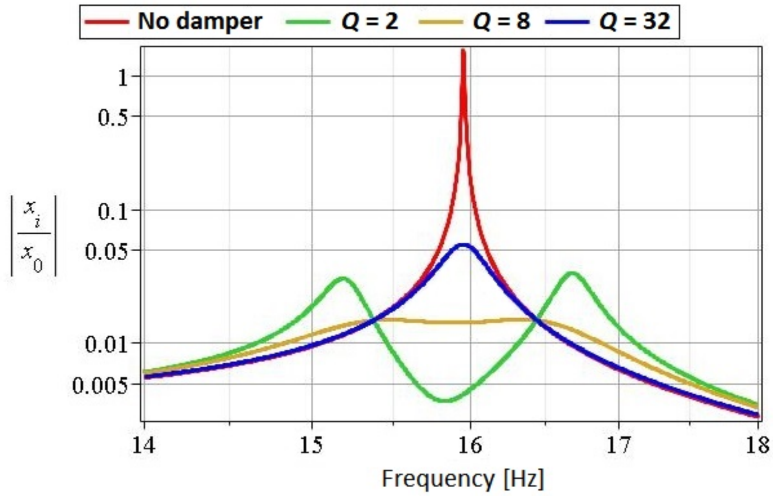

Figure 5.8: *The shape of the resonance peak in the transfer function for different values of the Q-factor of the damper. For optimal damping the Q-factor should be 10.*

Fig. 5.9a shows the horizontal transfer function with (dashed curve) and without (solid curve) eddy current damper around the 37 Hz peak. The damper is tuned to 34.75 Hz and has a Q-factor of 20. It reduces the amplitude of the resonance peak by 40%. The Q-factor of the damper does not match with that of the mode. The mode is overdamped and is split into two resonance peaks. One at 32 Hz, the other at 39 Hz. Damping of the resonance could be improved by decreasing the Q-factor of the damper.

Fig. 5.9b shows the vertical transfer function with (dashed curve) and without (solid curve) eddy current damper around the 48 Hz resonance peak. The damper was tuned to 47.25 Hz and has a Q-factor of 9. It nearly perfectly tuned and reduces the amplitude of the resonance peak with a factor 20.

Tuned damper with internal friction

Apart from the mentioned rigid body modes we found a springbox mode at 183 Hz that we would like to damp. To damp this mode with an eddy current damper we would need to increase the stiffness of the damper by a factor 16. As this is rather impractical we designed a different kind of resonant damper with uses viton to absorb the energy. It is shown in Fig. 5.10.

The damper consists of a steel beam of thickness d = 2.8 mm, width w = 40 mm and length L = 200 mm. It is bolted to a corner of the springbox*. A block aluminum of mass M = 550 gr is bolted to the center of the beam dividing it in two identical beams of length L that are clamped at both ends. The Q-factor of the damper can be influenced independently by placing some viton blocks between the damper's mass and the surface of the springbox.

*Exciting EIB-SAS at the precise resonance frequency with the piezoelectric shaker system it is easy to discover that this is a anti-node of the mode

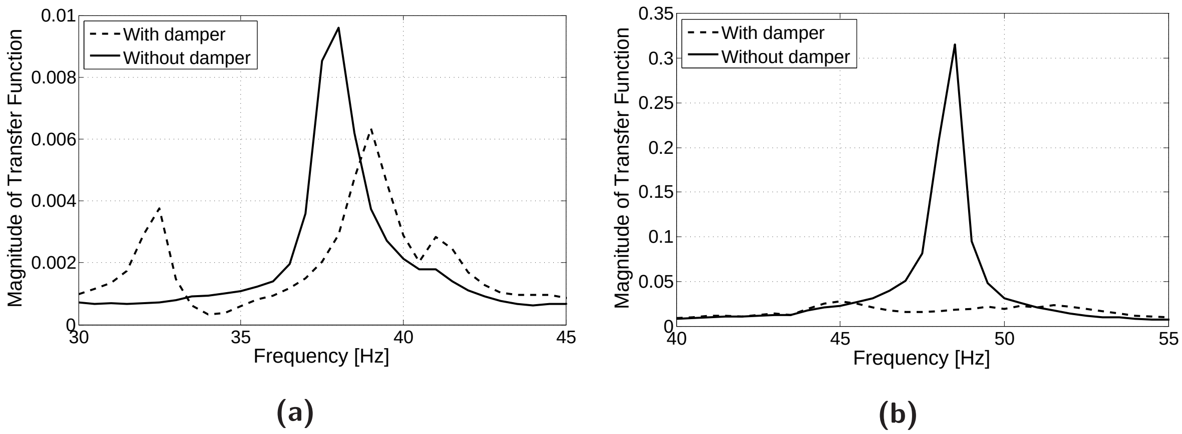

Figure 5.9: *a) Horizontal transfer function of EIB-SAS with (dashed curve) and without (solid curve) eddy current damper. The damper is tuned to a frequency of 34.5 Hz and has a Q-factor of 5. It lowers the amplitude of the 37 Hz mode by 40%. The Q-factor of the damper should be increased to 10 for optimal damping of the mode. b) Vertical transfer function of EIB-SAS with (dashed curve) and without (solid curve) eddy current damper. The damper is tuned to a frequency of 47.5 Hz and has a Q-factor of 10. It lowers the amplitude of the 48 Hz mode by a factor 20.*

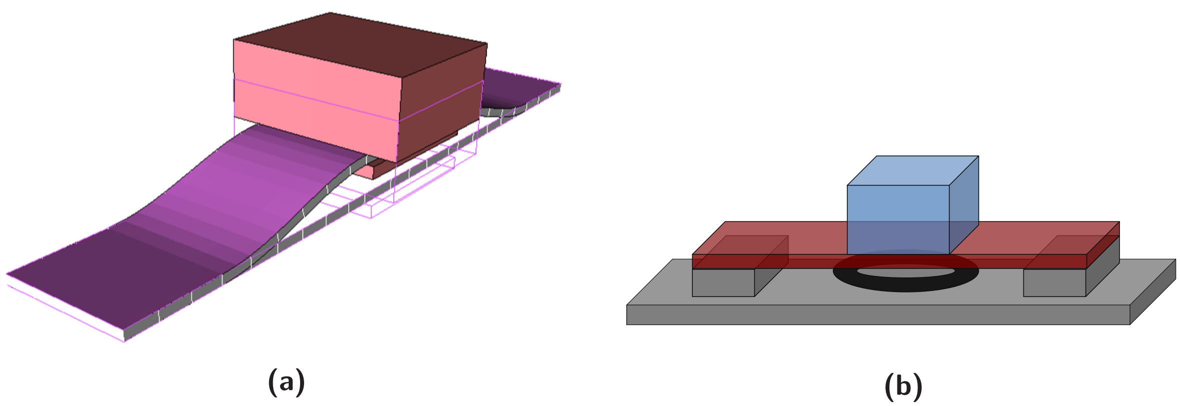

Figure 5.10: *Tuned damper for the 183 Hz resonance that makes use of internal friction. (a) FEM model of the damper. (b) Schematic representation of the damper. A mass is screwed to a bar which is bolted to the springbox. A piece of viton absorbs energy from the oscillator. The division of the bar creates two cantilever springs. The frequency of the damper is controlled by the length of the springs, its Q-factor by the amount of viton.*

The stiffness k of each beam is given by $k = 12EJ/L^3$, where $E =$ 70 GPa is the Young's modulus of aluminum and $J = wd^3/12$ is the moment of inertia of the cross section. The frequency f_d of the damper is given by $f_\mathrm{d} = \sqrt{2k/M}$ and can be tuned by adjusting the length of the clamped beams. For $L =$ 55 mm the resonance frequency of the damper will be 183 Hz.

Fig. 5.11 shows the horizontal transfer function TF_{xx} at 183 Hz with (solid curve) and without (dashed curve) the resonant damper. The damper was tuned to a frequency of 185 Hz with a Q-factor of 10. It damps the 183 Hz resonance by a factor 5.

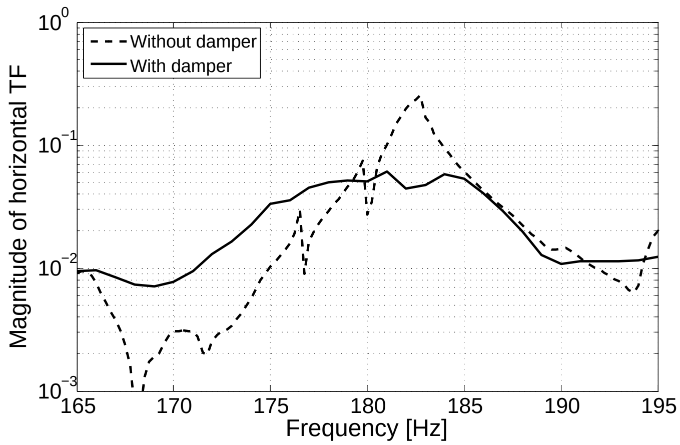

Figure 5.11: *183 Hz mode in the vertical transfer function with (solid curve) and without (dashed curve) the tuned damper. The damper reduces the amplitude of the resonance with a factor 5.*

5.3.2 Transfer function measurements

Performing a swept sine excitation of the entire EIB-SAS system with the piezoelectric shaker frame (see section 5.3.1) we were able to measure its ground to bench transfer functions. This measurement can be done in the vertical direction, the Tz tilt direction and in both horizontal directions. Good coherence between the ground sensors and those on the bench can be realized from 2 Hz upwards. We measure the transfer functions up to 400 Hz, because we do not have a measurement of the ground motion spectrum of the Virgo site above this frequency and no displacement projection is possible.

Vertical transfer function measurement between springbox and ground

The vertical isolation of the system is provided by the GAS filters. They are housed in the springbox which stands on the three inverted pendulum legs. At low frequencies, the inverted pendulum stage is tilt rigid; vertical and tilt motion of the ground is transmitted to the springbox. Due to the top flexures and tube, the leg has some vertical compliance which cause the vertical and tilt bouncing modes at 36.5, 41 and 48 Hz. Furthermore, any internal modes of the springbox will amplify the ground motion experienced by the GAS filters.

Fig. 5.12 shows the transfer function of vertical ground motion to vertical motion of the springbox. It has a large structure between 30 and 60 Hz and several peaks above 100 Hz that will amplify the motion of the ground. The three peaks between 35 and 50 Hz are the springbox bouncing modes. Those at 88 and 114 Hz do not belong to EIB-SAS, but to the piezoelectric shaker system. The collection of peaks around 350 Hz belongs to the internal modes of the GAS filter blades that we described in section 3.5.8. The remaining resonances have frequencies of: 140.5 Hz, 157 Hz, 166 Hz, 183 Hz, 238.5 Hz, 251.5 Hz and 300.5 Hz and correspond to structural modes of the springbox.

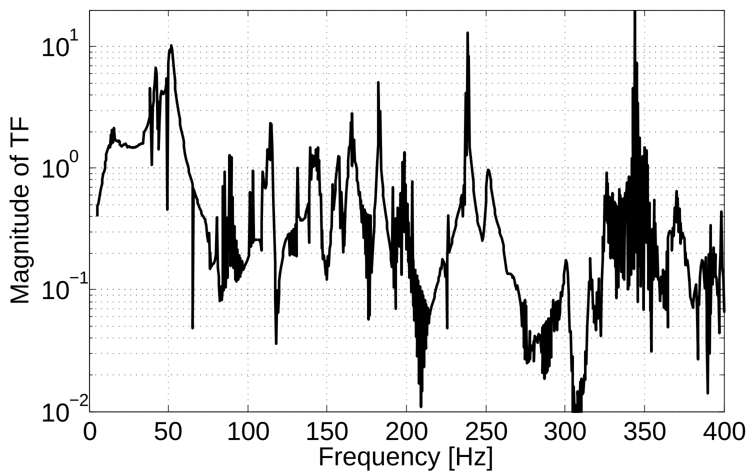

Figure 5.12: *Transfer function of vertical ground motion to vertical motion of the springbox. The resonance peaks between 35 and 50 Hz belong to the bounce modes, those at 88 and 114 Hz to the piezoelectric shaker system, those between 50 and 250 Hz to structural modes of the springbox and those between 340 and 350 Hz to internal modes of the GAS filter blades.*

Transfer function measurements of vertical ground motion

Fig. 5.13 shows the results of a vertical transfer function measurement: $\mathrm{TF}_{\mathrm{y}\to\mathrm{y}} = y_{\mathrm{bench}}/y_{\mathrm{ground}}$. It never exceeds 1, thus vertical ground motion will not be amplified at any frequency. The transfer functions roll off with f^{-2} as expected. At 10 Hz $\mathrm{TF}_{\mathrm{y}\to\mathrm{y}}$ levels off at -60 dB. Above 10 Hz a number of structures are visible.

The structure between 35 and 55 Hz is due to a resonance of the springbox. The peak at 113 Hz belongs to the piezoelectric shaker system. Finally, the peaks between 340 and 350 Hz belong to internal modes of the blades of the geometric anti-spring filters that were already identified in dedicated tapping tests discussed in section 3.5.8.

Transfer functions measurement of ground motion in the x-direction

Driving the base of EIB-SAS in the *x*-direction we can measure the system's horizontal transfer function in this direction. Due to the compliance of the GAS filters and the location of the bench's center of mass, the induced motion in the *Tz* direction is significant as well.

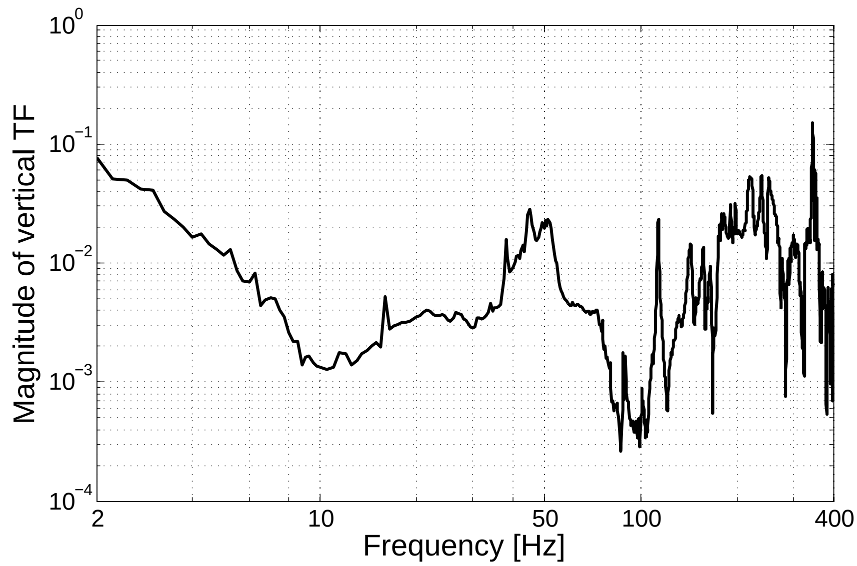

Figure 5.13: *Magnitude of vertical transfer function. The data points are listed in appendix A.*

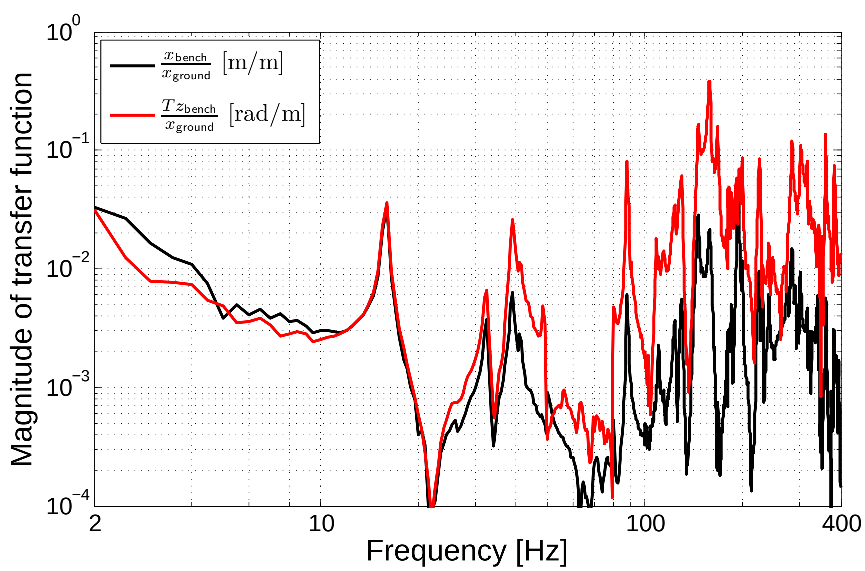

Figure 5.14: *Magnitude of the transfer functions of horizontal ground motion in the x-direction to horizontal bench motion in the x-direction (black curve) and to tilt motion in the Tz direction (red curve). The data points are listed in appendix A.*

Fig. 5.14 shows the transfer functions of horizontal ground motion in the *x*-direction to horizontal bench motion in this direction (black curve) and to the *Tz* direction (red curve): $\mathrm{TF}_{\mathrm{x}\to\mathrm{x}} = x_{\mathrm{bench}}/x_{\mathrm{ground}}$ and $\mathrm{TF}_{\mathrm{x}\to\mathrm{Tz}} = Tz_{\mathrm{bench}}/x_{\mathrm{ground}}$.

The two transfer functions look similar. The peak at 15.8 Hz belongs to the rigid body mode in the *x*-direction. The two peaks between 30 and 40 Hz are due to the non-perfect damping of the *Tz* structural mode at 36.5 Hz (see Fig. 5.9a). Springbox structural modes appear above 100 Hz. The peak at 88 Hz does not belong to EIB-SAS, but is the first mode of the shaking system. Above this frequency it is no longer guaranteed that the shaking of the system is a purely linear translational motion; tilt is also introduced. This is a limitation of the setup due to which these measurements have to be taken as an upper limit above 88 Hz.

Transfer functions measurement of ground motion in the z-direction

Fig. 5.15 shows the transfer functions of horizontal ground motion in the *z* direction to bench motion in the *z* (black curve) and the *Ty* (red curve) direction: $\mathrm{TF}_{\mathrm{z}\to\mathrm{z}} = z_{\mathrm{bench}}/z_{\mathrm{ground}}$ and $\mathrm{TF}_{\mathrm{z}\to\mathrm{Ty}} = Ty_{\mathrm{bench}}/z_{\mathrm{ground}}$.

The peaks at 12, 16 and 41 Hz correspond to the *Ty*, *z* and *Tx* rigid body modes. As already remarked in section 5.3.1 motion in the *z* direction naturally induces motion in the *Tx* and *Ty* directions. Therefore, it is no surprise that the resonances in these directions are present in these transfer functions. At 16 Hz both transfer functions have a peak that belongs to the resonance in the *z* direction, which was to be expected as we are exciting the system in this direction. Then there is a peak at 79.5 Hz that belongs to the system, but has not been identified. Above 100 Hz there are the structures of the springbox that were also present in the other transfer functions we have measured. Most significant is the structure at 225 Hz, whose amplitude is largest in $\mathrm{TF}_{\mathrm{z}\to\mathrm{z}}$.

5.3.3 Projected EIB-SAS motion spectrum

Figure 5.16 shows the projected motion spectrum of EIB-SAS at Virgo (red curve) together with that of the ground (green curve), that of the old EIB support structure (blue curve). The requirement for the motion of EIB-SAS is indicated by the dashed curve. The projection has peaks at 12 and 16 Hz that belong to the horizontal rigid body modes. In section 5.4 we will show that the control system damps these resonances to an acceptable level. The structures around 50 Hz belong to the springbox, the peaks above 100 Hz to structural modes of the springbox. The one at 225 Hz which is close to the requirement belongs to a resonance we observed in the $z_{\mathrm{ground}} \to z_{\mathrm{bench}}$ transfer function. Finally, the peaks between 340 and 350 Hz belong to internal resonances of the GAS filter blades. All in all, the projected motion spectrum of EIB-SAS is below the required limit over the entire frequency range.

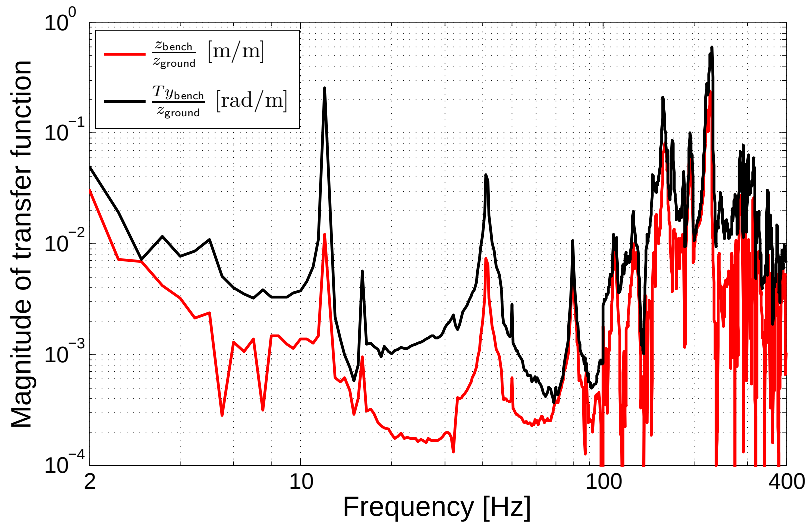

Figure 5.15: *Magnitude of the transfer functions of horizontal ground motion in the z-direction to horizontal bench motion in the z-direction (black curve) and to rotations in the Ty direction (red curve). The data points are listed in appendix A.*

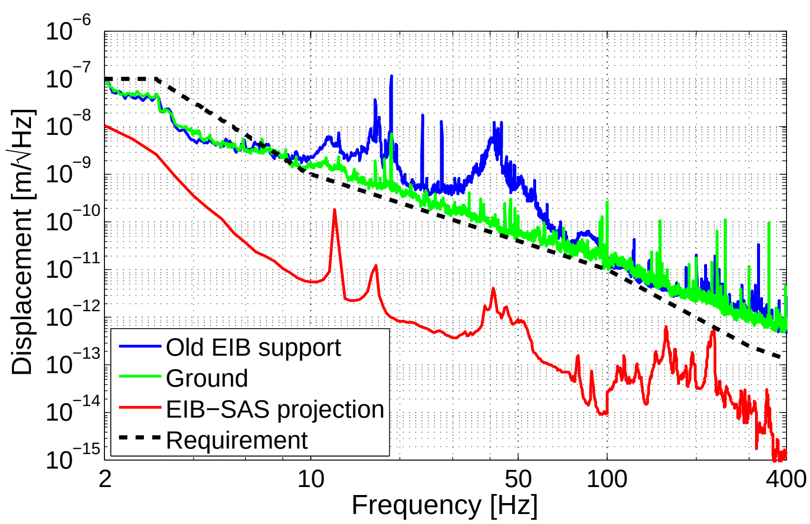

Figure 5.16: *Projected passive displacement spectrum of EIB-SAS at the Advanced Virgo site. The blue curve the displacement spectrum of the old support structure. The black dotted curve indicates the requirement. The peaks at 12 Hz and 16 Hz in the projection belong to the structural resonances in the Ty and z direction. These can be damped efficiently with active feedback (see Fig. 5.36).*

5.4 EIB-SAS control system

The inverted pendulums and geometric anti-spring filters effectively attenuate seismic ground motion above their resonance frequency, but in section 5.2.1 we saw that at this frequency they can amplify ground motion by as much as 20 dB. In EIB-SAS these rigid body modes are actively damped with a feedback controls system. In addition, the controls provide the long-term stability of the reference position.

The goal of a control system is to keep the output of the system close to a given value, the setpoint, when the system is being disturbed at its input. For EIB-SAS, the controls need to maintain its position, while the system is being disturbed by seismic ground motion.

The control scheme used for EIB-SAS is single input single output (SISO). Fig. 5.17 depicts its basic idea. The system to be controlled is represented by the plant **G**. Its properties, in our case displacement, are measured by sensors with response α. These provide the input for the controller **H**, which is called an error signal. The controller is a suitable filter which calculates the proper control signal that needs to be applied to the system in order for it to obtain, or remain in, the desired state. This correction is then applied by actuators of strength β.

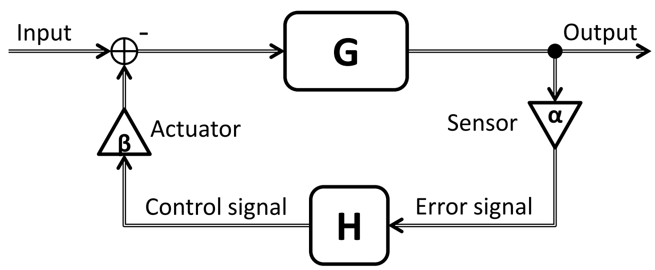

Figure 5.17: *Single input single output (SISO) control scheme.*

In the Laplace domain, the closed loop transfer function $\mathrm{TF}_{\mathrm{CL}}$ of the controlled system is

$$TF_{\mathrm{CL}} = \frac{G(s)}{1 + \alpha\beta G(s)H(s)}, \tag{5.1}$$

which shows that the application of feedback reduces the motion of the system with a factor $(1 + \alpha\beta G(s)H(s))^{-1}$, with $s = \sigma + i\omega$. The inverse Laplace transform of the closed-loop transfer function gives the impulse response of the system. In order for the controls not to amplify the response of the system, *i.e.* for the controls to be stable, the open loop transfer function

$$TF_{\mathrm{OL}} = \alpha\beta G(s)H(s), \tag{5.2}$$

may not equal -1 for any value of s, *i.e.* the phase of the open loop transfer function may not equal $-180°$, when its gain is 1.

EIB-SAS is equipped with position sensors (LVDTs) and inertial sensors (geophones) that continuously monitor the motion of the bench. The error signals for the EIB-SAS controls are generated by first, digitally, combining (*blending*) the readings of LVDTs and geophones in the frequency domain. At very low frequency (< 1 Hz) the LVDTs provide the information necessary to maintain the set point of the bench with respect to the ground, while the geophone signals are used to control the attenuator at frequencies greater than 1 Hz, well above the lowest order rigid body modes of the system, in order to not spoil the passive isolation provided by the mechanics.

The crossover frequency between position and inertial sensors is determined as the trade-off between ground noise re-injection from the LVDT contribution and low frequency noise from the geophones. Geophones have typically a self-noise larger than the ground motion below 50 mHz, and, in the case of the horizontal sensors, they suffer from tilt coupling. Due to the equivalence principle, horizontal inertial sensors cannot distinguish between a horizontal acceleration and a rotation with respect to gravity. This effect has been mitigated in EIB-SAS by locating the in-loop horizontal geophones on the springbox, which is tilt rigid by design.

Adjustments to the static position can be made with stepping motor driven positioning springs. These are out of loop and are mainly used to reposition the system after an intervention.

5.4.1 EIB-SAS coordinate frame

The Virgo coordinate system has been adopted for EIB-SAS (see Fig. 5.18). Its origin is defined as the 0 of the LVDTs, x is in the direction of the laser bench, y vertically upwards and z in the direction of the input mode cleaner.

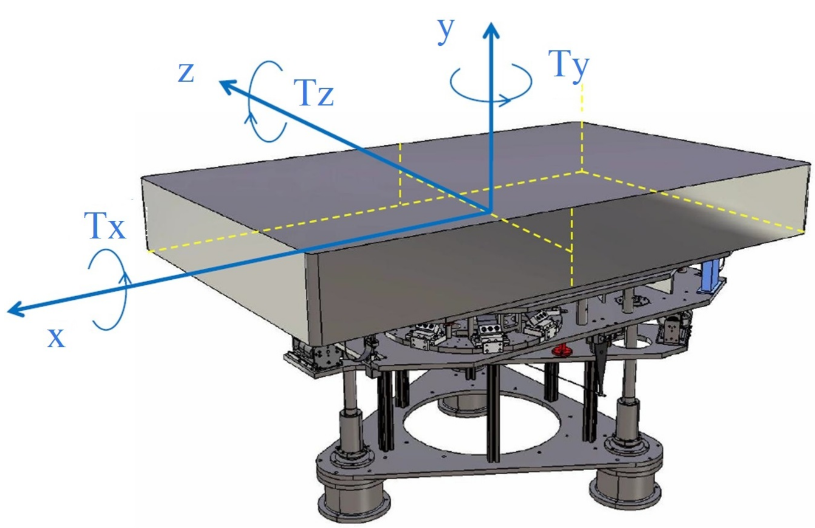

Figure 5.18: *The Virgo coordinate frame has been adopted for EIB-SAS. It is a right-handed coordinate system whose z-direction is the pointing direction of the beam, and vertical (y) direction is upwards.*

5.4.2 Sensors and actuators

Geophones

Geophones are velocity sensors. They are essentially damped harmonic oscillators that produce a voltage which is proportional to the velocity difference between the suspended reference mass and its housing.

Fig. 5.19 shows the electromechanical model of a geophone. The reference mass M is suspended by a spring of stiffness k. The dashpot represents a viscous damping force of strength b. A pick-up coil is attached to the mass. Due to the suspension, the mass does not directly follow the motion of the casing and an electromotive force $\mathcal{E}$ is induced in the pick-up coil by a permanent magnet which is attached to the geophone housing. This electromotive force is given by

$$\mathcal{E} = -\frac{\partial \Phi}{\partial t} = -\frac{\partial \Phi}{\partial x} v_{\mathsf{M}}, \tag{5.3}$$

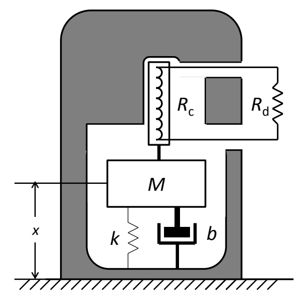

Figure 5.19: *Geophone electromechanical model.*

where Φ is the flux through the pick-up coil and v_{M} its velocity relative to the housing. The geophone sensitivity G is defined as $G = \mathcal{E}/v_{\mathsf{M}}$ and has units V/(m/s).

The geophone signal is read over a loading resistor R_{d} placed parallel to the pick-up coil, which has a series resistance R_{c}*. In the Laplace domain, the response of a geophone is then given by

$$H_{\mathsf{geo}} = G \frac{R_{\mathsf{d}}}{R_{\mathsf{d}} + R_{\mathsf{c}}} \frac{s^2}{\omega_0^2 + 2\omega_0 \zeta s + s^2} \quad \left[\frac{\mathsf{V}}{\mathsf{m/s}}\right], \tag{5.4}$$

where $\omega_0 = \sqrt{k/M}$ is the resonance frequency of the system and ζ is the damping coefficient of the system, which is given by

$$\zeta = \frac{1}{2M\omega_0}\left(b + \frac{G^2}{R_{\mathsf{c}} + R_{\mathsf{d}}}\right). \tag{5.5}$$

The signal to noise ratio of the geophone is dominated by the Johnson noise of the electronic circuit and the suspension thermal noise S_{nn} and was derived by Rodgers [105].

Johnson noise is a voltage that is generated randomly in the pick-up coil and damping resistor. The amplitude spectral density of the Johnson noise J_{nn} is given by

$$J_{\mathsf{nn}} = \sqrt{4 k_{\mathsf{B}} T \left(\frac{R_{\mathsf{d}} R_{\mathsf{c}}}{R_{\mathsf{d}} + R_{\mathsf{c}}}\right)} \quad \left[\mathsf{V}/\sqrt{\mathsf{Hz}}\right], \tag{5.6}$$

*The coil inductance is not included in the model, because it does not affect the sensor's response in the frequency region of interest.

where k_B is Boltzmann's constant and $T = 293$ K is the absolute temperature of the pick-up coil and damping resistor. For EIB-SAS J_nn ranges from 5 to 10 nV/$\sqrt{\mathrm{Hz}}$ depending on the sensor.

Suspension thermal noise arises from the Brownian motion of the reference mass. The amplitude spectral density of this random motion of the mass and pick-up coil is given by

$$A_\mathrm{nn} = \sqrt{\frac{8k_\mathrm{B}T\zeta\omega_0}{M}} \quad \left[\frac{\mathrm{m/s^2}}{\sqrt{\mathrm{Hz}}}\right], \tag{5.7}$$

which is equivalent to a displacement spectrum

$$S_\mathrm{nn} = \frac{A_\mathrm{nn}}{s^2} \quad \left[\mathrm{m}/\sqrt{\mathrm{Hz}}\right]. \tag{5.8}$$

To preserve the signal-to-noise ratio in the digitization process, each geophone is equipped with a low-noise preamplifier that is based on a chopper-stabilized CS3001 operational amplifier. It has a gain of 940. The total electronic noise of the amplifier is given by

$$E_\mathrm{nn} = \sqrt{V_{00}\left(1+\frac{f_\mathrm{cv}}{f}\right) + I_{00}\left(1+\frac{f_\mathrm{ci}}{f}\right)R_\mathrm{v}^2 + 4k_\mathrm{B}TR_\mathrm{v}} \quad \left[\mathrm{V}/\sqrt{\mathrm{Hz}}\right], \tag{5.9}$$

where $V_{00} = 3.6\times10^{-17}$ V^2/Hz represents the input voltage noise power spectral density, $f_\mathrm{cv} = 0.08$ Hz is the corner frequency of the voltage noise, $I_{00} = 10^{-26}$ A^2/Hz represents the input current noise power spectral density and, $f_\mathrm{ci} = 100$ Hz is the corner frequency of the current noise and R_v is the parallel replacement of R_d and R_c. The last term is the Johnson noise associated with R_v.

The three noise sources are uncorrelated, so the displacement noise of the geophone-amplifier combination D_nn is given by

$$D_\mathrm{nn} = \sqrt{\frac{J_\mathrm{nn}^2}{sH_\mathrm{geo}} + S_\mathrm{nn} + \frac{E_\mathrm{nn}^2}{sH_\mathrm{geo}}} \quad \left[\mathrm{m}/\sqrt{\mathrm{Hz}}\right]. \tag{5.10}$$

Figure 5.20 shows the total displacement noise D_nn and the contributions of the Johnson noise and suspension thermal noise of the L22E geophone. The sensitivity of the geophone is limited by Johnson noise and the noise of the amplifier.

EIB-SAS incorporates a total of twelve geophones. The top stage is equipped with three horizontal L-4C and three vertical L-22E geophones from Sercel and the springbox with three horizontal GS-1 geophones from Geospace. Two of these and one vertical HS-1 geophone from the same manufacturer are used to monitor the motion of the ground. Their properties are listed in Table 5.3. Their positions on EIB-SAS are shown in Fig. 5.22.

Fig. 5.21 shows the noise curves of the geophones together with the EIB-SAS displacement requirement. The horizontal GS-1 geophones on the springbox and vertical L-22E geophones on the bench are used in the controls. The sensitivity of each geophone is well below the displacement requirement for EIB-SAS.

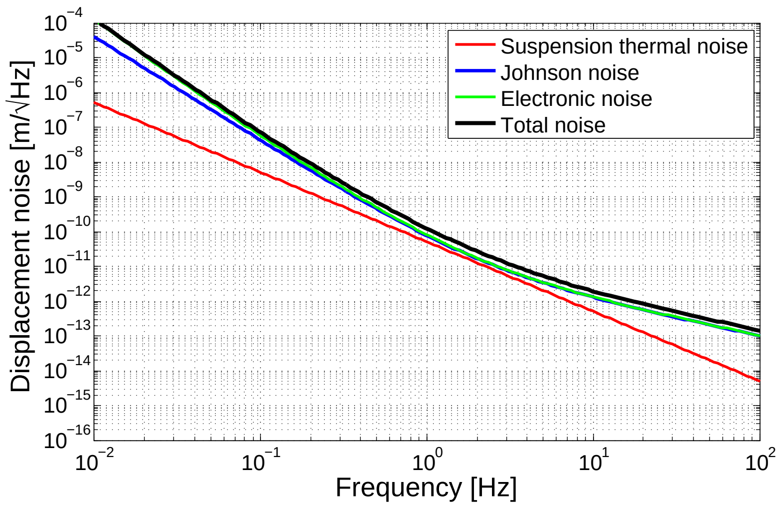

Figure 5.20: *Contributions of Johnson noise, suspension thermal noise and electronics noise of the pre-amplifier to the noise floor of the L22E geophone-amplifier combination.*

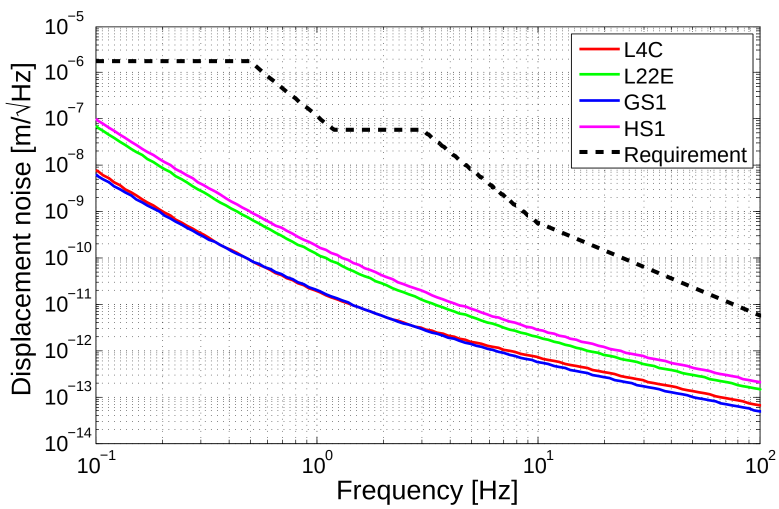

Figure 5.21: *Geophone sensitivity curves and the displacement noise requirement of EIB-SAS.*

Geophone	ω_0 (Hz)	ζ	R_c(kΩ)	R_d(kΩ)	G (V/(m/s))	M (g)
Sercel L-4C	1 $\pm$5%	0.28	5.5	open	280	965
Sercel L-22E	2 $\pm$10%	0.71	2.2	open	98	72.8
Geospace GS-1	1 $\pm$10%	0.7	4.55	100	354	700
Geospace HS-1	2 $\pm$10%	0.7	3.8	100	80	22.7

Table 5.3: *Properties of the geophones used in EIB-SAS.*

Voice-coil actuators and LVDT position sensors

Figs. 5.22a and 5.22b show the positions of the LVDT (linear variable differential transformer) position sensors [106]. Three vertical ones are situated at the center of the GAS filters, three horizontal ones on a circle centered around the center of the springbox.

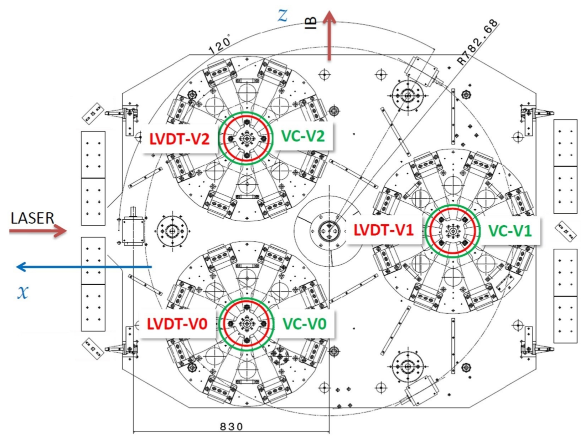

(a)

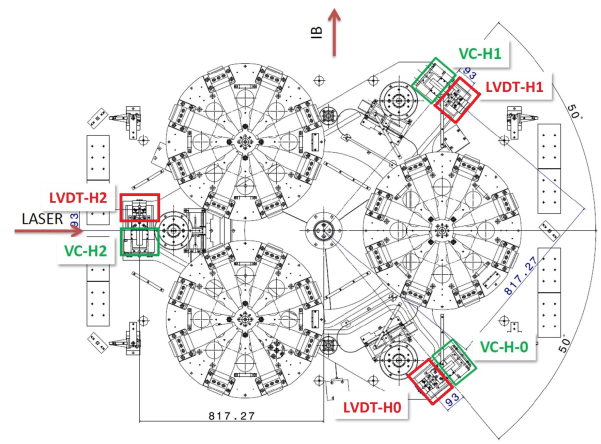

(b)

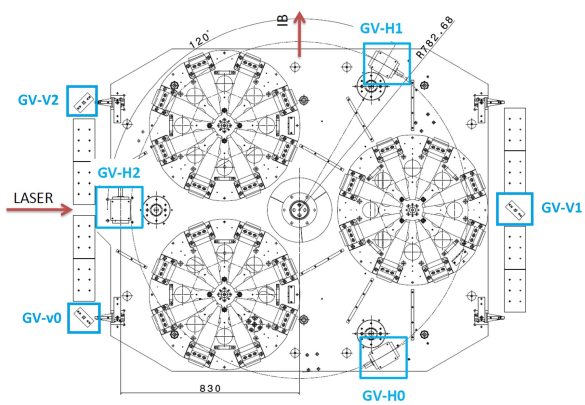

(c)

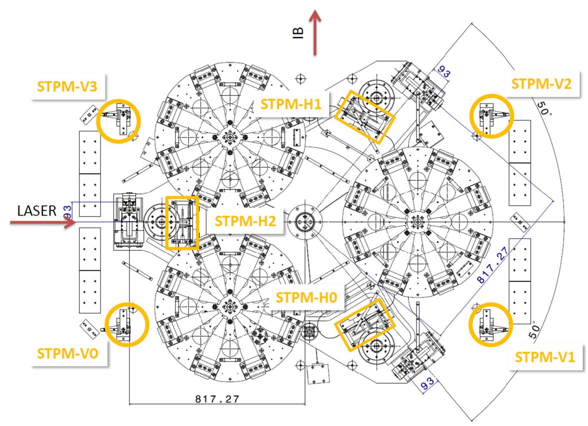

(d)

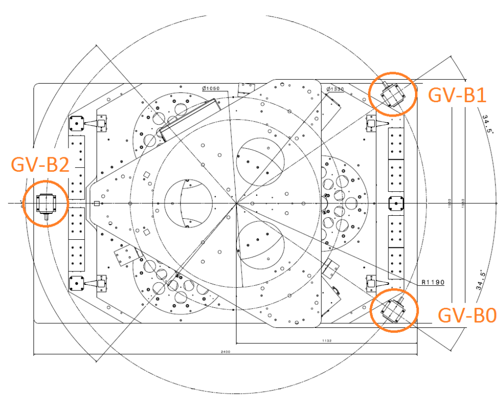

(e)

Figure 5.22: *Positions of the vertical and horizontal:*
(a) *LVDTs (LVDT-V/H),*
(b) *voice-coil actuators (VC-V/H),*
(c) *horizontal springbox geophones (GV-H), and vertical bench geophones (GV-V).*
(d) *stepper motors (STPM-V/H),*
(e) *and horizontal top stage geophones (GV-B).*

Each LVDT is composed of three coils. The primary coil of radius r_{pc} is placed inside the two secondary coils, such that the central axes of the coils coincide. The primary coil is driven with a 10 kHz sine-wave. The secondary coils are wound in opposite directions and connected in series. Therefore, no net signal is induced when the primary coil is exactly in the center.

The secondary coils are in a so-called Maxwell-pair configuration. The separation distance between the coils $d_{\mathrm{s}} = r_{\mathrm{pc}}\sqrt{3}$, which provides a uniform field gradient within the LVDT. This permits the output voltage of the LVDT to be proportional to displacement within 1% over a region of 8 mm. The electronic readout has a noise level of about 1 nm/$\sqrt{\mathrm{Hz}}$.

EIB-SAS is equipped with three vertical and three horizontal voice-coil actuators [107]. The vertical actuators are co-axially located with the LVDTs at the center of the GAS filters. A ring of permanent magnets is attached to the bottom of the springbox, a coil is attached to the bottom of the keystone. A force is applied to the top stage by inducing a current in the coil. The force exerted by the vertical actuators is 13 N/A. The maximum current that can be driven through their coils is ± 0.15 A, so that the peak force that can be applied with the actuators is 5.85 N. This allows them to compensate for a temperature difference of ± 3 K (see section 5.4.5). The horizontal actuators provide 5 N/A and have a maximum current of ± 0.06 A. They can exert a maximum force of 0.9 N.

As can be seen in Fig. 5.23, the horizontal voice-coil actuators are co-axially located with the horizontal LVDTs. The coil stands on the reference frame, a yoke containing permanent magnets is hanging from the springbox. These actuators need to deliver a constant force, within 1%, in a region of 10 mm in the horizontal plane. To accomplish this special care has been taken in the design of their racetrack coil and magnetic yoke. With these actuators, the top stage can be positioned within the resolution of the LVDTs.

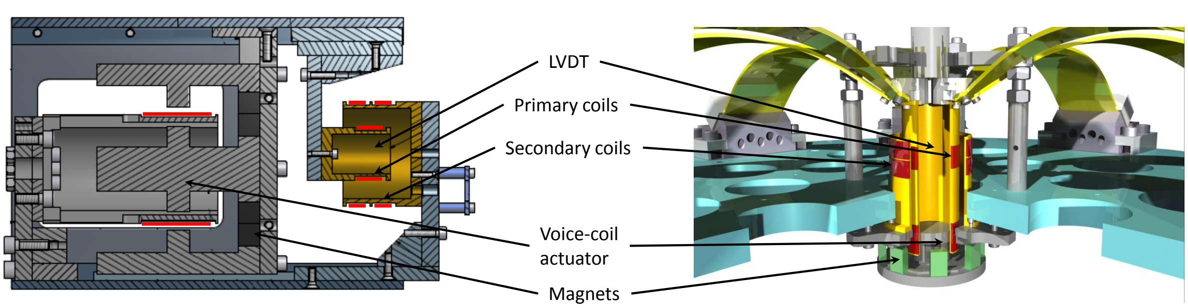

(a) *Horizontal unit.* **(b)** *Vertical unit.*

Figure 5.23: *Schematic representation of the vertical and horizontal LVDT voice-coil actuator units. In both units, the LVDT and actuator are co-axially located.*

Static positioning

EIB-SAS is furnished with three horizontal and four vertical stepping motor driven positioning springs to translate and rotate the bench. The vertical and horizontal positioning spring units are depicted in Fig. 5.24. The motors are Sanyo denki 103H5210-0440 motors that are regulated remotely with Sixpack2 controller units from Trinamic.

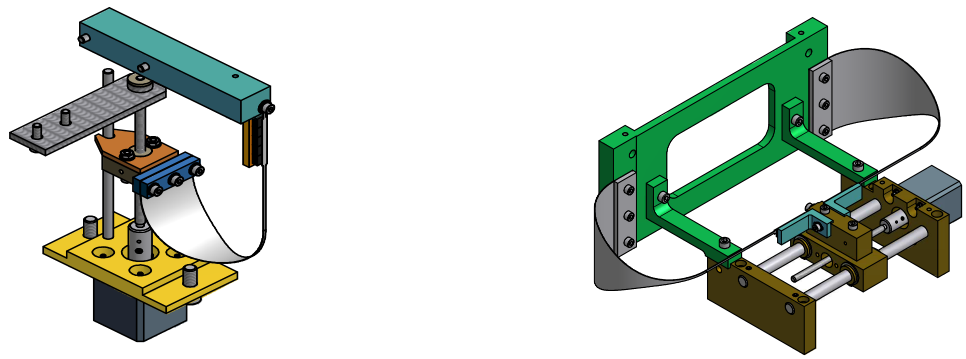

(a) **(b)**

Figure 5.24: *Vertical (a) and horizontal (b) stepping motor units. The vertical unit consists of a single cantilever blade whose base is attached to a stepper motor, and whose tip is attached to the bench. The horizontal unit has two cantilever blades, which makes its response more linear (see Fig. 5.25). The stepper motor acts on the tip of the blades. The base of the blades are attached to the springbox.*

The horizontal units are located on the reference platform and act on the springbox. The four vertical units are placed on the four corners of the springbox and act directly on the top stage. Fig. 5.25 shows the force delivered by the vertical (dots) and horizontal (squares) positioning springs as a function of displacement. The response of the horizontal springs is more linear than that of the vertical one, because there are two; when one spring pushes the other pulls. Together they deliver a force of ±7 N. The vertical unit only contains a single spring that delivers a force between −2 and +4 N. With these motorized adjustment springs the springbox and bench can be translated by ∼10 mm. End switches are in place to automatically interrupt the motors when they get out of range. With these motorized springs the bench can be positioned within an accuracy of 1 µm and 1 µrad.

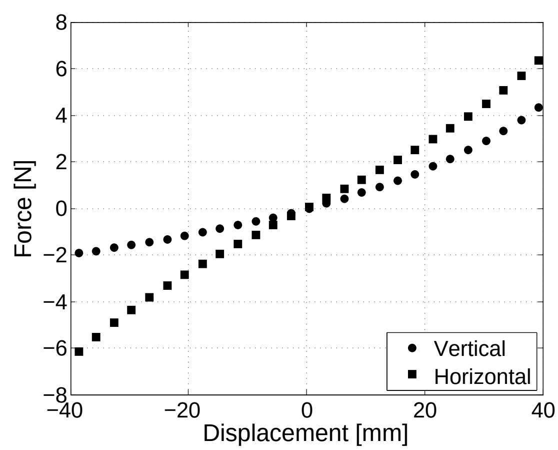

Figure 5.25: *Force exerted by the motorized positioning springs.*

5.4.3 Virtual sensors and actuators

The real LVDT and geophone signals are recombined to create *virtual* LVDTs and geophones that are only sensitive to motion along one of the coordinate axes. The first step in creating these virtual sensors is converting all sensor output to displacements. The LVDT response is proportional to displacement. They deliver 5.04×10^{-3} V/μm, hence

$$\mathsf{LVDT}\,[\mu\mathsf{m}] = \frac{\mathsf{LVDT}\,[\mathsf{V}]}{5.04\times10^{-3}}\,. \tag{5.11}$$

The response of the geophones is frequency-dependent. The response function $H_{\text{geo}}(s)$, given by Eq. (5.4), of every geophone has been calibrated by placing them on the ground next to a Trillium 240 seismometer and comparing their readings. An additional factor $1/s$ is added to convert the geophone signals from velocities to displacement;

$$\mathsf{GV}\,[\mu\mathsf{m}] = \frac{1}{\mathsf{sH_{geo}(s)}}\mathsf{GV}\,[\mathsf{V}]\,. \tag{5.12}$$

To remove the low-frequency response that is not used in the control of EIB-SAS, the geophone signals are digitally filtered with a fourth order high-pass filter

$$H_{\text{HP}} = \frac{s^2}{0.02+0.2s+s^2}\cdot\frac{0.4s+s^2}{0.02+0.2s+s^2}\quad(s_{\text{c}} = 0.1\ \text{rad/s}), \tag{5.13}$$

where s_{c} is the corner frequency of the filters. The second filter has a zero at $s = 0.4$ rad/s instead of at $s = 0$ rad/s to limit the phase delay of the signal at low frequency.

In order to obtain measurements along the chosen coordinates, the read-out of the real sensors is combined based purely on their measured location. The matrix that diagonalizes the system and transforms the real sensors y to the virtual sensors $\tilde{y}$ is known as the *sensing matrix*, *S*

$$\tilde{y} = Sy. \tag{5.14}$$

The sensing matrices for the EIB-SAS LVDTs and geophones are

$$
\begin{aligned}
\begin{pmatrix} \text{LVDT-X} \\ \text{LVDT-Ty} \\ \text{LVDT-Z} \end{pmatrix} &= \begin{pmatrix} -0.65270 & 0.65270 & 0 \\ 0.37421 & 0.37421 & 0.47863 \\ 0.30436 & 0.30436 & -0.60872 \end{pmatrix} \begin{pmatrix} \text{LVDT-H0} \\ \text{LVDT-H1} \\ \text{LVDT-H2} \end{pmatrix}, \\
\begin{pmatrix} \text{LVDT-Tx} \\ \text{LVDT-Tz} \\ \text{LVDT-Y} \end{pmatrix} &= \begin{pmatrix} 1.2716 & 0 & -1.2716 \\ -1.1456 & 0.5728 & 0.5728 \\ 0.30073 & 0.39854 & 0.30073 \end{pmatrix} \begin{pmatrix} \text{LVDT-V0} \\ \text{LVDT-V1} \\ \text{LVDT-V2} \end{pmatrix}, \\
\begin{pmatrix} \text{GP-X} \\ \text{GP-Ty} \\ \text{GP-Z} \end{pmatrix} &= \begin{pmatrix} -0.8828 & 0.8828 & 0 \\ 0.2303 & 0.2303 & 0.3797 \\ -0.2741 & -0.2741 & 0.5428 \end{pmatrix} \begin{pmatrix} \text{GP-H0} \\ \text{GP-H1} \\ \text{GP-H2} \end{pmatrix}, \\
\begin{pmatrix} \text{GP-Tx} \\ \text{GP-Tz} \\ \text{GP-Y} \end{pmatrix} &= \underbrace{\begin{pmatrix} 1.003 & 0 & -1.003 \\ 0.2496 & -0.4992 & 0.2496 \\ 0.25 & 0.5 & 0.25 \end{pmatrix}}_{S} \begin{pmatrix} \text{GP-V0} \\ \text{GP-V1} \\ \text{GP-V2} \end{pmatrix}.
\end{aligned}
\tag{5.15}
$$

Sensor blending

Geophones have a poor performance at very low frequency and generally they are not able to resolve the ground motion below 30 mHz. Therefore, it is necessary to control EIB-SAS on the LVDT signals below a certain frequency. The LVDT and geophone signals are respectively weighed with a low-pass and high-pass filter with the cross-over frequency at $s_0 = 6$ rad/s (0.95 Hz) to form a so-called virtual sensor:

$$
\text{Virtual sensor} = \frac{s_0^5 + 5s_0^4 s + 10s_0^3 s^2}{(s+s_0)^5}\ \text{LVDT} + \frac{s^5 + 5s_0 s^4 + 10s_0^2 s^3}{(s+s_0)^5}\ \text{geophone}. \tag{5.16}
$$

Note that the numerators of these two filters add up to $(s+s_0)^5$, so the filters add up to 1. These are the virtual sensors that provide the error signals for the various control loops.

In principle, since the LVDTs measure the position of the bench with respect to the ground, the controls benefit from setting the blending frequency as low as possible. Nevertheless, limitations on the blending frequency are imposed by the sensitivity of the horizontal geophones to the parasitic tilt of the springbox (the so-called cradle effect) due to machining and assembling inaccuracies, and ultimately to the ground tilt, which is known to be particularly severe around the micro-seismic peak in bad weather conditions. A method to mitigate the consequences of the cradle effect is to implement the so-called *sensor correction* scheme.

Sensor correction

To bring the motion of the bench below that of the ground, the LVDT signal is corrected by adding the signal from the geophones that are used to monitor the ground, $\mathrm{geo_{gr}}$. The corrected LVDT signal is given by

$$\mathrm{LVDT_{cor}} = \left(\frac{s^2}{0.02 + 0.2s + s^2} \times \frac{s^2}{0.08 + 0.4s + s^2}\right) \mathrm{geo_{gr}} + \mathrm{LVDT}. \tag{5.17}$$

The signals of the ground monitoring geophones are weighed with a fourth order high-pass filter, with corner frequencies of $s = 0.1$ Hz and $s = 0.2$ Hz. This is necessary, because at low frequencies (< 0.1 Hz) the geophone signals start to be dominated by noise. The high-pass filter needs to roll off faster than the noise of the geophones increases in order not to spoil the corrected LVDT signal.

In order for sensor correction to work the geophones need to be precisely calibrated at low frequencies. This is achieved by placing all geophones next to a broadband seismometer Trillium 240, which has excellent low-frequency performance, and reshaping their sensitivity curves off-line so that their response is identical to that of the Trillium.

Diagonalization of the actuators

Similar to the virtual sensors, the actuators are combined into virtual actuators which only act on a single degree of freedom *i.e.* only induce motion observed in one virtual sensor. The matrix transforming the virtual actuators to the real actuators is knows as the *driving matrix*, *D*

$$u = D\tilde{u}. \tag{5.18}$$

A first diagonalization of the actuators is made based on their position. Further diagonalization is done by injecting a sinusoidal signal with the actuators at a frequency well below the resonance frequencies of the GAS filters and IPs; typically 40 mHz. At this frequency the transfer function of the mechanical filters is 1 and the transfer functions from the virtual actuator to all virtual sensors are measured. If the virtual actuators are constructed correctly, then acting on one degree of freedom will only induce a signal in the virtual sensor of that degree of freedom. Taking the inverse of the matrix of transfer functions and multiplying it with the original actuation matrix diagonalizes the actuators. This process of measuring the transfer functions and adjusting the actuation matrix can be repeated to obtain an increasingly diagonalized system. For the EIB-SAS generally two, or three iterations are needed to make the transfer function between the actuated and sensed degree of freedom equal to $1 \pm 2\%$, with off-diagonal terms of the actuation matrix smaller than 0.03.

The actuation matrices for EIB-SAS are

$$
\begin{aligned}
(\text{Act-V0},\ \text{Act-V1},\ \text{Act-V2}) &= \begin{pmatrix} -7.3\times10^{-3} & -0.4\times10^{-3} & -7.9\times10^{-3} \\ -4.8\times10^{-3} & 8.2\times10^{-3} & 4.6\times10^{-3} \\ -6.5\times10^{-3} & -6.1\times10^{-3} & -6.1\times10^{-3} \end{pmatrix} \begin{pmatrix} \text{Act-Tx} \\ \text{Act-Tz} \\ \text{Act-Y} \end{pmatrix}, \\
(\text{Act-H0},\ \text{Act-H1},\ \text{Act-H2}) &= \underbrace{\begin{pmatrix} -32.8\times10^{-3} & 33.3\times10^{-3} & -0.6\times10^{-3} \\ -12.6\times10^{-3} & 11.9\times10^{-3} & 2.7\times10^{-3} \\ 20.6\times10^{-3} & 19.7\times10^{-3} & -24.2\times10^{-3} \end{pmatrix}}_{D} \begin{pmatrix} \text{Act-X} \\ \text{Act-Ty} \\ \text{Act-Z} \end{pmatrix},
\end{aligned}
$$

where all the element of D have been multiplied with the gain of the actuators so that they are in dimensions of [V/µm] or [V/µrad].

5.4.4 Control filters

For EIB-SAS, each degree of freedom is sensed an controlled independently. Hence, the control loops are single-input single-output (SISO) controllers. Furthermore, each of the six SISO control loops are split into two parallel paths. A viscous damping loop which lowers the Q-factor of the rigid body modes and a positioning loop which provides long-term stability of the DC position.

Viscous damping loop

The viscous damping loop consists of a Butterworth filter with a corner frequency $s_c = 100$ rad/s that produces a restoring signal proportional to the velocity of the system

$$H_{\text{VD}} = \frac{s}{1 + 0.01s + 5\times10^{-5}s^2} \quad (s_c = 100 \text{ rad/s}). \tag{5.19}$$

It is high-pass filtered with

$$H_{\text{HP2}} = \frac{s^2}{0.002 + 0.02s + s^2} \quad (s_c = 0.01 \text{ rad/s}), \tag{5.20}$$

to eliminate the DC contribution. The same filter is used for all six degrees of freedom. The full viscous damping loop is given by

$$H_{\text{vis}} = H_{\text{VD}} \times H_{\text{HP2}}. \tag{5.21}$$

A Bode plot of the filter is shown in Fig. 5.26 (red curve). It has significant gain above 0.2 Hz and damps the low-frequency as well as the high-frequency rigid body modes. It is always engaged to prevent large excitations. This is for instance helpful when adjusting the DC position with the stepping motors.

PID control

The position loop maintains the DC position of the system and thus provides the long-term stability of EIB-SAS. It is a PID filter with a large DC gain and adjustable set point. Its error signal is provided by the virtual sensors. To avoid oscillations and saturation of the actuators it is only engaged when the viscous damping control loop is active. For the same reason this loop is ramped up slowly (300 seconds). The applied PID filter has a proportional gain of 1.5, an integral gain of $0.5/s$ and a differential gain of $4s$:

$$H_{\mathsf{PID}} = \frac{0.5 + 1.5s + 4s^2}{0.005 + s}. \tag{5.22}$$

Once fully engaged, it has a higher gain than the viscous damping loop. Its signal is low-pass filtered with two Butterworth filters

$$H_{\mathsf{LP1}} = \frac{1.8 \times 10^5}{s^2 + 600s + 1.8 \times 10^5}, \quad (\mathsf{s_c} = 500 \text{ rad/s}), \tag{5.23}$$

$$H_{\mathsf{LP2}} = \frac{5 \times 10^5}{s^2 + 1000s + 5 \times 10^5}, \quad (\mathsf{s_c} = 300 \text{ rad/s}). \tag{5.24}$$

Furthermore a phase lead-lag filter is applied to compensate the phase

$$H_{\mathsf{LL}} = \frac{s^2 + 400s + 4 \times 10^4}{s^2 + 80s + 4 \times 10^4}, \tag{5.25}$$

and a flat filter with a notch at the Nyquist frequency

$$H_{\mathsf{notch}} = \frac{s^2 + 2s + 39478416}{s^2 + 300s + 39478416} \quad (f_{\mathsf{Nyquist}} = 2 \text{ kHz}), \tag{5.26}$$

ensures that the control signal vanishes at the Nyquist frequency.

These filters are used for the horizontal degrees of freedom. Those of the vertical degrees of freedom are almost identical, the only difference being that the second Butterworth filter also has a cut-off frequency of $s = 500$, which was done to increase the stability of the control loop. The full position control loops for the vertical ($Tx,\ Tz,\ y$) and horizontal ($x,\ Ty,\ z$) degrees of freedom are given by

$$H_{\mathsf{pos\_V}} = H_{\mathsf{PID}} \times H_{\mathsf{LP2}}^2 \times H_{\mathsf{LL}} \times H_{\mathsf{notch}}, \quad \text{and} \tag{5.27}$$

$$H_{\mathsf{pos\_H}} = H_{\mathsf{PID}} \times H_{\mathsf{LP1}} \times H_{\mathsf{LP2}} \times H_{\mathsf{LL}} \times H_{\mathsf{notch}}. \tag{5.28}$$

Fig. 5.26 (blue curve) shows the Bode plots of these two filters. At the frequencies of the rigid body modes the differential part of the filter dominates. At DC only the integrator plays a role. It has a memory of 20 minutes and the DC gain of the filter is 100.

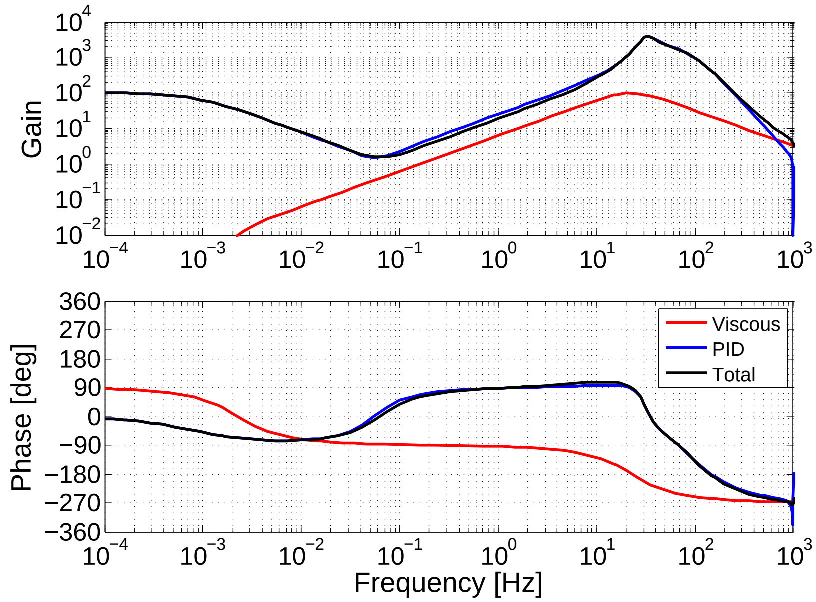

(a)

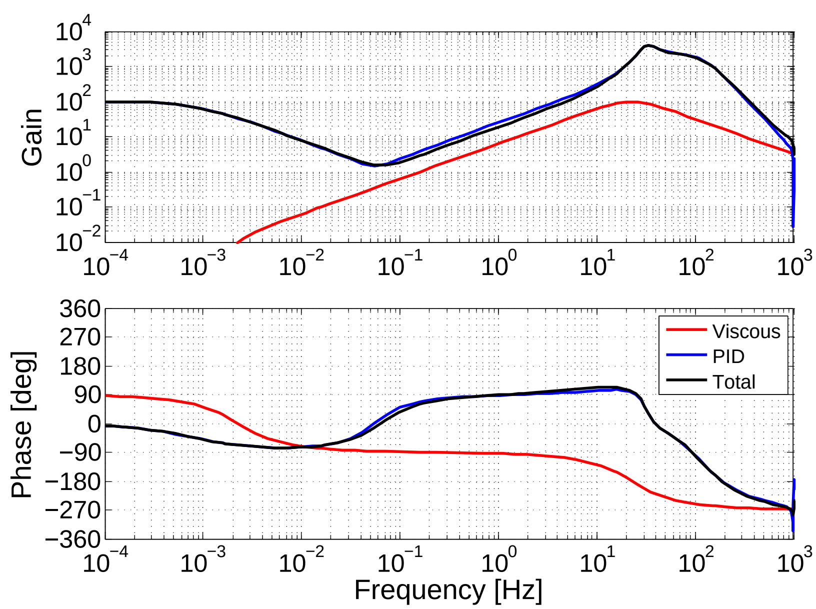

(b)

Figure 5.26: *Bode plots of the control filters for a) horizontal and b) vertical degrees of freedom.*

Total control filter

The full control filter H_c is obtained by summing the contributions of the position and viscous damping filters

$$H_\mathrm{c} = H_\mathrm{vis} + H_\mathrm{pos}. \tag{5.29}$$

The Bode plot of H_c is shown in Fig. 5.26 (black curve). The full control scheme for EIB-SAS is summarized in Fig. 5.27.

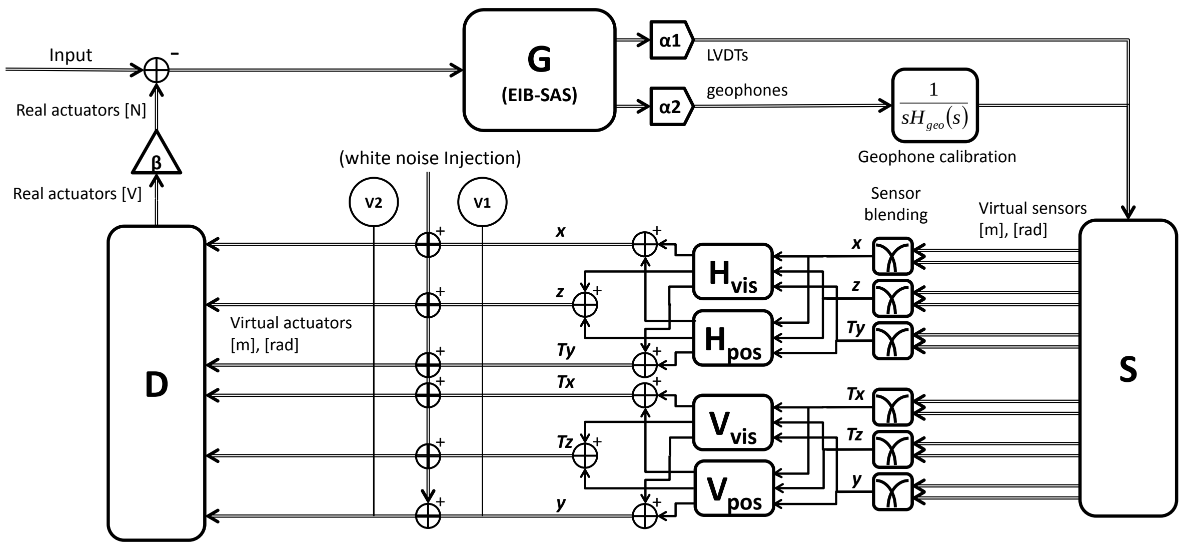

Figure 5.27: *EIB-SAS control scheme. The motion of EIB-SAS is monitored with LVDT position sensor and geophones. The sensing matrix S converts the real sensors into virtual sensors, each sensitive in only a single degree of freedom. The readings of the virtual LVDTs and geophones of each degree of freedom are combined (blended) to form a single error signal. In this way six error signals are obtained; one for each degree of freedom. These error signals are the input for two parallel control loops: the viscous damping loop, and the position loop. The sum of these two control loops is the correction signal that should be applied by the virtual actuators. The driving matrix D transforms these into real actuation signals that are applied by the real actuators.*

Stability of the controls

In order for the controls to be stable the open loop transfer function given by Eq. (5.2) may never equal -1. That is, its gain may need to be higher than 1, when the phase is greater than -180°. A quantitative measure for how far the system is from becoming unstable is given by the *gain and phase margins*, which can easily be obtained from a Bode plot. Fig. 5.28 shows a graphical representation of the procedure. The frequency at which the gain of the loop $G \equiv 1$ is called the unity gain frequency ω_{UGF}, or control bandwidth. Denoting the phase of the loop at this frequency ϕ_{UGF} the phase margin of the system is defined as $180° - \phi_{\mathsf{UGF}}$. Denoting the gain at the frequency at which the phase of the loop is 180° as $G_{180°}$, the gain margin is defined as $1/G_{180°}$.

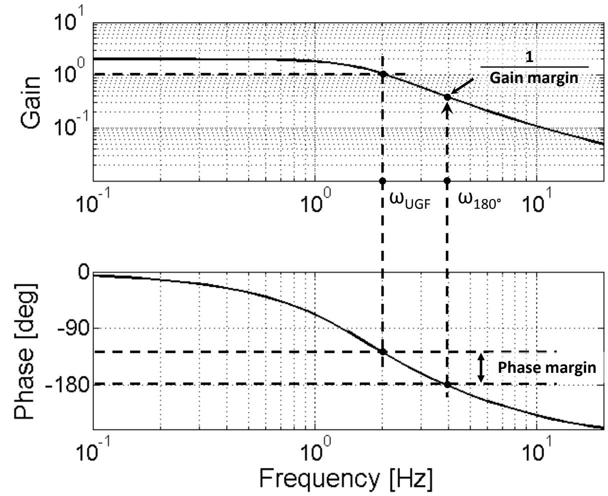

Figure 5.28: *Phase and gain margins.*

EIB-SAS open loop transfer functions

The open loop transfer function of EIB-SAS is given by Eq. (5.2), where the plant *G* for the vertical and horizontal (*z*) degrees of freedom is given by the force-displacement response functions calculated in chapter 4. The control filter *H* is given by Eq. (5.29) and α and β are the gains of the LVDTs and actuators. Their product gives the theoretical open loop transfer function, which is shown in Fig. 5.29.

When the controls are engaged, the open loop transfer function can be measured by injecting white noise, which is added to the control signals, and monitoring the applied control signal. The open loop transfer function $\mathsf{TF}_{\mathsf{OL}} = V1/V2$ (see Fig. 5.27). A meaningful measurement can only be done when the coherence between these two signals is high.

A measurement of the open loop transfer function has been performed where white noise was injected between 0.1 and 50 Hz. Fig. 5.30 shows the coherence between the input signal and the error signal during the noise injection. Fig. 5.29 shows the measurement in the *y* and *z* degrees of freedom together with the theoretical prediction. Above 0.5 Hz the measured transfer functions are well described by the model. Above 30 Hz the vertical measurement starts to deviate from the model. This is because at this frequency not enough noise is injected and the coherence between the noise and the control signal starts getting low. Between 0.1 and 0.6 Hz the coherence is also low. In both cases the motion from the environmental disturbances is higher than the one induced by the injected noise.

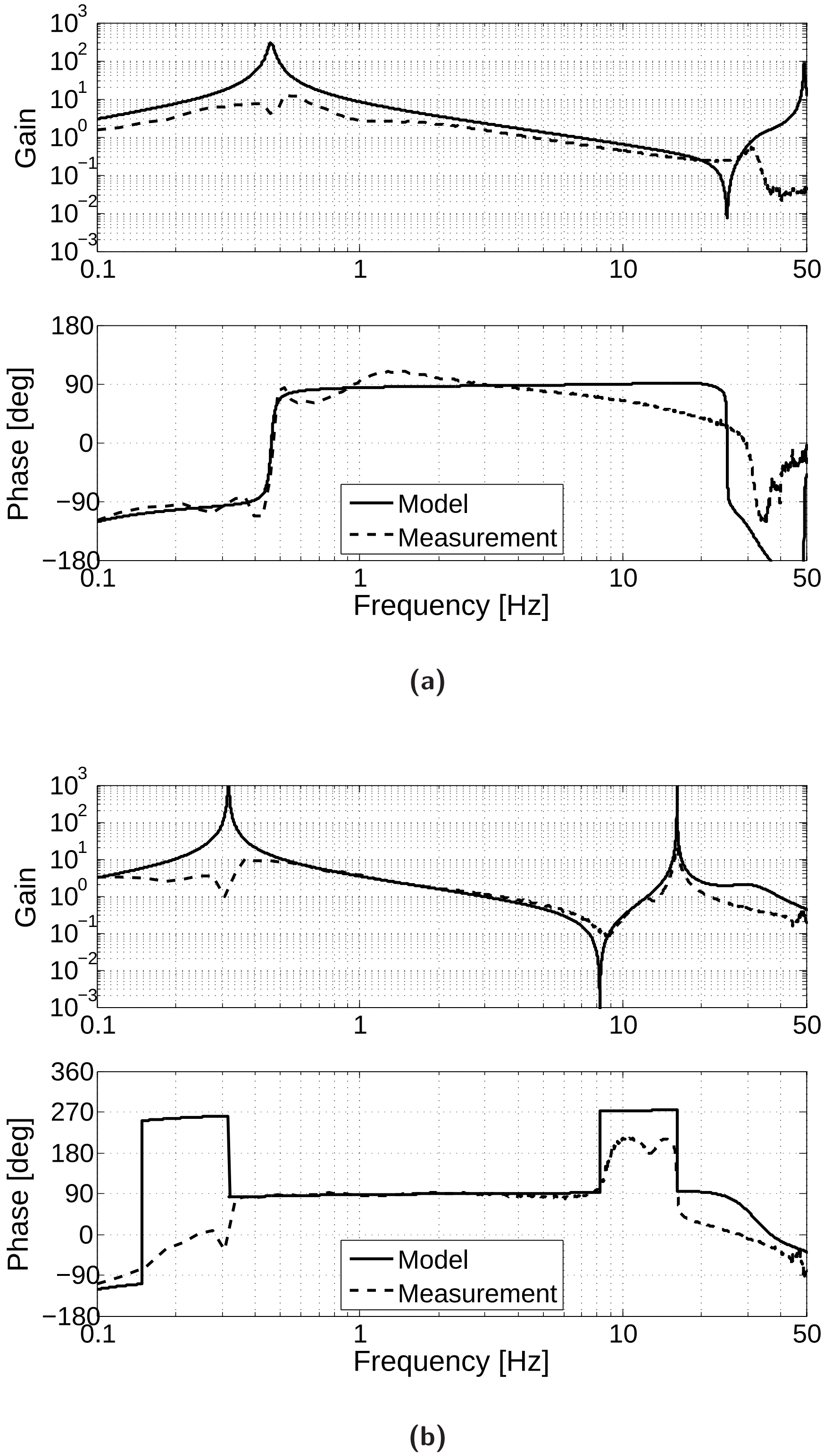

Figure 5.29: *Open loop transfer functions for the (a) vertical (y) and (b) horizontal (z) degrees of freedom. The dashed curves are the model predictions, while the black curves represent the results of the measurements in the y and z directions.*

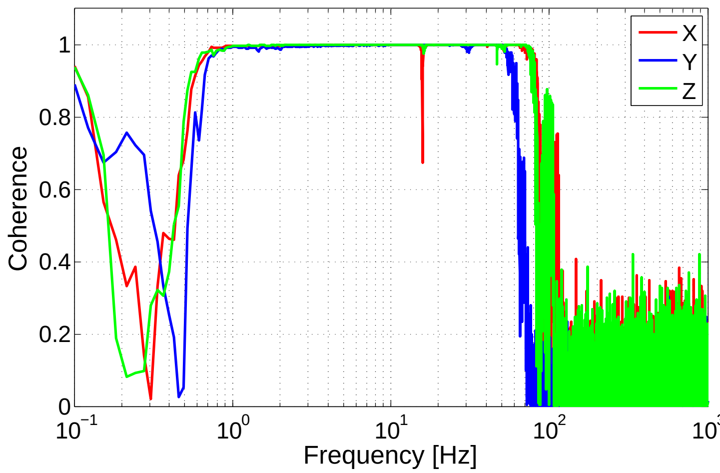

(a)

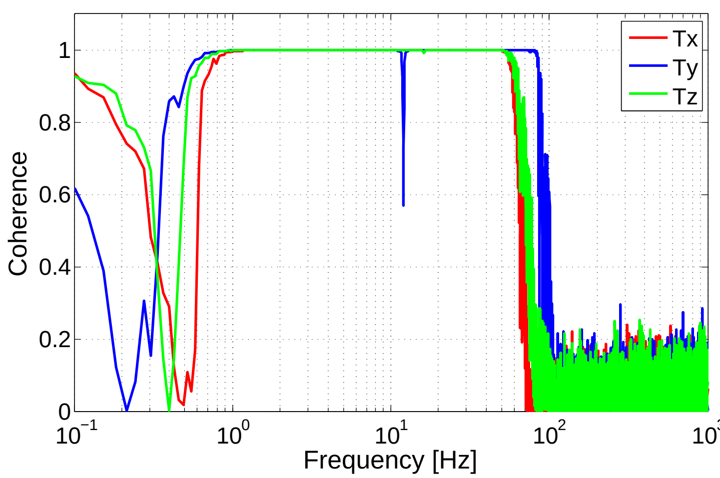

(b)

Figure 5.30: *Coherence between the injected noise and the control signal during the open-loop transfer function measurements for the (a) translational and (b) rotational degrees of freedom.*

Fig. 5.31 shows the measured open loop transfer functions for all six degrees of freedom. From these Bode plots the phase margins of the loops can be determined and the results are listed in Table 5.4. The gain margins could not be determined from the measurements, because in the interval where the measurement is valid (enough coherence between output and noise signal) the phase never reaches -180°. The only exception is the measurement of the control loop for the *z* degree of freedom which has a gain margin of 53. All phase margins are between 40° and 155°, which is more than adequate.

D.o.f.	Measurement							
	UGF [Hz]	Phase margin	UGF [Hz]	Phase margin	UGF [Hz]	Phase margin	UGF [Hz]	Phase margin
x	0.15	115°	0.80	90°	14.90	71°	17.00	110°
y	0.08	45°	3.70	95°				
z	0.10	90°	0.80	65°	15.35	46°	17.30	107°
Tx	0.08	40°	4.60	100°				
Ty	0.18	155°	0.50	155°	11.05	50°	13.12	132°
Tz	0.08	50°	2.80	90°				
	Model							
Hor	2.9	90°	12.50	93°	39.40	169°		
Ver	6.6	90°	32.50	29°	63.80	117°		

Table 5.4: *Phase margins obtained from the modeled (Fig. 5.29) and measured (Fig. 5.31) open loop transfer functions.*

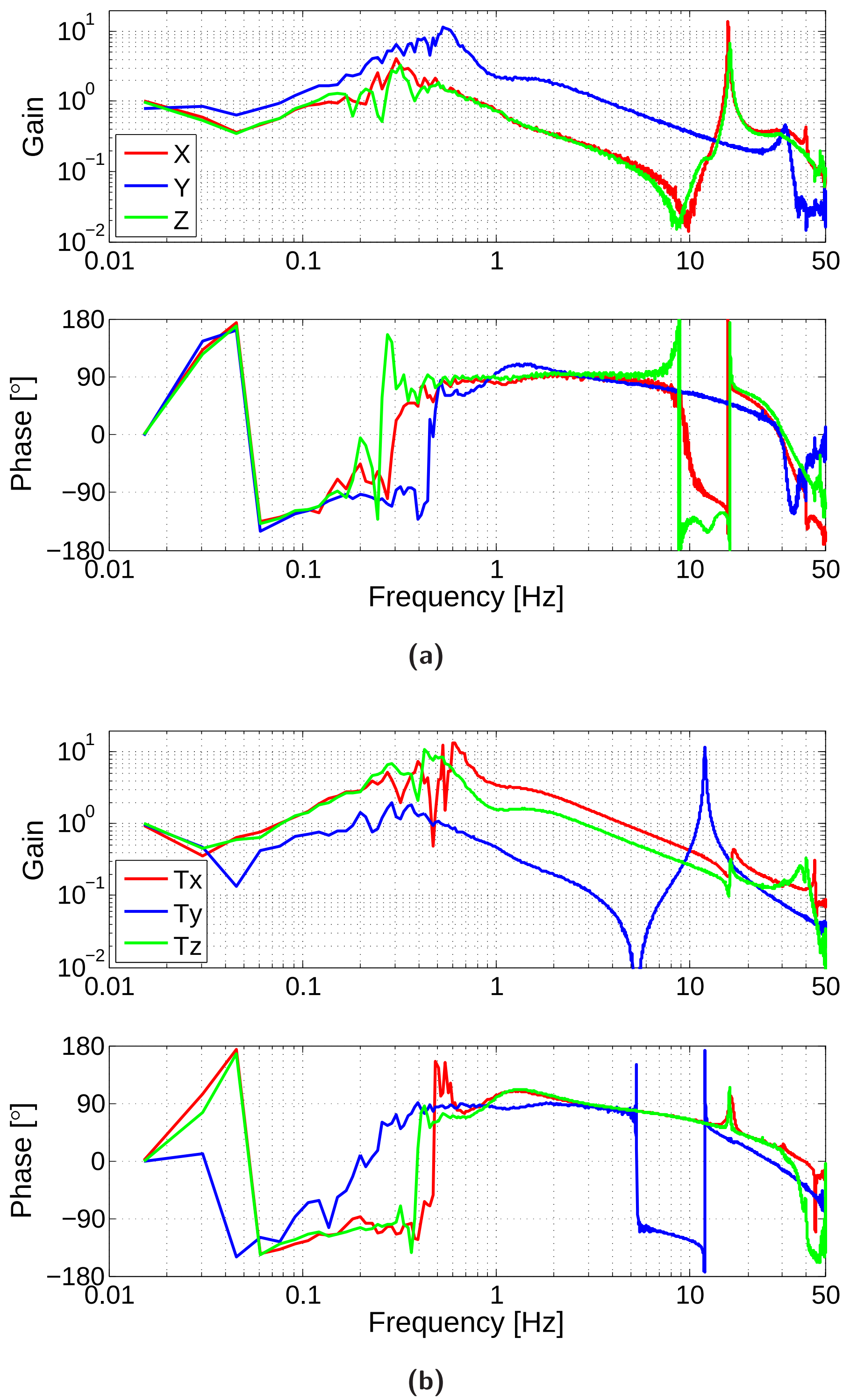

Figure 5.31: *Bode plots of the open loop transfer function measurements.*

5.4.5 Performance of control system

Damping of the rigid body modes

Fig. 5.32 shows the amplitude spectral densities of the vertical ground monitoring geophone (green curve), bench geophone (red curve), LVDT (black curve) and corrected LVDT (blue curve) of EIB-SAS in uncontrolled mode. The rigid body mode of this degree of freedom at 0.45 Hz is clearly visible in all sensors positioned on EIB-SAS. The structure at 0.15 Hz is due to the micro-seismic peak. It is less visible in the LVDT, because that sensor measures displacement of the bench with respect to the ground, and below the rigid body modes the system follows the ground, so this relative displacement vanishes.

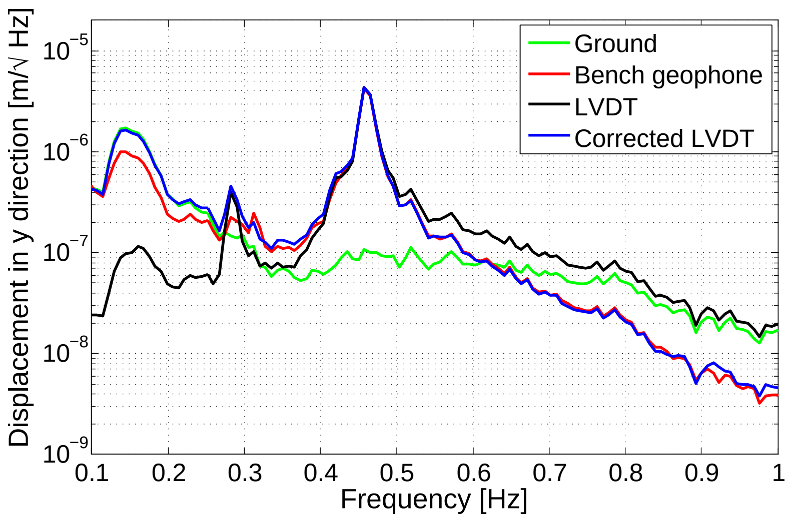

Figure 5.32: *Amplitude spectral densities of a number of sensors monitoring the vertical degree of freedom: the ground monitoring geophone (green curve), the geophone (red curve), the LVDT (black curve) and the corrected LVDT (blue curve).*

For frequencies greater than those of the rigid body modes, the bench is isolated and its motion is smaller than that of the ground. Therefore, above 0.45 Hz, the LVDT effectively measures the motion of the ground. This means that if the system would be locked on the LVDT signals, then above the rigid body modes, the motion would be enhanced instead of reduced. To minimize this effect, the translational degrees of freedom are controlled on the corrected LVDTs up to the blending frequency with the inertial sensors. For the rotational degrees of freedom, no ground motion inertial sensor is available to correct the LVDTs, so they are controlled on the uncorrected LVDT signals.

Fig. 5.33 shows the amplitude spectral density of EIB-SAS in controlled and uncontrolled mode for all degrees of freedom, measured at the Virgo site. The uncontrolled spectra are measured with the corrected LVDTs (blue dashed curves) and the springbox geophones (red dashed curves). For the vertical (y, Tx and Tz) degrees of freedom the geophones are placed on the bench instead of on the springbox; their spectra are given by the black dashed curves.

The system's motion in controlled state is measured with the corrected LVDTs (solid blue curves), which are now in-loop and the horizontal monitoring geophones on the bench (solid black curves) which are out-of-loop. A comparison of the corrected LVDT spectra in uncontrolled mode with the geophone spectra in controlled mode, shows that the peaks belonging to the rigid body modes are damped by a factor 10 to 30; down to the level of the ground motion or, as a result of the sensor correction, even a little below it. If the uncorrected LVDTs would be used as input for the controls, the motion of the bench could not be lower than that of the ground, so sensor correction is beneficial.

However, above 0.6 Hz the corrected LVDT spectra in controlled mode are above those of the geophones in uncontrolled mode. The controls do inject some motion at higher frequencies. This is to be expected, because the LVDTs are used for the control. Above ∼1 Hz the system starts to be controlled on the geophones and no ground motion will be injected.

Furthermore, around 1 Hz the corrected LVDT spectra in controlled mode lie above those in uncontrolled mode. This means that some noise is injected by the control loops. This is due to the sensor blending (see section 5.4.3). Around the blending frequency of 0.95 Hz, the phase of the blended signal may not be optimal, which causes the correction signal to be applied with the wrong phase increasing the motion around 1 Hz rather than lowering it.

Finally, the spectra show that even though the micro-seismic peak is visible in the corrected LVDT spectra, it is still present in the bench geophone spectra when the controls are engaged; the controls do not damp the motion of the bench at this frequency. Actually, in the x and y directions the motion of EIB-SAS at the frequency of the micro-seismic peak is a little higher when the controls are on.

Any residual tilt of the bench will create a fake displacement signal in the horizontal bench geophones. The tilt of the bench is given by the virtual LVDTs for Tx and Tz. The induced displacement signal in the horizontal bench geophones is than given by GEO_X$_{\text{fake}}$ = LVDT_Tz $\times$ g$/\omega^2$ and likewise for GEO_Z and LVDT_Tx.

Fig. 5.34 shows the spectra of the fake displacement signals seen by the bench geophones. Around the microseismic peak they are of the order of 10^{-6} m$/\sqrt{\text{Hz}}$ (Fig. 5.33).

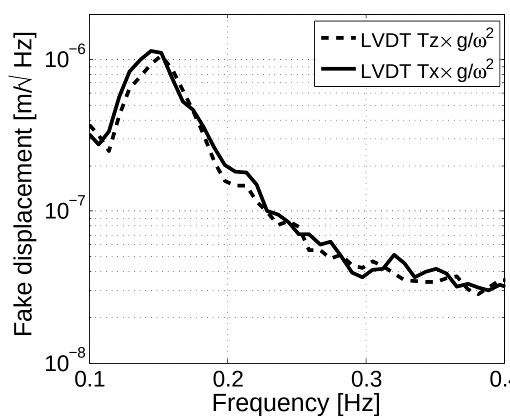

Figure 5.34: *Rotation of the bench seen as a displacement by the horizontal witness geophones.*

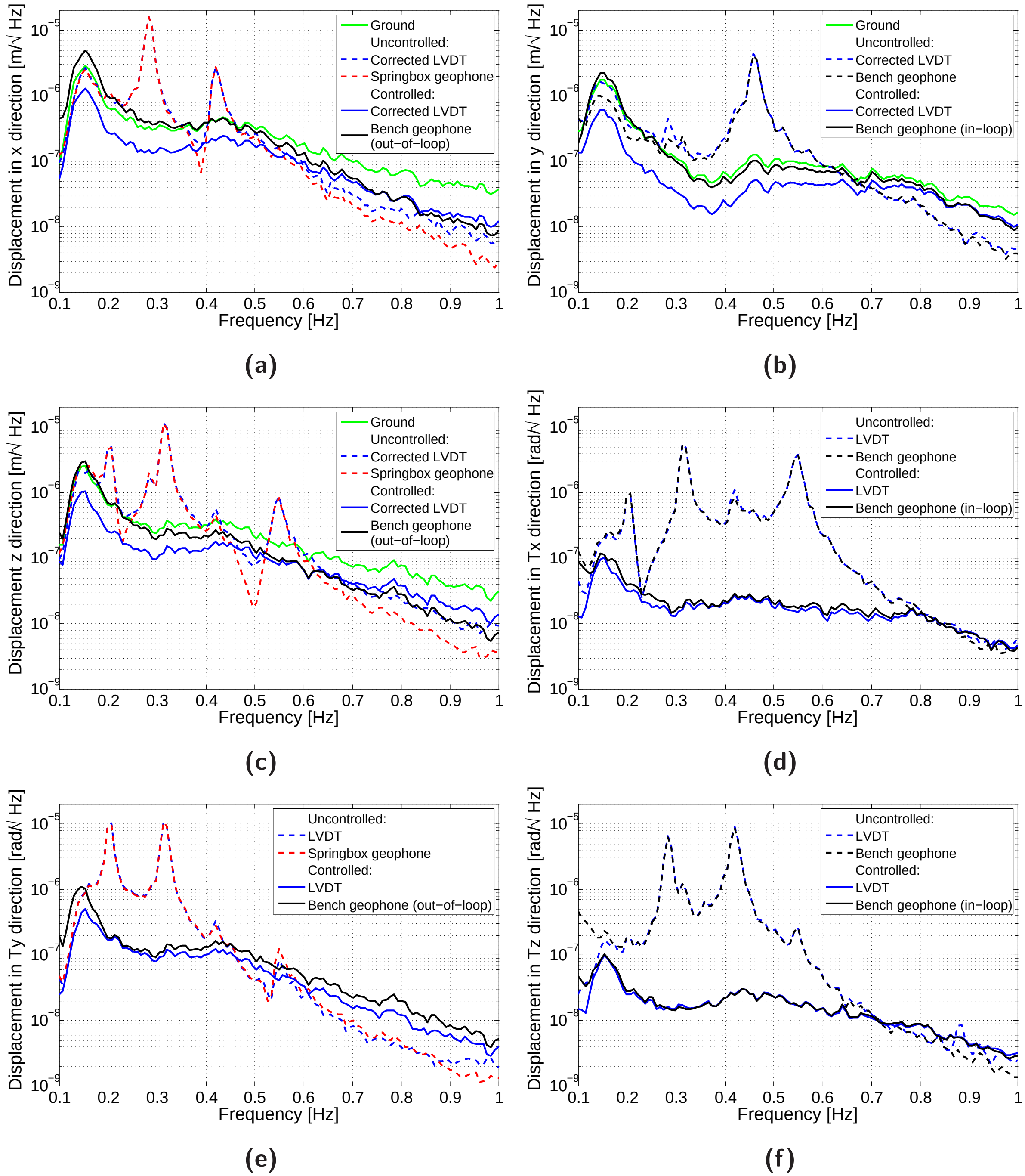

Figure 5.33: *The open-loop (dashed curves) and closed-loop (solid curves) motion of EIB-SAS in the (a) x, (b) y, (c) z, (d) Tx, (e) Ty, and (f) Tz directions. In the frequency region of the rigid body modes of the x, y and z degrees of freedom are controlled on the corrected LVDT signals (blue curves), those of the Tx, Ty and Tz degrees of freedom on the LVDT signals. The amplitude of the rigid body modes are lowered by a factor 10 to 30, but at the cost of introducing some displacement noise between 0.5 and 1 Hz in some of the degrees of freedom. The structure at 0.15 Hz is due to the micro-seismic peak. It is not attenuated, because the gains of the control loops are too small at its frequency.*

This is equal to the difference between the ground motion and the bench motion spectra. We can therefore conclude that the excess motion seen by the witness geophones is not an actual displacement of the bench, but a signal induced by the residual tilt of the bench.

To compare the motion of EIB-SAS in controlled mode with the requirement, Fig. 5.35 shows the length of the displacement vector in controlled and uncontrolled mode below 1 Hz together with that of the ground and with the requirement. In uncontrolled state it is obtained by quadratically adding the horizontal geophones on the springbox and the vertical bench geophones. In controlled state only the bench geophones are used, which are out-of-loop.

Only at the micro-seismic peak at 0.15 Hz does the EIB-SAS displacement spectrum exceed the requirement. This can probably be remedied by improving the low-frequency phase margin of the filters used for in the sensor correction of the LVDTs. The rigid body modes are damped with a factor 10 to 30, down to the level of the ground motion or below that. As expected, above the frequency of the rigid body modes the controls inject some displacement noise, because the LVDTs are used in the controls, but in this frequency range the application of sensor correction limits this effect.

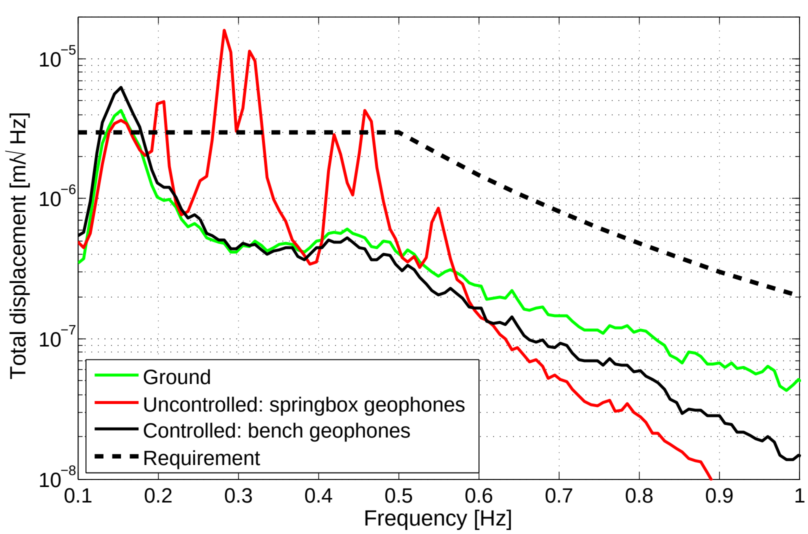

Figure 5.35: *Length of the displacement vector measured by different sensors in different states. The green curve represents the ground motion measured by the ground geophones. The black dashed curve represents the requirement. The red curve shows the EIB-SAS motion in uncontrolled state measured by the out-of-loop LVDTs. The blue curve that of the same LVDTs, but now in controlled state; they are in-loop. The black curve is the motion measured by the out-of-loop geophones in controlled state.*

Damping of the horizontal structural modes

The control bandwidth extends up to 30 Hz. The horizontal structural modes identified in section 5.3.1 had frequencies of 12 (Ty) and 16 Hz (x and z) and are therefore damped by the control system.

Fig. 5.36 shows the amplitude spectral density of the out-of-loop virtual geophones between 10 and 20 Hz in uncontrolled (gray curves) and controlled state (black curves). The modes at 11.90 and 16.05 Hz are damped effectively for the Ty and z degrees of freedom. The mode in the x-spectrum is damped by a factor 10. Some noise is injected above the modes frequency so that the mode seems to be shifted up by 0.2 Hz.

Figure 5.36d shows the length of the displacement vector obtained from quadratically adding the other three spectra. The dashed curve represents the requirement [80] in this frequency regime. Clearly, the horizontal structural modes are damped well below the required level.

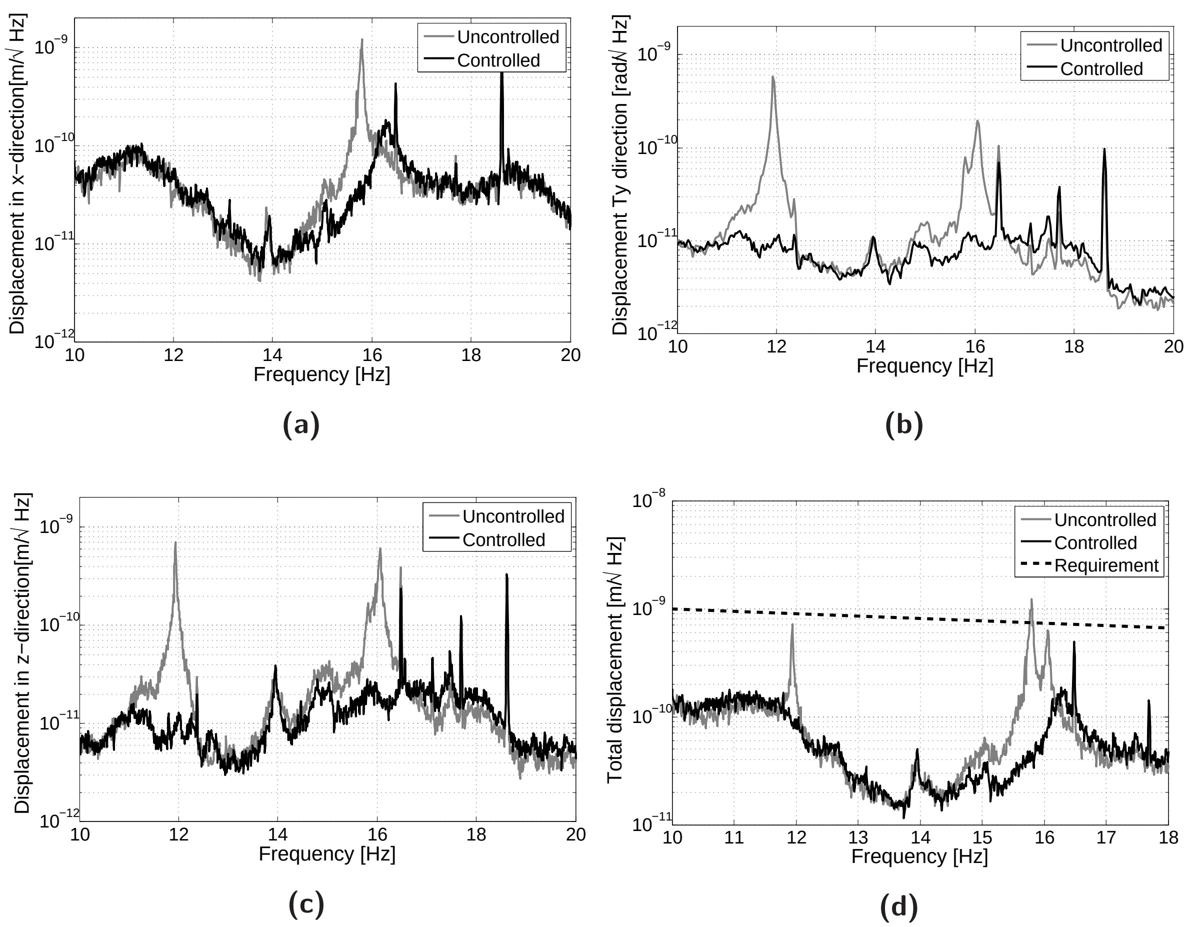

Figure 5.36: *The motion spectra measured by the out-of-loop geophones in controlled (black curves) and uncontrolled (gray curves) state.*

Thermal stability

To show that the system can cope with temperature variations of $\pm$ 1°C, the temperature of the cleanroom housing EIB-SAS was raised and lowered, while the system was in a controlled state. Figs. 5.37 and 5.38 show the ambient temperature and the LVDT values of all 6 degrees of freedom for a period of 15 hours during which the temperature was changed by 1 °C.

The data show that only the vertical (*y*) displacement has a clear correlation with the temperature. This correlation is due to the change in Young's modulus of the GAS filter blades caused by the temperature change. A temperature change of 1 °C induces a change in vertical position of -2.7 µm.

In section 3.5.3 the effect of the temperature on the equilibrium position of the GAS filters was deduced to be $-2.54\times10^{-4} \times g/w_0^2$ [m/°C]. The filter is tuned to a vertical resonance frequency of 446 mHz, and the change in equilibrium position is -317 µm/°C. The gain of the control loop at DC was approximately 130 during this test, and we would expect the vertical position of the bench to change with -317 µm/°C /130 $= -2.44$ µm/°C. This is in agreement with the observed -2.7 µm/°C.

Long-term stability

To demonstrate long-term stability of the controls, and to show that the RMS of the residual motion is below 20 µm for the translational degrees of freedom and 5 µrad for the rotational degrees of freedom, we monitored the DC position of the controlled system for 1 week. Therefore, the DC position of EIB-SAS in controlled mode was monitored by the LVDTs for 6.54 days. These data have been used to determine the RMS value of the residual drifts of the system and to calculate the Allan deviation of the system at different timescales [108].

Figure 5.39 shows the LVDT values of all 6 degrees of freedom for a period of 6.54 days together with the integrated RMS values for data stretches of 24 hours. The measurements show that the system is stable during the full duration of the test. The integrated RMS values of the DC position are a few tenths of micro-radians for the rotational degrees of freedom, where the largest drift was 0.39 µrad in the *Ty*-direction. For the translational degrees of freedom these RMS values are of the order of 1 µm. The largest drift was 1.39 µm in the *x*-direction. These values are only 8% of the required limit.

The Allan deviation σ_a on a time scale τ is given by [108]

$$\sigma_\mathrm{a}(\tau) = \left[\frac{1}{2\,(M-1)}\sum_{\mathrm{n}=1}^{\mathrm{M}-1}\left(y_{\mathrm{n}+1}\left(\tau\right) - y_\mathrm{n}\left(\tau\right)\right)^2\right]^{1/2}, \tag{5.30}$$

where y_i denotes the time-series data that is down-sampled to the desired timescale τ and $M = T/\tau - 1$, where T is the observation time. The Allan deviation can be thought

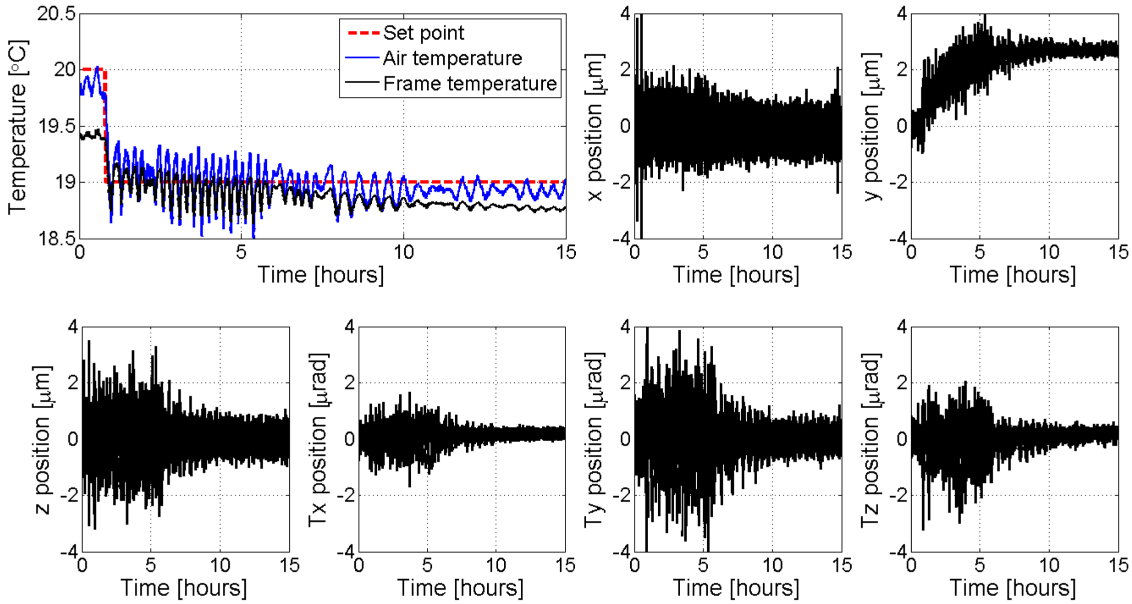

Figure 5.37: *Cleanroom temperature and LVDT values during thermal stability test. The red dashed line indicates the set point of the temperature. After 10 hours, the set point has been lowered by 1 °C and the system again reached a uniform temperature. Only the vertical (y) position increases by 300 microns, due to the temperature dependence of the Young's modulus of the maraging steel GAS filter blades.*

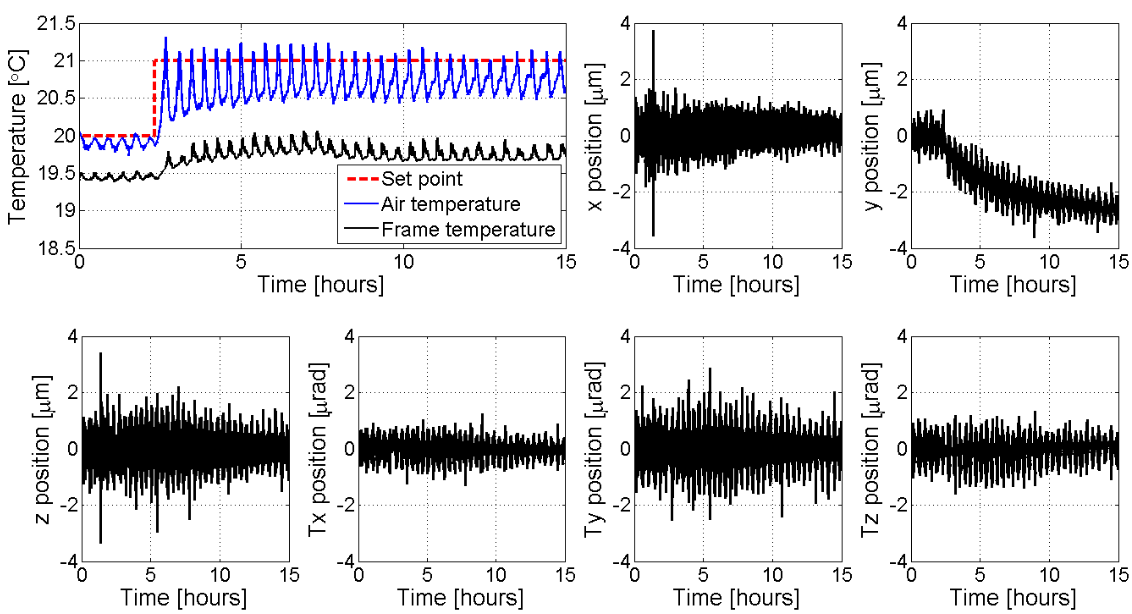

Figure 5.38: *Cleanroom temperature and LVDT values during thermal stability test where the temperature is raised by 1 °C. Again only the vertical (y) position is slightly affected.*

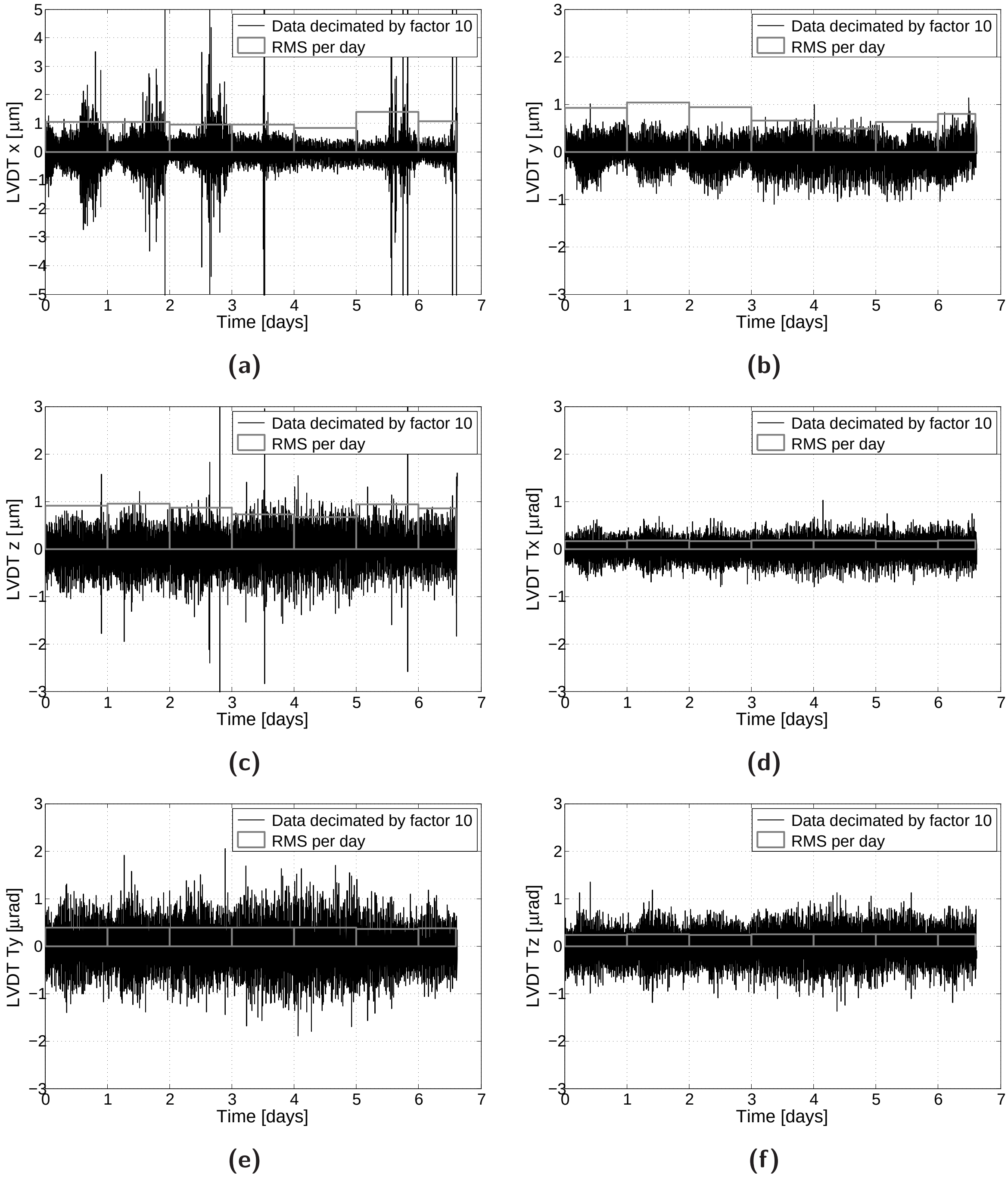

Figure 5.39: *LVDT values during the long-term stability measurement. The control loops of EIB-SAS were kept closed for 6.54 days. The RMS integrated over 24 hours is well below the required limits.*

of as the standard deviation of the distribution of the difference between sequential down-sampled data points. The timescale on which the system drifts is typical for the noise source causing the motion. If the main noise source disturbing the system is white, then the Allan deviation plot will decrease with $1/\sqrt{\tau}$. The Allan deviation plot of a system that is dominated by random walk motion will increase with $\sqrt{\tau}$.

Figure 5.40 shows the Allan deviation at timescales ranging from 1 second to 1 day. Fig. 5.40a shows the Allan deviation for the translational degrees of freedom, Fig. 5.40b that of the rotational ones together with that of the temperature (solid green diamonds). The black dotted line indicates the requirement. Clearly, the Allan deviation in all six degrees of freedom has a maximum around 5 to 7 seconds. This timescale corresponds to the frequencies of the rigid body modes, which is to be expected; the controls lower the quality factor of the rigid body modes, but some motion will persist at these frequencies.

All six degrees of freedom show drifts on the timescale of 600 seconds. This drift is also present in the Allan deviation plot of the temperature data. This timescale is exactly half the period of the air-conditioning of the cleanroom housing EIB-SAS, which turns on every 19.5 minutes. As expected, the effect is largest for the vertical (*y*) degree of freedom where these drifts are due to the thermo-elasticity of the maraging steel GAS filter blades.

In accordance with the vertical temperature induced motion we would expect the Allan deviation to satisfy $\sigma_{\mathsf{y}} = 2.44 \times 10^{-6} \times \sigma_{\mathsf{T}}$. The expected Allan deviations of the vertical motion based on the Allan deviation of the temperature is indicated by the open black diamonds and have good agreement with the measured values for timescales greater than 100 seconds.

The *x*, *y* and *Tz* degrees of freedom also show a drift on the timescale of 25,000 seconds, which is again correlated with the temperature. These drifts are due to the daily variation in temperature. For the *y* degree of freedom this is again due to the thermal expansion of the GAS filters, for the *x* and *Tz* degrees of freedom the mechanism is unknown. For the remaining degrees of freedom $\sigma_{\mathsf{a}}(\tau) \propto \sqrt{1/f}$ for timescales between a few hours and a day. This indicates that at these timescales the residual drift of the system is caused by random walk motion.

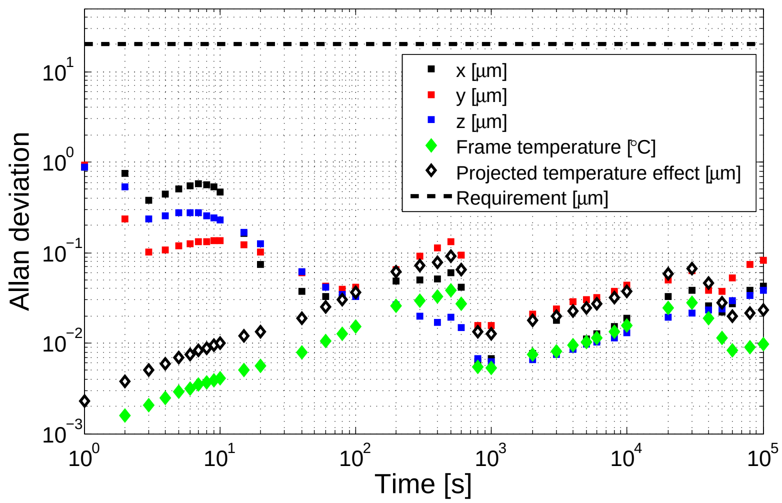

(a)

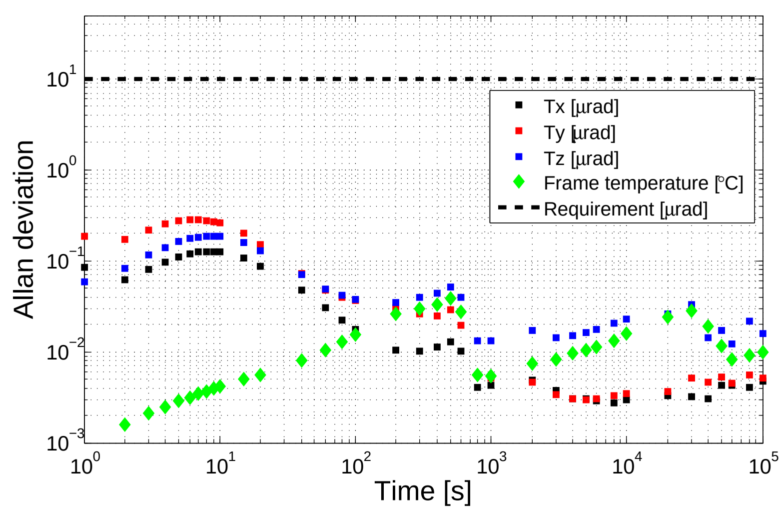

(b)

Figure 5.40: *Allan deviation on time scales between 1 second and 1 day.*

5.5 Performance tests with the Virgo+ injection system

The Virgo injection system, which is shown in Fig. 5.41, consists of the laser bench, external injection bench (EIB) and input mode cleaner (IMC). The latter consists of the suspended injection bench (SIB) and an end-mirror (for a detailed description the reader is referred to chapter 2). During the Virgo science run of 2011 two motion sensors were present on the EIB: a tri-axial force balance accelerometer (epi-sensor) with a bandwidth of 200 Hz, and a vertical piezoelectric accelerometer with a bandwidth of 1 kHz.

The EIB also houses quadrant photo-diodes that provide the error signals for the automatic alignment of the IMC. These sensors cannot distinguish between their own motion and that of the suspended injection bench, and the internal modes of the EIB will be visible in the power spectral densities of these sensors. Therefore, these photo-diodes can be used to compare the motion of EIB-SAS to that of the old EIB support structure.

In addition, the beam monitoring system (BMS), which lowers the beam jitter at low frequency, is situated on the EIB. The leaser beam is kept centered on two quadrant photo-diodes by two piezoelectric-actuated mirrors. The bandwidth of the control loop is 10 Hz, so above this frequency the amplitude spectral densities of the photo-diode signals contain information about the beam jitter of the laser beam exiting the EIB.

5.5.1 Direct comparison of the EIB displacement noise spectra

Fig. 5.42 shows the motion spectra of the epi-sensor and vertical accelerometer on the EIB on its olds support structure (gray curves) and after the installation of EIB-SAS (black curves). Comparing these spectra it is clear that the structures observed between 30 and 60 Hz are no longer present when the optical bench is supported by EIB-SAS.

5.5.2 Comparison of the input mode cleaner control signals

The angular control of the suspended injection bench and IMC end-mirror use error signals obtained from 6 quadrant photodiodes. Two of these are in transmission of the IMC end-mirror, four are situated on the EIB and monitor beams reflected from the suspended injection bench. Resonances of the EIB shake the photodiodes and hence show up in error signals for the angular control of the suspended injection bench.

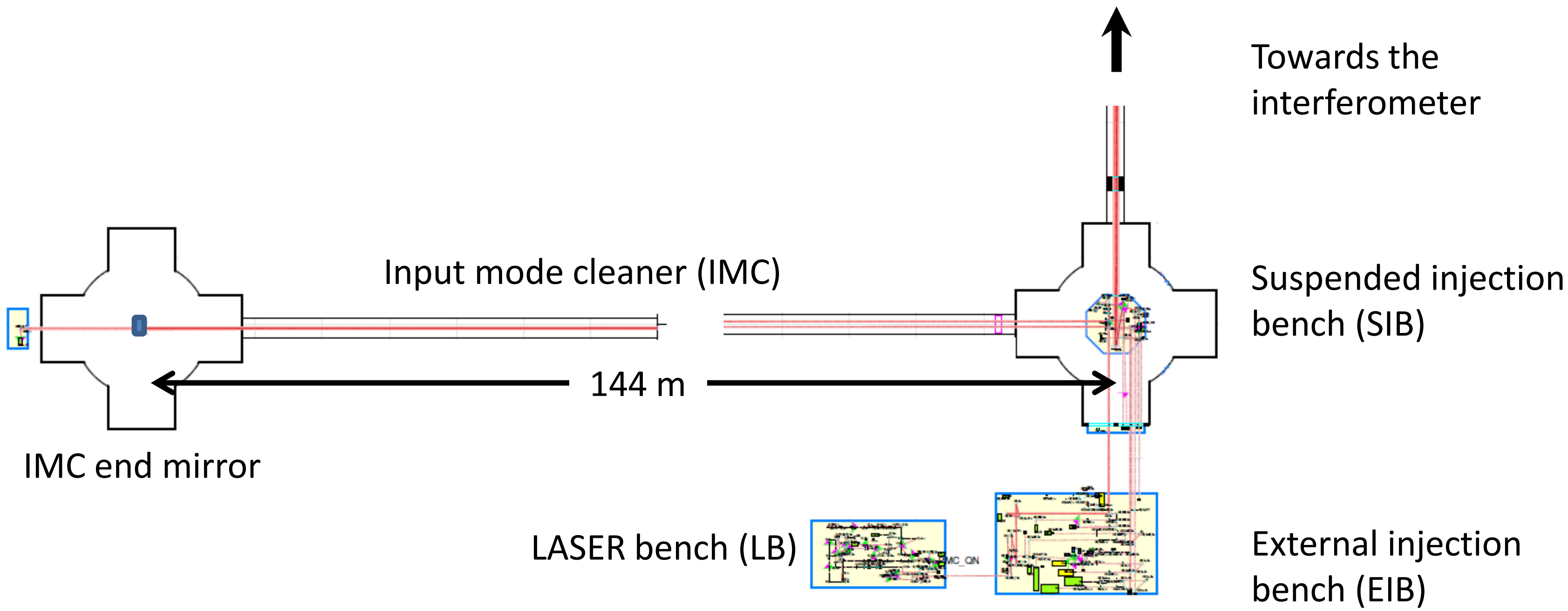

Figure 5.41: *Schematic layout of the Virgo injection system. The laser stands on the laser bench (LB). The laser beam travels via optics on the external injection bench (EIB) towards the suspended injection bench (SIB). Both the LB and the EIB are operated outside the vacuum. The SIB is suspended from a short superattenuator and is situated in vacuum. Optics on the SIB together with a suspended mirror placed 144 m away form a triangular cavity: the input mode cleaner (IMC). The SIB and IMC end-mirror are controlled with error signals coming from 6 quadrant photodiodes; 2 in transmission of the end-mirror and 4 on the EIB looking at beams reflected from the SIB.*

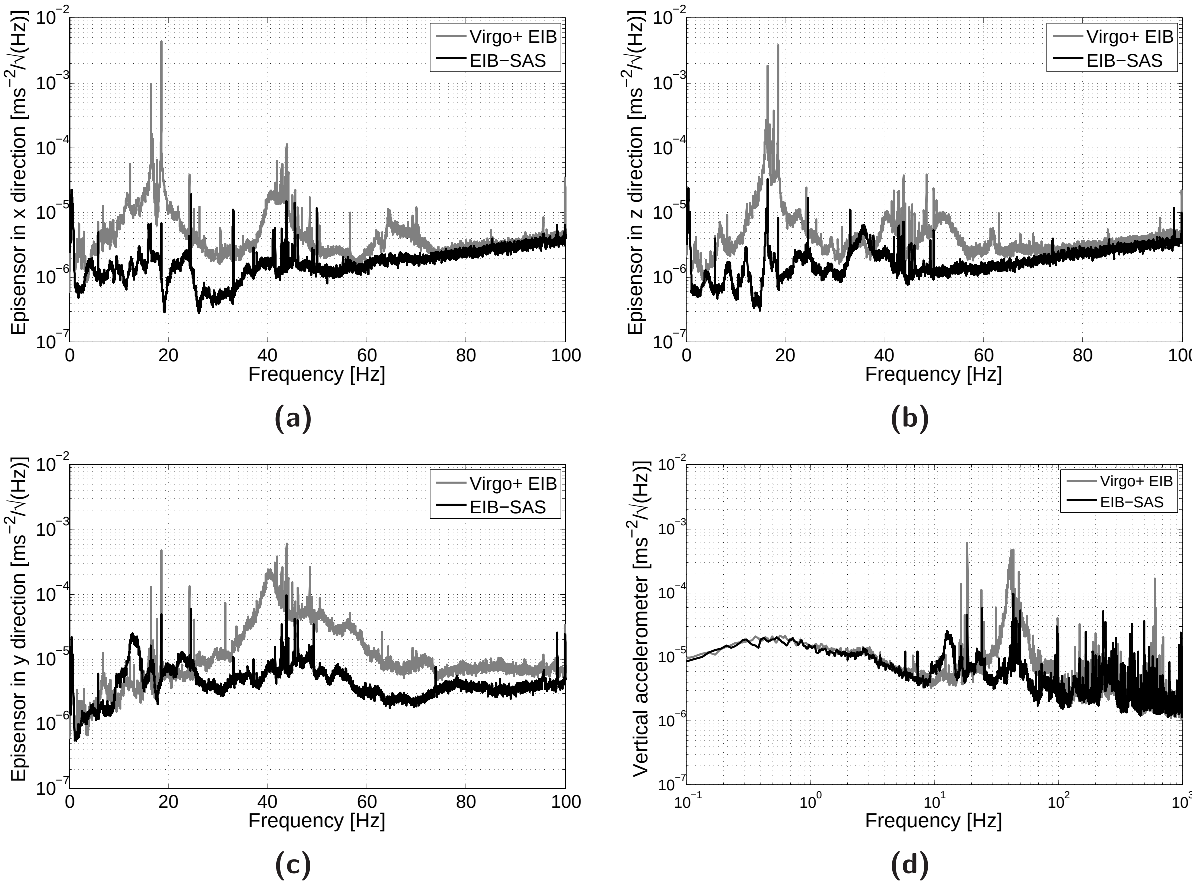

Figure 5.42: *Amplitude spectral densities of motion sensors atop the external injection bench on the old support structure (gray curves) and on EIB-SAS (black curves).*

Fig. 5.43 shows the amplitude spectral densities of the error signals used to control the tilt degrees of freedom of the SIB (the SIB automatic alignment signals) measured in closed-loop. During this measurement the EIB is on its old support structure. Especially in the error signal of the *Tz* degree of freedom there are structures between 30 and 60 Hz that belong to the structural modes of the EIB support structure.

Fig. 5.44 shows the amplitude spectra densities of the SIB *Tz* error signal measured on the old support structure (black curve) and on EIB-SAS (red curve). As expected, when the external injection bench is carried by EIB-SAS the peaks due to the structural resonances are gone. A small structure at 36.5 Hz can be observed due to the not perfectly damped rigid body mode of EIB-SAS in the *Tz* degree of freedom. Between 52.5 and 53.5 Hz and at 80 Hz two structures can be seen in the spectrum. These are not present in the epi-sensor measurements of Fig. 5.42. Therefore, they do not belong to the EIB or EIB-SAS. More likely, they are resonances of the SIB. There are two more structures in both spectra at 16.5 and 91 Hz that are induced by acoustic noise.

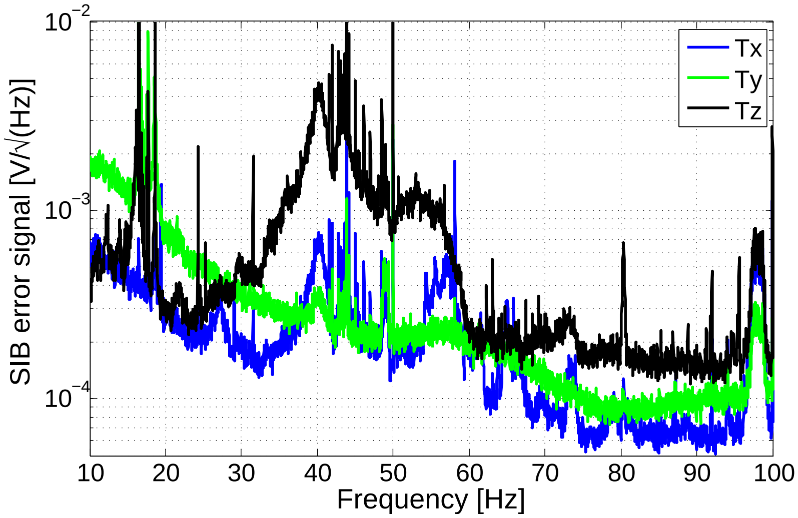

Figure 5.43: *Amplitude spectral densities of the error signals for the control of the tilt degrees of freedom (automatic alignment signals) of the suspended injection bench (SIB), measured in closed loop. These spectra have been measured while the EIB was on its old support structure. Especially the Tz error signal spectrum shows a structure between 30 and 60 Hz that is due to the support structure of the EIB.*

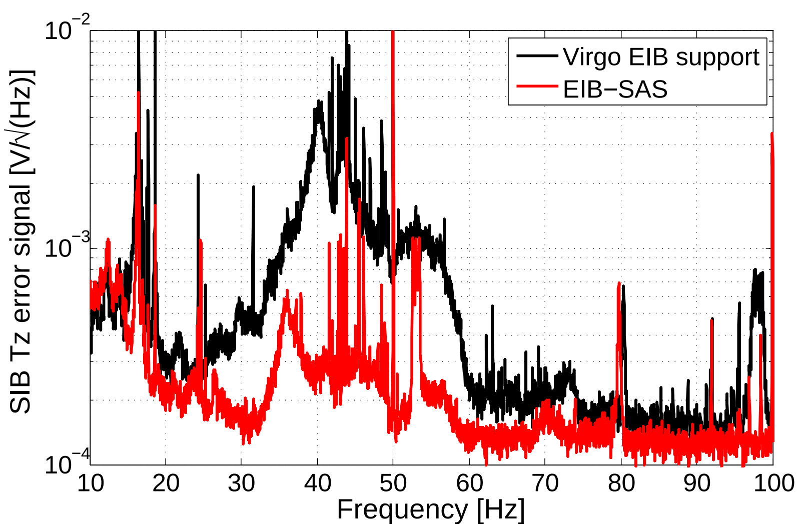

Figure 5.44: *Amplitude spectral density of the error signal for the Tz control of the SIB, measured with the EIB on its old support structure (black curve) and on EIB-SAS (red curve). The structure in the spectrum due to resonances of the old EIB support is no longer present when the EIB is on EIB-SAS. The remaining peaks at 53 Hz and 80 Hz belong to the SIB, the one at 91 Hz is induced by acoustic noise and the peak between 30 and 40 Hz belongs to the EIB-SAS rigid body mode that is not perfectly damped.*

5.5.3 Comparison of the beam jitter measurements

Fig. 5.45 shows the beam jitter spectra in the horizontal (x) and vertical (y) directions and in the yaw (Ty) and pitch (Tx) directions, observed by the beam monitoring system (BMS) photo-diodes on the old EIB support structure (gray curves) and on EIB-SAS (black curves). The dashed curves indicate the beam jitter requirement at the entrance of the IMC, which have been recently formulated in Ref. [109].

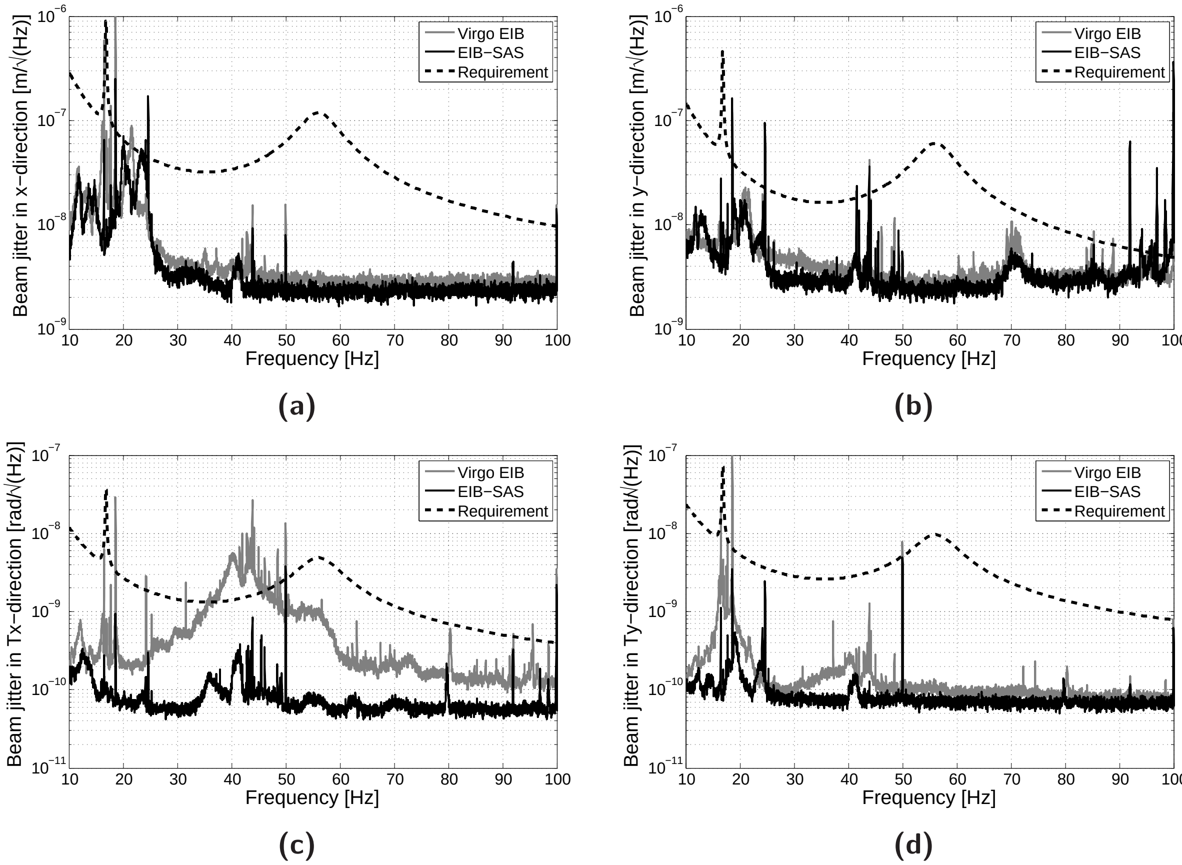

Figure 5.45: *Beam jitter in the x, y, Tx and Ty degrees of freedom of the laser beam entering the IMC measured with the beam monitoring system quadrant photo-diodes for the old bench support structure (gray curves) and EIB-SAS (black curves). The dashed curves indicate the beam jitter requirements which have been calculated in Ref. [109].*

Comparing the beam jitter measurements in Fig. 5.45 shows that the stability of th beam entering the IMC is improved by EIB-SAS. Especially the large structures in the tilt degrees of freedom associated with the internal modes of the old EIB support structure have been eliminated. In the horizontal (x) direction a structure remains between 10 and 30 Hz, while the epi-sensor spectra of Fig. 5.42 indicate that the motion in this degree of freedom and in this frequency region has decreased. It could be that the structure remaining in the beam jitter spectrum is due to motion of the laser bench, not of the EIB.

5.6 Characterization of acoustic coupling

EIB-SAS is a soft system. This is necessary to deliver the required attenuation of seismic ground motion with minimal injection of control noise, but makes the system susceptible to pressure waves: acoustic noise. At high frequencies the residual motion of EIB-SAS should be dominated by acoustic noise.

To improve the acoustic environment of EIB-SAS the walls of the laser lab, where EIB-SAS is housed, have been made soundproof and an effort has been made to minimize the number of acoustic noise sources in the laboratory. Only an electronic rack for the laser remains. To determine the coupling of EIB-SAS to acoustic noise several acoustic noise injections have been performed.

5.6.1 Acoustic noise injections

White acoustic noise between 50 and several hundred Hz was injected inside the laser laboratory and from outside the laser laboratory. The sound level in the laser laboratory and in the main hall of the central building were measured with calibrated microphones. During the injections the injection laboratory's climate control and air-conditioning were off and the control loops of EIB-SAS were open. The effects of acoustic noise from the laser rack and of the acoustic noise from the laser laboratory's climate control in science mode have been determined. These last two measurements will give a good indication of the nominal acoustic environment in the Advanced Virgo era and its effects on EIB-SAS.

Acoustic noise injection inside the laser laboratory

Fig. 5.46 shows the acoustic noise level measured with a calibrated microphone in quiet conditions and during the injection of acoustic white noise between 30 and 1200 Hz. Fig. 5.47 shows the amplitude spectral densities of the virtual sensors of EIB-SAS and their coherence with the microphone signal under these conditions. The acoustic noise increases the residual motion of the system by 1 to 2 orders of magnitude.

In absence of acoustic noise the sensors lack the sensitivity to measure the residual motion of the bench above 100 Hz; vertically only the springbox modes are observable. The coherence between the sensors and the microphone is only significant up to 30 Hz and at frequencies that correspond to structural resonances of the system (see section 5.3.1). It is no surprise that the vertical degree of freedom has the greatest coherence, as it has the largest area.

Even with the injection of acoustic noise up to 1200 Hz, the residual motion of the bench is only observable up to 500 Hz in the x and z directions and up to 900 Hz in the y direction. Below 60 Hz, the injection of acoustic noise does not change the coherence between the motion

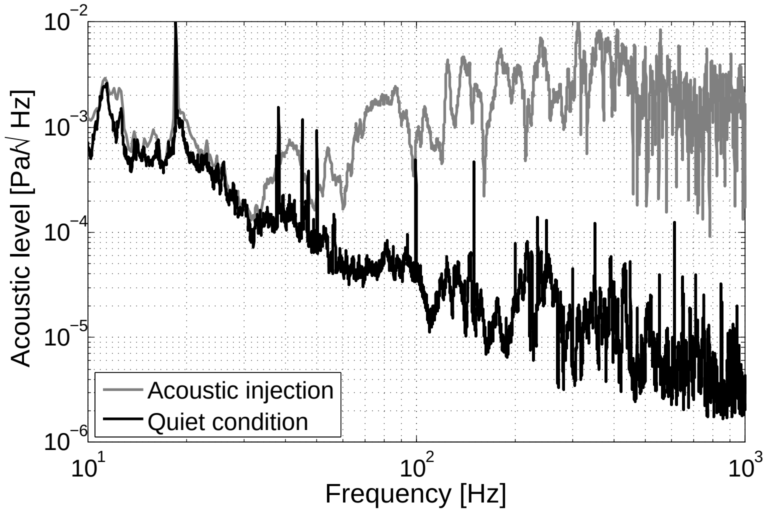

Figure 5.46: *Amplitude spectrum density of the microphone signal under quiet conditions (black curve) and during the injection of acoustic white noise (30 - 1200 Hz) inside laser laboratory (gray curve).*

sensors and microphone. Between 60 and approximately 800 Hz the coherence increases to 1. This allows us to measure the transfer function between acoustic noise and bench motion. The results are shown in Fig. 5.48 for the vertical degree of freedom, which is the most interesting, because it has the largest interaction surface.

The measurement results show that the acoustic to motion transfer function is more or less flat between 100 and 600 Hz and exponentially decreases with frequency above 600 Hz. At 60, 158−166 and 270−300 Hz the acoustic to vertical motion transfer function has large peaks. These have been identified as springbox modes in section 5.3.1.

Outside the laser laboratory

Injecting acoustic noise inside the laboratory we realized strong coherence between the bench motion sensors and the microphone, which allowed us to measure the transfer function between the two. Injecting the same acoustic noise from outside the laboratory tells us something about the acoustic isolation of the lab. Apart from an electronics rack for the Advanced Virgo laser, whose acoustic contribution will be measured separately, all acoustic noise sources will be situated outside the lab.

Fig. 5.49 shows the acoustic noise level measured with a calibrated microphone in quiet condition and during the injection of acoustic white noise between 30 and 1200 Hz from inside (red curve) and *outside* (blue curve) the laser lab. Clearly the laser laboratory walls stops most of the pressure waves.

Fig. 5.50 shows the fraction of acoustic noise that penetrates the laboratory's wall. Apart from at 60 Hz, 100 Hz and 120 Hz, more than 90% of the acoustic noise is stopped.

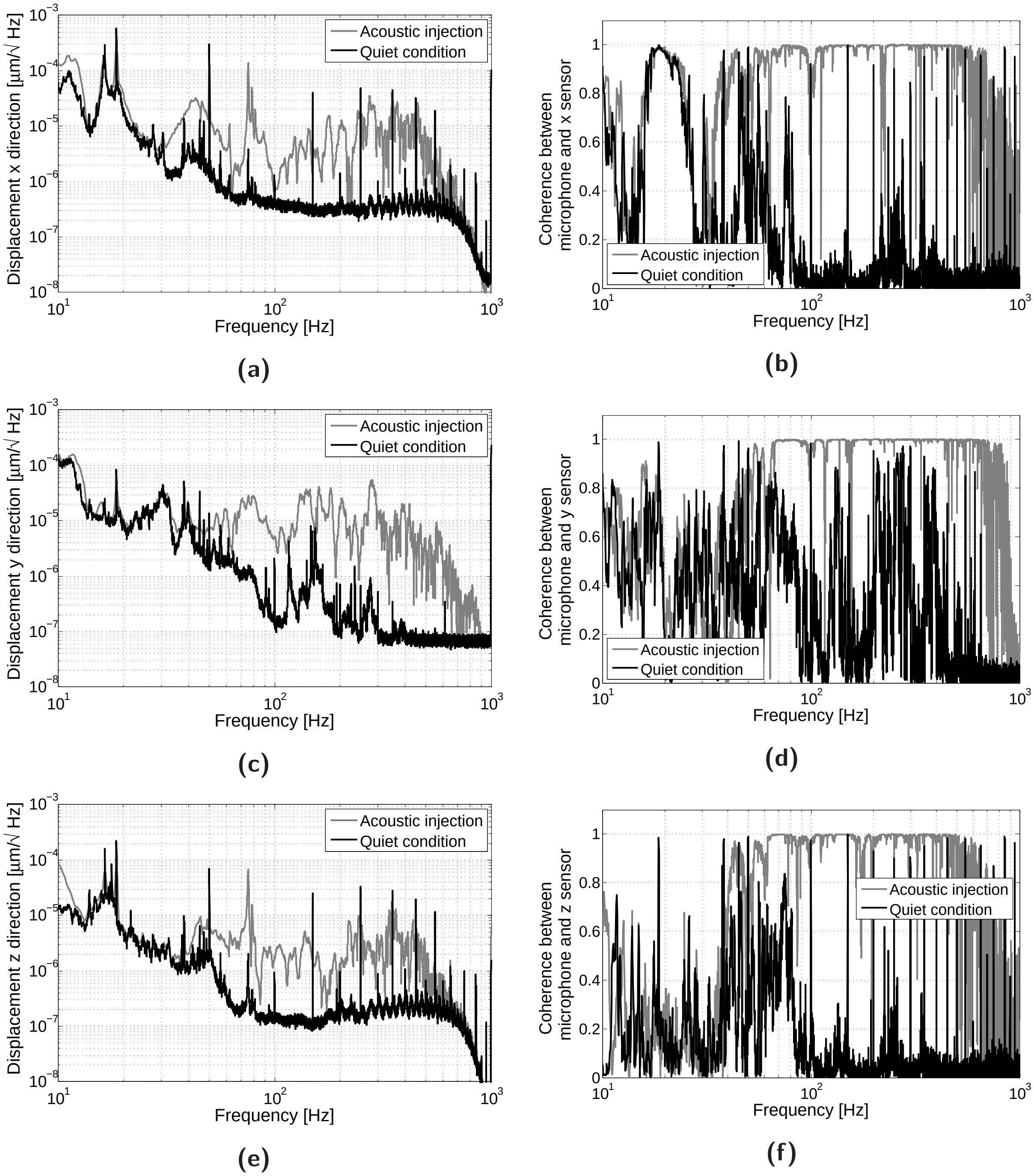

Figure 5.47: *Displacement noise spectra of EIB-SAS and coherence between the motion sensors and microphone under normal acoustic conditions (black curves) and during an acoustic noise injection inside the laser laboratory for frequencies between 30 Hz and 1200 Hz (gray curves).*

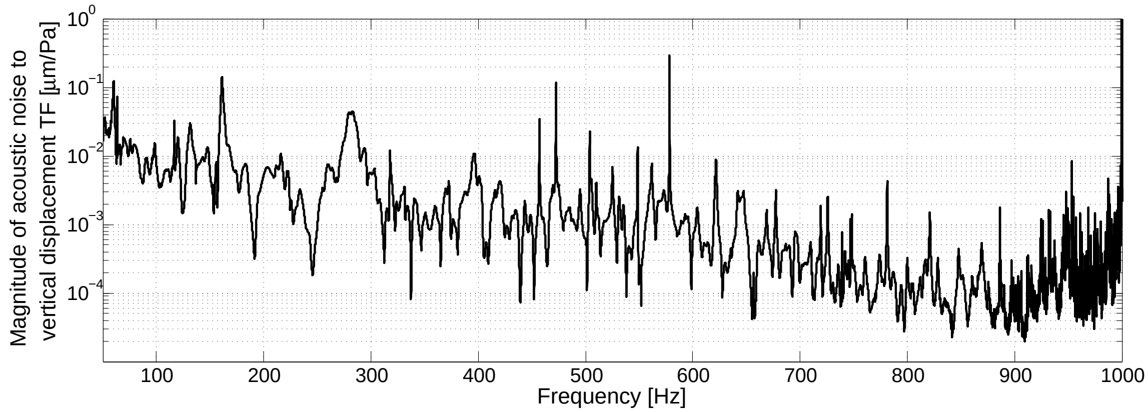

Figure 5.48: *Transfer function between virtual motion sensors and microphone signal.*

Fig. 5.51 shows the amplitude spectral densities of the virtual sensors of EIB-SAS and their coherence with the microphone signal under these conditions. For the *x* degree of freedom their is no clear increase in the residual motion spectrum. There is a small increase in the coherence with the microphone between 100 and 500 Hz.

For the *y* degree of freedom the motion between 100 and 170 Hz, and between 280 and 400 Hz increases slightly. The coherence with the microphone signal also increases at these frequencies.

For the *z* degree of freedom two peaks appear in the motion spectrum due to the acoustic noise. One at 143 Hz the other at 160 Hz. These have been identified as springbox modes in section 5.3.1. At these frequencies also the coherence with the microphone improves.

All in all, EIB-SAS is hardly affected by acoustic noise from outside the laser laboratory.

5.6.2 Realistic acoustic conditions

During science mode operation of Advanced Virgo there will be two sources of acoustic noise. The first is the electronics rack of the laser which is situated in the laser lab. The second is the laser lab's climate control (the laser laboratory is a cleanroom). In science mode the air-conditioning of the room is such that it should not introduce any air currents. However, some acoustic noise from the neighboring cleanroom could affect the system.

Noise from the electronics rack

Fig. 5.52 shows the acoustic noise level measured with a calibrated microphone in quiet condition (black curves) and with acoustic noise coming from the electronics rack of the laser (gray curves). The microphone acoustic spectra in Fig. 5.52d show that the rack produces 40 to 60 dB* of acoustic noise between 5 Hz and 1 kHz.

*This is comparable to a dishwasher.

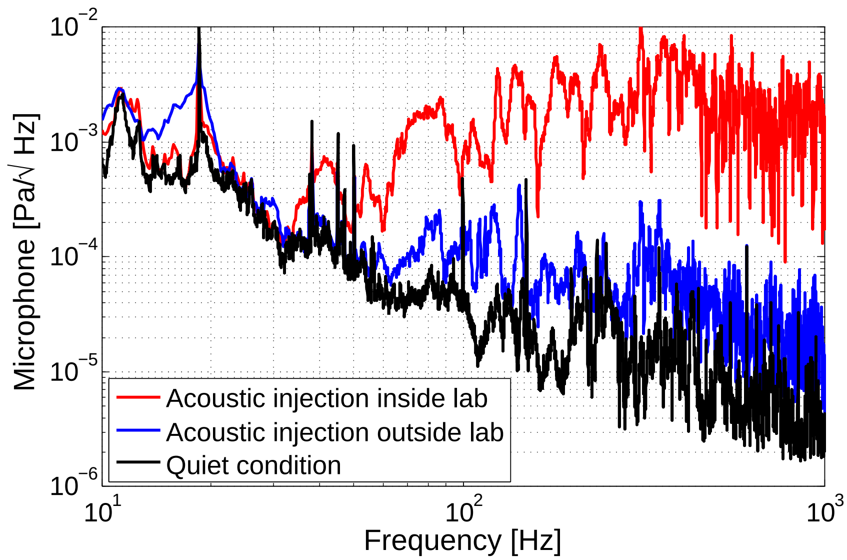

Figure 5.49: *Amplitude spectral densities of the microphone signal in quiet conditions (black curve) and during acoustic white noise injection inside (red curve) and outside (blue curve) the laser laboratory.*

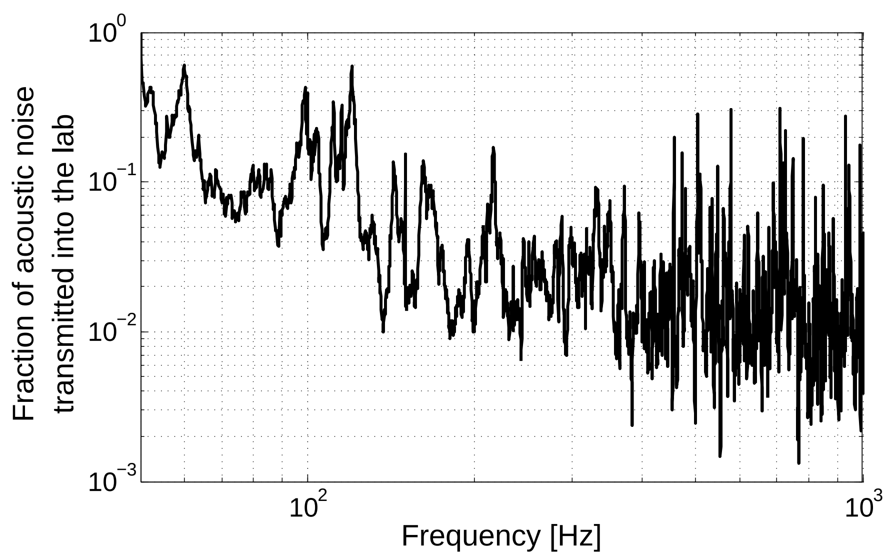

Figure 5.50: *During the acoustic white noise injection outside the laser lab, the acoustic noise level on both sides of the laser laboratory wall was measured. Both calibrated microphones were far away from the acoustic noise source. From these signals we can calculate that the laser laboratory acoustic isolation stops 90 – 95% of the acoustic noise.*

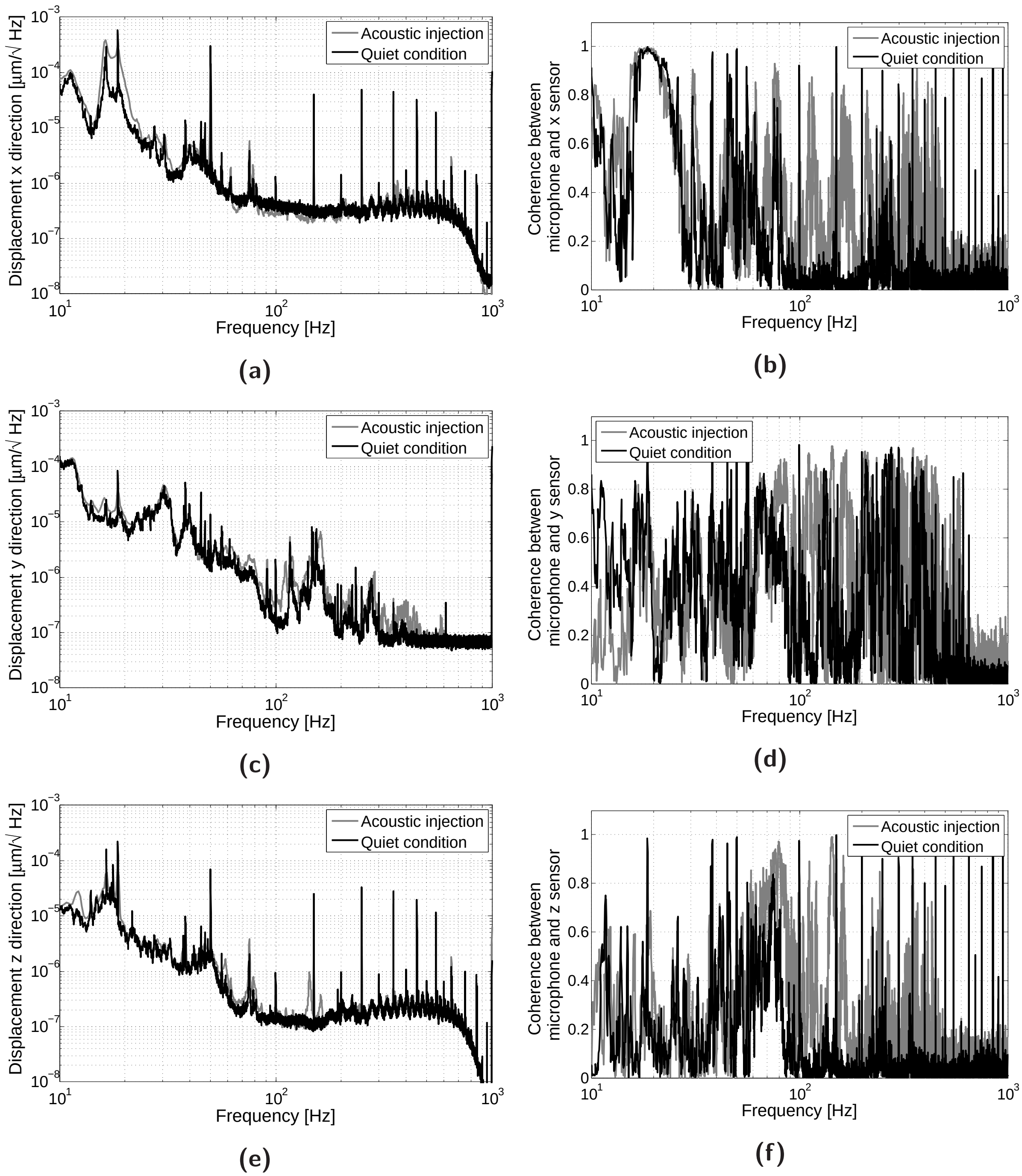

Figure 5.51: *Amplitude spectral densities of the virtual displacement sensors and their coherence with the microphone signal under quiet conditions (black curves) and during strong (up to 80 dB) acoustic noise injection from outside laser laboratory (gray curves).*

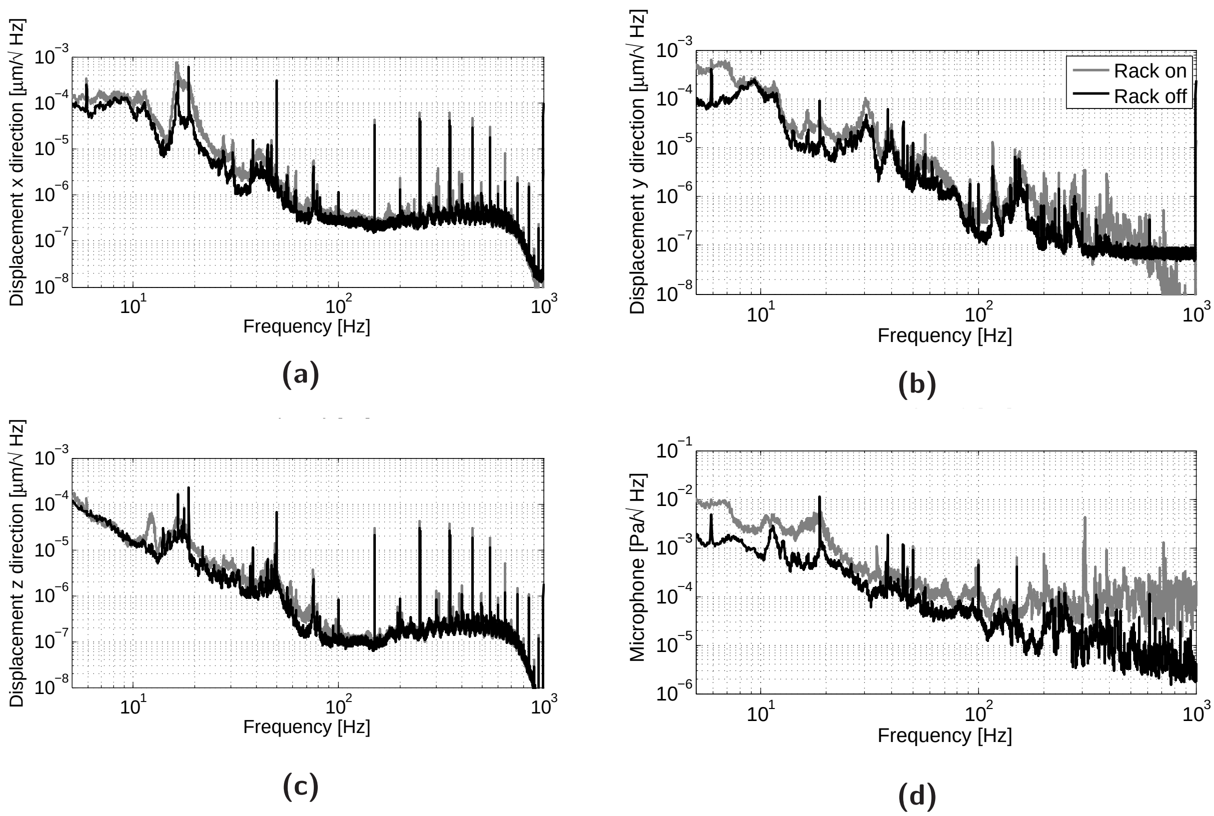

Figure 5.52: *Amplitude spectral densities of microphone and virtual displacement sensor signals in quiet conditions (black curves) and during acoustic noise injection from the electronics rack (gray curves). The controls are engaged.*

In the horizontal degrees of freedom the structural modes at 16 Hz, the springbox modes between 30 and 60 Hz are excited slightly. Above 100 Hz the motion remains imperceptible to the sensors. In the *y* degree of freedom the motion at every frequency is somewhat increased. Still, the effects of the acoustic noise from the rack are modest and acceptable.

Noise from the climate control system in science mode

Fig. 5.53 shows the amplitude spectral densities of the virtual motion sensors, the ground motion sensors and the microphone in the Advanced Virgo laser laboratory under quiet conditions and with the cleanroom air-conditioning system in science mode. According to the microphone the air-conditioning system does not introduce acoustic noise. However, the displacement spectra with the air-conditioning in science mode show a slight increase in bench motion and ground motion up to 10 Hz. This is caused by stronger winds during climate control tests than during the reference measurements (some 12 hours earlier, the night before). The effects of the air-condition in science mode are negligible.

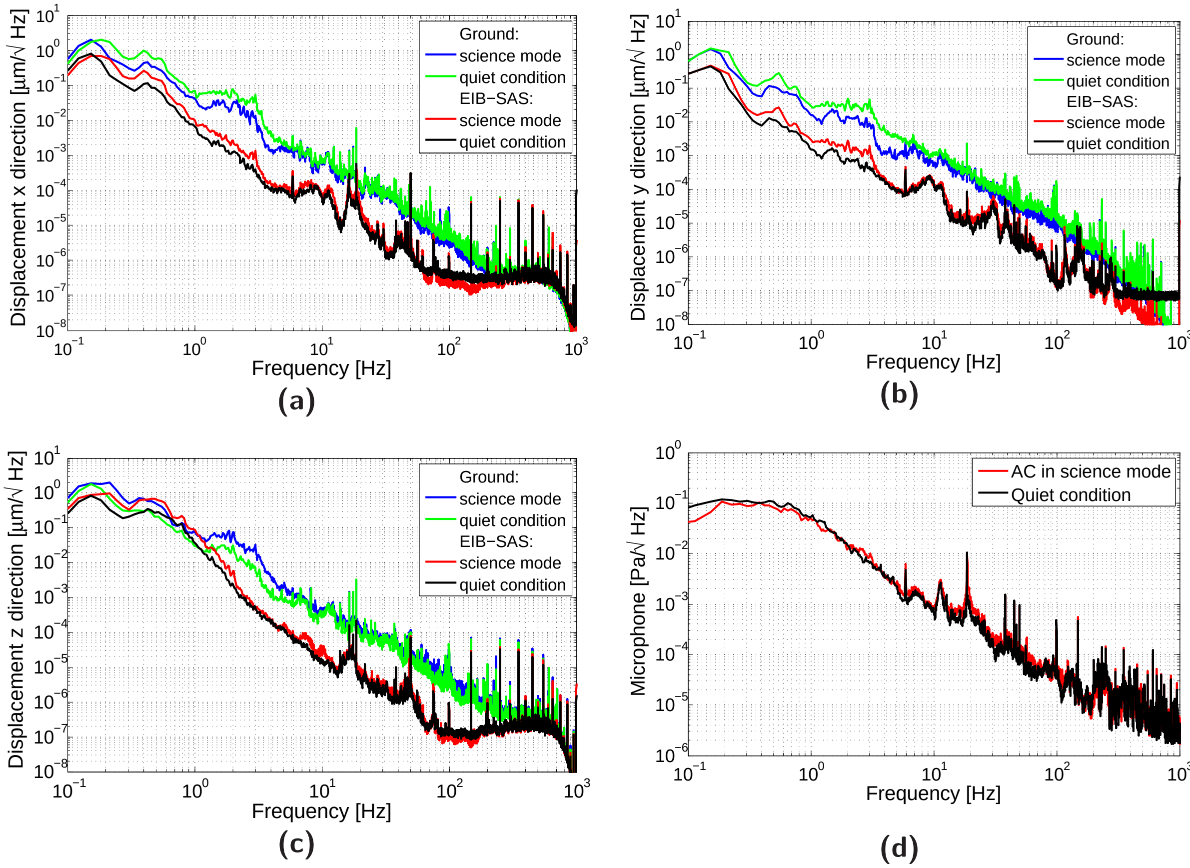

Figure 5.53: *Amplitude spectral densities of the ground motion sensors, the virtual displacement sensors and the microphone under quiet conditions and with the air-conditioning engaged in science mode. The difference in displacement spectra is due to increased ground excitation by the wind. The acoustic noise generated by the cleanroom climate control in science mode is negligible.*

5.7 EIB-SAS Advanced Virgo displacement noise

Fig. 5.54 shows the displacement spectrum of EIB-SAS with the electronics rack for the laser on (gray curve) together with a measurement result obtained in quiet conditions (solid black curve), that of the old bench support structure (blue curve) and the requirement [80] (dashed curve). The spectra have been measured with the bench geophones, of which the vertical one is in-loop and the horizontal ones are not.

The first thing to note is that above 100 Hz the residual motion of the bench is below the noise floor of the sensors. Above this frequency, only resonances are seen by the sensors. Therefore, we can only compare this direct measurement with the requirement below 200 Hz.

Below 200 mHz, the residual motion of the bench just overshoots the requirement curve. This is due to the small phase margin of the controls at this frequency, which causes a small amplification of the micro-seismic peak, which was already mentioned in section 5.4.5.

In the absence of acoustic noise EIB-SAS meets the requirement at every frequency, except 154 Hz. The measured motion spectrum is close to the one we had predicted based on the displacement noise projections made in section 5.3.3. Only, the 154 Hz structural mode of the springbox is excited slightly more than projected.

With the acoustic noise of the laser rack present, a few more structural resonances of the springbox are excited, two of which (at 116 and 203 Hz) to just above the requirement. The springbox is also excited between 20 and 40 Hz, but stays below the required limit. Borne by EIB-SAS, the displacement noise spectrum of the external injection bench is reduced by 1 to 3 orders of magnitude compared to the old support structure.

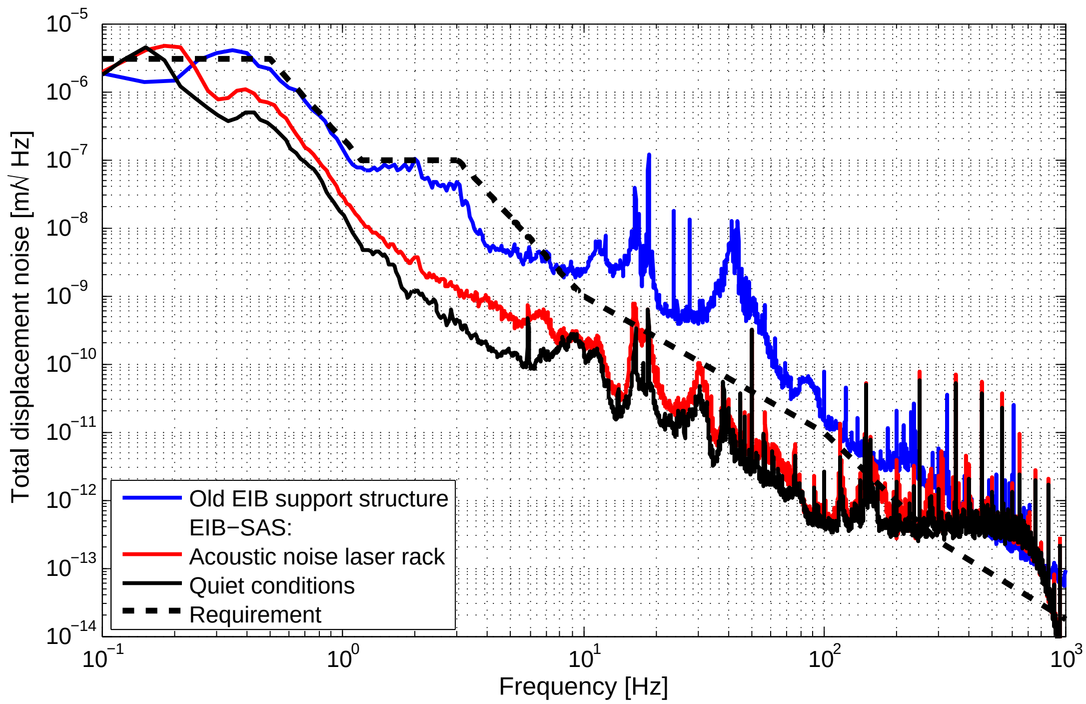

Figure 5.54: *Displacement noise of EIB-SAS versus requirement. The amplitude spectral densities of the residual motion of EIB-SAS in controlled mode under quiet conditions (solid black curve) and under realistic noise conditions (red curve). The blue curve represents the motion spectrum of the old support structure, while the dashed black curve indicates the requirement for Advanced Virgo. The spectra have been measured with the geophones positioned on the bench. The vertical geophone is in-loop, while the horizontal geophones are out-of-loop.*

5.8 Summary

The low-frequency rigid body modes of EIB-SAS have been identified. Due to the inertia of the bench and the height of its center of mass, the frequencies of the *Tx* and *Tz* rigid body modes were below 200 mHz, which caused them to exhibited too much hysteresis. By incorporating a tilt stabilizer, these modes have been successfully stiffened and their resonance frequency raised. All six low-frequency rigid body modes have a resonance frequency between 200 and 550 mHz, which ensures the desired level of attenuation, while keeping the system robust.

A number of mechanical transfer functions of EIB-SAS have been directly measured. These measurements exhibit the systems isolation characteristics and indicate its high-frequency rigid body modes.

The transfer functions of vertical ground motion to vertical motion of the springbox, and of the bench have been measured. Between 35 and 250 Hz, the springbox has a number of structural modes. The high-frequency rigid body mode, in which the springbox bounces on the top flexible joints and tubes of the inverted pendulums has been observed at 49 Hz. This mode is damped with a custom eddy current damper. Between 340 and 350 Hz, a number of resonances have been observed, which had already been identified as internal modes of the GAS filter blades in section 3.5.8. At these frequencies, EIB-SAS delivers 20 dB of isolation. Outside this frequency range it provides between 30 and 60 dB attenuation of vertical ground motion.

The transfer functions of horizontal ground motion in the x and z directions to translational motion of the bench in the same direction, and rotational motion around the orthogonal axes, have also been measured. They show that the high-frequency rigid body modes of the x and z degrees of freedom occur at 16 Hz, for the *Ty* degree of freedom at 12 Hz, and those of the *Tx* and *Tz* degrees of freedom at 41 and 36.5 Hz respectively. The *Tx* and *Tz* modes have also been damped with a custom eddy current dampers. The *Ty*, x and z modes are damped by the control system. In the x and z directions, the system has high-frequency structural modes at respectively 183 and 225 Hz. The Q-factor of the 183 Hz mode has been lowered with a structural damper, whose damping is based on internal friction. In the horizontal directions, EIB-SAS provides between 20 and 80 dB vibration isolation, depending on the frequency of the disturbance.

The motion of the bench is monitored with LVDT position sensors, which measure displacement with respect to the ground, and with inertial sensors (geophones). Geophones that monitor the motion of the ground are used to correct the LVDTs. The readings of the corrected LVDTs and geophones are combined into virtual sensors, which are sensitive in only a single degree of freedom each. These virtual sensors provide the error signals for the control loops. Appropriate correction signals are applied with voice-coil actuators. The control filters are divided into two parts: a viscous damping filter that lowers the Q-factor of the rigid body modes, and a PID filter that provides the long-term stability of the reference position.

We have shown that the controls are stable. Long-term stability measurements show that the residual motion of the system is a factor 10 below the required limits. As expected, the vertical degree of freedom is the most sensitive to temperature variations, and the observed temperature induced motion is well described by the theoretical relation derived in section 3.5.3.

EIB-SAS has been tested with the Virgo+ injection system. A comparison of a number of control signals and sensor readings with the external injection on its old support structure and on EIB-SAS shows that the structural modes of the old support structure have been eliminated, and no new ones have been introduced.

After the final installation of EIB-SAS in January 2014, acoustic noise injections have been performed. Acoustic noise from outside the injection laser laboratory does not affect EIB-SAS. The room effectively stops acoustic pressure waves. Under realistic acoustic noise conditions inside the laser laboratory, the rigid body modes of EIB-SAS and a number of structural modes of the springbox are excited enough to slightly exceed the requirement. This happens at 16, 116, and 154 - 164 Hz.

Below 1 Hz, EIB-SAS follows the ground motion. Above this frequency it is controlled on the inertial sensors and the full isolation capabilities of EIB-SAS are exploited. Except at the frequencies that correspond to the rigid body modes listed above, the residual displacement spectrum of EIB-SAS is a factor 5 to 10 below the requirement.

6 GAS filter blade design

"Fashion is architecture. It is a matter of proportions.",
Gabrielle Bonheur (Coco) Chanel,
Coco Chanel: Her Life, Her Secrets (1971)

6.1 Introduction

In section 3.5.4 we showed that given a certain load, the bending profile of the blade, and therefore its internal stress levels are determined by its width profile $\gamma(\lambda)$, with λ the curvilinear coordinate along the symmetry axis of the blade. The stress is maximum in the central region of the blade. Making the blade wider in the middle will reduce the maximum stress level. We have designed new low-stress blades. These new designs as well as their characterization measurements are reported in this chapter.

6.2 Design of low-stress blades

A shape function for cantilever blades in GAS filters has been designed by Cella *et al* [101]. We refer to these blades, which are used in EIB-SAS, as Type A. We have designed two new blades that are wider in the high stress region of the EIB-SAS blade. They are predicted to have a more uniform radius of curvature and lower maximum stress, while carrying the same load. Fig. 6.1 shows the width profile of these new blades. The black curve indicates the width profile of the Type A blades. The red and blue curves correspond to those of the new blades, and will be referred to as *Type B* and *Type C*. Their properties are listed in Table 6.1.

The bending profiles of these two new blades have been calculated with the numerical model. GAS filters with four of these blades have been constructed. For these blades too, their shapes under load have been measured with a Wenzell 3D measuring device. Fig. 6.2a shows the radius of curvature obtained from the model (curves) and blade shape measurements (dots) for the blades of Type A (black), Type B (red) and Type C (blue).

For the blades of Type B the model agrees well with the measurement results and the minimal radius of curvature of the blade is increased by 11%. For Type C blades the model

Blade property	Type A	Type B	Type C	Unit
Length, L	273.8	270.0	267.0	mm
Thickness, d	2.4	2.5	2.6	mm
Width at base, w_0	80.0	76.0	68.8	mm
Max width, w_{max}	80.0	80.3	88.1	mm

Table 6.1: *Summary of the properties of the Type A, B and C blades.*

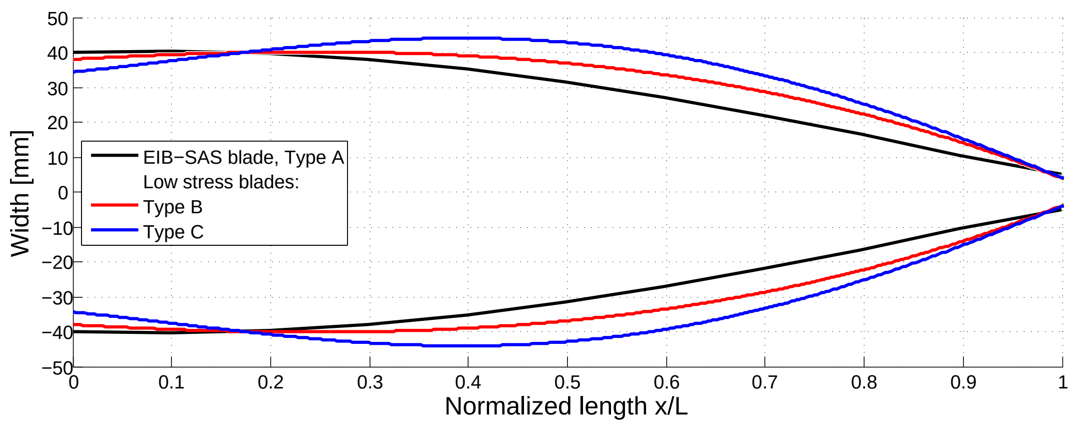

Figure 6.1: *Low-stress blade shapes. The black curve represents the Type A blade which is used in the EIB-SAS GAS filters, the red and blue curve represent two newly designed low-stress blades, with a more uniform radius of curvature when loaded. These blades are referred to as Type B and Type C.*

does not agree with the measurements. The radius of curvature predicted by the model has one minimum, just like Type A and B blades. The measured radius of curvature has two minima and a local maximum at $x/L = 0.575$, while the model predicts a minimum at this location.

Based on these radii of curvature the stress in the blades can be calculated. In these calculations we neglect the effects from the Poisson ratio. It is shown in Fig. 6.2b. The stresses from the model are depicted by the solid curves, those from the measurements by the dots (black for Type A, red for Type B, blue for Type C). The maximum stress in Type B blades is 1.37 GPa according to the numerical model and 1.27 GPa according to the blade shape measurements. The maximum stress in Type C blades is 1.33 GPa according to the numerical model and 1.27 GPa according to the blade shape measurements, although in a smaller region. Both these values are significantly lower than the maximum stress that was measured in Type A blades used in the EIB-SAS GAS filters; the numerical model predicts a value of 1.48 GPa. We conclude that changing the shape of the blade lowers the maximum stress that in the blades by about 10% according to the numerical model.

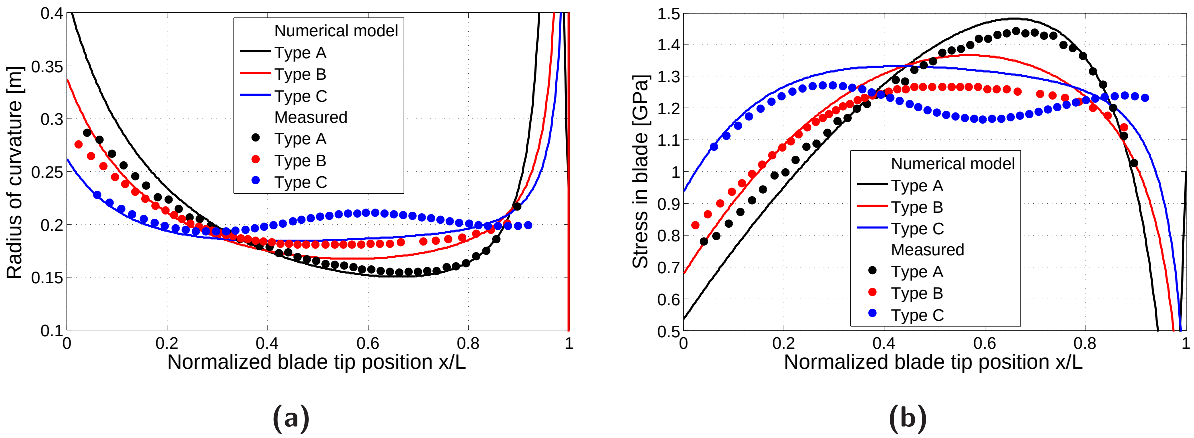

Figure 6.2: *Radius of curvature (ROC) and stress of the different types of blades. a) According to the numerical model the minimal ROC of Type A blades (EIB-SAS) is 0.150 m, of Type B blades 0.170 m and of Type C blades 0.185 m. According to the measurements they have a minimal ROC of respectively 0.155 m, 0.181 m and 0.193 m (averaged over 4 blades per filter respectively). b) A minimal radius of curvature corresponds to a maximum stress. According to the numerical model the maximum stress is 1.48 GPa in Type A blades, 1.37 GPa in Type B blades and 1.33 GPa in Type C blades. According to the measurements the maximum stress is 1.44 GPa in Type A blades and 1.27 GPa in both Type B and Type C blades.*

6.3 FEM model of low-stress blades

Up to now the effects of the Poisson ratio have been neglected (also in the literature [101, 102, 94, 100] the Poisson effect was never considered). In section 3.5.7 we have seen that these effects can be significant: ignoring the Poisson effect, the FEM model predicts a maximum stress of 1.53 GPa in Type A blades, while with the Poisson effect taken into account 1.80 GPa is predicted. This latter value corresponds to 90% of the ultimate tensile stress of maraging steel. Being so close to this increases the risk of plastic deformation of the blades, stress corrosion and creep. The Type B and C blades should have significant lower maximum stresses.

To take into account the Poisson effect in the Type B and Type C blades, FEM models were constructed. Due to the symmetry of the blade it suffices to model half a blade. In the models a half blade consists of 160 quadratic shell elements which are bent from their straight, unloaded shape to their curved, loaded shape in 100 steps.

Fig. 6.3a shows the stress in Type B blade according to the FEM model; the upper part shows the stress in the top surface of the blade, the bottom one that in the bottom surface of the blade. The maximum stress is 1.44 GPa in the bottom surface of the blade and 1.56 GPa in its top surface.

Fig. 6.3b shows the stress in the Type C blade according to the FEM model; the upper part shows the stress in the top surface of the blade, the bottom one that in the bottom surface of the blade. The maximum stress is 1.21 GPa in the bottom surface of the blade and 1.35 GPa in its top surface.

The stresses in the different types of blades obtained from the blade shape measurements, the numerical model and the finite element model are summarized in Table 6.2. We conclude that according to the FEM models, the stress in Type B blades is 87%, and the stress in Type C blades only 75% of that in Type A blades. The stresses in Type B and C blades is only 79% and 68% of the ultimate tensile stress of maraging steel, and the risk on plastic deformation and stress corrosion is greatly reduced with respect to Type A blades.

	Maximum stress at the working point (GPa)			
	FEM model		Numerical model	Measurement
Blade	Top	Bottom		
Type A	1.79	1.63	1.48	1.44
Type B	1.56	1.44	1.37	1.27
Type C	1.35	1.21	1.33	1.27

Table 6.2: *Summary of the stresses in the different types of blades according to the FEM model, numerical model and blade shape measurements. Note that the newly designed blades show a significant stress reduction, while delivering the same performance.*

6.4 Tuning of the low-stress blades

When the GAS filters comprised of Type B and C blades (referred to as Filter B and Filter C) were loaded and tuned to their working point, we discovered that their minimal resonance frequency was higher than that of the EIB-SAS GAS filter with Type A blades.

Fig. 6.4a shows the height of the keystone of Filter B as a function of its load for compressions ranging from 8.40% to 9.30%. From these measurements it is clear that compressing the blades more than 9.30% would make the filter bi-stable (see Fig. 3.23).

The resonance frequency of the filter as a function of the keystone height is shown in Fig. 6.4b. At the highest stable compression the minimum frequency of the filter is 277 mHz. Filter B cannot be tuned lower than this frequency, while the EIB-SAS filter was tuned to 150 mHz with little difficulty.

The same was done for Filter C. Fig. 6.5a shows the height of the keystone of Filter C as a function of its load for a compression of 8.08% (green dots), 8.10% (red dots) and 8.13% (black dots). Fig. 6.5b shows its frequency. Compressing the filter by more than 8.13% would make it bi-stable. In this compressed state the minimum resonance frequency of the filter is 320 mHz.

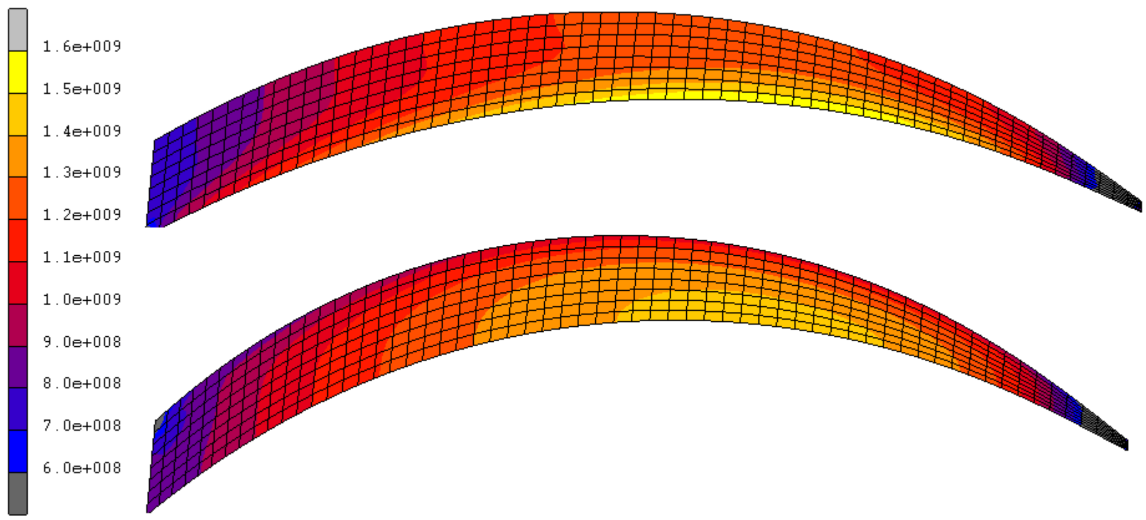

(a) *Type B blade*

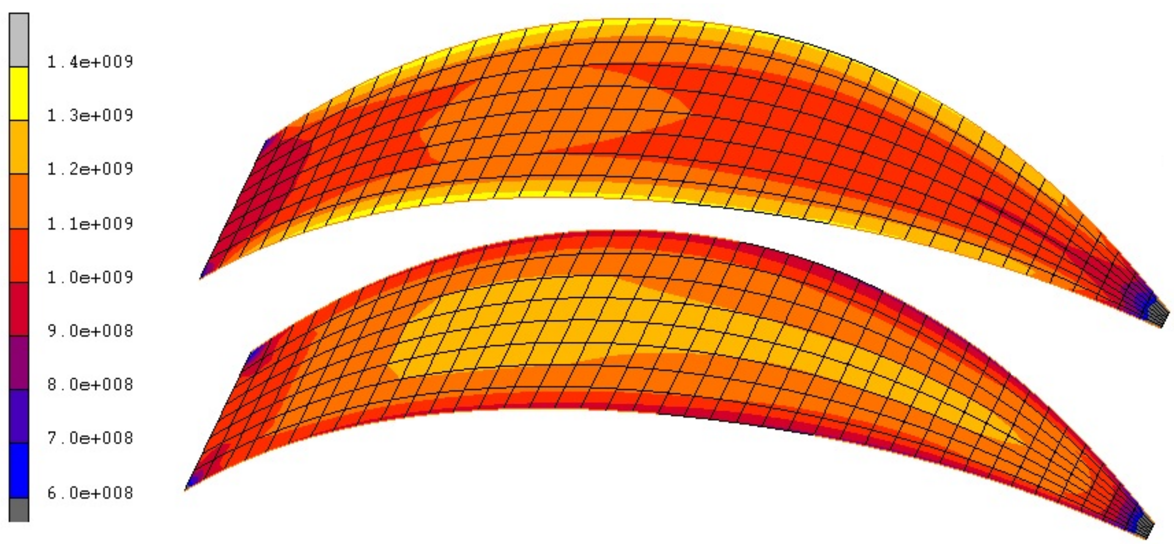

(b) *Type C blade*

Figure 6.3: *Von Mises stress in the top (upper) and bottom (lower) surface of fully loaded (a) Type B and (b) Type C blades according to the finite element model. The Poisson ratio ν = 0.32. The maximum stress induces in these new blades, carrying the same load, is 12% and 25% lower than that induced in Type A blades installed in the GAS filters incorporated in EIB-SAS.*

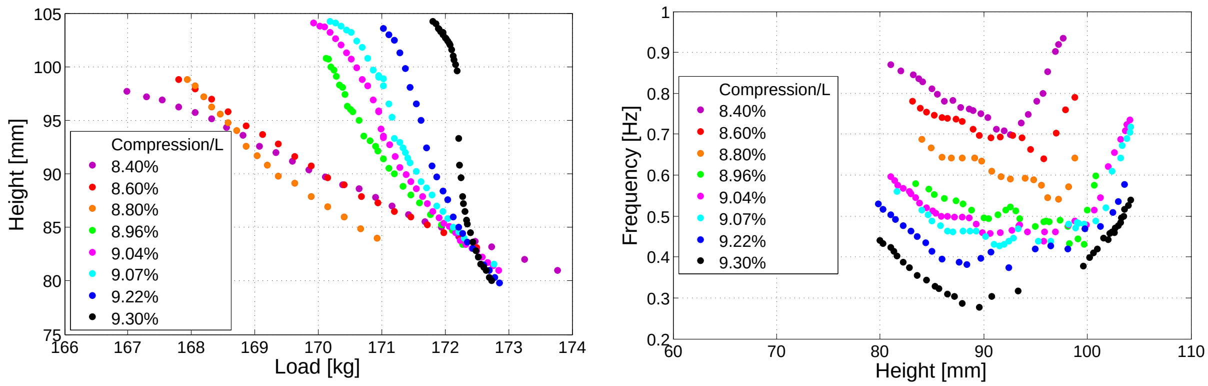

(a) **(b)**

Figure 6.4: *a) Load-height curves and b) height-frequency curves of the filter with Type B blades at different compression.*

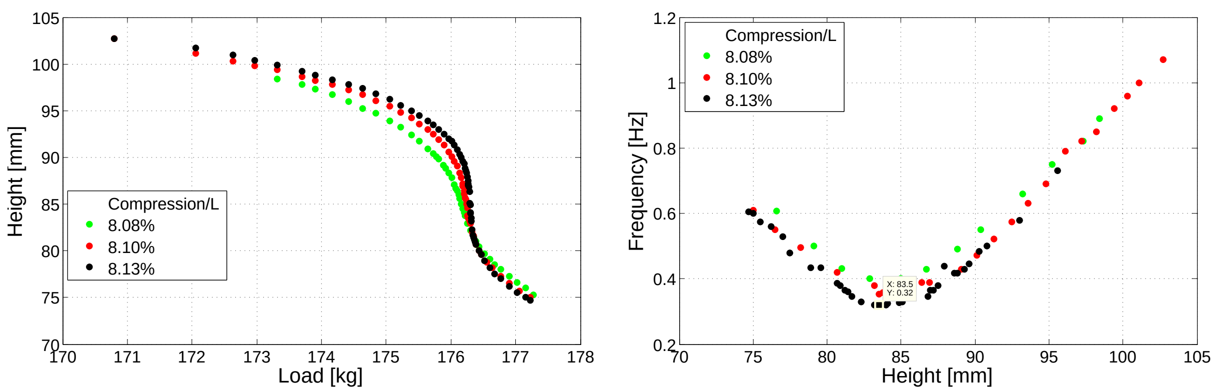

(a) **(b)**

Figure 6.5: *a) Load-height curves and b) height-frequency curves of the filter with Type C blades at different compression.*

In conclusion, while they can carry a heavier load, filters composed of the Type B and Type C blades cannot be tuned to frequencies below 277 and 320 mHz, which limits the amount of seismic isolation they can provide.

6.5 Frequency of the filters based on their stiffness

The resonance frequencies in Figs. 6.4 and 6.5 were measured by counting small amplitude oscillations of the filter. The same measurements can also be used to determine the frequency of the filter in a different way. As the stiffness of the filter is a change in displacement due to a change in force, the change in keystone height due to a load variation is an estimate of the stiffness of the filter, *i.e.* $k_{\text{filter}} = g\partial m/\partial h$. The frequency of the filter is then given by $f_{\text{filter}} = \sqrt{k_{\text{filter}}/m}/2\pi$.

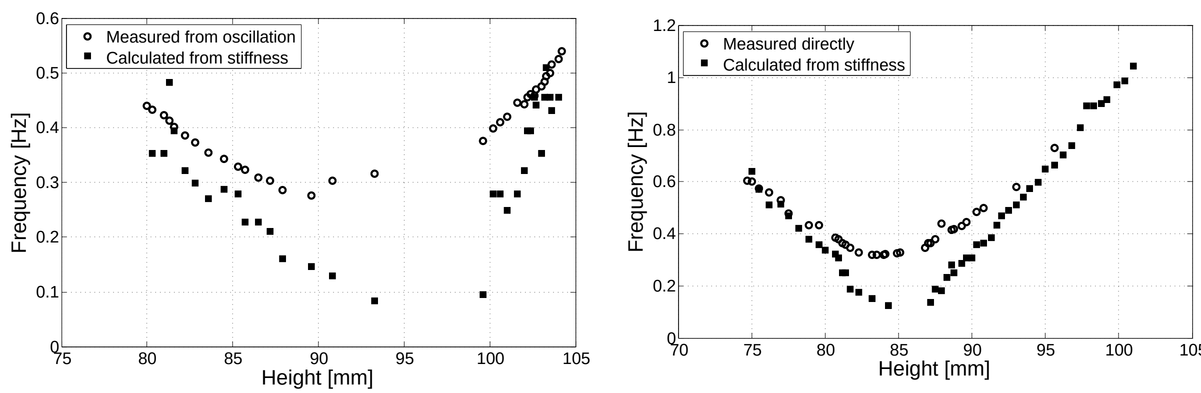

(a) *B filter.* **(b)** *C filter.*

Figure 6.6: *Height-frequency curves of (a) Filter B with a compression of 0.093 for a resonance frequency of 84 mHz and (b) Filter C with a compression of 0.0813 for a resonance frequency of 125 mHz. The frequency was determined in two ways: by counting oscillations (black circles), and by determining the stiffness of the filter (black squares). The latter follows from the change in equilibrium position due to a load change. The frequencies given by these two approaches differ significantly.*

Fig. 6.6 shows the frequency of Filters B and C determined by counting oscillations (black circles) and from calculating the stiffness of the filter (black squares). Near the working point, calculating the frequency from the measured stiffness gives a lower value than measured. This discrepancy between the two frequencies is explained by hysteresis.

6.6 Hysteresis in low-stress blades

Fig. 6.7 shows two load-height curves of Filter C. The first was measured loading the filter (red dots), the second unloading the filter (blue squares). Even more so than for the EIB-SAS blades (see section 3.5.7), the height of the keystone does not only depend on the instantaneous load, but also on the load history. The filters with low-stress blades exhibit a significant amount of hysteresis.

According to the red curve, the filter seems to be in a maximum compressed state. The slope of the linear fit (short dashed curve) to the data is -155 mm/kg and was used earlier to estimate the stiffness of the filter. However, the measurement where the filter was unloaded, shows that this is clearly not the case. According to that measurement, the stiffness of the filter is only -22.9 mm/kg which is much smaller. Based on the two slopes the filter would have two resonance frequencies for the same load: 95 mHz and 253 mHz.

Measuring the stiffness of the filter based on its resonance frequency would not agree with either the loading nor unloading curve. It should be more similar to loading the filter until it is beyond its working point and consecutively unloading it beyond its working point, simulating an oscillation.

The results of two such measurements are shown in Fig. 6.8. One starting with loading the filter (red dots) and consecutively unloading and reloading the filter (green dots). The other starting with unloading the filter (dark blue dots) and consecutively loading and unloading the filter (light blue dots). The dotted and dashed curves are fits to the final loading/unloading part of the measurement. Their slopes are -9.3 mm/kg and -11.9 mm/kg. Taking their average to approximate the stiffness of the filter in the working point (925.5 N/kg) gives a resonance frequency of 365 mHz, which is in much better agreement with the 320 mHz from the oscillation measurement.

6.7 Summary

The stress distribution in the GAS filter blades is determined by the width profile of the blades. Making the blades wider, with respect to the EIB-SAS GAS filter blades, in the central, high-stress region improves the stress distribution and hence, lowers the maximum stress value up to 25%.

Two new, low-stress blades have been designed. Referring to the EIB-SAS blades as Type A blades, the new blades are referred to as Type B and Type C blades. According to both a FEM model and a numerical model, the maximum stress that occurs in these blades in 88% and 75% of the value that occurs in Type A blades. Calculating the stress from the blade shape measurements shows that the maximum stress in both new blades is reduced by as much as 25% with respect to the Type A blades, while they carry the same load. Taking the Poisson effect into account, the maximum stress in Type B and C Blades is only 69% and 78% of the ultimate tensile stress of maraging steel, while it was 90% in Type A blades. The risks of unwanted phenomena like creep and stress corrosion are lower for these new blades.

GAS filters incorporating they new blades have been constructed and tested. These test filters demonstrate strong hysteresis; loading or unloading the filters gives a very different load-height curve, and hence, different value of the vertical stiffness and resonance frequency.

From the unloaded curves one would conclude the filter is still stable, while in fact, it is not. Mimicking an oscillation quasi-statically, by consecutively loading and unloading the filter, we see that the loading and unloading curves provide similar load-height curves. The stiffness that can be inferred from these measurements is consistent with that calculated from the resonance frequency measurement.

In this way, we have shown that the new filters cannot be tuned to frequencies as low as the filter with Type A blades. The lowest possible frequency of a Type B blade is 277 mHz, and that of a Type C blade 320 mHz, while the GAS with Type A blades could easily be tuned to 150 mHz. Therefore, the amount of isolation the filters consisting of Type B and C can provide is limited with respect to that with Type A blades.

It seems that a high stress region in the blades is necessary for the ability of the filter to be tuned to ultra low resonance frequencies.

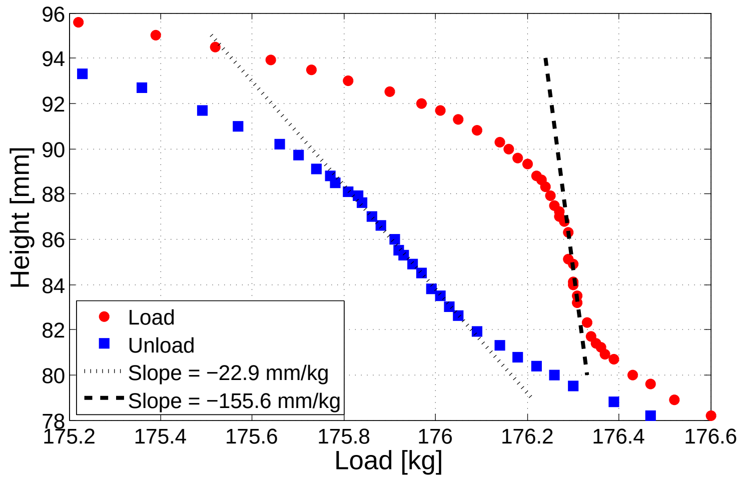

Figure 6.7: *Hysteresis in test Filter C. The load-height curve of this new filter has been measured loading (red dots) and unloading (blue squares) the filter. These two curves are different, indicating hysteresis. The vertical stiffness of the filter is given by the slope of a linear fit to the data in the working point (black dotted/dashed curves). Is this case there are two working points and hence two stiffnesses. The unloading data have a slope of -22.9 mm/kg, which corresponds to a resonance frequency of 253 mHz. The loading data have a slope of -155.6 mm/kg, which corresponds to a resonance frequency of 95 mHz.*

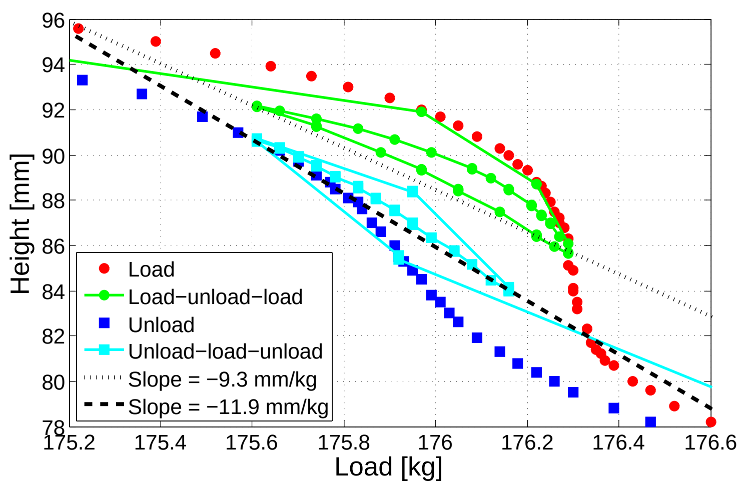

Figure 6.8: *Frequency of the filters based on their stiffness. The blue and red data points correspond to the loading and unloading curves of Fig. 6.7. The red and green data points correspond to consecutively loading and unloading the filter beyond its working point. In this way an oscillation is performed quasi-statically. The blue data points are similar, but in reversed order. The stiffness given by the slopes of the linear fit in the working point are -11.9 mm/kg and -9.3 mm/kg. These correspond to resonance frequencies of 345 and 390 mHz, which agrees much better with the 320 mHz resonance frequency determined by counting oscillations.*

A Transfer function data points

Table A.1 contains the data points of the transfer functions depicted in Figs. 5.13, 5.14, and 5.15 for frequencies up to 100 Hz.

Freq. [Hz]	y→ y	x→ x	x→ Tz	z→ z	z→ Ty
2.0	0.0772	0.0330	0.0317	0.0499	0.0242
2.5	0.0500	0.0267	0.0123	0.0190	0.0095
3.0	0.0413	0.0165	0.0079	0.0072	0.0036
3.5	0.0233	0.0124	0.0077	0.0116	0.0058
4.0	0.0166	0.0109	0.0073	0.0077	0.0039
4.5	0.0146	0.0075	0.0054	0.0086	0.0037
5.0	0.0117	0.0039	0.0049	0.0109	0.0032
5.5	0.0087	0.0050	0.0036	0.0051	0.0025
6.0	0.0069	0.0041	0.0036	0.0040	0.0019
6.5	0.0044	0.0045	0.0038	0.0035	0.0018
7.0	0.0051	0.0039	0.0034	0.0032	0.0015
7.5	0.0040	0.0042	0.0027	0.0039	0.0019
8.0	0.0026	0.0036	0.0028	0.0033	0.0016
8.5	0.0022	0.0036	0.0030	0.0033	0.0016
9.0	0.0016	0.0033	0.0028	0.0033	0.0016
9.5	0.0014	0.0029	0.0024	0.0036	0.0018
10.0	0.0013	0.0030	0.0025	0.0037	0.0019
10.5	0.0013	0.0030	0.0027	0.0045	0.0023
11.0	0.0013	0.0030	0.0027	0.0061	0.0031
11.5	0.0018	0.0029	0.0028	0.0109	0.0054
12.0	0.0017	0.0030	0.0030	0.2547	0.1274
12.5	0.0014	0.0033	0.0033	0.0047	0.0048
13.0	0.0015	0.0037	0.0037	0.0022	0.0022
13.5	0.0017	0.0041	0.0041	0.0014	0.0014
14.0	0.0018	0.0048	0.0049	0.0010	0.0010

14.5	0.0020	0.0060	0.0063	0.0008	0.0008
15.0	0.0022	0.0087	0.0095	0.0006	0.0006
15.5	0.0020	0.0207	0.0230	0.0008	0.0004
16.0	0.0052	0.0342	0.0358	0.0056	0.0010
16.5	0.0028	0.0084	0.0096	0.0012	0.0003
17.0	0.0030	0.0042	0.0050	0.0013	0.0003
17.5	0.0030	0.0026	0.0032	0.0012	0.0003
18.0	0.0031	0.0017	0.0022	0.0011	0.0002
18.5	0.0032	0.0014	0.0016	0.0009	0.0002
19.0	0.0032	0.0010	0.0012	0.0012	0.0002
19.5	0.0034	0.0008	0.0008	0.0011	0.0002
20.0	0.0036	0.0004	0.0006	0.0010	0.0002
20.5	0.0036	0.0004	0.0004	0.0011	0.0002
21.0	0.0038	0.0003	0.0003	0.0011	0.0002
21.5	0.0040	0.0001	0.0002	0.0012	0.0002
22.0	0.0040	0.0001	0.0001	0.0011	0.0002
22.5	0.0037	0.0001	0.0001	0.0011	0.0002
23.0	0.0036	0.0002	0.0002	0.0012	0.0002
23.5	0.0036	0.0003	0.0003	0.0012	0.0002
24.0	0.0037	0.0003	0.0005	0.0012	0.0002
24.5	0.0036	0.0004	0.0005	0.0013	0.0002
25.0	0.0033	0.0004	0.0007	0.0013	0.0002
25.5	0.0033	0.0005	0.0007	0.0013	0.0002
26.0	0.0034	0.0005	0.0008	0.0014	0.0002
26.5	0.0039	0.0004	0.0007	0.0014	0.0002
27.0	0.0038	0.0005	0.0008	0.0015	0.0002
27.5	0.0037	0.0005	0.0009	0.0015	0.0002
28.0	0.0034	0.0006	0.0011	0.0014	0.0002
28.5	0.0033	0.0007	0.0012	0.0014	0.0002
29.0	0.0031	0.0008	0.0014	0.0015	0.0002
29.5	0.0029	0.0009	0.0015	0.0016	0.0002
30.0	0.0029	0.0010	0.0018	0.0017	0.0002
30.5	0.0029	0.0012	0.0021	0.0019	0.0002
31.0	0.0034	0.0014	0.0025	0.0019	0.0002
31.5	0.0034	0.0017	0.0035	0.0021	0.0002
32.0	0.0034	0.0029	0.0057	0.0023	0.0002
32.5	0.0035	0.0038	0.0066	0.0018	0.0004

33.0	0.0036	0.0015	0.0029	0.0017	0.0004
33.5	0.0038	0.0006	0.0013	0.0019	0.0004
34.0	0.0046	0.0003	0.0006	0.0022	0.0004
34.5	0.0039	0.0004	0.0005	0.0024	0.0004
35.0	0.0042	0.0006	0.0009	0.0026	0.0004
35.5	0.0042	0.0008	0.0013	0.0028	0.0005
36.0	0.0043	0.0009	0.0016	0.0031	0.0005
36.5	0.0045	0.0012	0.0021	0.0034	0.0006
37.0	0.0053	0.0015	0.0033	0.0036	0.0006
37.5	0.0074	0.0020	0.0060	0.0038	0.0007
38.0	0.0156	0.0029	0.0100	0.0044	0.0008
38.5	0.0112	0.0047	0.0158	0.0056	0.0009
39.0	0.0084	0.0063	0.0258	0.0073	0.0011
39.5	0.0086	0.0046	0.0216	0.0091	0.0014
40.0	0.0092	0.0029	0.0135	0.0122	0.0020
40.5	0.0102	0.0020	0.0095	0.0191	0.0033
41.0	0.0114	0.0028	0.0115	0.0421	0.0073
41.5	0.0117	0.0025	0.0106	0.0369	0.0065
42.0	0.0108	0.0017	0.0076	0.0182	0.0032
42.5	0.0126	0.0013	0.0063	0.0125	0.0022
43.0	0.0140	0.0010	0.0055	0.0101	0.0018
43.5	0.0125	0.0010	0.0052	0.0085	0.0015
44.0	0.0189	0.0010	0.0047	0.0072	0.0013
44.5	0.0254	0.0010	0.0040	0.0062	0.0011
45.0	0.0280	0.0009	0.0038	0.0056	0.0010
45.5	0.0250	0.0007	0.0033	0.0052	0.0010
46.0	0.0209	0.0007	0.0030	0.0038	0.0007
46.5	0.0179	0.0006	0.0029	0.0023	0.0005
47.0	0.0158	0.0006	0.0027	0.0019	0.0004
47.5	0.0154	0.0006	0.0027	0.0018	0.0004
48.0	0.0166	0.0006	0.0034	0.0017	0.0004
48.5	0.0184	0.0005	0.0048	0.0015	0.0004
49.0	0.0194	0.0005	0.0034	0.0014	0.0004
49.5	0.0220	0.0004	0.0007	0.0015	0.0004
50.0	0.0194	0.0009	0.0004	0.0028	0.0006
50.5	0.0227	0.0009	0.0004	0.0013	0.0003
51.0	0.0206	0.0007	0.0005	0.0012	0.0003

51.5	0.0231	0.0006	0.0006	0.0011	0.0003
52.0	0.0218	0.0006	0.0006	0.0011	0.0003
52.5	0.0194	0.0005	0.0006	0.0010	0.0003
53.0	0.0163	0.0005	0.0007	0.0010	0.0003
53.5	0.0137	0.0004	0.0007	0.0009	0.0003
54.0	0.0119	0.0004	0.0007	0.0009	0.0003
54.5	0.0104	0.0004	0.0007	0.0008	0.0002
55.0	0.0101	0.0004	0.0007	0.0007	0.0002
55.5	0.0069	0.0004	0.0007	0.0007	0.0002
56.0	0.0062	0.0004	0.0009	0.0007	0.0002
56.5	0.0058	0.0003	0.0010	0.0006	0.0002
57.0	0.0055	0.0003	0.0008	0.0006	0.0002
57.5	0.0052	0.0003	0.0007	0.0006	0.0002
58.0	0.0050	0.0003	0.0007	0.0006	0.0002
58.5	0.0049	0.0003	0.0007	0.0006	0.0002
59.0	0.0048	0.0003	0.0006	0.0006	0.0002
59.5	0.0045	0.0003	0.0006	0.0006	0.0003
60.0	0.0045	0.0003	0.0005	0.0006	0.0002
60.5	0.0044	0.0002	0.0005	0.0006	0.0003
61.0	0.0044	0.0002	0.0005	0.0006	0.0002
61.5	0.0046	0.0002	0.0004	0.0006	0.0003
62.0	0.0045	0.0002	0.0005	0.0005	0.0003
62.5	0.0044	0.0001	0.0006	0.0005	0.0003
63.0	0.0044	0.0000	0.0007	0.0005	0.0003
63.5	0.0045	0.0001	0.0008	0.0004	0.0003
64.0	0.0045	0.0001	0.0007	0.0004	0.0002
64.5	0.0044	0.0002	0.0006	0.0004	0.0003
65.0	0.0043	0.0001	0.0005	0.0004	0.0003
65.5	0.0043	0.0001	0.0004	0.0005	0.0003
66.0	0.0042	0.0001	0.0004	0.0005	0.0003
66.5	0.0041	0.0001	0.0004	0.0005	0.0003
67.0	0.0039	0.0001	0.0003	0.0005	0.0003
67.5	0.0039	0.0000	0.0002	0.0004	0.0003
68.0	0.0039	0.0001	0.0002	0.0004	0.0003
68.5	0.0039	0.0001	0.0003	0.0004	0.0003
69.0	0.0039	0.0002	0.0006	0.0004	0.0004
69.5	0.0038	0.0002	0.0005	0.0005	0.0004

70.0	0.0037	0.0002	0.0004	0.0005	0.0004
70.5	0.0038	0.0002	0.0005	0.0004	0.0004
71.0	0.0039	0.0003	0.0006	0.0004	0.0004
71.5	0.0038	0.0002	0.0006	0.0005	0.0005
72.0	0.0039	0.0002	0.0005	0.0005	0.0005
72.5	0.0041	0.0002	0.0004	0.0006	0.0005
73.0	0.0040	0.0002	0.0005	0.0006	0.0005
73.5	0.0040	0.0001	0.0005	0.0007	0.0006
74.0	0.0036	0.0001	0.0005	0.0007	0.0007
74.5	0.0030	0.0002	0.0005	0.0008	0.0007
75.0	0.0031	0.0002	0.0003	0.0009	0.0008
75.5	0.0027	0.0002	0.0004	0.0011	0.0010
76.0	0.0033	0.0003	0.0003	0.0012	0.0011
76.5	0.0023	0.0003	0.0004	0.0014	0.0013
77.0	0.0019	0.0002	0.0004	0.0018	0.0017
77.5	0.0020	0.0002	0.0004	0.0023	0.0022
78.0	0.0016	0.0002	0.0004	0.0031	0.0030
78.5	0.0016	0.0002	0.0003	0.0049	0.0046
79.0	0.0016	0.0002	0.0001	0.0092	0.0088
79.5	0.0014	0.0003	0.0011	0.0106	0.0102
80.0	0.0013	0.0005	0.0048	0.0060	0.0058
80.5	0.0014	0.0003	0.0046	0.0039	0.0038
81.0	0.0009	0.0002	0.0037	0.0029	0.0028
81.5	0.0007	0.0002	0.0036	0.0023	0.0022
82.0	0.0007	0.0002	0.0035	0.0020	0.0019
82.5	0.0006	0.0002	0.0034	0.0018	0.0017
83.0	0.0006	0.0002	0.0038	0.0013	0.0012
83.5	0.0006	0.0002	0.0042	0.0012	0.0012
84.0	0.0006	0.0003	0.0046	0.0011	0.0011
84.5	0.0007	0.0003	0.0052	0.0010	0.0010
85.0	0.0006	0.0004	0.0060	0.0010	0.0009
85.5	0.0005	0.0005	0.0075	0.0009	0.0009
86.0	0.0004	0.0007	0.0092	0.0010	0.0009
86.5	0.0003	0.0010	0.0135	0.0008	0.0008
87.0	0.0003	0.0014	0.0212	0.0009	0.0009
87.5	0.0004	0.0026	0.0367	0.0007	0.0007
88.0	0.0006	0.0061	0.0805	0.0008	0.0007

88.5	0.0017	0.0033	0.0408	0.0006	0.0005
89.0	0.0007	0.0027	0.0340	0.0007	0.0005
89.5	0.0017	0.0016	0.0179	0.0006	0.0005
90.0	0.0010	0.0012	0.0100	0.0006	0.0005
90.5	0.0008	0.0011	0.0113	0.0005	0.0005
91.0	0.0007	0.0009	0.0093	0.0005	0.0005
91.5	0.0007	0.0008	0.0078	0.0005	0.0005
92.0	0.0006	0.0007	0.0068	0.0005	0.0005
92.5	0.0005	0.0007	0.0061	0.0005	0.0005
93.0	0.0005	0.0006	0.0055	0.0005	0.0005
93.5	0.0004	0.0006	0.0049	0.0005	0.0005
94.0	0.0004	0.0005	0.0043	0.0005	0.0005
94.5	0.0005	0.0005	0.0038	0.0005	0.0005
95.0	0.0004	0.0005	0.0034	0.0006	0.0006
95.5	0.0004	0.0005	0.0033	0.0006	0.0006
96.0	0.0004	0.0004	0.0032	0.0007	0.0006
96.5	0.0004	0.0004	0.0028	0.0007	0.0007
97.0	0.0005	0.0004	0.0027	0.0008	0.0007
97.5	0.0004	0.0004	0.0027	0.0009	0.0007
98.0	0.0003	0.0004	0.0024	0.0009	0.0007
98.5	0.0004	0.0004	0.0021	0.0009	0.0007
99.0	0.0004	0.0004	0.0020	0.0008	0.0007
99.5	0.0003	0.0004	0.0018	0.0008	0.0008
100.0	0.0005	0.0003	0.0020	0.0009	0.0008

Table A.1: *Data points of Figs. 5.13, 5.14, and 5.15.*

Bibliography

[1] A. Einstein, "Die Grundlage der allgemeinen Relativitätstheorie," *Annalen der Physik*, 1916.

[2] R. Hulse and J. Taylor, "Discovery of a pulsar in a binary system," *The Astrophysical Journal*, vol. 195, 1975.

[3] WGBH Boston, 2014. URL: www.ast.cam.ac.uk/research/cosmology.and.fundamental.physics/gravitational.waves.

[4] J. Weisberg, J. Taylor, and L. Fowler, "Gravitational Waves from an Orbiting Pulsar," *Scientific American*, vol. 245, 1981.

[5] NASA, 2014. URL: www.nasa.gov/images/content/681325main_gravitational-waves.jpg.

[6] J. Weisberg and J. Taylor, "Relativistic Binary Pulsar B1913+16: Thirty Years of Observations and Analysis," *Binary Radio Pulsars, Proc. Aspen Conference*, vol. 328, 2005.

[7] M. Gertsenshtein and V. Pustovoit, "On the Detection of Low-Frequency Gravitational Waves," *Soviet Journal of Experimental and Theoretical Physics*, vol. 16, p. 433, 1963.

[8] R. Forward, "Wideband laser-interferometer gravitational-radiation experiment," *Phys. Rev. D*, vol. 17, no. 2, pp. 379 – 390, 1978.

[9] R. Weiss, "Quarterly Progress Report, MIT Research Lab of Electronics 105," tech. rep., MIT, 1972.

[10] LIGO. URL: www.ligo.org/index.php.

[11] GEO600 gravitational wave detector. URL: www.geo600.org/.

[12] KAGRA gravitational wave detector. URL: gwcenter.icrr.u-tokyo.ac.jp/en/.

[13] Virgo gravitational wave detector. URL: wwwcascina.virgo.infn.it/.

[14] T. Accadia *et al.*, "Advanced Virgo Technical Design Report," 2012. Virgo note VIR-0128A-12.

[15] A. Stochino *et al.*, "The Seismic Attenuation System (SAS) for the Advanced LIGO gravitational wave interferometric detectors," *Nucl. Instrum. Methods Phys. Res. A*, vol. 598, pp. 737 – 753, 2009.

[16] S. Gossler *et al.*, "The AEI 10 m prototype interferometer," *Class. Quantum Grav.*, vol. 27, 2010.

[17] U. Le Verrier, "Lettre de M. Le Verrier à M. Faye sur la théorie de Mercure et sur le mouvement du périhélie de cette planète," *Comptes rendus hebdomadaires des séances de l'Académie des sciences (Paris)*, vol. 49, pp. 379 – 383, 1859.

[18] J. A. Wheeler, *Geons, Black Holes, and Quantum Foam*. W. W. Norton & Company, 1^{st} ed., 2000.

[19] S. Carroll, *An Introduction to General Relativity Spacetime and Geometry*. Addison Wesley, 1st ed., 2004.

[20] B. Schutz, *A First Course in General Relativity*. Cambridge University Press, 2nd ed., 2011.

[21] J. Aasi *et al.*, "The NINJA-2 project: detecting and characterizing gravitational waveforms modeled using numerical binary black hole simulations," *Class. Quantum Grav.*, vol. 31, 2014.

[22] M. Maggiore, *Gravitational Waves. Volume 1: Theory and experiments*. Oxford University Press, 1st ed., 2008.

[23] A. Corsi *et al.*, "Gravitational waves and gamma-ray bursts," *Proceedings IAU Symposium*, vol. 279, 2012.

[24] B. Baret *et al.*, "Multimessenger Sources of Gravitational Waves and High-energy Neutrinos: Science Reach and Analysis Method," *J. Phys.: Conf. Ser.*, vol. 363, 2012.

[25] B. Abbott *et al.*, "An upper limit on the stochastic gravitational-wave background of cosmological origin," *Nature*, vol. 460, pp. 990 – 994, 2009.

[26] H. Karttunen, P. Kröger, H. Oja, M. Poutanen, and K. Donner, *Fundamental Astronomy*. Springer, 4th ed., 2003.

[27] D. Lorimer, "Binary and Millisecond Pulsars," *Living Rev. Relativity [Online Article]*, vol. 8, no. 7, 2005.

[28] "Gravitational waves from known pulsars: results from the initial detector era," *The Astrophysical Journal*, vol. 785, 2014.

[29] J. Abadie *et al.*, "Beating the spin-down limit on gravitational wave emission from the Vela pulsar," *The Astrophysical Journal*, vol. 737, 2011.

[30] J. Aasi *et al.*, "Einstein@Home all-sky search for periodic gravitational waves in LIGO S5 data," *Phys. Rev. D*, vol. 87, 2013.

[31] J. Abadie *et al.*, "Predictions for the Rates of Compact Binary Coalesence Observable by Ground-based Gravitational-wave Detectros," *Class. Quantum Grav.*, vol. 27, 2010.

[32] G. Vajente, "Virgo logbook," 2011. URL: tds.ego-gw.it/itf/osl_virgo/index.php?callRep=30283.

[33] J. Aasi *et al.*, "Prospects for Localization of Gravitational Wave Transients by the Advanced LIGO and Advanced Virgo Observatories," *arXiv:1304.0670 [gr-qc]*, 2013.

[34] J. Abadie *et al.*, "Predictions for the Rates of Compact Binary Coalescences Observable by Ground-based Gravitational-wave Detectors," *Classical and Quantum Gravity*, vol. 27, no. 17, 2010.

[35] F. Acernese *et al.*, "Advanced Virgo: a 2nd generation interferometric gravitational wave detector," *Class. Quantum Grav.*, vol. 32, no. 2, 2015. doi:10.1088/0264-9381/32/2/024001.

[36] J. Vinet *et al.*, *Optica and related topics*. The Virgo collaboration, 2nd ed., 2006.

[37] E. Hecht, *Optics*. Addison Wesley, 4th ed., 2002.

[38] R. W. P. Drever, J. L. Hall, F. V. Kowalski, J. Hough, G. M. Ford, and A. J. H. W. Munley, "Laser phase and frequency stabilization using an optical resonator," *Appl. Phys. B*, vol. 31, no. 2, pp. 97 – 105, 1983.

[39] D. Rabeling, *Global Sensing and Control for Interferometric Gravitational Wave Detection*. PhD thesis, The Australian National University, 2009.

[40] P. Saulson, *Fundamentals of interferometric gravitational wave detectors*. World Scientific Singapore, 1st ed., 1994.

[41] B. Meers, "Recycling in laser-interferometric gravitational-wave detectors," *Phys. Rev. D*, vol. 38, no. 8, pp. 2317 – 2326, 1988.

[42] M. Beker, *Low-frequency sensitivity of next generation gravitational wave detectors*. PhD thesis, VU University Amsterdam, 2013.

[43] F. Acernese *et al.*, "Measurements of superattenuator seismic isolation by Virgo interferometer," *Astroparticle Physics*, vol. 33, pp. 182 – 189, 2010.

[44] S. Braccini *et al.*, "Measurements of the seismic attenuation performance of the VIRGO Superattenuator," *Astroparticle Physics*, vol. 23, pp. 557 – 565, 2005.

[45] H. Callen *et al.*, "Irreversibilty and Generalized Noise," *Physical Review*, vol. 83, no. 1, pp. 34 – 40, 1951.

[46] G. Harry *et al.*, "Thermal noise in interferometric gravitational wave detectors due to dielectric optical coatings," *Class. Quantum Grav.*, vol. 19, no. 5, p. 897, 2002.

[47] P. Saulson, "Thermal noise in mechanical experiments," *Phys. Rev. D*, vol. 42, no. 8, pp. 2439 – 2445, 1990.

[48] K. Numata, K. Yamamoto, H. Ishimoto, S. Otsuka, K. Kawabe, M. Ando, and K. Tsubono, "Systematic measurement of the intrinsic losses in various kinds of bulk fused silica," *Physics Letters A*, vol. 327, 2004.

[49] C. Comtet *et al.*, "Reduction of tantala mechanical losses in Ta_2O_5/SiO_2 coatings for the next generation of VIRGO and LIGO interferometric gravitational waves detectors," 2007. Proceedings of the 42th Rencontres de Moriond.

[50] E. Black *et al.*, "Direct observation of broadband coating thermal noise in a suspended interferometer," *Phys. Lett. A*, vol. 328, no. 1, pp. 1 – 5, 2004. URL: dx.doi.org/10.1016/j.physleta.2004.05.052.

[51] M. Pitkin, S. Reid, S. Rowan, and J. Hough, "Gravitational Wave Detection by Interferometry (Ground and Space)," *Living Reviews in Relativity*, vol. 14, no. 5, 2011.

[52] I. Martin *et al.*, "Measurements of a low-temperature mechanical dissipation peak in a single layer of Ta_2O_5 doped with TiO_2," *Classical and Quantum Gravity*, vol. 25, no. 5, 2008. URL: stacks.iop.org/0264-9381/25/i=5/a=055005.

[53] T. Corbitt, *Quantum Noise and Radiation Pressure Effects in High Power Optical Interferometers*. PhD thesis, Massachusetts Institute of Technology, 2008.

[54] W. Heisenberg, "Über den anschaulichen Inhalt der quantentheoretischen Kinematik und Mechanik," *Zeitschrift fur Physik*, vol. 43, pp. 172–198, Mar. 1927.

[55] C. Caves, "Quantum-Mechanical Radiation-Pressure Fluctuations in an Interferometer," *Physical Review Letters*, vol. 45, no. 2, pp. 75 – 79, 1980.

[56] C. Caves, "Quantum-mechanical noise in an interferometer," *Phys. Rev. D*, vol. 23, no. 8, pp. 1693 – 1707, 1981.

[57] The LIGO Scientific Collaboration, "A gravitational wave observatory operating beyond the quantum shot-noise limit," *Nature Physics*, vol. 7, no. 12, 2011. URL: stacks.iop.org/0264-9381/19/i=5/a=305.

[58] S. Chelkowski, H. Vahlbruch, B. Hage, A. Franzen, N. Lastzka, K. Danzmann, and R. Schnabel, "Experimental characterization of frequency-dependent squeezed light," *Phys. Rev. A*, vol. 71, 2005.

[59] E. Mikhailov, K. Goda, T. Corbitt, and N. Mavalvala, "Frequency-dependent squeeze-amplitude attenuation and squeeze-angle rotation by electromagnetically induced transparency for gravitational-wave interferometers," *Phys. Rev. A*, vol. 73, 2006.

[60] T. Accadia *et al.*, "Virgo: a laser interferometer to detect gravitational waves," *Journal of Instrumentation*, vol. 7, 2012.

[61] T. Accadia *et al.*, "Status of the Virgo project," *Class. Quantum Grav.*, vol. 28, 2011.

[62] J. Abadie *et al.*, "Search for gravitational waves from compact binary coalescence in LIGO and Virgo data from S5 and VSR1," *Phys. Rev. D*, vol. 82, 2010.

[63] Virgo optics group. URL: wwwcascina.virgo.infn.it/optics/measurements/VIRGO_Mirrors, Last accessed: 2014-07-16.

[64] G. Vajente, *Analysis of sensitivity and noise sources for the Virgo gravitational wave interferometer*. PhD thesis, Scuola Normale Superiore di Pisa, 2008.

[65] M. Mantovani, *The automatic alignment system of the Virgo interferometer*. PhD thesis, University of Siena, 2008.

[66] S. Braccini *et al.*, "An improvement in the VIRGO superattenuator for interferometric detection of gravitational waves: The use of magnetic antispring," *Rev. Sci. Instrum.*, vol. 64, pp. 310 – 313, 1993.

[67] M. Beccaria *et al.*, "Extending the VIRGO gravitational wave detection band down to a few Hz: metal blade springs and magnetic antisprings," *Nucl. Instrum. Methods Phys. Res. A*, vol. 394, pp. 397 – 408, 1997.

[68] T. Accadia *et al.*, "Status of the Virgo project," *Class. Quantum Grav.*, vol. 28, no. 11, 2011. doi:10.1088/0264-9381/28/11/114002.

[69] T. Accadia, "A Thermal Compensation System for the gravitational wave detector Virgo," *Proceedings of the Twelfth Marcel Grossmann Meeting on General Relativity*, 2012.

[70] M. Lorenzini *et al.*, "The monolithic suspension for the Virgo interferometer ," *Class. Quantum Grav.*, vol. 27, no. 8, 2010. doi:10.1088/0264-9381/27/8/084021.

[71] H. Heitmann, "Advanced Virgo planning 20/06/2014," 2014. Virgo note VIR-0588U-09.

[72] L. Pinard, R. Flaminio, and D. Forest, "Bulk absorption measurement at 1064 nm of the new Heraeus ultra pure fused silica used for the Advanced Virgo Test Mass: effect of the annealing," 2010. Virgo note VIR-0091A-10.

[73] A. Freise, G. Heinzel, H. Lück, R. Schilling, B. Willke, and K. Danzmann, "Frequency-domain interferometer simulation with higher-order spatial modes," *Classical and Quantum Gravity*, vol. 21, no. 5, 2004.

[74] M. Evans, "Optickle," *LIGO document server*, October 26, 2012. LIGO document T070260; URL: dcc.ligo.org/LIGO-T070260/public.

[75] H. Yamamoto, "e2e - LIGO end to end time domain simulation," *LSC/Virgo Collaborations Meeting, October 22-25 2007*, 2007. LIGO document G070658; URL: dcc.ligo.org/LIGO-G070658/public.

[76] G. Vajente, "Advanced Virgo Length Sensing and Control steady state design," 2011. Virgo note Virgo Note VIR-0738A-11.

[77] M. Mantovani, "Automatic Alignment Sensing and Control scheme for Advanced Virgo MSRC configuration," 2011. Virgo note VIR-0201A-11.

[78] M. Punturo, "Advanced Virgo sensitivity curve study," 2012. Virgo note VIR-0073A-12.

[79] V. Fafone *et al.*, "The noise budget of Virgo+ with monolithic suspensions," 2010. Virgo note VIR-0677E-09.

[80] I. Fiori, F. Frasconi, and E. Genin, "Acceptance criteria for EIB-SAS," 2011. Virgo note VIR-0077A-11.

[81] L. LaCoste, "A new type long pendulum vertical seismograph," *J. Appl. Phys.*, vol. 5, pp. 178 – 180, 1934.

[82] C. Harrison, "Lucien J. B. LaCoste (1908âĂŞ1995)," *Eos Trans. AGU*, vol. 76, no. 50, pp. 516 – 516, 1995.

[83] E. Wielandt and G. Streckeisen, "The leaf-spring seismometer: design and performance," *Bull. Seismol. Soc. Am.*, vol. 72, pp. 2349 – 2367, 1982.

[84] J. Winterflood and D. Blair, "A long-period vertical vibration isolator for gravitational wave detection," *Phys. Lett. A*, vol. 243, pp. 1 – 6, 1998.

[85] J. Winterflood and D. Blair, "A long-period conical pendulum for vibration isolation," *Phys. Lett. A*, vol. 222, no. 3, pp. 141 – 147, 1996.

[86] L. Holloway, "The superattenuator: a mirror suspension system for reducing seismic induced noise in the VIRGO gravitational wave interferometer," *Nuclear Physics B - Proceedings Supplements*, vol. 54, no. 3, pp. 176 – 178, 1997.

[87] G. Losurdo, *Ultra-low frequency inverted pendulum for the Virgo test mass suspension*. PhD thesis, Scuola Normale Superiore di Pisa, 1998.

[88] A. Bertolini, G. Cella, R. DeSalvo, and V. Sannibale, "Seismic noise filters, vertical resonance frequency reduction with geometric anti-springs: a feasibility study," *Nucl. Instrum. Meth. A*, vol. 435, pp. 475 – 483, 1999.

[89] G. Cella, R. DeSalvo, V. Sannibale, H. Tariq, N. Viboud, and A. Takamori, "Seismic attenuation performance of the first prototype of a geometric anti-spring filter," *Nucl. Instrum. Methods Phys. Res. A*, vol. 487, 2002.

[90] M. Szabolcs *et al.*, "Anatomy of the TAMA SAS seismic attenuation system," *Class. Quantum Grav.*, vol. 19, no. 7, 2002.

[91] A. Bertolini, "Design and prototype tests of a seismic attenuation system for the advanced-LIGO output mode cleaner," *Class. Quantum Grav.*, vol. 23, no. 8, 2006.

[92] G. Losurdo *et al.*, "An inverted pendulum pre-isolator stage for the Virgo suspension system," *Rev. Sci. Instrum.*, vol. 70, 1999.

[93] URL: www.aubertduval.com/uploads/tx_obladygestionproduit/gb_MARVAL18.pdf, Last accessed on 23-04-2013.

[94] S. Braccini *et al.*, "The maraging-steel blades of Virgo superattenuator," *Meas. Sci. Technol.*, vol. 11, pp. 467 – 476, 2007.

[95] V. Boschi, *Modeling and simulation of seismic attenuation systems for gravitational wave interferometers*. PhD thesis, University of Pisa, 2010.

[96] R. DeSalvo *et al.*, "A proposal for a Pre-Isolator Stage for the VIRGO Superattenuator," 1996. Virgo note VIR-NOT-PIS-1390-31.

[97] E. Hennes, 2013. private communication.

[98] H. Sodano *et al.*, "Concept and model of eddy current damper for vibration suppression of a beam,"

[99] A. Takamori, *Low Frequency Seismic Isolation for Gravitational Wave Detectors*. PhD thesis, California Institute of Technology, Massachusetts Institute of Technology, 2003.

[100] F. Cordero *et al.*, "Elastic and anelastic properties of Marvel 18 steel," *Journal of alloys and compounds*, vol. 310, pp. 400 – 404, 2000.

[101] G. Cella *et al.*, "Monolithic geometric anti-spring blades," *Nucl. Instrum. Meth. A*, vol. 540, pp. 502 – 519, 2005.

[102] S. Braccini *et al.*, "Measurement of creep on the mechanical filter blades: improvements with maraging steel," 1997. Virgo note VIR-NOT-PIS-1390-87.

[103] N. Virdone *et al.*, "Extended-time-scale creep measurements on maraging cantilever blade springs," *Nucl. Instrum. Meth. A*, vol. A593, pp. 597 – 607, 2008.

[104] M. Abernathy *et al.*, "Einstein gravitational wave telescope conceptual design study," 2011. ET-0106C-10.

[105] P. Rodgers, "Frequency limits for seismometers as determined from signal-to-noise ratios. Part 1. The electromagnetic seismometer," *Bulletin of the Seismological Society of America*, vol. 82, no. 2, pp. 1071 – 1098, 1992.

[106] H. Tariq *et al.*, "The linear variable differential transformer (LVDT) position sensor for gravitational wave interferometer low-frequency controls," *Nucl. Instrum. Methods Phys Res A*, vol. 489, pp. 570 – 576, 2002.

[107] C. Wang *et al.*, "Constant force actuator for gravitational wave detector's seismic attenuation systems (SAS)," *Nucl. Instrum. Methods Phys Res A*, vol. 489, pp. 563 – 569, 2002.

[108] D. Sullivan, D. Allan, D. Howe, and F. Walls, *Characterization of Clocks and Oscillators*. U.S. government printing office, Washington DC, 1^{st} ed., 1990.

[109] B. Canuel *et al.*, "Sub-nanoradiant beam pointing monitoring and stabilization system for controlling input beam jitter in gravitational wave interferometers," *Applied Optics*, vol. 53, no. 13, 2014. URL: dx.doi.org/10.1364/AO.53.002906.

Samenvatting

"Has this book been a best seller?
Did the New York Times like it?
Has this book been made into a movie?
Could we be watching this on video?"
Bill Watterson: Calvin and Hobbes.

Alles beweegt...

Terwijl u dit proefschrift leest zit u hoogstwaarschijnlijk op een stoel en eventueel aan een tafel. Op het eerste gezicht lijken deze tafel, deze stoel, de muren van het gebouw waarin u zich bevindt, stil te staan. Maar schijn bedriegt...

In het geval van een aardbeving is het duidelijk waarneembaar dat de grond, de bomen, de gebouwen allemaal bewegen. Tijdens een aardbeving schudt het tafelblad heviger dan de grond, in ieder geval bij bepaalde frequenties. De tafel heeft zogenaamde resonantiefrequenties waarbij de beweging van de grond wordt versterkt door de tafelpoten. Gebouwen hebben ook resonanties. Vandaar dat, als de aardbeving krachtig genoeg is, de trillingingen van huizen, bruggen en dergelijke zo hevig kunnen zijn dat ze instorten.

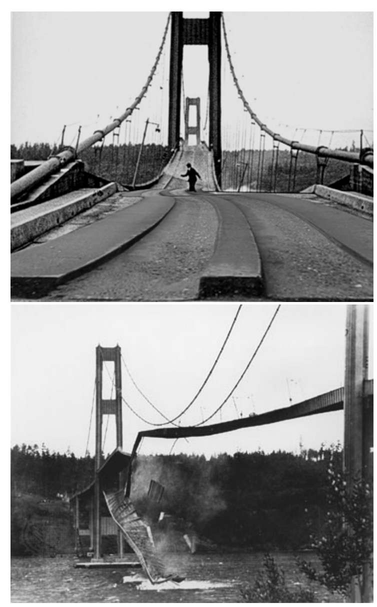

Figuur A: *Instorten van de (voormalige) Tacoma Narrows brug door de wind.*

De trillingen die een voorwerp aanslaan hoeven niet van seismische aard te zijn. Drukgolven, zoals wind en geluid, zijn ook prima in staat iets in beweging te krijgen. Zo kunnen bij een flinke onweersbui de ramen behoorlijk rinkelen van de donder. Ook wind en geluid kunnen resonanties opwekken. Denk hierbij bijvoorbeeld aan een sopraan die een kristallen glas stuk zingt. Dit lukt alleen bij een specifieke toon die hoort bij het glas. Een ander bekend voorbeeld is dat van de Tacoma Narrows brug die door de aanhoudende wind langzaam maar zeker zo sterk in beweging werd gebracht dat zij instortte (zie Figuur A).

Onder normale omstandigheden zijn deze effecten nauwelijks te merken. In afwezigheid van een aardbeving staan de dingen om ons heen behoorlijk stil, in ieder geval, voor zover wij dat kunnen waarnemen.

Dit proefschrift gaat over een vibratie-isolatiesysteem voor gravitatiegolfdetectoren. Tenzij u natuurkunde heeft gestudeerd, of toevalligerwijs zeer geïnteresseerd bent in deze tak van de wetenschap, zegt dat u nog niet zo veel. Wat is een gravitatiegolf? Waarom zouden we die willen waarnemen? Waarom is daar een seismisch isolatiesysteem voor nodig? Deze vragen zal ik beantwoorden in het vervolg van deze samenvatting. Daarna bespreek ik het seismisch isolatiesysteem EIB-SAS waaraan ik de afgelopen jaren gewerkt heb.

Wat zijn gravitatiegolven?

Aan het begin van de vorige eeuw publiceerde Albert Einstein een nieuwe manier om de werking van de zwaartekracht te beschrijven: de *algemene relativiteitstheorie*. In deze theorie spelen tijd en ruimte een gelijkwaardige rol. Zij vormen samen *ruimtetijd*. Begrippen als gelijktijdigheid en afstand zijn niet meer zo vanzelfsprekend. Er bestaat echter een combinatie van de ruimte en tijd die wel behouden blijft: de kwadratische optelling van de afstand en de tijd tussen twee gebeurtenissen (waarbij de tijd een minteken krijgt). Deze grootheid heet *het interval*.

De algemene relativiteitstheorie ziet zwaartekracht als een kromming van de ruimtetijd, die wordt veroorzaakt door de aanwezigheid van massa en energie. Een veelgebruikte metafoor voor dit fenomeen is dat van een zware knikker die op een elastisch, gespannen vel ligt. De knikker vervormt het vel, zoals de Zon ruimtetijd vervormt. Een tweede, veel kleinere knikker die over het vel rolt volgt een baan die lijkt op die van de Aarde rond de Zon (zie Figuur B).

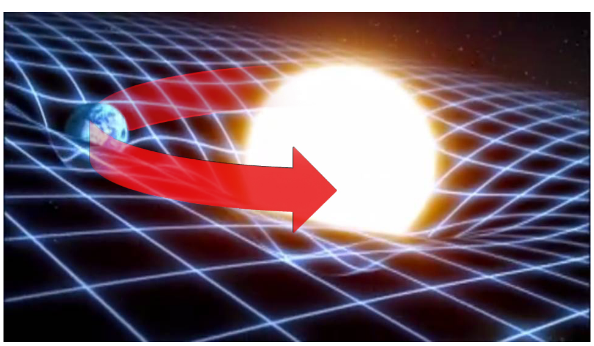

Figuur B:
Volgens de algemene relativiteitstheorie is de zwaartekracht die de Aarde ondervindt van de Zon niets anders dan de kromming van de ruimtetijd door de Zon [3].

Stel nu dat twee zware objecten (bijvoorbeeld twee zwarte gaten) om elkaar heen cirkelen. Deze beweging veroorzaakt een periodieke vervorming van de ruimtetijd. Omdat kromming van de ruimtetijd wordt ervaren als zwaartekracht, noemen we dat een *gravitatiegolf*. Omdat de gravitatiegolf een periodieke vervorming van de ruimtetijd is, is het interval tussen twee gebeurtenissen tijdsafhankelijk.

Gravitatiegolven waarnemen

In Italië staat de Virgodetector (zie Figuur C) die dit principe toepast om gravitatiegolven te observeren: de detector meet het interval tussen twee spiegels. Eigenlijk meet de detector de intervallen tussen twee sets van spiegels en vergelijkt deze met elkaar.

De detector is een zogenaamde Michelson-interferometer. Een uiterst stabiele laserstraal wordt door een halfdoorlatende spiegel (een *beam splitter*) in twee indentieke laserstralen gesplitst. Ieder van de laserstralen reist op en neer tussen twee spiegels door een 3 km lange vacuümbuis. De twee armen van de interferometer staan onder een hoek van 90°. De twee laserstralen worden bij de beam splitter weer gecombineerd, wat een interferentiepatroon oplevert. Omdat de snelheid van de laserstralen altijd gelijk is aan de lichtsnelheid, is de tijd die zij nodig hebben om van spiegel naar spiegel te reizen en weer terug een maat voor de afstand, of liever gezegd, een maat voor het interval tussen iedere spiegelset.

Figuur C: *Luchtfoto van (Advanced) Virgo. [Credit: Virgo [13]].*

De spiegels zijn zo opgehangen dat zij zich gedragen als vrijvallende objecten. Een passerende gravitatiegolf zal de afstand (het interval) tussen de ene set spiegels verkleinen, en die tussen de andere set vergroten. Wiskundig is het effect op de laserstralen equivalent aan het langer worden van de ene arm van de interferometer, en het korter worden van de andere. Daardoor zit er een verschil in de tijd die de twee laserstralen nodig hebben om tussen de twee spiegels op en neer te reizen en dat veroorzaakt een intensiteitsverandering van het interferentiepatroon.

De vervorming van ruimtetijd door gravitatiegolven is klein. De lengteverandering van de 3 km lange armen van Virgo is slechts 3 zeptometer (1 zeptometer is 10^{-21} meter). Dit is een miljoen keer kleiner dan de grootte van een proton! Het waarnemen van een gravitatiegolf is dan ook geen gemakkelijke onderneming. Alhoewel er sterke aanwijzingen zijn dat dit fenomeen bestaat, zijn dergelijke golven tot op heden nog niet direct waargenomen.

Tijdens het schrijven van dit proefschrift ondergaat de Virgodetector een uitgebreide upgrade. De detector die daaruit voortkomt heet Advanced Virgo. Naar verwachting zal Advanced Virgo eind 2015 operationeel zijn en tussen de 1 en 100 gravitatiegolven per jaar kunnen meten. De eerste detectie lijkt op handen te zijn! Advanced Virgo zal een nieuwe manier van kijken naar het Universum inluiden.

Seismische ruis

De grond is continu in beweging. Hij wordt voortdurend aangeslagen door de golfslag van zeeën en oceanen op hun bodem en op de kusten. Ook de mensheid (verkeer en industrie) is een belangrijke bron van seismische ruis. Tot slot is ook het weer van belang: bij slecht weer en sterke wind is de beweging van de grond aanzienlijk. Hoewel we daar in het dagelijks leven niets van merken, is seismische activiteit een belangrijke stoorzender voor (Advanced) Virgo.

Omdat de signalen die gravitatiegolven teweegbrengen in interferometers zo klein zijn, hebben deze detectoren geavanceerde mechanische filters en meet- en regelsystemen. Deze zorgen ervoor dat de seismisch geïnduceerde bewegingen van de spiegels het gravitatiegolfsignaal niet overstemmen.

Vibratie-isolatie systemen

De mechanische filters die worden gebruikt in gravitatiegolfdetectoren maken gebruik van het feit dat een resonator ook een filter is. Iedere resonator, bijvoorbeeld een slinger, heeft een natuurlijke frequentie: zijn *eigenfrequentie*. Voor frequenties die kleiner zijn dan deze eigenfrequentie volgt de massa van de slinger de top. We zeggen dat de overdrachtsfunctie van de slinger voor deze frequenties 1 is. Voor trillingen bij de eigenfrequentie is de beweging van de massa veel groter dan die van de top van de slinger. De slinger versterkt hier de beweging; de overdrachtsfunctie van de slinger is groter dan 1. Trillingen met frequenties groter dan de eigenfrequentie worden echter slecht doorgegeven door de slinger. Hoe hoger de frequentie van de verstoring, hoe slechter deze wordt doorgegeven. Een slinger is een filter voor trillingen (zie Figuur D).

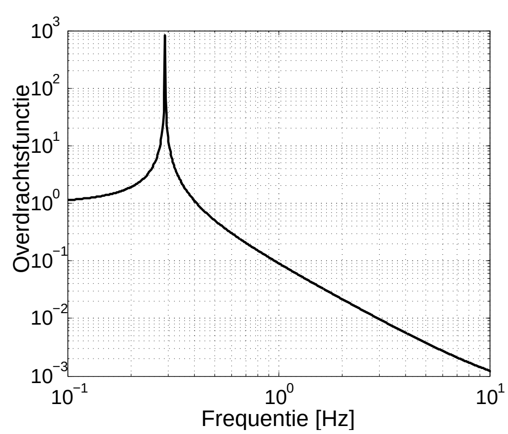

Figuur D: *Typische vorm van een overdrachtsfunctie: >1 bij de resonantie frequentie, 1 eronder, en $\propto 1/f^2$ erboven.*

Voor alle resonatoren geldt dat de overdrachtsfunctie afneemt met de tweede macht van de frequentie. Dat betekent dat hoe lager de eigenfrequentie van een resonator is, hoe beter hij isoleert. Deze eigenschap maakt dat verscheidene resonatoren, met zeer lage eigenfrequenties, als mechanische filters worden toegepast in gravitatiegolfdetectoren. Tijdens mijn promotie heb ik me gewijd aan een seismisch isolatiesysteem voor Advanced Virgo: EIB-SAS.

EIB-SAS: vibratie-isolatie voor Advanced Virgo

EIB-SAS is een vibratie-isolatiesysteem voor een optische tafel van (Advanced) Virgo: de external injection bench (*external* omdat deze tafel zich buiten het vacuüm van de interferometer bevindt). Deze tafel bevat spiegels en lenzen om de laserstraal te manipuleren en deze met de juiste eigenschappen de daadwerkelijke interferometer in te sturen. Daarnaast herbergt hij sensoren die worden gebruikt bij de actieve regeling van de interferometer.

In het verleden veroorzaakten seismisch geïnduceerde bewegingen van deze tafel fluctuaties van de intensiteit en richting van de laserstraal. Deze veroorzaakten op hun beurt weer ruis op het gravitatiegolfsignaal dat werd geproduceerd door de interferometer. Deze ruisbron zou de gevoeligheid van de Advanced Virgodetector sterk limiteren.

Vandaar dat een nieuw vibratie-isolatiesysteem voor deze optische tafel is ontwikkeld: de external injection bench seismic attenuation system, oftewel EIB-SAS. Een schematische weergave van het systeem is te zien in Figuur E. EIB-SAS heeft verticale en horizontale resonatoren waarvan de resonantiefrequenties naar zeer lage waarden kunnen worden afgestemd. Die van de verticale filters is 460 mHz, die van de horizontale filters 220 mHz. Bij deze waarden levert het systeem de benodigde isolatie van een factor 100 bij 10 Hz.

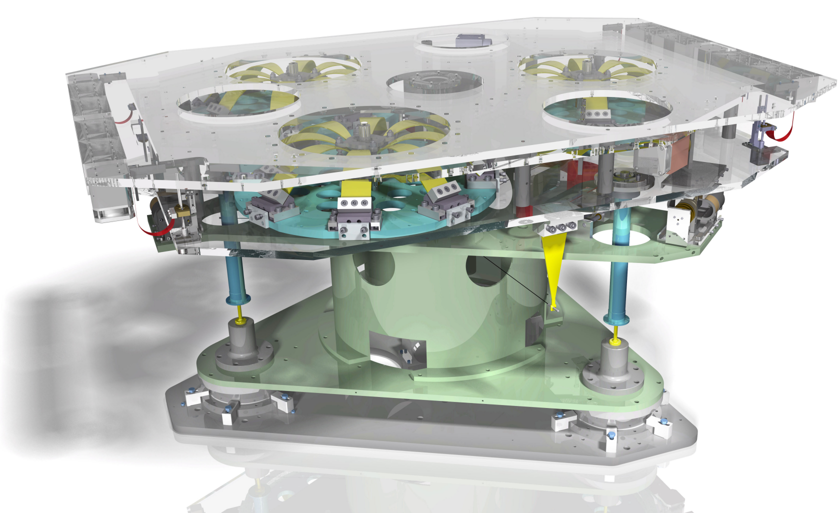

Figuur E: *Het external injection bench seismic attenuation system EIB-SAS.*

Voor frequenties dicht bij de resonantiefrequenties van het systeem zou EIB-SAS de grondvibraties versterken in plaats van verzwakken. Om dit tegen te gaan is EIB-SAS uitgerust met positie- en bewegingssensoren en met een aantal actuatoren. Op basis van de signalen van de sensoren wordt met de actuatoren een geschikt correctiesignaal toegepast. Op deze manier wordt de laagfrequente beweging van de tafel actief verminderd.

Prestaties van EIB-SAS

Tijdens mijn promotie heb ik, samen met een team van wetenschappers en technici, EIB-SAS gebouwd en getest. Nadat we hadden laten zien dat het systeem goed werkt en aan alle eisen van de Virgocollaboratie voldeed hebben we het geïnstalleerd in Virgo.

De eigenfrequenties van de verticale en horizontale mechanische filters leiden tot 6 laagfrequente resonanties die optreden bij 233, 294, 355, 446, 479 en 542 mHz. Bij deze frequenties versterken de filters de grondvibraties. Dit wordt tegengegaan met negatieve terugkoppeling. Een aantal bewegings- en positiesensoren monitoren de bench voortdurend. Op basis van hun waarnemingen oefenen de actuatoren krachten uit om de optische tafel op zijn plaats te houden.

De eigenschappen van de individuele filters zijn vergeleken met voorspellingen van analytische, numerieke en finite-elementmodellen. Zo hebben we de mechanische overdrachtsfuncties van het gehele geassembleerde systeem gemeten met behulp van een trillingplaat met piezo-elektrische kristallen. Deze metingen laten zien dat EIB-SAS de beweging van de optische tafel terugbrengt met een factor 10 - 5000. EIB-SAS heeft 6 hoogfrequente modes waarbij het platform met de verticale filters en de bench in tegenfase bewegen. Deze modes hebben de volgende frequenties: 12 Hz (Ty), 16 Hz (x en z), 36.5 Hz (Tx), 41 Hz (Tz) en 49 Hz (y). De eerste drie modes vallen binnen de bandbreedte van de elektronische besturing en worden dus actief gedempt. Voor de overige drie modes zijn speciale passieve dampers ontworpen. Verdere interne modes van het systeem zijn geïdentificeerd en zo nodig gedempt met passieve dampingstechnieken.

Met behulp van de controls blijft de drift van het systeem binnen 10% van de limiet die is gesteld door de Virgocollaboratie. Verder kunnen de actuatoren de positie van de bench corrigeren voor temperatuursveranderingen tot ± 3 °C.

Begin 2014 is EIB-SAS succesvol geïnstalleerd in Virgo. Ter plekke is gemeten in hoeverre het omgevingsgeluid EIB-SAS in beweging brengt. Akoestische ruis van buiten het injectielaboratorium, waar EIB-SAS zich bevindt, hebben geen enkele invloed op het systeem. Metingen die gedaan zijn onder condities waarin Advanced Virgo data zal verzamelen laten zien dat een aantal interne modes van EIB-SAS lichtelijk akoestisch worden aangeslagen.

Figuur F laat het bewegingsspectrum van de external injection bench zien. De blauwe curve correspondeert met de oude situatie, de zwarte met EIB-SAS als het helemaal stil is en de rode met EIB-SAS onder omstandigheden die lijken op die waarin Advanced Virgo zal werken. Op enkele discrete frequenties overtreft de beweging van het systeem net de gestelde limiet, maar voor alle andere frequenties is de beweging van EIB-SAS een factor 5 tot 10 beneden de eis. Met EIB-SAS zal de external injection bench geen ruisbron meer zijn voor Advanced Virgo, zodat deze zijn optimale gevoeligheid zal kunnen behalen.

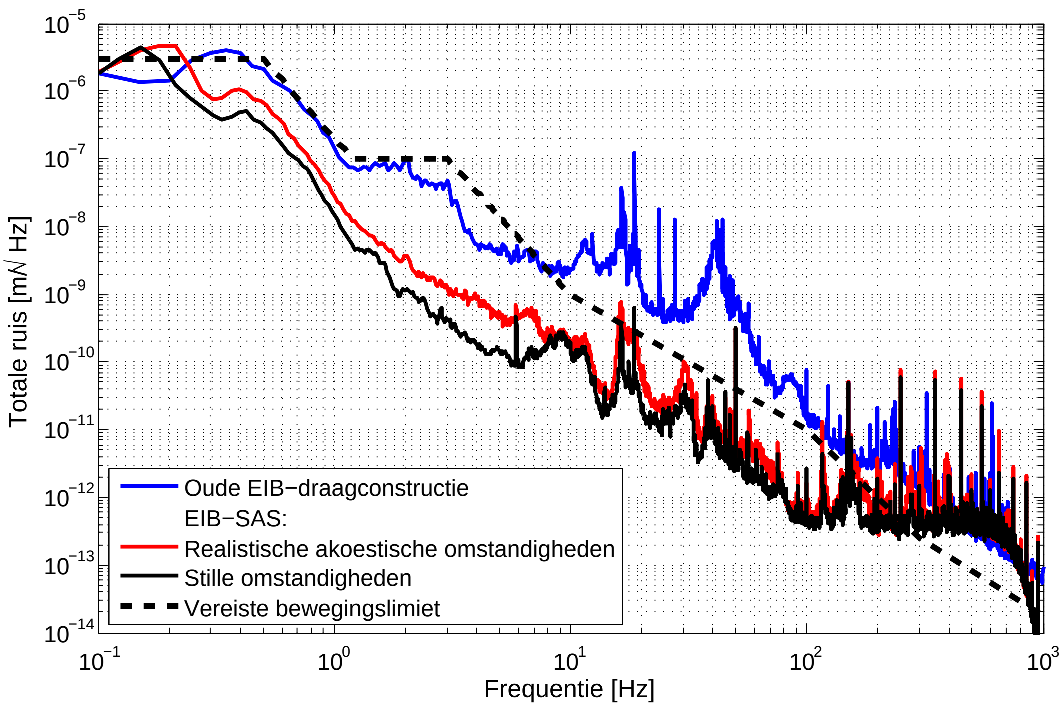

Figuur F: *Het bewegingsspectrum van EIB-SAS onder stille omstandigheden (zwarte curve) en onder realistische (akoestische) omstandigheden (rode curve). De gestippelde curve correspondeert met de gestelde limiet en de blauwe curve is het bewegingsspectrum van het vroegere systeem dat nu vervangen is door EIB-SAS. Onder stille omstandigheden voldoet EIB-SAS aan de eis. Boven 200 Hz isoleert EIB-SAS zo goed dat de sensoren niet gevoelig genoeg zijn om de beweging waar te nemen. Bij deze frequenties correspondeert de curve met de ruisvloer van de sensoren. Onder realistische omstandigheden worden enkele resonanties van EIB-SAS aangeslagen door akoestische ruis en wordt de limiet bij deze frequenties net overschreden. Voor alle andere frequenties is de beweging van EIB-SAS een factor 5 tot 10 beneden de eis.*

Summary

"Life is like topography, Hobbes. There are summits of happiness and success, flat stretches of boring routine and valleys of frustration and failure."
Bill Watterson: Calvin and Hobbes.

Everything moves...

While you are reading this thesis, chances are you're sitting on a chair, potentially at a table. At first glance the table, the chair, the walls of the building you are residing in, seem to be standing still. But appearances can be deceiving...

In the case of an earthquake, it is readily observable that the ground, the trees, the buildings, all move. During an earthquake the table top shakes more violently than the ground, at least, at certain frequencies. The table has what are called *resonance frequencies* at which the motion of the ground is enhanced by the table legs. Buildings also have resonance frequencies. That is why a potent enough earthquake can induce vibrations strong enough to destroy a building.

The vibrations that make an object resonate need not be of a seismic nature. Pressure waves, such as wind or sound, are also perfectly capable of inducing vibrations. For example, during a storm the thunder may shake the windows, or a soprano may cause a champaign glass to burst. In the latter case, the note sung by the soprano needs to be identical to the resonance frequency of the glass. One final famous example is the Tacoma Narrows bridge: a steady wind blew at exactly the right speed to excite the resonance frequency of the bridge and made it collapse (see Figure A).

Under normal circumstances these effects are hardly noticeable. In the absence of an earthquake, most objects that surround us remain reasonably stationary, that is, as far as we can see.

This thesis is about a vibration isolation system for a gravitational wave detector. Unless you are a physicist, or you happen to be interested in this particular branch of science, this will mean little to you. What is a gravitational wave? Why would we like to observe them? Why does this require a vibration isolation system? I will answer these questions in the next part of this summary. Then, I will discuss the vibration isolation system EIB-SAS, on which I have worked these past few years.

What are gravitational waves?

At the turn of the last century, Albert Einstein published a paper in which he introduced a new way of looking at gravity: his theory of general relativity. In this theory space and time stand on equal footing. Together they form *spacetime*. The notions of simultaneousness and distance can not be taken for granted. Rather, there exists a combination of space and time that is conserved: the quadratic sum of the time and distance between two events (where the time coordinate receives a minus-sign). This quantity is called *the interval*.

In general relativity, gravity is seen as a curvature of spacetime which is caused by the presence of mass and energy. A much-used metaphor is that of a heavy marble that lies on an elastic sheet. The marble deforms the sheet in a way that is similar to how the Sun deforms spacetime. A second, much smaller marble that rolls over the sheet will follow a trajectory similar to that of the Earth orbiting the Sun (see Figure B).

Take two heavy objects (for example two black holes) that are orbiting each other. Their motion will cause a periodic deformation of spacetime. And as we observe the curvature of spacetime as a gravitational force, we call this disturbance a *gravitational wave*. As the gravitational wave is a periodic disturbance of spacetime, the interval between two events is time-dependent.

Observing gravitational waves

In Italy, just south of Pisa, stands the Virgo detector (see Figure C) which makes use of the principle just described to observe gravitational waves. The detector measures the interval between two mirrors. More to the point: it measures and compares the interval between two sets of mirrors.

The detector is a so-called Michelson interferometer. An exceptionally stable laser beam is divided into two identical beams by a so-called *beam splitter*. Each of these beams travels up and down between two mirrors that are placed at the ends of two vacuum tubes that are 3 kilometers long and make an angle of 90°. The two laser beams are reunited at the beam splitter and form an interference pattern. As the laser beams always travel at the speed of light, the time it takes them two travel to the end of the vacuum tube and back is a measure for the distance, or rather, the interval between the mirrors.

The mirrors are suspended is such a way that they behave as freely falling objects. A passing gravitational wave traveling in the optimal direction will shorten the distance (the interval) between one set of mirrors and enlarge the other. For the laser beams this is mathematically equivalent to a length increase of one arm and a length reduction of the other arm. This introduces a difference in the time it takes the laser beams to make a round trip between the two mirrors which, in turn, causes an intensity fluctuation of the interference pattern.

The deformation of spacetime caused by a gravitational wave is tiny. The length change of the 3 km arms is only 3 zeptometer (1 zeptometer is 10^{-21} meter). This is a million times smaller than the size of a proton! This makes observing a gravitational wave a sizeable task. Although there are some strong indications that this phenomenon exists, to date, no gravitational waves have been directly observed.

As this thesis was being written, the Virgo detector was undergoing an extensive upgrade. The resulting detector is called Advanced Virgo. This detector is expected to be operational at the end of 2015, and, in time, should be able to observe between 1 and 100 gravitational waves a year. The first detection seems at hand! Advanced Virgo will initiate a new way of looking at the Universe.

Seismic noise

The ground is moving continuously. It is constantly being excited by the ocean waves hitting the coast and exerting forces on the seabed. Mankind (traffic and industry) is also a considerable source of seismic noise. Finally, also the weather plays an important role: if the weather is bad and the wind is strong, then the motion of the ground is substantial. Though we do not notice it in everyday life, seismic activity can be a nuisance for (Advanced) Virgo.

Because the signals generated by gravitational waves are so small, the interferometer is equipped with sophisticated mechanical filters and feedback systems. These help assure that the seismically induced motion of the mirrors does not eclipse the gravitational wave signal.

Vibration isolation systems

The mechanical filters that are used in gravitational wave detectors make use of the fact that a resonator is also a filter. Every resonator, a pendulum for example, has a natural frequency: its *eigenfrequency*. For frequencies smaller than this eigenfrequency the bob of the pendulum follows the motion of the top. We say that the pendulum's transfer function equals 1 for these frequencies. For vibrations at the resonance frequency, the motion of the bob will be greater than the top. The pendulum amplifies the motion and we say that the transfer function is greater than 1. Vibrations that have a frequency greater than the eigenfrequency are not well transferred to the bob. The greater the frequency of the disturbance, the smaller the induced motion of the bob. A pendulum is a filter for vibrations (see Figure D).

All resonators have a transfer function that, above their resonance frequency, decreases with the second power of the frequency. This means that the lower the eigenfrequency of the resonator, the better its isolation capabilities at high frequencies. That is the reason why gravitational wave detectors make use of mechanical filters with very low eigenfrequencies. My PhD was dedicated to a system that employs a number of such filters: EIB-SAS.

EIB-SAS: vibration isolation system for Advanced Virgo

EIB-SAS is a vibration isolation system for an optical bench of (Advanced) Virgo: the external injection bench (external because it is located outside the detector's vacuum system). This optical bench houses lenses and mirrors that are used to manipulate the laser beam and send it into the interferometer with the right properties. Apart from that, the bench accommodates a number of sensors that are used in the feedback loops that control the interferometer.

In the past, seismically induced vibrations of this bench caused fluctuations of the intensity and direction of propagation of the laser beam. These, in turn, caused noise on the output of the interferometer. This noise source would significantly limit the sensitivity of Advanced Virgo.

For that reason a new vibration isolation system for this optical bench was developed: the external injection bench seismic attenuation system, or EIB-SAS. A schematic representation of the system is depicted in Figure E. EIB-SAS has vertical and horizontal resonators whose resonance frequencies can be tuned to very low values. The vertical filters are tuned to 460 mHz, the horizontal filters to 220 mHz. At these values the system provides the necessary isolation of a factor 100 at 10 Hz.

For frequencies close to the resonance frequencies of the system, EIB-SAS would amplify the ground vibrations. To counter this, EIB-SAS has been equipped with position sensors, motion sensors and a number of actuators. Based on the information of the sensors the actuators apply a suitable force and keep the low-frequency motion of the bench in check.

Performance of EIB-SAS

During my PhD, a number of scientists, engineers and myself built and tested EIB-SAS. After we had shown that the system functioned properly and met all the requirements posed by the Virgo collaboration, we installed it in Virgo.

The eigenfrequencies of the vertical and horizontal mechanical filters give rise to 6 low-frequency internal modes that occur at 233, 294, 355, 446, 479, and 542 mHz. At these frequencies, the filters amplify the motion of the ground. This is counteracted with negative feedback. The sensors continuously monitor the motion of the bench and, based on their readings, the actuators continuously apply correction forces that allow the bench to maintain its position.

The properties of the individual filters have been compared to predictions of analytical, numerical, and finite element models. The mechanical transfer functions of the assembled system have been measured using a vibrating platform with piezoelectric crystals. These measurements show that EIB-SAS reduces the motion of the optical bench by a factor 10 - 5000.

EIB-SAS has 6 high-frequency modes in which the optical bench and the platform containing the vertical filters vibrate 180° out of phase. These modes have the following frequencies: 12 Hz (Ty), 16 Hz (x en z), 36.5 Hz (Tx), 41 Hz (Tz), and 49 Hz (y). The first three modes are within the bandwidth of the controls and are actively damped. For the remaining three modes special passive dampers have been designed. Additional internal modes of the system have been identified and, when necessary, have been damped using passive damping techniques.

With the aid of the control loops, the system maintains its position to within 10% of the margin posed by the collaboration. In addition, the actuators can correct for temperature changes up to ± 3 °C.

At the beginning of 2014, EIB-SAS was successfully installed in Virgo. On site, we measured the acoustically induced motion of the bench due to ambient noise. Acoustic noise from outside the laser laboratory, in which EIB-SAS is located, does not affect the system. Measurements that have been performed under conditions comparable to those under which EIB-SAS will operate show that the internal modes of the system are slightly excited by the ambient noise.

Figure 5.54 shows the displacement spectrum of the optical bench. The blue curve corresponds to the old support structure, the black curve to EIB-SAS under quiet conditions, and the red curve to EIB-SAS under realistic conditions. At a number of discrete frequencies, EIB-SAS exceeds the requirement. At all other frequencies the motion of the EIB-SAS lies a factor 5 to 10 below the required limit. With EIB-SAS in place, the external injection bench will not be a noise source for Advanced Virgo, making it possible for the detector to reach its optimal sensitivity.

Dankwoord

"So long, and thanks for all the fish."
- Douglas Adams (1984)

De eerste stap op weg naar de voltooiing van dit manuscript werd reeds in januari 2009 gezet. Ik was toevallig aanwezig op een feestje van de Rijksuniversiteit Groningen. Ik was toentertijd bezig met mijn masterscriptie op het Nikhef. Een aantal Nikhefmedewerkers was ook aanwezig op dit feest, en waren verbaasd, maar blij, mij daar te zien. Een van deze mensen was Jo van den Brand. Na over koetjes en kalfjes gepraat te hebben kwamen we bij mijn studievoortgang - hij was toch een van mijn docenten. Toen ik hem liet weten over een paar maanden af te studeren en mijn interesse in promoveren uitsprak zei hij: "Kom maar eens praten als je klaar bent." Zo begon het...

Nu, jaren later, heb ik mijn proefschrift voltooid. Al het onderzoek gedaan. Alle data geanalyseerd. Alle puntjes op de spreekwoordelijke "i" gezet. Dat hoop ik in ieder geval; ik moet binnenkort nog met een aantal opponenten van gedachten wisselen. Gelukkig heb ik al dat werk niet alleen hoeven verzetten. Ik heb hulp gehad van slimme en ontzettend aardige mensen van wie ik veel heb geleerd. Op deze plaats wil ik ieder van hen graag bedanken. Voor alle hulp die ze mij geboden hebben, maar vooral voor de leuke tijd. Nu ik deze laatste pagina's van dit boekwerk schrijf, weet ik dat het niet de kennis en vaardigheden zijn die ik in de afgelopen jaren heb opgedaan die promoveren de moeite waard maken, maar de vriendschappen die ik heb gevormd.

Allereerst wil ik graag mijn promotor, Jo van den Brand, bedanken voor zijn uitnodiging in 2009, de kans mijn promotieonderzoek in zijn groep te doen en vooral voor alle aandacht die hij mijn proefschrift heeft geschonken.

Alessandro, you not only seem to know absolutely everything, you almost always have hands-on experience. I cannot count the numbers of times I had a question about some obscure physical phenomenon, loosely related to the subject of gravitational waves (or not) that your answer began with the words: "Yeah, I tried/did that a few years ago". I am grateful for everything you taught me, your help with the writing of this thesis, and the fact that you always found time to explain or show something to me. Thank you.

Als ik ooit moeilijkheden ervaarde die te maken hadden met de mechanica of regeling van EIB-SAS, dan waren, naast Alessandro, ook Eric en Henk Jan altijd in staat licht in de duisternis te brengen. Ik wil jullie dan ook graag bedanken dat jullie steeds weer bereid waren jullie kennis met mij te delen en altijd tijd voor mij vrijmaakten als ik iets wilde weten. En niet in de laatste plaats, voor de prettige samenwerking al die jaren.

Frans, Martin, samen zijn jullie soms net die twee heren die vanaf het balkon op extreem grappige wijze de show van de Muppets verstoren. Als jullie er niet bij zijn maakt dat in Italië aan EIB-SAS werken een stuk minder aangenaam. Maar jullie zijn altijd eerste klas engineers. Problemen die mij soms onoverkomelijk lijken lossen jullie steevast in een handomdraai op. Naast een fantastische mechanicus is Frans ook een zeer vaardige kunstenaar. Ik ben dan ook erg dankbaar dat jij de omslag van dit boek hebt willen ontwerpen. Het mag dan mijn naam zijn die op de rug staat, ik ben blij dat jij ook op de kaft te vinden bent.

Op het Nikhef, maar ook in Italië, heb ik op fijne wijze samengewerkt met Willem, Michiel en Arnold. Ik wil jullie bedanken voor alles wat jullie gedaan hebben en dat jullie, naast al het werk dat jullie al deden, altijd bereid waren om even een kort klusje tussendoor te doen.

Fred, bedankt voor jouw bijdrage aan EIB-SAS. Alleen al het meetprogramma dat jij in Labview geprogrammeerd hebt reduceerde metingen die anders maanden zouden duren tot een paar uur werk. Daarnaast weet je ook nog eens alles over elektronica en aanverwante zaken. Menigmaal wist jij wat er scheelde, of wat ik fout deed. Ik heb genoten van onze gesprekken over het werk en het leven en zal je verhalen over vroeger missen als ik niet meer op het Nikhef te vinden ben.

Door de jaren heen hebben vele promovendi, post-docs en andere wetenschappers de gravitiegroep tot een gezellige club gemaakt. Walter, Salvatore, Gideon, Chris, Thomas, John, Jeroen, Tjonnie, Michaelis, Reinier, Joris, Kazuhiro, Laura, bedankt dat jullie mijn tijd op het Nikhef zo aangenaam hebben gemaakt.

David, Mark en Sipho hebben het meeste kleur gegeven aan de jaren die ik op het Nikhef heb doorgebracht. Sipho, ik mis je humor. Ik denk nog vaak terug aan ons avontuur in de binnenstad met Caela. Wat kon die meid drinken... David en Sipho wonen tegenwoordig in het buitenland en zullen waarschijnlijk niet bij de promotie aanwezig zijn. Maar Mark is ook nog eens mijn paranimf. Mark, ik heb gehoord dat paranimfen stammen uit een tijd waarin de verdediging van een proefschrift nog wel eens kon uitmonden in verhitte discussies, waarbij de gemoederen zo hoog konden oplopen dat men op de vuist ging. Omdat er slechts één promovendus was en er meerdere opponenten waren, zorgden twee paranimfen ervoor dat het een wat eerlijkere strijd was. Dus Mark, je bent gewaarschuwd.

Tijdens het lezen van mijn proefschrift bent u misschien een aantal afbeeldingen van EIB-SAS of een van haar onderdelen tegengekomen waarvan u dacht: wauw, die is mooi. Ik wil bij dezen graag mijn dank betuigen aan Marco Kraan voor het feit dat hij de tijd heeft genomen deze plaatjes voor mij te maken. Ze verfraaien dit boek en zorgden ervoor dat mijn poster- en powerpointpresentaties er goed uitzagen.

I would like to thank everyone at EGO for making the time that I've spend living in Pisa an enjoyable one. A special thank you for Bas and Gabriele for teaching me about the Virgo controls and the lock aquisistion. Especially enjoyable were the Wednesday poker nights and weekend skiing trips. In that respect I would like to give special thanks to Martin, because I think if I won any money, his contribution was probably the greatest.

Ik wil Jorn, Thomas, Thijs en Wilco bedanken voor hun vriendschap, steun en gezelligheid voor, tijdens en na mijn promotie.

Voor het leven buiten de wetenschap hebben mijn teamgenoten bij het badminton voor veel lol gezorgd. Duc, Koen, Noortje, Mara, Sonja, Ashley en natuurlijk Joyce, bedankt voor de leuke tijd. Ik ben blij dat Christiaan (mijn broertje en paranimf nummer 2) mij aan het badmintonnen heeft gekregen.

Ik wil mijn familie bedanken voor al hun steun die ze mij mijn hele leven hebben gegeven. Dat jullie altijd vragen bleven stellen en interesse bleven tonen in mijn onderzoek heb ik altijd gewaardeerd. Ik weet dat het niet een alledaags onderwerp was.

Lieve Joyce, jou wil ik het meest bedanken van iedereen. Je hebt veel geduld moeten hebben, maar je hebt me altijd gesteund, je hebt altijd in me geloofd, je staat altijd voor me klaar en je bent ontzettend lief. Van alles wat er de laatste jaren gebeurd is, ben ik het gelukkigst dat ik jou heb ontmoet.

Amsterdam, 19 oktober 2015